Health monitoring of a Brayton cycle-based power conversion unit

Thesis submitted for the degree Doctor of Philosophy
at the Potchefstroom Campus of the
North-West University

Carel P. du Rand

Promoter: Prof. G. van Schoor
December 2007

Abstract

The next generation nuclear power plants like the Pebble Bed Modular Reactor (PBMR) permit for the design of advanced health monitoring (fault diagnosis) systems to improve safety, system reliability and operational performance. Traditionally, fault diagnosis has been performed by applying limit value checking techniques. Although simple, the inability of these techniques to model parameter dependencies and detect incipient fault behaviour renders them unfavourable. More recent approaches to fault diagnosis can be attributed to the advances in computational intelligence. Data driven methods like artificial neural networks are more widely used when modelling complex nonlinear systems, using only historical plant data. These methods are however dependent on the quality and amount of data used for model development.

The key to developing an advanced fault diagnosis system is to adopt an integrated approach for monitoring the different aspects of the total process. Within this context, this goal is realized by presenting a new integrated architecture for sensor fault diagnosis in addition to the enthalpy-entropy graph approach for process fault diagnosis. The integrated architecture for sensor fault diagnosis named SENSE, exploits the strengths of several existing techniques whilst reducing their individual shortcomings. A novel approach for process fault diagnosis is proposed based on the characteristics inherent in the design of the PBMR. Power control by means of an inventory control system and no bypass valve operation facilitates a reference model that remains invariant over the power range. Consequently, the devised reference fault signatures remain static during steady state and transient variations of the normal process.

In the thesis, both single and multiple fault conditions are considered during steady state and transient variations of the normal process. It is demonstrated that by applying SENSE, the fused variable estimates are consistent and more accurate than the individual sensor readings. Test cases corresponding to 32 single and multiple fault conditions confirmed that it is possible to use the enthalpy-entropy graph approach for process fault diagnosis. In addition, the proposed fault diagnosis approach is validated through an application to real data from the prototype Pebble Bed Micro Model (PBMM) plant. This application demonstrated that the proposed approach is ideally suited for early detection of faults and greatly reduces the amount of plant data required for model development.

Acknowledgements

To God with Love

I would like to extend my sincere gratitude to everybody that helped me to complete the work presented in the thesis:

To my supervisor, Prof. George van Schoor for his persistent guidance and valuable inputs.

I would like to thank MTech Industrial (Pty.) Ltd. for the use of the simulation software Flownex.

I greatly appreciate the assistance from the PBMR (Pty.) Ltd. team for all the resources they made available to me.

Furthermore, I am deeply grateful to Chris Nieuwoudt for all his valuable remarks, suggestions and the long discussions.

To all my colleagues at the McTronX Research Group who contributed in various degrees.

The financial support of THRIP and MTech Industrial is gratefully acknowledged.

Lastly, I would like to thank my family and all my friends for their constant support, encouragement and inspiration.

Contents

List of figures

List of tables

Notation and symbols

General notation

PBMR	PBMR (Pty) Ltd.
Flownex	Flownex®
Simulink	Simulink®
Matlab	Matlab®

List of symbols

I	Unit matrix
$v(t)$	Noise vector
$\Phi(\tau)$	Correlation matrix
E	expectation of $x(t)$
t	discrete time
τ	discrete time shift
Q_{PT}	work deliverd by turbine
Q_{HPC}	work absorbed by HPC
Q_{LPC}	work absorbed by LPC
Q_{RU}	heat supplied by reactor
η_{cycle}	cycle efficiency
η_{sy}	switchyard efficiency
η_m	mechanical efficiency
η_{gen}	generator efficiency
P_{house}	house load power
P_{grid}	grid power
m_{RU}	reactor mass flow
c_p	constant pressure specific heat
R	gas constant
h	enthalpy

s	entropy
T	temperature
P	pressure
μ	normal distribution mean
σ	standard deviation
σ^2	normal distribution variance
γ	normal distribution skew
Δx	maximum process change
τ	normal distribution confidence value
x_f	fused estimate
s_c	sensor configuration matrix
s	fault signature
p_{ref}	reference parameter value
p	measured parameter value
s_{norm}	normalized fault signature
r	Euclidean distance
r	error vector
$\mathbf{r_N}$	noise vector
s_{area}	Area error signature
ψ	covariance matrix
χ^2_α	hypothesis threshold
Δp_0	pipeline pressure drop
ε	heat exchanger effectiveness
η	turbo machinery efficiency
AU	product of the heat transfer area and the overall heat transfer coefficient
PR	turbo machinery pressure ratio
p	parity vector
V	projection matrix
X	measurement matrix
E	residual space matrix
P	principles components vector
δ^2_{SPE}	SPE threshold
ξ_i	fault direction vector

Acronyms

AANN	Auto-associative neural network
CBCS	Core barrel conditioning system
CC	Correlation coefficient
CFD	Computational fluid dynamics
CWT	Cooling water temperature
EPRI	Electric power research institute
FDI	Fault detection and isolation
FII	Fault isolation index
GBPC	Gas cycle bypass control valve
HP	High pressure
HPC	High pressure compressor
HTGR	High-temperature gas-cooled reactor
HV	High voltage
ICA	Independent component analysis
ICMP	Instrument and calibration monitoring program
ICS	Inventory control system
LP	Low pressure
LPC	Low pressure compressor
MCR	Maximum continuous rating
MCRI	Maximum continuous rating inventory
MPS	Main power system
MSET	Multivariate state estimation
NLPLS	Nonlinear partial least squares
NN	Neural network
NPP	Nuclear power plant
NRC	National regulatory commission
OLM	On-line monitoring
PBMM	Pebble bed micro model
PBMR	Pebble bed modular reactor
PCA	Principle component analysis
PCU	Power conversion unit
PLS	Partial least squares
PPB	Primary pressure boundary

PR	Pressure ratio
PT	Power turbine
RBP	Recuperator bypass valve
RMSE	Root mean squared error
ROT	Reactor outlet temperature
RSQ	r-square statistic
RU	Reactor unit
RUCS	Reactor unit conditioning system
SENSE	Sensor validation and fusion module
SPE	Square prediction error
VM	Variance and mean index
VRE	Variance of the reconstruction error
VS	Variation surface

CHAPTER 1

Introduction

This chapter lists the primary objectives of the study together with an overview of the chapters presented.

1.1 Motivation

Advanced system diagnostics have been extensively researched the past few years to support nuclear power plant (NPP) utilities in plant supervision. The most important tasks of these diagnostic systems are fault detection and isolation. Even though research shows that these diagnostic systems are essential to prolong the lifespan of the plant, only a few real systems are actually installed in operating units [1], [2]. For the next generation type NPPs, it is expected that these diagnostic systems will become a necessity.

From a theoretical point of view, fault diagnosis of nonlinear systems is particularly difficult [2]. In addition, obtaining a sufficient accurate analytical model for complex processes like NPPs could take years. Traditionally, limit value checking techniques have been proven to perform well if the plant operates close to steady state. However, implementing a diagnostic system that performs well only during steady state conditions is not a desirable trait. Another traditional approach to fault diagnosis is signal processing. The difficulties with these techniques are distinguishing between changes in the signal properties due to faults or transient variations of the process.

More recent approaches to fault diagnosis can be attributed to the advances in computational intelligence [3]. The methods are however data-driven and dependent on the quality and amount of data used for model development. Acquiring such data for the entire operating range in the next generation NPPs will be very difficult due to economical impacts on normal operation.

All these factors motivate the development of a new approach to NPP supervision. The goal is to realize a total health monitoring system that is simplistic, reliable and most important, accurate for different variations of the supervised process.

1.2 Problem description

Given the preceding motivation, the goal of the study is to develop an advanced fault diagnosis approach for NPP supervision. The approach should facilitate a novel sensor and process fault diagnosis technique that functions independently. To address these problems, the following solutions are proposed:

- The goal of advanced sensor fault diagnosis is realized by integrating existing techniques in a new way to reduce their individual shortcomings. Measurement redundancy is exploited to allow early detection of instrument drift.

- A novel approach to process fault diagnosis is accomplished by developing a new method based on a graphical representation of the supervised process. This technique aims to minimize the amount of monitored variables necessary to quantify the overall health of the system without any knowledge of the mathematical structure of the nonlinear dynamic process.

1.3 Thesis objectives

The goal of the thesis is to develop a novel approach to fault diagnosis in a nonlinear high-temperature gas-cooled reactor (HTGR) NPP. To address the shortcomings of current fault diagnosis techniques, the main objectives of the study are:

1. Determine the most relevant mechanisms for component degradation in an HTGR main power system (MPS) and formulate suitable fault classes.

2. Develop and implement a comprehensive fault diagnosis approach for health monitoring in an HTGR MPS. The approach must comprise independent sensor and process fault diagnosis methods. Specifically, the following areas are addressed:

   2.1 Propose and implement a novel integrated architecture for sensor fault diagnosis to take advantage of the strengths of existing techniques. For this goal, the independent detection of instrument drift is emphasized.

   2.2 Propose and implement a novel approach for process fault diagnosis. The goal is to develop a method that adheres to the strengths of existing techniques without incorporating their general deficiencies. The following desirable qualities must be realized:

      2.2.1 Robustness with regard to fault propagation, noise and modelling errors.

      2.2.2 Model development and re-training should be simplistic.

      2.2.3 Early detection of small faults with incipient time behaviour.

2.2.4 Supervision of the process during transient variations of the normal process.

2.2.5 Isolation of single faults for multiple fault symptoms.

3. Validate the proposed process fault diagnosis approach through application in the Pebble Bed Micro Model (PBMM). Since there are many ambiguities inherent from directly inducing faults in the real system with regard to control and safety concerns, faults are only simulated.

The following constraints are imposed on the simulated HTGR NPP:

1. Since the HTGR NPP is mostly operated at full power, only normal power operation of the plant is investigated. This includes steady state operation and transient variations of the normal process.

2. The number of system faults is limited. Also, critical system faults that cause mode and state transitions of the plant are not applicable (discussed in Chapter 3). These faults are accommodated in the automated plant protection systems. From this constraint, it is concluded that the faults will typically be characterized with incipient time behaviour caused by plant degradation.

1.4 The diagnostic methodology

The engineering aspects of the study commence in Chapter 3. Firstly, a simplified model of an HTGR is developed in Flownex® comprising the key MPS components. Through a sensitivity analysis of the model, the most relevant system faults are identified (caused by the component degradation mechanisms). The fault parameters are grouped with regard to cause and effect and the final listing of probable single system faults is summarized. The choices for the fault symptoms are motivated and their importance was confirmed with engineers at PBMR (Pty.) Ltd. Following this, an optimized design of the PBMR that includes the inventory control system (ICS) is modelled in Flownex which serves as the reference NPP.

The sensor and process fault diagnosis system is developed using Matlab®, Simulink® and Flownex. By means of a Flownex and Simulink interface, data is collectively transferred between the Flownex and Simulink models. Firstly, random noise with different variance is added to the Flownex measurements, which is then passed through a filter model that infers the appropriate sensor malfunctions on the signals. Next, the signals are evaluated by SENSE (Simulink m-file) and the fused estimates are passed to the process fault diagnosis module (Simulink m-file). After signal transformation, the model residuals are checked for consistency. If a discrepancy is detected, fault signatures are extracted from the residuals and matched to the reference fault database with a statistical classifier. Finally, the relevant information regarding process status and sensor health is collectively displayed.

1.5 Thesis layout

An overview of health monitoring techniques is presented in **Chapter 2** together with some basic terminology. For the purpose of advanced sensor fault diagnosis and parameter estimation, two redundant and three non-redundant techniques are investigated. To incorporate techniques that will be readily acceptable to regulatory bodies, the Nuclear Regulatory Commission regulations pertaining to on-line monitoring techniques are examined. For the second part of the chapter, process monitoring methods are discussed with their advantages and shortcomings. Lastly, the overall structure of the proposed process fault diagnosis approach is presented.

Chapter 3 describes the general topology of the PBMR MPS and stipulates the relevant operating conditions. Through a sensitivity analysis of a simplified PBMR model, the type and origin of the component performance parameters are identified that are synonymous to the probable fault parameters caused by the component degradation mechanisms.

Chapter 4 describes the development of a comprehensive sensor fault diagnosis methodology. The relevant monitoring techniques identified in Chapter 2 are integrated to reduce their individual shortcomings and improve measurement integrity. The fault detection and isolation capabilities of the proposed methodology are demonstrated through application to PBMR and PBMM data. With regard to the latter, real plant data obtained from the PBMM prototype plant is used for the validation.

Chapter 5 applies two traditional process fault diagnosis techniques to the PBMR. These methods are based on limit value checking of the monitored variables and mathematical modelling of the plant for the purpose of residual generation. The implementation of the methods in the PBMR highlights their general limitations.

Chapter 6 derives the *h-s* graph approach for process fault diagnosis. Firstly, two analytical techniques are utilized to generate reference fault signatures (with Flownex) for the related fault symptoms; whereafter the correlation among the fault signatures is established. It is demonstrated that each of the different reference fault signatures are highly correlated during transient variations of the normal process with negligible variation. Following this, the fault detection and isolation tasks are developed by means of a statistical hypothesis test and classifier that decide whether a given set of process observations contains any faults. In the presence of multiple fault symptoms, a single fault subtraction procedure is formulated to extract and classify the contributing single faults. To incorporate normal process variations like valve changes into the reference system model, the variation surface is proposed. In the final part of the chapter, the proposed methodology is applied to the PBMR. Fault detection and isolation is demonstrated for both steady state and transient conditions.

Chapter 7 validates the *h-s* graph approach for process fault diagnosis through application in the prototype PBMM plant. Firstly, plant measurements captured during test runs are used to validate the integrity of the FLOWNEX simulation model. Following this, a reference system model together with fault signatures is derived for two emulated fault conditions. Lastly, the *h-s* graph approach is utilized for process fault diagnosis to identify the emulated fault symptoms in the plant data.

Chapter 8 summarizes the most important conclusions reached in the thesis and documents the original scientific contributions of the study. Recommendations and suggestions for future research are also presented.

Appendix A lists the central limit theorem. In the thesis, assumptions regarding the measurement noise are based on the theorem.

In **Appendix B**, the prove for the constant shape of the *h-s* graph at different power levels (bounded by constraints) is derived. This idea forms the basis for the proposed methodology. Following this, the improvement in model prediction is demonstrated through transformation of the measured variables.

1.6 Original contributions

The main scientific contributions of the thesis are summarized as follows:

- A novel approach is proposed for process fault diagnosis in an HTGR NPP. Plant supervision is realized with a graphical model-based process model (*h-s* graph) that remains invariant over the power range. The proposed error and area error methods provide static reference *h-s* fault signatures that remain invariant to operating point changes, transient variations of the normal process and changes in the fault magnitude. There was no reference found to such an approach for process fault diagnosis in an HTGR NPP.

- In addition, a new integrated architecture is proposed for sensor fault diagnosis that forms a comprehensive methodology of existing techniques. In a multi-sensor environment, the unique reasoning structure of this approach produces more accurate and reliable estimates of the sensed variables. A literature survey revealed that this unique and integrated reasoning structure has not been developed for application in an HTGR NPP.

1.7 Publications

"Enthalpy-entropy graph approach for the classification of faults in the main power system of a closed Brayton cycle HTGR", Annals of Nuclear Energy, Article in press.

Article abstract:

An enthalpy-entropy (h-s) graph approach for the classification of faults in a new generation type high temperature gas-cooled reactor (HTGR) is presented. The study is performed on a 165 MW model of the main power system (MPS) of the pebble bed modular reactor (PBMR) that is based on a single closed-loop Brayton thermodynamic cycle. In general, the h-s graph is a useful tool in order to understand and characterise a thermodynamic process. It follows that it could be used to classify system malfunctions from fault patterns (signatures) based on a comparison between actual plant graphs and reference graphs. It is demonstrated that by applying the h-s graph approach, different

fault signatures are derived for the examined fault conditions. The fault conditions that are considered for the MPS are categorized in three fault classes and comprise the main flow bypass of the working fluid, an increase in main flow resistance, and a decrease in component effectiveness or efficiency. The proposed approach is specifically illustrated for four single and two multiple fault conditions during normal power operation of the plant. The simulation of the faults suggests that it is possible to classify all of the examined system malfunctions correctly with the h-s graph approach, using only single reference fault signatures.

CHAPTER 2

Fault detection and isolation

This chapter gives a comprehensive review of advanced health monitoring techniques used in NPPs. In addition, the mechanisms for component degradation in HTGRs are discussed.

2.1 Introduction

Health monitoring is an important component in any large scale engineering plant to improve safety, reliability and overall plant performance. With this in mind, the next generation HTGR NPPs offer more complex challenges for advanced system diagnostics. This chapter gives a summary of the different health monitoring techniques that are currently either implemented or proposed for implementation in NPPs.

In section 2.2, the fundamental concepts and basic terminology of health monitoring are introduced together with the total health monitoring framework. The framework includes several different tasks and comprises fault detection, fault isolation and fault identification.

Section 2.3 presents an overview of different techniques that are applicable to NPP sensor fault diagnosis and process state estimation. Furthermore, the motivations for the techniques used in the thesis are also discussed.

Section 2.4 summarizes some of the most relevant process fault diagnosis techniques. These techniques are mainly model-and process history based methods, each with their own unique strengths and weaknesses. In the final part of this section, the desirable qualities of an advanced fault diagnostic approach are presented, together with the general framework of the proposed approach.

In order to determine the specific fault classes in the PBMR, section 2.5 presents an outline of the most relevant mechanisms for component degradation in HTGRs. These mechanisms include component corrosion, erosion, fouling and leakage.

A summary of this chapter is presented in section 2.6.

2.2 The scope of health monitoring

In modern NPPs, information about the current health of the system is essential to improve plant safety and operational levels [4]. Therefore, it is important to detect component faults and irregular system operation promptly.

2.2.1 Fault classification

In general, unpermitted deviations from the normal behavior of the components or process are termed faults or failures. Faults are caused by physical defects or imperfections that occur within the component, whilst a failure suggest complete breakdown of the component [5]. The faults that are applicable for this investigation can be divided into the following categories [6]:

- *Additive process faults*: These faults are caused by unknown inputs acting on the plant, which results in a shift in the plant outputs, independent of the measured inputs. A plant leak is a typical example of an additive fault.

- *Multiplicative process faults*: These faults result in system parameter changes, where the outputs are dependent on the magnitude of the inputs. Such faults are mostly associated with component degradation and include fouling and efficiency changes.

- *Sensor faults*: Any discrepancies between the measured and the expected values of the process variables are considered to be sensor malfunctions.

- *Actuator faults*: These faults are described by discrepancies between the intended control actions and the actual realization of these commands by the actuators.

2.2.2 The health monitoring tasks

In order to identify and characterize the faults, the health monitoring system should comprise the following tasks [6]:

- *Fault detection*: The identification of an irregularity in the monitored system.

- *Fault isolation/classification*: The origin and the type of fault are determined.

- *Fault identification*: The magnitude of the fault is established.

The fault identification phase generally does not justify the additional computation it requires, and for this reason, most monitoring systems only comprise the fault detection and isolation (FDI) phases [6]. For the proposed diagnostic system, real-time computational complexity is reduced by implementing only the fault detection and

isolation tasks. The drawback from this restriction is that the fault magnitude will not be directly calculated, but rather estimated from the fault signature magnitude before normalization.

With the help of early fault detection and accurate fault isolation, process and component malfunctions can therefore be identified at an early stage to reduce the risk of sudden failure as well as allow enough time for maintenance or repair. Given the complex and safety critical nature of NPPs, the advanced FDI tasks should adhere to the following requirements [7]:

- Reduce the occurrence of false alarms during operation due to normal transient variations of the process.
- Original fault detection in the event of multiple fault conditions and propagation across subsystems.
- Early detection of small faults with abrupt or incipient time behavior.
- Reducing misdiagnosed faults due to modelling uncertainties and noise.

2.2.3 The health monitoring method

Designing a system for advanced fault diagnosis is a challenging engineering task, particularly in fields related to nuclear processes, owing to the stringent safety and environmental regulations. For these reasons, it is important that the diagnostic method meet the following performance requirements [6]:

- *Fault detection*:
  - *Fault sensitivity*: The method must detect incipient faults with a small magnitude.
  - *Detection time*: The method must be able to detect faults with the smallest time delay after induction.
  - *Robustness*: The method must be able to function in the presence of noise, modelling uncertainties and disturbances, with minimal false alarms.
- *Fault isolation*: The method must be able to distinguish between the different types of faults (single or multiple simultaneous faults) in the presence of noise and modelling errors. It is important to note that some faults, single or multiple, might be non-isolable, since their influence on the system is undistinguishable [6].

The health monitoring system, which constitutes sensor and process FDI, is illustrated in Fig. 2.2.1.

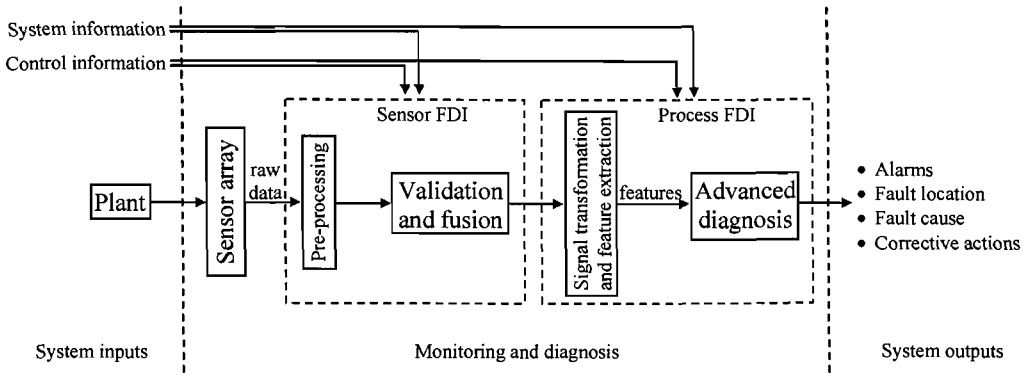

Fig. 2.2.1 The health monitoring system.

2.3 Sensor fault detection and isolation

This section reviews current sensor fault diagnosis techniques ranging from basic, well established methods to the latest reported advanced strategies. Throughout the literature, various methods are proposed by the industry and academia [8] - [15]. Advanced in this context signifies methods that will allow nuclear power utilities to diverge from utilizing a periodic based maintenance approach to condition based strategies. In general, these advanced methods aim at describing the sensors health whilst the plant is operational. A simple block diagram illustrating a sensor monitoring system is depicted in Fig. 2.3.1.

Based on research applications, the most relevant techniques used in NPPs include the parity space method, principle component analysis (PCA), independent component analysis (ICA), instrumentation and calibration monitoring program (ICMP), nonlinear partial least squares (NLPLS), multivariate state estimation (MSET) and auto-associative neural networks (AANN) [16]. These techniques can roughly be classified into two categories: techniques that model a redundant group of sensors to obtain the estimate (first four) and models that include non-redundant measurements that are correlated, but not redundant (last three).

A study conducted by [16] concluded that the simplicity of redundant techniques and the tractability of their uncertainty calculations could favour them for acceptance by regulatory bodies. For this reason, the non-temporal parity space and PCA techniques are adopted for sensor fault diagnosis based on their relative simplicity and individual strong points (discussed in Chapter 4).

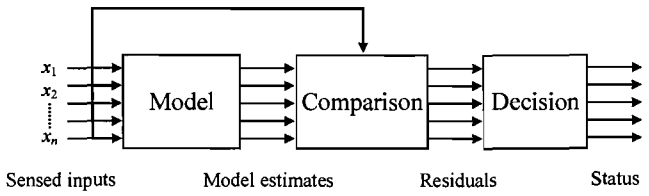

Fig. 2.3.1 A simple sensor monitoring system [16].

The following sections discuss and compare the applicability of the remaining techniques for sensor fault diagnosis and highlight their general limitations.

In this thesis, it is important to note that only a general overview of each technique is presented together with the basic notation. For the complete mathematical formulations, the reader is referred to the literature referenced.

2.3.1 Independent component analysis

In ICA, the sensed variables are described by means of a linear transformation of independent components that is maximally non-Gaussian (normally) distributed [16]. An important characteristic of this technique is its ability to separate the true signal (includes process noise) from the independent measurement noise [17]. This makes ICA a notable candidate for signal pre-processing and filtering. The ICA model is given by (2.3.1)

$$\mathbf{X} = \mathbf{AS} \tag{2.3.1}$$

with **X** the observed data of n samples from m sensors, **S** is the matrix of m independent components and **A** the mixing matrix. The linear transformation of the observed data into non-Gaussian distributed components **Y** is

$$\mathbf{Y} = \mathbf{WX} \tag{2.3.2}$$

where **W** is the weight matrix. The parameter estimate, which denotes the true signal with process noise, is then given by one of the independent components.

2.3.2 Instrumentation and calibration monitoring program

The ICMP was developed by the Electric Power Research Institute (EPRI). The ICMP algorithm is based on a weighted average of each sensor, which is denoted by consistency values c_i [16]. The consistency values signify how much a sensor reading contributes to the final estimate. If the value correlates within the defined limits to another, they are consistent. The consistency value c_i of the i-th sensor is calculated with

$$\left|x_i - x_j\right| \leq \partial_i + \partial_j, \text{ then } c_i = c_i + 1 \tag{2.3.3}$$

with x_i, x_j the values of the i-th and j-th sensors and ∂_i, ∂_j the consistency check allowance for sensor i and j respectively. The values are checked for consistency in an iterative way against the remaining sensors. The ICMP parameter estimate $\hat{x}$ is calculated with

$$\hat{x} = \frac{\sum_{i=1}^{n} x_i c_i w_i}{\sum_{i=1}^{n} c_i w_i} \tag{2.3.4}$$

where w_i is the weight related to the i-th sensor. The influence of more reliable sensors within a redundant group can therefore be increased by varying their weights. If there is no preference between the sensors, the weights are set to 1. Following this, the performance of each sensor is determined in relation to $\hat{x}$ through an acceptance criterion

$$\left|\hat{x} - x_i\right| < a_i \tag{2.3.5}$$

where a_i is the acceptance criterion of the i-th sensor. If the condition stipulated by (2.3.5) is not met, x_i has potentially drifted beyond the acceptable limits and its value is not considered.

2.3.3 Nonlinear partial least squares

The NLPLS technique is an extended nonlinear version of the partial least squares method (PLS) [18], [19]. For a theoretical overview of the PLS algorithm, the reader is referred to [20]. In NLPLS, the linear regression between pairs of score vectors is substituted by a single input single output neural network (NN). Each NN constitute a single hidden layer with a single output neuron. The number of NNs required is equivalent to the number of orthogonal input score vectors retained in the model. Moreover, the amount of NNs is considerably smaller than the number of input sensors. The NLPLS structure, together with the inner workings of one of the NNs, is illustrated in Fig. 2.3.2. The notation and complete structure is documented in [18].

2.3.4 Multivariate state estimation

MSET is a non-parametric kernel regression technique, which utilizes a similarity operator to compare new observations with stored measurements [16]. Unlike neural networks, the optimal weights are not determined a priori. Through comparison, a weight vector is determined to compute a weighted sum of the stored measurements. This is done to generate an estimate for the sensor value.

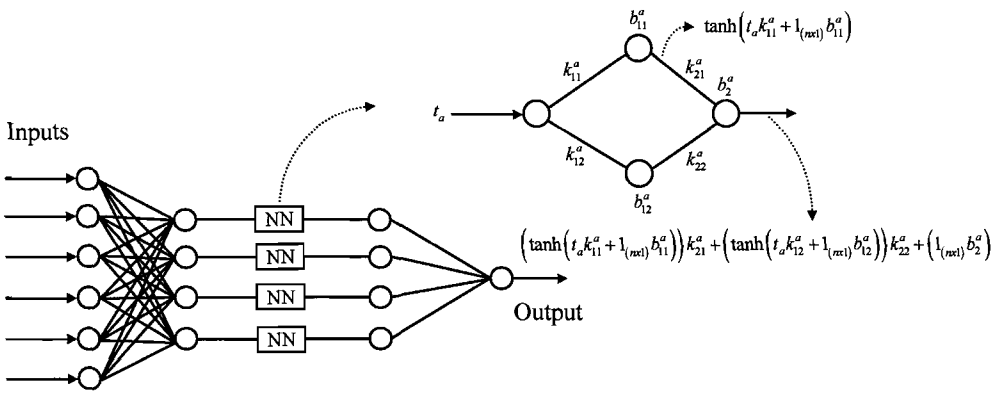

Fig. 2.3.2 The structure of a NLPLS [18].

The MSET technique is based on linear regression [21], with the estimate $\hat{\mathbf{x}}$ equal to the product of a reduced measurement matrix **A** (prototype matrix) and weight vector **w**

$$\hat{\mathbf{x}} = \mathbf{A}\mathbf{w} = \mathbf{A}\left[\left(\mathbf{A}^T\mathbf{A}\right)^{-1}\left(\mathbf{A}^T\mathbf{x}\right)\right] \tag{2.3.6}$$

where **x** is the observed state, the left factor of the matrix product is the recognition matrix and **A** is reduced to only include the variations in the measured data. In (2.3.6), the linear relations in **A** results in conditioning problems related with the inversion of the recognition matrix.

In contrast to linear regression, MSET introduces nonlinear operators and consequently, the recognition matrix is better conditioned. The estimate $\hat{\mathbf{x}}$ is given by

$$\hat{\mathbf{x}} = \mathbf{A}\mathbf{w} = \mathbf{A}\left[\left(\mathbf{A}^T \oplus \mathbf{A}\right)^{-1}\left(\mathbf{A}^T \otimes \mathbf{x}\right)\right] \tag{2.3.7}$$

with $\otimes$ and $\oplus$ representing nonlinear similarity operators termed kernel operators. A typical similarity operator is the Gaussian operator [22]

$$k_s\left(x, x_i\right) = \frac{1}{\sqrt{2\pi}s} e^{\frac{(x-x_i)^2}{2s^2}} \tag{2.3.8}$$

with s the smoothing parameter, x the data point that is being compared to x_i, and x_i the data point around which the kernel is placed.

2.3.5 Auto-associative neural networks

The AANN structure utilizes an input layer, three hidden layers and an output layer [23], [24] and is illustrated in Fig. 2.3.3. The hidden layers comprise a mapping layer, bottleneck layer and de-mapping layer. The number of neurons in the mapping and de-mapping layers is always greater than the input/output layers, whilst the bottleneck layer has the least amount of neurons in the structure.

Basically, the reduction of the data from input to output is similar to PCA. The mapping layer compresses the data in a more compact representation of the training data by eliminating any redundancies whilst extracting the dominating features (principle components). The data is then recovered via the de-mapping layer from the principle components. Therefore, if a measurement is corrupted, it can be substituted with an estimate from the remaining valid sensors.

2.3.6 Comparisons and limitations

This section documents some of the shortcomings and desirable qualities of the advanced OLM techniques discussed [16]. Firstly, although most of the techniques are very little

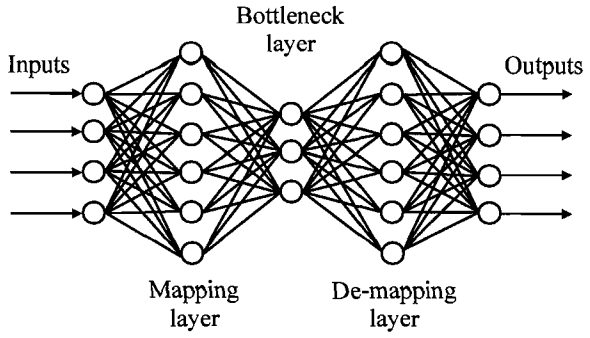

Fig. 2.3.3 The structure of an AANN.

affected by spillover, non-redundant techniques perform better in this situation. Spillover is a measure of how a drifting sensor input affects the predictions of the remaining sensors. A technique that is resistant to spillover will not be influenced by a drifting sensor, i.e. the other sensor estimates will not be degraded.

The ICA technique has the ability to separate the true signal from channel noise, which renders it as a filtering technique also. Nevertheless, some of the ambiguities of ICA are that neither the variances nor the order of the independent components can be determined. This can be problematic when performing OLM since the component containing the estimate needs to be selected and scaled back to its original units. Furthermore, ICA is based on the assumption that the measurement data is time invariant, which does not hold when the plant undertakes a significant transient. During the transient, the data becomes nonstationary and the ICA method fails.

The ICMP technique delivers excellent results overall. Some of its shortcomings are that the failed sensor (acceptance criterion exceeded) value can still influence the ICMP estimate. The failed sensor is only excluded form the estimate once the consistency check factor is also exceeded. Also, ICMP is unable to detect common mode failure (all the redundant sensor values drift in the same direction at the same rate).

It is well established in the industry that all of the non-redundant OLM techniques discussed perform well. Some of the notable differences are:

- MSET is easier to implement and requires no training. The model is extended to include new operating conditions by simply adding the new data vector to the prototype matrix.

- NLPLS techniques inherently produce more consistent estimates and are quicker to train with regard to AANN models.

However, many aspects may limit the usefulness of these techniques. One limitation is that the model can only make confident predictions in the region of the training data. For inputs outside this space, there will be no confidence associated with the model's prediction. Also, the uncertainty inherent in the model predictions must be correctly calculated. This factor is of main concern with regard to applicability and is discussed in the following section.

2.3.7 Uncertainty analysis

Uncertainty analysis refers to the quantification of the prediction uncertainty associated with the model estimate when safety-critical parameters are being monitored. This is a prerequisite by regulatory bodies for approval of the OLM technique [25], [26]. The requirement stated in the Nuclear Regulatory Commission (NRC) safety evaluation reads as follows:

The submittal for implementation of the on-line monitoring technique must confirm that the impact of the deficiencies inherent in the on-line monitoring technique (inaccuracy in process parameter estimate single-point monitoring and untraceability of accuracy to standards) on plant safety be insignificant, and that all uncertainties associated with the process parameter estimate have been quantitatively bounded and accounted for either in the on-line monitoring acceptance criteria or in the applicable set point and uncertainty calculations.

The various methods of uncertainty analysis belong to either analytical or Monte Carlo based algorithms, each of which constitutes different assumptions. The analytical based methods comprise analyses for NLPLS, MSET and AANN, whilst Monte Carlo based analysis are conducted for ICMP and ICA [16]. A detailed technical description of each algorithm is given in [27].

Factors that contribute to prediction uncertainty are model structure including complexity and misspecification, accuracy and selection of training data, the selected predictor variables, and noise. Over complex models will tend to fit the noise in the training data, while models without flexibility will bias the predictions. Also, improper model specification will result in a biased estimate. Different training data sets will produce different models, which results in a distribution of estimates for a given observation. In addition, selecting unrelated predictor variables increase the solution variance.

Therefore, to demonstrate to validity of the uncertainty for an OLM technique, the prediction uncertainty must be lower than the allowable drift for each parameter to ensure the sensor is operating in its normal range. To date, the techniques that have undergone a full uncertainty analysis are MSET, ICMP, ICA, PCA [16], [28], [29].

2.3.8 Conclusions

The following conclusions are formulated from the literature reviewed:

- While many of the complex non-redundant OLM techniques deliver accurate estimates together with acceptable uncertainty analyses, it is concluded that the uncertainty associated with redundant techniques and their relative simplicity makes them more readily acceptable by nuclear regulatory bodies [16].

- Neural networks are generally excluded from consideration as state predictors for OLM applications in NPPs [16]. However, they are well suited for fault pattern recognition in process fault diagnosis systems [1], [4], [31]-[34].

For these reasons, redundant techniques will be applied for sensor fault diagnosis. These techniques will be applied in an original integrated way to form a comprehensive sensor diagnostic system which aims to minimize their individual shortcomings. The redundant techniques considered are:

- The non-temporal parity space (NTPS) algorithm: NTPS is utilized for consistency analysis of similar measurements [30]. The consistent measurements are fused together to reduce the size of the measurement matrix.

- The PCA algorithm: PCA is employed for state prediction [8]-[10], [29]. Although ICA has some advantages over PCA (does not assume the principle components are orthogonal), it does not perform well during significant transients of the process.

2.4 Process fault detection and isolation

Objective two of the study listed the desirable qualities of advanced process fault diagnosis techniques in NPPs. With this in mind, current well established techniques are evaluated in this section to determine their strong points and shortcomings, i.e. techniques incorporating artificial intelligence [31]-[39] and traditional model-based techniques [40]-[44]. The proposed approach will aim to incorporate these strong points whilst minimizing their individual shortcomings.

Process fault diagnosis techniques can be broadly classified as model-or process history based. *Model-based* techniques rely on a fundamental understanding of the process using mathematical relations or first principle knowledge [7]. These methods are further classified as either *quantitative*, which includes parity equations, state and parameter estimation, or *qualitative* methods, which include digraphs and fault trees [40]. When information about the complex process is not available, qualitative methods are used to build constrained models that describe how parameters are related to each other. Limitations of qualitative methods include generation of a large number of hypotheses which makes the decision process uncertain, computational intense and complex.

Process history based methods on the other hand rely on an abundance of process data. These methods can also be classified as *quantitative* methods, which includes NNs and PLS, or *qualitative* methods which include expert systems and qualitative trend analysis. Although qualitative methods are good at representing heuristic knowledge (provided by experts, operators etc.), they are hard to verify, are not good at representing time-varying phenomena, and their accuracy is difficult to prove.

In contrast, the majority of quantitative model-or history based techniques offer some strong points for application in NPPs. To incorporate these qualities in the proposed approach, their characteristics are summarized next.

2.4.1 Model-based methods

Process model-based fault detection methods [7], [40]-[44] use residuals which indicate any discrepancies between the model and the monitored process. A basic scheme of process model-based FDI is depicted in Fig. 2.4.1. One drawback of these FDI methods is that they rely on an explicit mathematical model of the monitored process. This model may be representative of a state space representation, steady state balance equations, first principles modelling, partial differential equations or a transfer function. Any inconsistencies in the residuals can then be used for fault diagnosis. To test the residuals for abnormal behaviour, a statistical test is usually implemented as a decision rule or hypothesis.

In a practical application, all the model-based methods perform differently. Parity equations are typically limited to faults that do not include large process parameter drifts. Parameter estimation on the other hand is computationally intensive for complex nonlinear processes, therefore not favouring a real-time solution. Although the latter does not require a precise model *a priori*, this approach to FDI is one of complexity throughout. State estimators in contrast require a precise dynamic process model and can mostly only detect large abrupt faults. This is due to the fact that the state variables are not so often directly affected by multiplicative process faults (changes in fluid resistance, heat exchanger coefficients etc.).

In conclusion, the desirable characteristics of model-based methods are that potential faults are directly reflected in the residuals, which functions as the fault detection task. One major disadvantage of these methods is their applicability to nonlinear applications. For a nonlinear process, a linear transformation is usually required which may be very difficult to obtain [40].

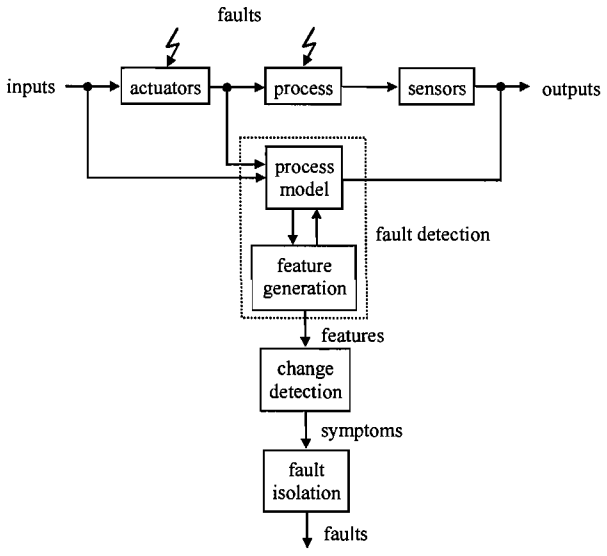

Fig. 2.4.1 A basic process model-based fault FDI scheme [41].

2.4.2 Process history based methods

In the case of a complex nonlinear process, where mathematical models are hard to develop, NNs emerged as a suitable solution in NPPs [1], [3]-[4], [31]-[34]. The processing elements of a NN are similar to those depicted in figures 2.3.2 and 2.3.3. The appropriate training of such a network forms input-output relations into a 'black box' model which is difficult to comprehend. This unknown internal reasoning structure of the network is inherent one of its drawbacks.

For the task of fault isolation, the success of this approach is highly dependent on the amount and quality of the training data, i.e. examples from which it will infer a decision. In addition, the data must cover operating conditions that is representative of all the transient variations of the monitored process, including the faulty ones. Acquiring such data for a safety critical process is unrealistic and therefore, the NN may be used as a model-based predictor instead.

In conclusion, one of the main drawbacks of NNs is the lack of knowledge about the internal reasoning process. Consequently, the accuracy of the results is uncertain for unknown process variations or new operating conditions. Additionally, NNs require large amounts of quality training data that covers the entire range of process operation. Nevertheless, they are especially suitable for nonlinear model development since an explicit mathematical model of the process is not required.

2.4.3 Desirable qualities of the fault diagnosis approach

The desirable qualities and general shortcomings of current process fault diagnosis techniques are listed in the previous section. In view of these characteristics, the following desirable qualities should be adopted for advanced process fault diagnosis in addition to section 2.2.3 [40]:

- *Adaptability*: The process generally changes or evolves during the lifespan of the plant due to normal component ageing. The diagnostic approach should adapt to these changes.

- *Modelling requirements*:
  - The modelling effort should be minimal.
  - Knowledge about the mathematical structure should not be a prerequisite.
  - The reasoning structure must be clearly understood.
  - A relative small dataset must quantify the entire range of operation.

- *Storage/computational requirements*: The approach should be computationally noncomplex and require the least amount of storage space.

2.4.4 The proposed process fault diagnosis approach

In the thesis, a novel process fault diagnosis approach is proposed comprising the following characteristics:

- The overall approach is model-based, realized by a graphical reference process model. This incorporates the 'no mathematical model' advantage of process history based methods into a model-based approach.
- The model-based approach is utilized to monitor the model residuals for any discrepancies.
- The proposed graphical process model is representative of a nonlinear dynamic process.
- Unlike process history based methods, the graphical process model is trained with a minimal amount of steady state data.
- Graphical fault signatures (patterns) are derived from the model residuals.
- A statistical classifier is employed for fault pattern recognition.

The proposed approach is shown schematically in Fig. 2.4.2. The objective of this approach is to decide if a given set of process measurements contains any faults and to isolate them. In order to achieve this goal, reference fault signature patterns are utilized which are derived by means of simulations of the process in Flownex. The residuals features are extracted and a reference fault signature database is generated. Once the database is developed, the proposed approach can be used to classify system faults. The FDI procedure is as follows: for a given time instant, the graphical process model shifts

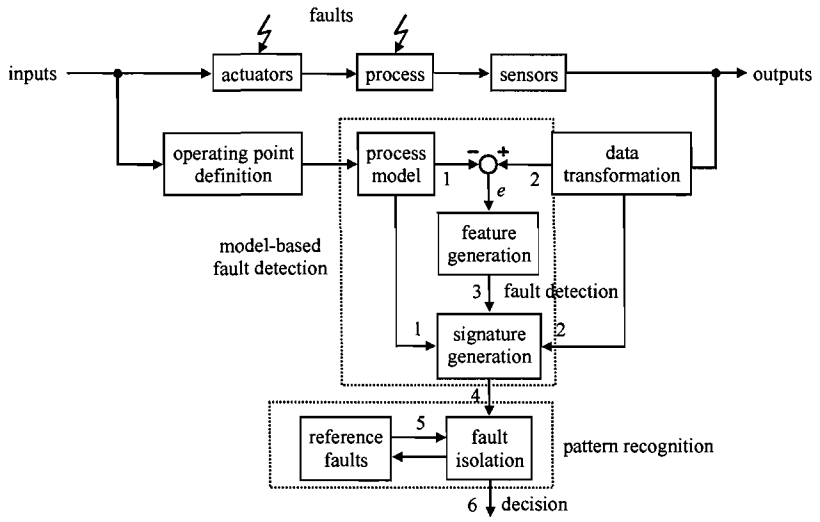

Fig. 2.4.2 The proposed novel process FDI scheme.

to the operating point defined whereafter a residual is generated between the transformed measurements and the graphical reference model. In order to detect a fault, the residuals are evaluated with a statistical hypothesis test. If the thresholds are exceeded, a fault signature is generated and compared to the reference fault database using a statistical classifier (fault pattern recognition).

2.4.5 Conclusions

The following conclusions are formulated regarding the proposed process fault diagnosis approach:

- The tasks of fault detection and isolation are achieved by applying a graphical model-based approach for the dynamic nonlinear process.
- By applying a graphical model-based approach, the mathematical model of the plant is not required.
- The process model is developed with minimal training data.

2.5 Component and system degradation in HTGRs

In HTGRs, the mechanisms of component degradation include corrosion, erosion, fouling and leakage. It must be noted that the objective of the thesis is to determine the most relevant fault symptoms in HTGRs (Chapter 3) and therefore, the chemical reactions that cause these symptoms are not discussed.

During the past few decades, material behaviour in HTGRs has been mainly focused on steam-cycle and process-nuclear-heat based applications. In this time period, very little knowledge was developed with the emphasis on direct-cycle gas-turbine-based HTGRs [45].

Helium, because of its chemical inertness and attractive thermal properties, is used as primary coolant (working fluid) in gas-turbine-based HTGRs. Although helium by itself is inert to the materials it is exposed to, small amounts of gaseous impurities such as H_2, H_2O, CH_4, CO, CO_2 and O_2 contaminate the coolant. Within the MPS, structural alloys of components and pipelines can be significantly corroded by these gaseous impurities at high temperatures [45]. Corrosion of heat resistant materials include oxidation, carburization and decarburization, which are dynamic in nature, i.e. the corrosion process is a function of exposure time, gas chemistry variations and the presence of particulates in the gas phase. Carburization and decarburization are determined by the amount of carbon activity in the gas relative to the exposed metal surface. In addition, the effects of these impurities on the mechanical properties of the structural alloys include fatigue, fracture and rupture.

Material degradation in particle laded-gases (hard particles suspended in the gas stream) also needs consideration and is called erosion. Erosion is a complex phenomenon because of the dynamic changes that occur on the eroding surface [45]. The main cause

of erosion in HTGRs is carbon dust particles originating from the fuel spheres in the nuclear reactor. One study conducted on an HTGR (reactor contained ± 100 000 fuel spheres) showed that some components were significantly degraded, with the cause unknown [45]. At the end of the reactor's lifespan, 60 kg of carbon dust was collected. Since the PBMR contains in the order of 450 000 fuel spheres, this form of degradation is important. Factors that influence erosion degradation include particle size, hardness and velocity.

The next type of system degradation is fouling. Fouling is characterized by any deposit or extraneous material that appears on the surface of the structural alloys and results in an increase in thermal resistance, fluid flow resistance and pressure drop. Fouling is produced by different mechanisms and depends on several conditions and variables. The following mechanisms apply:

- *Particulate/Sedimentation*: Many cooling streams contain deposits or particles that settle on the heat transfer surface of the heat exchangers. This type of fouling is strongly dependant on the velocity of the steams and less by the wall temperature. However, some particles can 'bake' on to the hot wall and can be very difficult to remove.

- *Chemical reaction*: This type of fouling involves physical changes that are the result of a chemical reaction that produce a solid phase near the surface. For example, the hot temperatures may cause thermal degradation of the components that result in carbon deposits on the surface.

- *Corrosion fouling*: This type of fouling is associated with the corrosion of the heat transfer surface by one of the streams which increase the thermal resistance and surface roughness.

- *Biological*: Cooling streams (usually seawater) contain organisms that will attach to surfaces and grow.

- *Inverse solubility*: Certain salts are less soluble in warm water than in cold. If the stream encounters a temperature above saturation for the dissolved salt, the salt will crystallize on the surface.

The last degradation mechanism is leakage. A leakage is an undesired and unintended opening through which the coolant of the enclosed system passes. In HTGRs, leakage occurs between two streams and includes transfer of coolant between gas-gas, gas-fluid or fluid-fluid streams. Leakage occurs due to improper welding, sealing or joining of components, damage (fractures, rapture or cracks) and deterioration of materials from wear and fatigue such as corrosion, erosion and rusting. The pressure difference between the two streams and the size of the opening are important factors that influence the mass flow rate of the leakage.

In conclusion, these four mechanisms are deemed to be the most relevant factors in HTGR component and system degradation. The fault symptoms associated with these mechanisms will typically be characterized by incipient time behaviour.

2.6 Summary and conclusions

This chapter summarized the various methods proposed or implemented for sensor and process fault diagnosis in NPPs together with the component degradation mechanisms in HTGRs.

Section 2.2 lists the concepts and basic requirements for an advanced health monitoring system. The fault detection and isolation tasks are identified as the most crucial components in these diagnostic frameworks. Consequently, these tasks will be applied in the study for sensor and process fault diagnosis.

Section 2.3 discussed the redundant and non-redundant techniques that are applicable to NPP sensor fault diagnosis. It is concluded that an uncertainty analysis is an important factor for acceptance of an OLM technique. Redundant techniques emerged as the most favourable for OLM, and accordingly, redundant techniques will be applied in the thesis for consistency analysis and state estimation of critical system variables. In order to establish a reliable framework for sensor fault diagnosis, a novel integrated approach is proposed and is presented in Chapter 4.

Section 2.4 summarizes the most relevant techniques for process fault diagnosis. The different model-and process history based techniques each offer some desirable qualities for application in NPPs and are discussed. In order to incorporate these qualities into a FDI system, the structure of the proposed process fault diagnosis approach is presented.

In section 2.5, the most relevant mechanisms for component degradation in HTGRs are discussed and comprise component corrosion, erosion, fouling and leakage.

The following chapter discusses the topology of the reference HTGR NPP together with the fault symptoms and component performance parameters associated with the degradation mechanisms.

CHAPTER 3

The plant model and examined system faults

This chapter focuses on the PBMR plant model comprising the MPS and ICS. Three main fault classes are identified for the MPS through a sensitivity analysis and include the main flow bypass of the working fluid, an increase in main flow resistance, and a decrease in component efficiency or effectiveness.

3.1 Introduction

In this chapter, the theory regarding the thermodynamic Brayton cycle, the components comprising the PBMR plant and the Flownex simulation model are discussed. In addition, a sensitivity analysis of the system is performed to identify the fault parameters and classify the different fault classes.

Firstly, section 3.2 describes the thermodynamic system applicable for the investigation. The PBMR, which is a Brayton cycle-based modular nuclear gas power plant, is analyzed and the eight sub-processes together with the system components are discussed. In addition, plant mode and state transitions are examined to define normal power operation and to classify critical system faults. These faults are accommodated in the automated plant protection systems and are for this reason not applicable to the investigation.

In section 3.3, a sensitivity analysis of the main power system (MPS) is performed to determine the influence of system/component parameters on system performance and to identify the fault parameters that are synonymous with the degradation mechanisms.

Three main fault classes are identified in the MPS and are discussed in section 3.4. A motivation is formulated for the probable fault causes and their degrading effect on system performance is demonstrated. In total, 25 single and 7 multiple faults conditions are investigated in the study.

Section 3.5 describes the Flownex MPS plant model comprising the reactor unit (RU), the power conversion unit (PCU) and the inventory control system (ICS). The basic control structures are discussed together with critical model parameters.

Lastly, some conclusions are summarized in section 3.6.

3.2 Theoretical analysis of the PBMR plant model

The PBMR MPS utilizes a closed direct Brayton cycle with helium (He) gas as the working fluid and a graphite-moderated nuclear core as heat source. Helium is chosen as coolant since it is chemically inert and has a high thermal conductivity. The MPS is divided into two main subsystems, the RU and the PCU. The helium gas transfers thermal energy generated by a nuclear reaction in the RU to the PCU, which consists of gas turbo-machinery and heat exchangers. The resultant thermal energy is converted into electrical energy by an electric generator connected to the gas power turbine. Figures 3.2.1 and 3.2.2 shows the layout and solid model of the PBMR MPS respectively.

The numbers depicted in Fig. 3.2.1 correspond to the eight sub-processes employed in the Brayton cycle. Starting at (1), helium at low pressure and temperature is compressed by the low-pressure compressor (LPC) to an intermediate pressure (2) and then cooled in the intercooler (3). Next, the helium is compressed to a higher pressure (4) by the high-pressure compressor (HPC) and preheated in the recuperator (5) before entering the RU. After the process in the reactor (6), high pressure and temperature helium is expanded in the gas power turbine (PT) (7), which in turn drives the electrical generator. The low pressure hot helium is then cooled at constant pressure in the recuperator (8) and further cooled in the pre-cooler to state 1. This completes the thermodynamic cycle [46]. Table 3.2.1 shows the typical parameters of the PBMR MPS for normal operation at full power.

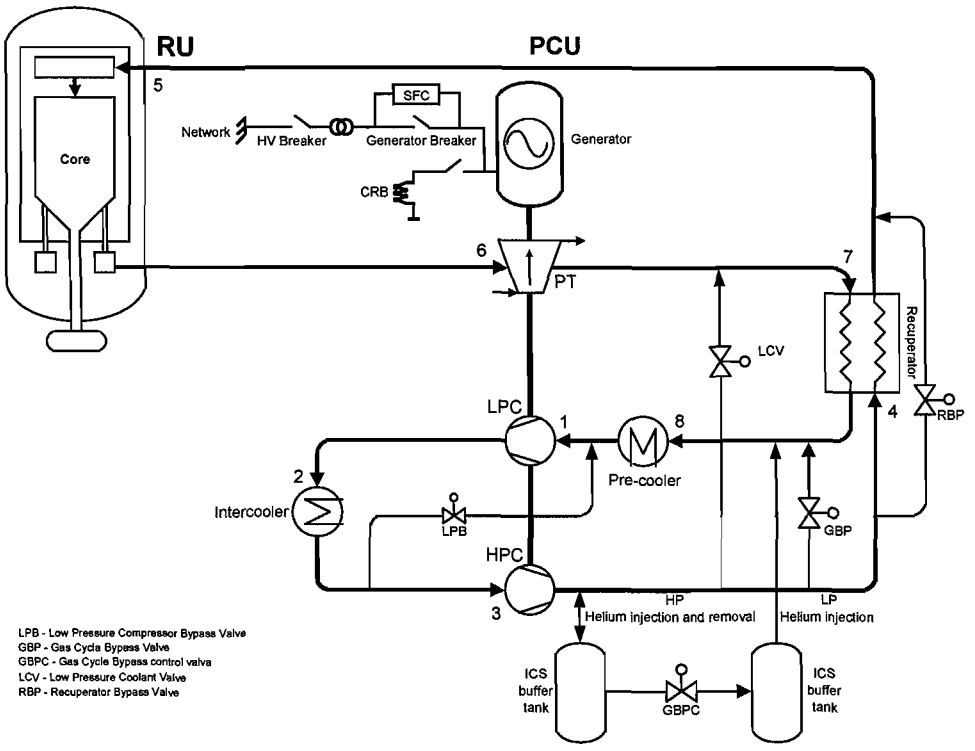

Fig. 3.2.1 PBMR MPS layout.

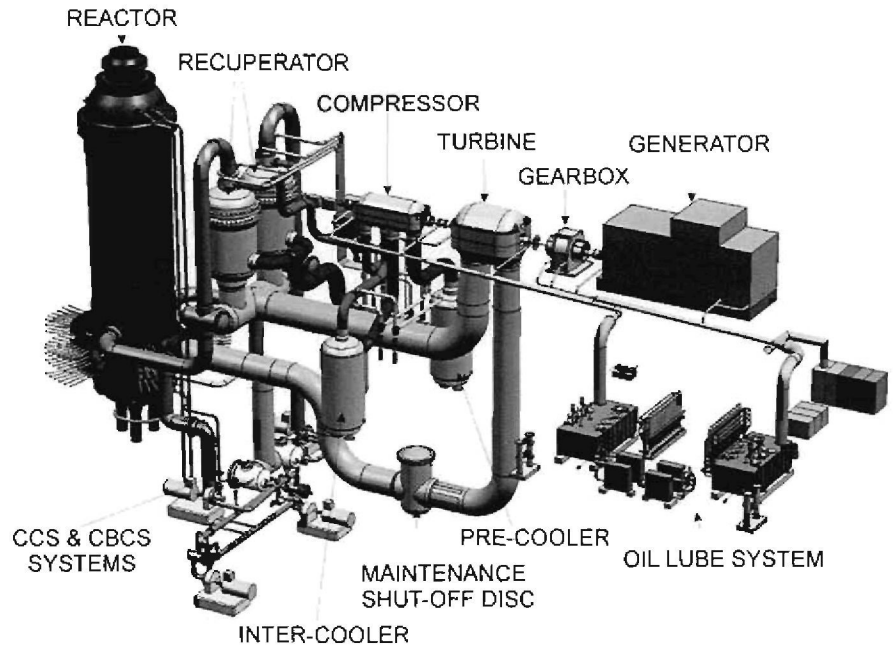

Fig. 3.2.2 Solid model of the PBMR MPS.

The PBMR MPS comprises the following components: Reactor, HPC, LPC, PT with electric generator, recuperator, pre-cooler, intercooler, pipelines and valve systems. The functions of the components in the sub-processes are [46]:

- *Reactor unit*
  The reactor provides the heat energy required for conversion into electrical energy. The RU consists of the reactor pressure vessel, the nuclear core containing the fuel spheres and the core structures. Since the RU is an absolute safety critical component

Component (at inlet)	Cycle parameters			
	Efficiency (%)/ effectiveness	T (°C)	P (MPa)	m (kg/s)
1. LPC	89	22	2.9	201
2. Intercooler	0.82	109	5.0	201
3. HPC	89	22	5.0	201
4. Recuperator HP	0.97	106	8.9	190
5. Reactor		500	8.9	190
6. Turbine	91	900	8.6	190
7. Recuperator LP	0.97	510	2.9	201
8. Pre-cooler	0.84	140	2.9	201

Performance parameters	
Cycle efficiency (%)	46
Reactor thermal power (MWt)	400
Generator output (MWe)	165
Helium mass in PPB (kg)	5800

Table 3.2.1 Typical parameters of the PBMR MPS for normal operation at full power.

with integrated protection systems, no internal reactor faults are examined. However, faults that influence system performance (e.g. gas leakage) are examined.

- *Turbo units*
  The HPC and LPC provide the pressure in the Brayton cycle to drive the PT. The compressors use simple dump diffusers instead of complex inlet/outlet volutes and the blades adjust with a ±15 ° angle for the purpose of plant control.

- *PT and electric generator*
  The PT absorbs the energy from the high pressure and temperature helium to drive the electrical generator. In turn, the generator supplies the high voltage (HV) electrical network with power.

- *Recuperator*
  The recuperator returns heat downstream of the PT back to the flow path ahead of the reactor to raise the gas temperature, thus reducing the heating demand on the reactor. This exchange of thermal energy improves the efficiency of the Brayton cycle.

- *Heat exchangers*
  Within the closed Brayton cycle, the pre-cooler anchors the temperature of the low pressure line. The function of the intercooler is to reduce the volume flow to the HPC, causing a reduction of compressive work. This multistage compression with intercooling improves the efficiency of the Brayton cycle. The heat exchangers utilized in the PBMR are compact counter flow, finned-tubed heat exchangers.

- *Pipelines*
  Helium and secondary coolant is transported via the pipelines between the MPS components and the auxiliary systems.

- *Valves*
  The valves are mainly used to manipulate helium flow for inventory control and several MPS safety features.

The controllability and response of the PBMR MPS is determined by the dynamic characteristics of the PCU and the reactor. Two system characteristics are highlighted to better comprehend the fault simulation responses [47]:

- Since the PBMR utilizes a closed direct Brayton cycle, all the dynamics are interlinked. The time constant for the gas cycle is approximately 5 seconds, i.e. the time it takes for an operational disturbance like a fault to propagate throughout the system.

- The nuclear core has a large thermal capacity. Since the temperature coefficient of the reactor is negative, the reactivity and neutronic power changes to counteract temperature variations. As a result, the reactor is nearly self-regulating and minimal

control is required to maintain the reactor outlet temperature (ROT) at a given set point.

The main advantage of the slow thermal response of the reactor is to allow fast load changes without requiring a fast response from the core. During normal power operation, the ROT is controlled at 900 °C by means of the control rods (reactivity control). This average ROT results in the highest cycle efficiency. The other contributing factor that influences cycle efficiency during normal power operation is the type of load/power control.

The primary power control of the MPS is achieved by adding or removing helium inventory from the primary pressure boundary (PPB) with the ICS. By using inventory control, the cycle temperatures and pressure ratios stay the same whilst only the gas density and mass flow rates change. The change in mass flow rates in turn varies the power output of the gas turbine and electrical generator. This method allows high efficiency at all power levels above 40 % of the maximum continuous rating (MCR). Transport of helium mass between the MPS and ICS is realized by means of pressure differential. Helium is extracted at the HPC outlet (highest pressure point in the MPS) and injected at the pre-cooler inlet.

Alternatively, the gas cycle bypass (GBPC) valves are used in combination with the ICS to realize faster load changes and accurate set point tracking. By opening the valves, the mass flow through the reactor and turbine is reduced, thus decreasing the output power of the electrical generator. The drawback of this method is lower cycle efficiencies and changes in the cycle temperatures.

Although the PBMR plant encompasses several additional subsystems, e.g. systems for cooling, purification, shutdown, pressure relief etc., the plant model used in the study comprises only the MPS (includes RUCS and CBCS conditioning/cooling systems) and the ICS. Additionally, since the MPS is mostly operated at full power, the study mainly focuses on normal power operation of the plant. The modes and operational states of the PBMR are illustrated in Fig. 3.2.3. In the normal power mode (mode 5b), the Brayton cycle is self-sustaining and the generator is synchronized with the power grid (generator and HV breakers are closed). The ROT is controlled at 900 °C (reactor critical) and the power delivered to the grid varies between 40 % MCR and 100 % MCR. Power control is realized by means of the ICS and manipulation of the GBPC valves.

Fig. 3.2.3 shows that four critical fault transients are incorporated in the automated plant safety systems. These transients comprise a PCU trip, reactor or control rod SCRAM (emergency shutdown procedure of the reactor) and loss of load. In all these cases, the Brayton cycle stops functioning and the plant protection systems initiate mode and state transitions to ensure the plant is kept within defined limits. As a result, these faults are not investigated in the study and not included in the proposed fault diagnosis scheme. The system faults include electrical malfunctions, turbo machinery over speed, compressor surge, excessive vibration, electro-magnetic bearing failure, loss of cooling, power oscillations, manifold over pressurization, increase in reactor outlet/differential temperature, and unexpected reactor neutron flux variations.

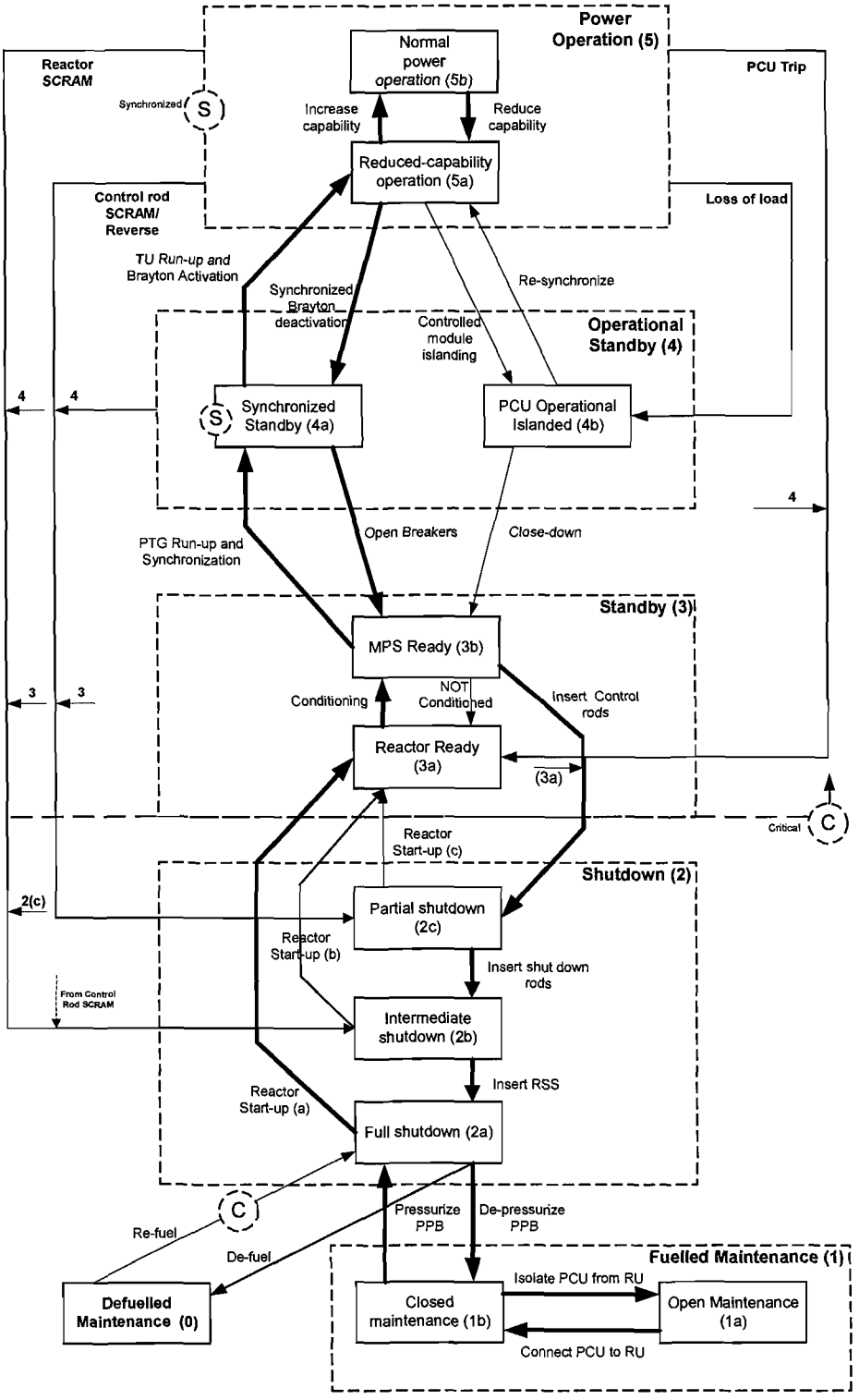

Fig. 3.2.3 Modes and states for normal operation of the PBMR [47].

3.3 Sensitivity analysis of the PBMR MPS

In this section, a simplified simulation model of the PBMR MPS is used to determine the influence of certain component parameters on system/cycle performance [48]. This is done to identify the probable fault parameters that are associated with degrading component and system performance.

Firstly, the type and origin of the component performance parameters are identified that are synonymous to the degradation mechanisms. These parameters are varied between upper and lower limits to determine the influence on system performance. The performance of the MPS is calculated by means of three parameters that serve as reference for normal power operation.

3.3.1 The component and system performance parameters

This section elaborates on the chosen component parameters that are varied for the sensitivity analysis. The influence of the following component parameters is considered:

- *Loss factors/resistive losses*
  The secondary loss coefficients are varied in the equivalent intake pipe models to emulate a variation in resistive losses. This in turn varies the pressure losses around the circuit.

- *Leakage flows*
  Unavoidable leakage flows occur between the manifold and the turbo machinery inlets and outlets, between the recuperator high pressure and low pressure streams and the reactor inlet and outlet plenums.

- *Turbo machine isentropic efficiency*
  The isentropic efficiencies of all the turbo machines are essential to achieve a high efficiency MPS. The HPC, LPC and PT efficiencies are adjusted.

- *Turbo machine pressure ratio*
  Since the cycle efficiency is a function of the overall pressure ratio, the pressure ratio of the HPC, LPC and PT are varied.

- *Heat exchanger effectiveness*
  To vary the effectiveness of the pre-cooler, intercooler and recuperator, the heat transfer area of the specific component are changed.

- *Minimum cycle temperature*
  This is one of the critical parameters in the PBMR to achieve the highest possible cycle efficiency. The minimum gas temperatures are located directly after the pre- and intercoolers and vary with variations in ultimate heat sink (cooling towers, seawater) temperature.

Two additional parameters that influence system performance are the maximum cycle pressure (manifold) and temperature (ROT). Since both parameters are controlled within predefined limits and integrated in the automated protection systems, they are not considered as potential fault parameters.

The system performance is measured in terms of power delivered to the grid, cycle efficiency and mass flow through the reactor. The cycle efficiency is a function of the net work and the heat added to the process and is defined by (3.3.1)

$$\eta_{cycle} = \frac{Q_{PT} - Q_{HPC} - Q_{LPC}}{Q_{RU}} \tag{3.3.1}$$

with Q_{PT}, Q_{HPC}, Q_{LPC} the work delivered or absorbed by the turbo machinery and Q_{RU} the heat supplied by the reactor. The power delivered to the grid is given by

$$P_{grid} = n_{sy}\left(n_m n_{gen} P_{PT} - P_{house}\right) \tag{3.3.2}$$

where η_{sy}, η_m and η_{gen} are the switchyard, mechanical and generator efficiencies respectively and P_{house} is the house load (power supplied to the installation). The mass flow through the reactor is calculated as follows

$$\dot{m}_{RU} = \frac{Q_{RU}}{c_p\left(T_{out} - T_{in}\right)} \tag{3.3.3}$$

with c_p the constant pressure specific heat and T_{out}, T_{in} the reactor outlet and inlet temperatures respectively.

3.3.2 Simplified simulation model of the Brayton cycle

The simplified model of the PBMR MPS is constructed in Flownex and is given in Fig. 3.3.1. The following settings apply to the model:

- The reactor is modelled as a simple pipe element with a fixed exit temperature of 900 °C.
- The manifold pressure is fixed at 7 MPa.
- All the flow resistances in the system are negligibly small.
- The speed of the shaft connecting the turbo machinery is fixed at 6000 rpm.
- The cooling water temperature (CWT) is set at 18 °C.
- In (3.3.2), P_{PT} corresponds to the excess shaft power.

To conduct the sensitivity analysis of the MPS, the system performance parameters are firstly calculated. This is done to establish the baseline values for the component parameters that result in the best realistic cycle efficiency.

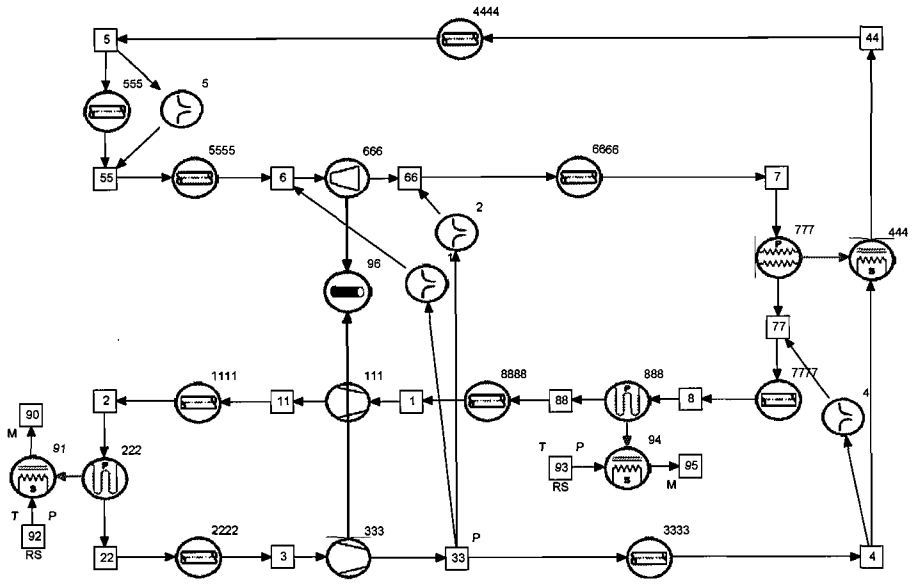

Fig. 3.3.1 A network diagram of a simplified Brayton cycle-based MPS.

The baseline values for the component and system parameters are listed in Table 3.3.1. The table shows that the highest realistic cycle efficiency obtained for the Brayton cycle is 45.7 %. Realistic in this context signifies component baseline values that can be realized, i.e. component geometry and performance are limited.

The sensitivity analysis is performed by setting the component parameters equal to the baseline values and varying the appropriate parameters as defined in section 3.3.1. Table 3.3.2 summarizes the results obtained with the sensitivity analysis.

Component	Cycle parameters	
	Efficiency (%)/ effectiveness	Pressure ratio
LPC	90.5	1.69
Intercooler	0.956	
HPC	89.8	1.64
Recuperator	0.976	
Power turbine	89.6	2.68
Pre-cooler	0.957	
Performance parameters		
Cycle efficiency (%)	45.7	
Grid power (MW)	123.8	
Reactor mass flow (kg/s)	130.6	
Shaft power (MW)	132.5	
Reactor thermal power (MW)	295.0	
Total pressure losses (kPa)	184.1	
Total leakage mass flows (kg/s)	11.3	
Minimum cycle temperature (°C)	21.5	

Table 3.3.1 Simplified Flownex model reference values.

Component parameters	Change	Change in system performance parameters		
		Grid power (MW)	Cycle efficiency (%)	Reactor mass flow rate (kg/s)
Pressure losses (kPa)	+10 %	-1.1	-0.4	-0.3
PT inlet leakage (kg/s)	+10 %	-0.9	-0.4	-0.6
PT outlet leakage (kg/s)	+10 %	-4.8	-1.7	-0.5
Recuperator leakage (kg/s)	+10 %	-0.1	-0.2	0
Core bypass leakage (kg/s)	+10 %	-0.1	-0.1	-2.5
All leakages (kg/s)	+10 %	-5.6	-2	-3.5
All efficiencies (%)	-1 %	-3.5	-1.3	0
LPC efficiency (%)	-1 %	-0.6	-0.3	0
HPC efficiency (%)	-1 %	-0.6	-0.2	0
PT efficiency (%)	-1 %	-2.4	-1.0	0
All pressure ratios	-1 %	-0.8	-0.3	-0.7
LPC pressure ratio	-1 %	-0.6	-0.2	-0.2
HPC pressure ratio	-1 %	-0.1	-0.1	-0.1
PT pressure ratio	-1 %	-0.3	-0.1	-0.4
Minimum cycle temperature (°C)	+1 °C	-0.3	-0.3	-0.1
Pre-cooler effectiveness	-1 %	-0.1	-0.1	0
Intercooler effectiveness	-1 %	-0.1	-0.1	0
Recuperator effectiveness	-1 %	-0.6	-0.1	0
All effectivenesses	-1 %	-0.8	-0.3	-0.1

Table 3.3.2 Summary of sensitivity analysis results.

Table 3.3.2 shows that changes in leakage flows and turbo machinery efficiencies have a profound effect on the cycle efficiency as well as the power delivered to the grid. The most noticeable contributors are the leakage flow between the manifold and the PT outlet, and the PT efficiency. A ten percent increase in the outlet leakage flow of the PT results in a mass flow of approximately 4.5 kg/s and a decrease in cycle efficiency and grid power of 1.7 % and 4.8 MW respectively. Furthermore, a 1 % percent decrease in PT efficiency results in a reduction in grid power and cycle efficiency of 2.8 MW and 1 %.

The system pressure losses, turbo machinery pressure ratios and the heat exchanger effectivenesses are also important and show a decrease in system performance for a small change in component parameters.

It is evident from the table that the core bypass leakage has a major effect on the mass flow through the reactor. A ten percent increase results in a leakage flow of approximately 12 kg/s, and a reduction in mass flow through the reactor of 2.5 kg/s.

Overall, the sensitivity analysis shows that the effects of all the selected component parameters are detrimental on the Brayton cycle. In reality, this will be associated with degraded components due to normal wear or system faults. Table 3.3.2 shows that a small change in some component characteristics result in an indistinguishable change in system performance. Accordingly, incipient fault behaviour will be very difficult to detect at an early stage and can result in component failure.

The following section describes the correlation between the chosen component parameters and probable fault causes as well as the PBMR MPS fault classes.

3.4 Fault classification in the PBMR MPS

As demonstrated in section 3.3, changes in certain component parameters influence the performance of the Brayton cycle. During normal power operation of the plant, these changes are associated with known fault conditions and may be attributed to normal component wear, ageing effects, material defects or operation of the plant beyond the defined limits.

In the thesis, faults in the MPS are defined as any malfunction or abnormal behaviour of the components or the process. By means of the sensitivity analysis, three different fault classes are identified. The fault classes characterize or group the individual faults according to cause and effect, and include:

- Changes in bypass flows.
- Changes in the main flow resistance.
- Changes in efficiency or effectiveness.

Firstly, flow bypass faults disturb the natural flow path of the working fluid and are mainly caused by leakage flows between components or nodes. The second fault class is defined as faults that increase the resistance of fluid flow and is the result of fouling, erosion, corrosion and surface roughness. The increase in resistive losses, in turn increases the pressure losses around the system. Lastly, the third fault class is described as faults that influence the efficiency or effectiveness of the components.

The following paragraph elaborates on the selected component parameters that are varied to reflect the appropriate fault conditions. In total, 25 component parameters are varied in the MPS to denote the most likely single and multiple (combination of single faults) fault conditions.

3.4.1 Fault class 1: Flow bypass

This fault class results in helium gas that bypasses components or whole parts of the process. In the MPS, these alternative paths are modelled by parallel 'equivalent' resistive elements. The mass flow through the element is given by [49] (3.4.1)

$$\dot{m} = MAC_d p_{01} \frac{\sqrt{\gamma}}{\sqrt{RT_{01}}} \left[1 + \frac{\gamma - 1}{2} M^2\right]^{\frac{-(\gamma+1)}{2(\gamma-1)}} \tag{3.4.1}$$

with M the mach number and A the area in the throat, C_d the discharge coefficient, p_{01} and T_{01} the total upstream pressure and temperature, and γ the ratio of specific heats. The faults considered are the leak flows between the HP manifold and the turbine inlet and outlet respectively, the recuperator HP and LP streams, and the reactor core bypass leak (between inlet and outlet plenums). By varying the resistance of the element, any change

in the leakage mass flow can be simulated. It is expected that the leakage flows would increase over time in the MPS.

3.4.2 Fault class 2: Main flow resistance (resistive losses)

An important quantity of interest is the pressure losses Δp in the MPS since it directly relates to the power required to maintain the flow. The secondary loss coefficients of the main components' intake pipe models are used to vary the pressure losses around the circuit. It is important to note that the objective is to create a change in Δp between the eight sub-processes of the Brayton-cycle and not in a single specific component. In the MPS, the pressure drop across an intake pipe with variable inlet and outlet areas is defined by [49] (3.4.2)

$$\Delta p_0 = \frac{p_0}{p}\left(\frac{1}{2}\rho|V|V\left(\frac{fL}{D_{Hm}}+\sum K_S+\frac{\Delta T_0}{T_0}\right)+\rho g\Delta z+K_i\frac{1}{2}\rho V_i^2+K_e\frac{1}{2}\rho V_e^2\right) \tag{3.4.2}$$

with p_0 and p the mean and static pressures, V, V_i and V_e the mean, inlet and outlet velocities. f, Δz and ρ are the friction factor, inlet/outlet height difference and mean density. L and D_{Hm} represent the length and mean hydraulic diameter, and K_i, K_e, K_s the inlet, outlet and secondary loss coefficients. In the MPS, the loss coefficients are varied to an upper limit since it is expected that Δp would more likely increase than decrease.

3.4.3 Fault class 3: Effectiveness or efficiency

As illustrated in section 3.3, the effectiveness of the heat exchangers (ε) and efficiency of the turbo machinery (η) are important to maximize the efficiency of the cycle. The effectiveness of a heat exchanger (intercooler, pre-cooler, and recuperator) is a function of the AU value and the primary and secondary mass flow rates. The AU value is the product of the heat transfer area and the overall heat transfer coefficient. The effectiveness of the heat exchangers is defined by [50] (3.4.3)

$$\varepsilon = \frac{1-e^{-\frac{A_pU_p\left(1-C_{\min}/C_{\max}\right)}{C_{\min}}}}{1-\frac{C_{\min}}{C_{\max}}e^{-\frac{A_pU_p\left(1-C_{\min}/C_{\max}\right)}{C_{\min}}}} \tag{3.4.3}$$

with A_p the primary side heat transfer area, U_p the overall heat transfer coefficient and $C_{\min}$, $C_{\max}$ the minimum and maximum values of the heat capacity rates. A lower limit was chosen for the variation in heat transfer area (A) since a lower effectiveness is expected during fault conditions.

The performance of the turbo machines (LPC, HPC, and turbine) is a function of the pressure ratio (PR), isentropic efficiency, corrected mass flow rate and corrected speed [51]. The function is given by (3.4.4)

$$f\left(PR, \frac{(PR)^{\gamma-1/\gamma}-1}{\left(T_{0e}/T_{0i}\right)}, \frac{\dot{m}\sqrt{T_{0i}}}{p_{0i}}, \frac{N}{\sqrt{T_{0i}}}\right) = 0 \tag{3.4.4}$$

with p_{0i} and T_{0i} the inlet total pressure and temperature, T_{0e} the exit total temperature and N the speed. For the variables defined in (3.4.4), the performance of the turbo machines is given by two curves namely pressure ratio and isentropic efficiency as a function of corrected mass flow rate for various corrected speed curves. To vary the performance of the turbo machines, scaling factors are used to change the performance characteristics of the two curves. The pressure ratio and efficiency scaling factors are varied between upper and lower limits to simulate the different fault conditions.

Table 3.4.1 summarizes the faults in the PBMR MPS together with the selected component parameter variations.

Component	Fault description	Mechanism	Class	Direction	Parameter
1. Pre-cooler	Heat transfer area	fouling	3	decrease	a (m^2)
2. Intercooler	Heat transfer area	fouling	3	decrease	a (m^2)
3. Recuperator	Heat transfer area	fouling	3	decrease	a (m^2)
4.	HP to LP leakage	leakage	1	increase	d (m)
5. LPC	Pressure ratio	combined	3	increase	scaling factor
6.	Pressure ratio	combined	3	decrease	scaling factor
7.	Efficiency	combined	3	decrease	scaling factor
8. HPC	Pressure ratio	combined	3	increase	scaling factor
9.	Pressure ratio	combined	3	decrease	scaling factor
10.	Efficiency	combined	3	decrease	scaling factor
11. Turbine	Pressure ratio	combined	3	increase	scaling factor
12.	Pressure ratio	combined	3	decrease	scaling factor
13.	Efficiency	combined	3	decrease	scaling factor
14.	Manifold leakage to outlet	leakage	1	increase	d (m)
15.	Manifold leakage to inlet	leakage	1	increase	d (m)
16. Pipelines	LPC inlet	combined	2	increase	k
17.	Intercooler inlet	combined	2	increase	k
18.	HPC inlet	combined	2	increase	k
19.	Recuperator HP inlet	combined	2	increase	k
20.	Reactor inlet	combined	2	increase	k
21.	Turbine inlet	combined	2	increase	k
22.	Recuperator LP inlet	combined	2	increase	k
23.	Pre-cooler inlet	combined	2	increase	k
24. Reactor	Reactor bypass leakage	leakage	1	increase	a (m^2)
25.	Reactor pressure drop	combined	2	increase	l (m)
26. Multiple	LPC efficiency + fault 2	combined		combined	
27.	LPC efficiency + fault 3	combined		combined	
28.	LPC efficiency + fault 22	combined		combined	
29.	LPC efficiency + fault 10	combined		combined	
30.	LPC efficiency + fault 15	combined		combined	
31.	LPC efficiency + fault 23	combined		combined	
32.	LPC efficiency + fault 24	combined		combined	

Table 3.4.1 Summary of faults in the PBMR MPS.

Faults 1 to 25 correspond to single faults and faults 26 to 32 denote multiple fault conditions. To demonstrate multiple fault symptoms in the MPS, the LPC efficiency fault is used in combination with a single fault from each of the three fault classes.

These 32 faults form the basis for the fault study in the PBMR MPS. As discussed, the sensitivity analysis indicated that certain faults will be difficult to detect at an early stage. The task at hand is therefore to devise an advanced fault diagnosis method that will be able to detect and isolate all the faults within a given fault magnitude. This will not only promote early FDI, but reduce the risk of unexpected component failure and allow enough time for planned maintenance or repair.

In order to investigate the responses of the MPS and the fault diagnosis method to incipient and abrupt faults, a maximum fault magnitude of 10 % (referenced to the baseline values) is deemed sufficient. In the thesis, the objective of early FDI is achieved if a fault condition with a magnitude of ≤ 1 % is correctly identified.

Since the prototype PBMR plant is not operational at the time of the investigation, a complex simulation model of the plant is used as substitute, and is discussed in the following section.

3.5 The PBMR simulation model

The system CFD (Computational Fluid Dynamics) code named Flownex [49] is used for the development and optimization of the PBMR plant. The Flownex model comprising the MPS, ICS, and various conditioning subsystems, serves as an evaluation and testing platform for the complex dynamic behaviour of the PBMR design. Some of the unique features of Flownex are steady state and transient solutions of the system as well as its ability to incorporate control strategies. The network diagram of the Flownex model is illustrated in Fig. 3.5.1.

In order to maintain stable Brayton operation in the PBMR, several control objectives are achieved with different control mechanisms. Three of these controlled variables, together with a non-controlled parameter, determine the operating point of the Flownex model. The controlled variables are the ROT, the pressure in the HP manifold and the position of the bypass valves. The fourth parameter, the CWT, is a function of the site location, type of main heat sink used and the time of the year.

As discussed, during normal power operation of the plant, the ROT is controlled by means of the control rods. Calculations for the reactivity controller include the ROT, reactor neutronic power and the reactor fluidic power. In the Flownex model, the ROT is controlled by varying the cooling flow area over the control rods.

The pressure in the HP manifold is controlled by changing the gas inventory in the PPB, which in turns varies the output power of the plant. In the Flownex model, the ICS isolation valves together with the ICS flow control valve are used for injection, extraction and flow control of helium between the ICS and MPS. The ICS controller selects the correct tank during helium mass transfer and normally switches if the mass flow decreases below 75 % of the setpoint value.

To obtain the required setpoint mass flows through the MPS and ICS control valves, the valve openings are corrected using valve controllers.

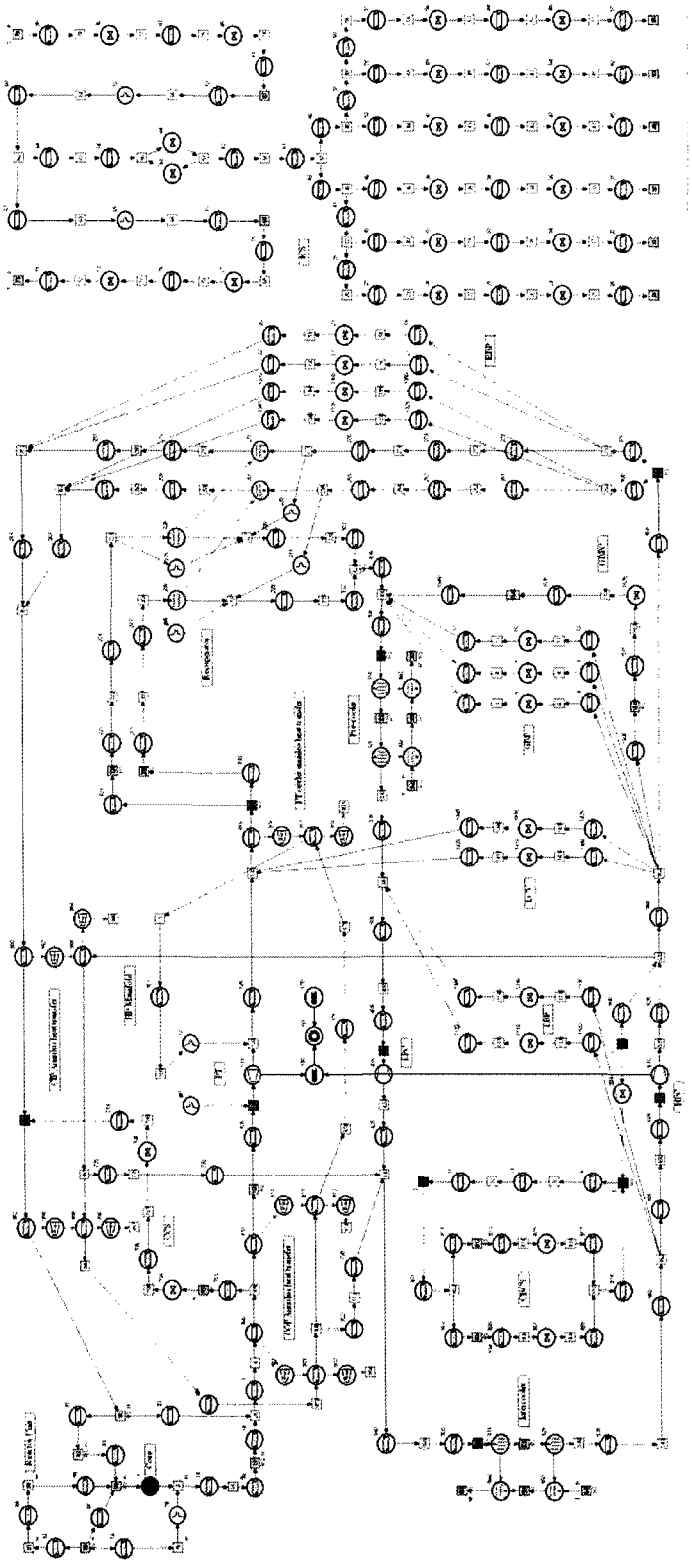

Fig. 3.5.1 A network diagram of the PBMR Flownex model.

Lastly, the CWT changes the operating point of the plant since it directly influences the minimum cycle temperature. The CWT, which is the inlet water temperature of the pre-and intercoolers, varies with ambient conditions during the year and is usually taken as an average. Therefore, to vary the heat transfer through the heat exchangers, the mass flow rate of the cooling water is adjusted accordingly.

In general, Flownex requires detailed input data for all the components and fluid parameters to simulate a model that is highly accurate. Although the objective of the study is to show a general implementation of the proposed fault diagnosis method in a thermodynamic system, the Flownex model employed comprises a detailed and optimised design of the PBMR. The normal expected operating conditions applied in Flownex include the following assumptions and parameters:

- The ROT is controlled at 900 °C and the HP manifold pressure is limited to 9 MPa.
- The average CWT is taken as 18 °C. This is derived from an average seawater temperature at Koeberg[2] of 13 °C.
- The generator is synchronized to the power grid with the turbine-compressor shaft speed fixed at 6000 rpm.

To construct the *h-s* graph (discussed in Chapter 5), the eight sub-processes depicted in Fig. 3.2.1 are monitored. The Flownex model illustrated in Fig. 3.5.1 shows the location of the monitoring points (green nodes). The system variables, which comprise only the pressures and temperatures, are measured at each of the eight nodes. Table 3.5.1 summarizes the average Flownex measurements for normal power operation.

Node	Operating point (% MCR)						
	100	90	80	70	60	50	40
*T*1	22.873	22.973	22.664	22.456	22.679	22.805	22.791
*T*2	109.001	109.256	109.080	109.011	109.245	109.427	109.752
*T*3	21.829	21.936	21.695	21.548	21.270	21.046	21.610
*T*4	106.316	106.689	106.758	106.910	106.982	106.99	107.01
*T*5	499.086	499.845	499.340	499.628	499.632	499.989	499.99
*T*6	899.521	899.638	899.448	899.488	899.517	899.737	899.786
*T*7	510.499	510.458	509.865	509.519	509.469	509.498	509.607
*T*8	139.867	139.415	139.312	138.783	138.736	138.774	139.002
*P*1	2909.802	2602.754	2292.503	1999.661	1709.241	1418.262	1127.775
*P*2	5089.092	4552.149	4011.535	3500.618	2988.692	2478.153	1973.505
*P*3	5058.270	4524.604	3987.247	3479.414	2970.566	2463.100	1961.520
*P*4	8978.038	8030.415	7082.779	6185.007	5287.228	4389.433	3491.609
*P*5	8896.449	7957.271	7018.225	6128.523	5238.921	4349.278	3459.601
*P*6	8551.313	7646.421	6741.859	5884.966	5028.497	4172.210	3316.354
*P*7	2970.539	2657.920	2342.031	2043.584	1747.386	1450.423	1153.770
*P*8	2928.874	2619.873	2307.673	2012.974	1720.691	1427.837	1135.455

Table 3.5.1 Summary of the Flownex model results for normal power operation.

[2]The prototype demonstration plant of the PBMR will be constructed at Koeberg. Koeberg is currently the only nuclear power station in South Africa comprising two uranium pressurized water reactors.

3.6 Summary and conclusions

In this chapter, the PBMR plant model together with probable component and system malfunctions are discussed. The plant model is developed in Flownex, which serves as evaluation and testing platform for the performance of the proposed fault diagnosis method.

In section 3.2, the operation of the MPS comprising the PCU and RU are described. The PBMR utilizes a recuperative, pre-and intercooled topology that includes eight sub-processes. Following this discussion, the conditions for normal power operation are defined. During this state of operation, a number of critical system faults may put the plant at risk. These faults are integrated in the automated protection systems and are for this reason not included in the proposed fault diagnosis scheme.

In section 3.3, probable component and system faults are identified by means of a sensitivity analysis of a simplified MPS. These faults are normally associated with degraded components and can be attributed to the degradation mechanisms. The results showed that variations in the selected component parameters have a detrimental effect on system performance.

By grouping the fault parameters with regard to cause and effect, three fault classes are identified and are motivated in section 3.4. The three fault classes comprise changes in main flow bypass, main flow resistance and component efficiency or effectiveness. The mathematical descriptions that describe the behaviour of the specific components and consequently the fault classes are also discussed. In total, 32 single and multiple fault conditions in the PBMR MPS are selected for the study.

The PBMR MPS is realized in section 3.5 with a simulation model in Flownex. Several plant control objectives are implemented in Flownex using different control mechanisms and include pressure, temperature and mass flow control. Lastly, section 3.5 describes the selected measurements and the monitoring points in the PBMR MPS. The proposed fault diagnosis scheme monitors only temperature and pressure measurements, captured at the inlets of the eight sub-processes. The total amount of measurements required to monitor the health of the MPS is therefore limited to 16.

To provide the process fault diagnosis scheme with accurate plant measurements, sensor fault diagnosis is formulated in the next chapter.

CHAPTER 4

Sensor fault detection and isolation

This chapter presents an integrated framework for intelligent sensor validation and fusion in the PBMR MPS. The comprehensive sensor fault diagnosis scheme includes a validation procedure comprising a signal pre-processing, non-temporal parity space, and principle component and shape statistical analyses. These, together with the data fusion procedure, provide consistent and accurate information for the process FDI scheme.

4.1 Introduction

In this chapter, an integrated framework for intelligent sensor fault diagnosis is proposed. The methodology uses a combination of analytical techniques to reduce their individual shortcomings.

The sensor malfunctions that are considered for the study are discussed in section 4.2. The sensor faults include dead, bias, drift, excessive noise and random spikes.

Section 4.3 explains the individual monitoring and conditioning techniques employed for measurement validation. Firstly, section 4.3.1 discusses the use of redundant measurements in a critical process plant, which is checked for consistency with the non-temporal parity space algorithm. To condition the signals before the consistency check, a signal pre-processing procedure validates the absolute limits of the measurement intervals and the maximum acceptable variable change per time step.

Data reconstruction is an important part of the sensor validation system and is described in section 4.4. To compensate for erroneous measurements, the sensor configuration is validated with a principle component analysis (PCA) model together with the squared prediction error (SPE) index. Moreover, once the SPE threshold is exceeded, the PCA model can reconstruct the faulty measurement from the remaining healthy ones. The validated variables are then combined with a fusion technique based on a confidence level associated with each sensor's residual distribution.

In section 4.5, the proposed sensor validation and fusion module (SENSE) is discussed. The basic steps and detailed reasoning structure of the methodology are explained together with the rules employed for the statistical expert system. The proposed methodology is applied to data from the PBMM and PBMR and is presented in section 4.6. The chapter is summarized in section 4.7.

4.2 Sensor malfunctions

In general, sensor malfunctions are roughly classified into two types of fault classes, abrupt sensor faults or sensor degradation. Abrupt sensor faults result in either complete failure or erroneous readings from the sensor, whilst sensor degradation changes the performance of the sensor. Abrupt faults are due to power failures, corroded or loose contacts and mechanical failure. Sensor degradation on the other hand is the result of a variety of circumstances and includes incorrect calibration, fouling and electrical or mechanical malfunction.

For the investigation, both types of fault classes are considered, although the primary goal is to identify and correct the latter. Sensor degradation normally exhibits incipient fault behaviour, and is for this reason more difficult to detect. The following faults are examined given the common sensor malfunctions [52]: dead/stuck, bias/offset, drift, noisy and random spikes. Figure 4.2.1 illustrates the different sensor malfunctions.

4.3 Sensor validation

In a sensor network, the validation of sensor readings entails the verification regarding the integrity of the measurements. This is crucial in plants comprising safety critical processes since plant performance and stability may be adversely affected by erroneous measurements. It is therefore important to determine if a sensor reading is a true representation of the measured quantity.

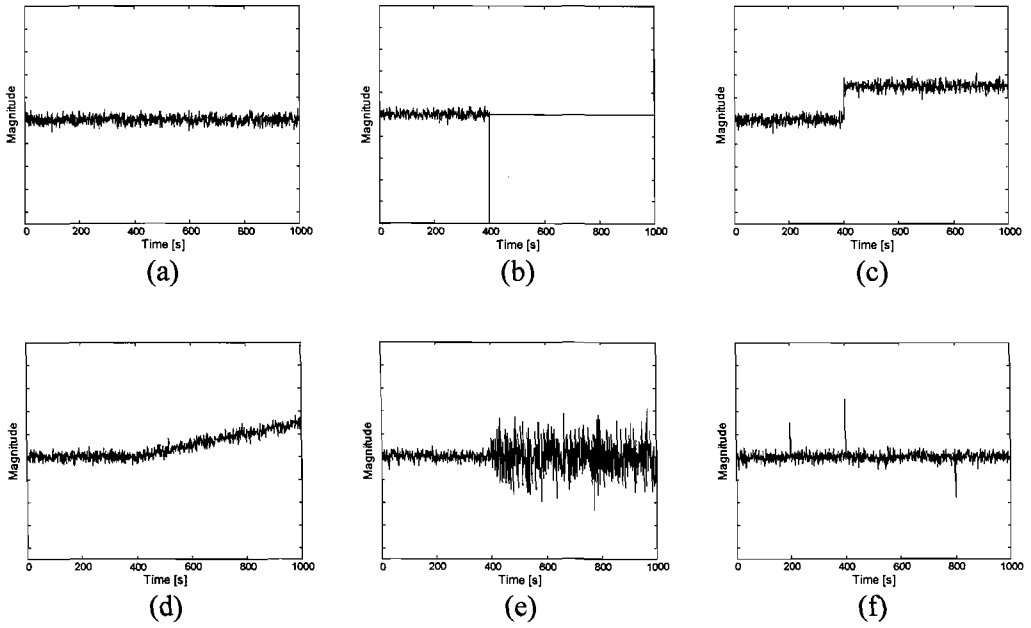

Fig. 4.2.1 Sensor malfunctions: (a) normal; (b) dead/stuck; (c) bias/offset; (d) drift; (e) noisy; (f) spikes.

The sensor validation scheme must accomplish the following two tasks: detection of sensor malfunctions and isolation of the faulty sensors [53]. These tasks become difficult if a large number of different sensors and configurations are used. Therefore, the validation module must be flexible and include different methods to accommodate sensor configurations that constantly change due to faulty sensors. The following sections motivate and describe the methods used in the thesis and discuss the complete architecture of the validation module.

4.3.1 Measurement redundancy

The most commonly used technique for measurement validation is the comparison of a set of redundant measurements. Measurement redundancy is divided into two groups, i.e. spatial and temporal redundancy. The former is realized by means of multiple sensors or functional relationships among different measurements. Functional relationships are also referred to as analytical redundancy where the process is described by a mathematical model. Temporal redundancy is achieved by means of repetitive measurements of the sensor values at regular time intervals.

As discussed in Chapter 2, quantities that are of great importance to the safety of the plant are measured by multiple sensors and named 'hardware redundant'. In addition, the nuclear power industry requires that safety critical parameters be monitored by several redundant sensors [1], [16], [54]. Consequently, the inlet parameters of the main components in the PBMR MPS are monitored with 3 redundant sensors, i.e. 48 temperature and pressure sensors in total.

One concern of hardware redundant measurements is common mode failure among sensors. Although this condition is extremely uncommon [16], the integrity of each redundant measurement set in the PBMR is increased by shielded and physically isolated channels. The assumption is therefore made that not all of the three sensors may fail simultaneously in each measurement set/channel. Common mode failure is generally corrected and replaced with a sensor estimate, i.e. the unavailable information is predicted using the remaining valid measurements. In the study, the PCA technique is used to predict sensor estimates.

Given that the measurements in the PBMR MPS are hardware redundant, the non-temporal parity space algorithm is first applied to the measurements and is discussed next.

4.3.2 Non-temporal parity space analysis

To check the hardware redundant measurements for consistency, the non-temporal parity space technique is applied [30]. The non-temporal algorithm allows the system to be described by the actual time instant, i.e. the measurements are time-independent and therefore the process history is not applicable.

Consider a measurement set comprising n redundant measurements m_i, all representing the scalar quantity x, are corrupted by sensor errors e_i

$$\mathbf{m} = \mathbf{H}x + \mathbf{e} \tag{4.3.1}$$

with $\mathbf{H} = [1, 1, \ldots, 1]^T$. Since the correct value of the measurement is not known, x is removed by projecting the n-dimensional measurement space to the n–1-dimensional parity space

$$\mathbf{p} = \mathbf{V}\mathbf{m} \tag{4.3.2}$$

The $(n-1) \times n$ projection matrix $\mathbf{V}$ has the following properties:

- $\mathbf{VH} = \mathbf{0}_{n-1}$
- $\mathbf{VV}^T = \mathbf{I}_{n-1}$
- $\mathbf{VV}^T = \mathbf{I}_n - \mathbf{H}(\mathbf{H}^T\mathbf{H})^{-1}\mathbf{H}^T$

where $\mathbf{I}$ represents the unity matrix and $\mathbf{0}$ the null vector. The residual vector is defined by

$$\mathbf{r} = \mathbf{V}^T\mathbf{p} \tag{4.3.3}$$

with $\mathbf{r}^T\mathbf{r} = \mathbf{p}^T\mathbf{p}$ and $\mathbf{r} = \mathbf{m} - \mathbf{H}\langle\mu\rangle$. $\langle\mu\rangle$ denotes the mean of all n measurements. The n redundant measurements m_i are inconsistent if the parity vector $\mathbf{p}$ exceeds a threshold δ_n

$$\mathbf{p}^T\mathbf{p} = \left(\sum_{i=1}^{n-1} p_i^2\right) \geq \delta_n \tag{4.3.4}$$

Assuming that the magnitudes of all sensor errors are uniformly limited by b, i.e. $|e_i| < b$, the threshold δ_n is determined by

$$\delta_n = \begin{cases} nb^2 & n \text{ even} \\ \dfrac{n^2-1}{n}b^2 & n \text{ odd} \end{cases} \tag{4.3.5}$$

To isolate the faulty sensor, the direction of the parity vector is examined. The magnitude of the parity vector's projection orthogonal to the direction of the i-th sensor is given by

$$p_{i\perp}^2 = |\mathbf{p}|^2 - \frac{n}{n-1}r_i^2 \tag{4.3.6}$$

In the fault free case, the projection must be lower than δ_{n-1}.

Although the consistency of redundant measurements is easily validated with this technique, one limitation is that isolation is impossible if more than one sensor fails. For this reason, additional methods are used if the measurements are inconsistent and multiple sensors are erroneous.

4.3.3 Statistical shape analysis

Even though the parity space technique is an uncomplicated yet effective way of checking measurement consistency, it cannot classify the type of sensor fault. To classify the faults depicted in Fig. 4.2.1, some features regarding the measurement distribution are evaluated. First, a motivation for the use of the normal distribution is presented.

In the proposed process fault diagnosis approach, noise originating from the sensors is assumed to be Gaussian or normally distributed. This statement is justified by [6], [16] and verified in section 7.6 with real measurement data from the PBMM. Gertler [6], using the central limit theorem, states that many random processes can be approximated by the normal distribution. In addition, [16] states that research has shown that nuclear power plant data normally has a Gaussian distribution

The central limit theorem states that the distribution of the average of random variables (measurements) tends to be normally distributed as the number of observations approaches infinity. The basic form of the central limit theorem is given in Appendix A.

Although the theorem states exact equality in the limit ($n\rightarrow\infty$), any limited number of variables (sample window) can be fairly accurately characterized by the standard normal distribution, given an approximation error. However, the choice of sample window size versus approximation error is dependent on the type of implementation and the sampling time. The choice of sample size for the PBMR is discussed in section 4.5.

In order to classify sensor faults, some characteristic features regarding the sensor's distribution are evaluated. These features include the mean, standard deviation/variance, and skewness. Another important feature is the minimum and maximum values of the variable. These values are used to identify the absolute limits of the measured quantity. To illustrate the different features, the normal distribution is firstly calculated by computing the mean and standard deviation of the variable. The mean is the arithmetic average of the measurements, and is given by

$$\mu = \frac{1}{n}\sum_{i=1}^{n} x_i \tag{4.3.7}$$

where n is the number of measurements and x_i is the i-th measurement. The standard deviation is a measure of the dispersion of the measurements, and is defined by

$$\sigma = \sqrt{\frac{1}{n}\sum_{i=1}^{n}(x_i - \mu)^2} \tag{4.3.8}$$

The probability density function of the normally distributed measurement is

$$f(x) = \frac{1}{\sigma\sqrt{2\pi}} e^{\frac{(x-\mu)^2}{2\sigma^2}} \tag{4.3.9}$$

In (4.3.9), σ^2 is also known as the variance. The bell-shaped probability density function of the normal distribution is shown in Fig. 4.3.1.

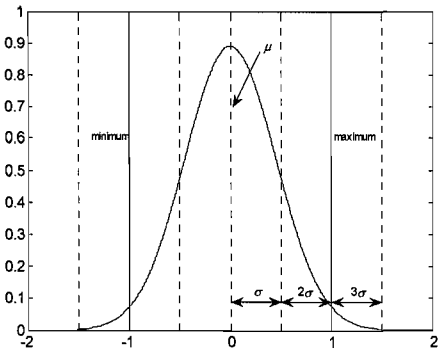

Fig. 4.3.1 Probability density function for the normal distribution.

In probability theory, the skewness is a measure of the asymmetry of the measurements around the mean. For the normal distribution, the skewness is zero and defined by

$$\gamma = \frac{\sqrt{n}\sum_{i=1}^{n}(x_i - \mu)^3}{\left(\sum_{i=1}^{n}(x_i - \mu)^2\right)^{3/2}} \tag{4.3.10}$$

To realize the design objective of simplicity with high interpretability, an uncomplicated rule-based expert system is used for fault classification and is based on the behaviour of the distribution features. The following mechanisms are utilized for sensor FDI:

- The absolute limits of the variables are set that approximately 95 % of the measurements lie between them. For the normal distribution, this corresponds to approximately $\pm 2\sigma$. These limits are used to identify outliers in the measurements caused by spikes, missing data or dead sensors (zero value). In addition, sensor bias and excessive noise can be detected if the variable surpasses the limits for an extensive time period.

- To classify bias and drift faults, the distributions of the sensor residues are examined. Since these faults manifest themselves as changes in the mean or variance, a change in the mean is associated with sensor bias and changes in the variance an indication of excessive noise.

- As discussed, the skewness is a measure of the asymmetry of the probability distribution. Therefore, for either positive or negative skew, an uneven distribution is an indication of sensor degradation.

Given that the distributions of the sensor residues are evaluated for changes, an approximation of the sensor values is needed. To perform this task, a principle component analysis is applied to the measurements and is discussed in section 4.3.5.

4.3.4 Maximum process change

In order to detect an unexpected abrupt step in a sensor value, a maximum process change parameter is defined. For any process variation, the maximum process change signifies a theoretical limit for change per time instant, and is determined by means of the system characteristics. The maximum change parameter for any two consecutive samples is defined as

$$\Delta x_i = x_i(k) - x_i(k-1) \tag{4.3.11}$$

where x_i denotes the i-th variable. As discussed in Chapter 3, the different variations for normal power operation include injection, extraction, valve manipulation and normal steady state operation.

By applying the maximum process limit, any large deviation can be detected and isolated at the specific time instant. Normal statistical methods will however only identify the deviation after the mean of the sample window changes. One of the main drawbacks of the method is that incipient faults are only detected once the limit is surpassed.

The implementation of a maximum process change parameter is demonstrated in Fig. 4.3.2. A good first choice of the parameter during normal steady state conditions is the standard deviation of the measurements.

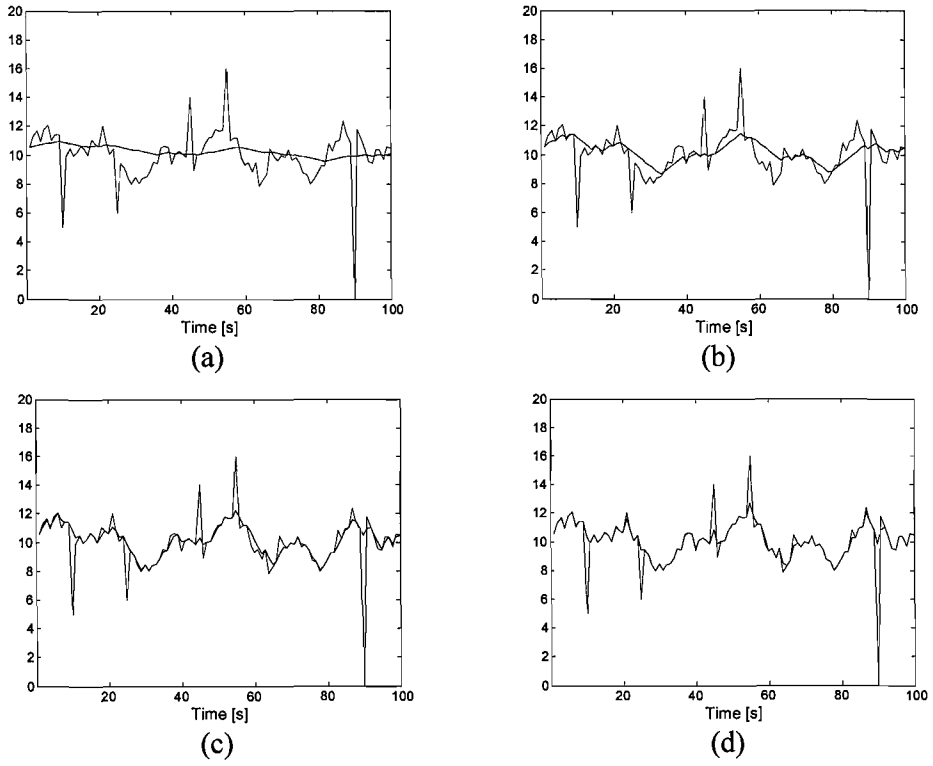

Fig. 4.3.2 Varying the maximum process change: (a) 0.05; (b) 0.2; (c) 0.5; (d) 1.

Fig. 4.3.2 shows that the filtered signal (blue) approaches the original (red) if the maximum step increases. As a result, the maximum step minimizes the effects of noise and produces a 'smoother' signal. For implementation in the PBMR MPS, the maximum process parameter will be determined by the characteristics of the measurement distributions.

4.3.5 Principle component analysis

The PCA method is employed to perform the tasks of sensor FDI and state prediction [8]-[10], [29]. The reasons for this choice are:

- The method is applied independent of the mathematical model of the process.
- A model of low dimensions can be realized with a small amount of process data. Given that the characteristics of the process may change, the principle components can simply be altered or new ones added.
- The method is very successful if the process dynamics are relatively slow and sensor FDI is achieved faster than process feedback control. In this case, the feedback control system will not mask the effects of faults [55].

PCA is a statistical method that forms linear combinations of the original variables, which aims to account for all the variation in the data [56], [57]. The following notation is applied:

Consider a measurement vector at time instant k, with m observed variables

$$\mathbf{x}(k)=\left[\mathbf{x}_1(k),\,\mathbf{x}_2(k),\ldots,\mathbf{x}_m(k)\right]^T \tag{4.3.12}$$

The measurement matrix comprising n samples (k = 1,..., n) and zero mean, is calculated with

$$\mathbf{X}=\left[\left[\mathbf{x}(1),\,\mathbf{x}(2),\ldots,\mathbf{x}(n)\right]^T-\left[\mu(1),\,\mu(2),\ldots,\mu(n)\right]^T\right] \tag{4.3.13}$$

with μ the matrix mean vector. The n × m measurement matrix $\mathbf{X}$ is decomposed as follows

$$\mathbf{X}=\hat{\mathbf{X}}+\mathbf{E} \tag{4.3.14}$$

The matrices $\hat{\mathbf{X}}$ and $\mathbf{E}$ signify the modelled (component space) and unmodelled (residual space) variations of $\mathbf{X}$

$$\begin{aligned}\hat{\mathbf{X}} &= \hat{\mathbf{T}}\hat{\mathbf{P}}^{\mathrm{T}} \\ \mathbf{E} &= \tilde{\mathbf{T}}\tilde{\mathbf{P}}^{\mathrm{T}}\end{aligned} \tag{4.3.15}$$

where $\mathbf{T}\in\Re^{n\times l}$ and $\mathbf{P}\in\Re^{m\times l}$ are the score and loading matrices respectively, and l the number of principle components. Normally, the first few principle components can describe most of the variation in the data, and the original set of variables is reduced to l. Therefore, the partition of the principle components and the principle vectors give

$$\mathbf{P}=\left[\hat{\mathbf{P}}_l\ \tilde{\mathbf{P}}_{m-l}\right] \quad \text{and} \quad \mathbf{T}=\left[\hat{\mathbf{T}}_l\ \tilde{\mathbf{T}}_{m-l}\right] \tag{4.3.16}$$

The original measurement matrix is projected onto the principle component space and the residual space, i.e.

$$\mathbf{X}=\hat{\mathbf{T}}_l\hat{\mathbf{P}}_l^{\mathrm{T}}+\tilde{\mathbf{T}}_{m-l}\tilde{\mathbf{P}}_{m-l}^{\mathrm{T}}=\hat{\mathbf{C}}_l\mathbf{X}+\tilde{\mathbf{C}}_{m-l}\mathbf{X} \tag{4.3.17}$$

where the projection matrices $\hat{\mathbf{C}}_l=\hat{\mathbf{P}}_l\hat{\mathbf{P}}_l^{\mathrm{T}}$ and $\tilde{\mathbf{C}}_{m-l}=\mathbf{I}_m-\hat{\mathbf{C}}_l$.

After the PCA model is constructed, the model is used for fault detection. Consider a new sample vector $\mathbf{x}(k)$ that is scaled to zero mean and unit variance. Following the decomposition with (4.3.14)

$$\mathbf{x}(k)=\hat{\mathbf{x}}(k)+\mathbf{e}(k)=\hat{\mathbf{C}}_l\mathbf{x}(k)+\left(\mathbf{I}_m-\hat{\mathbf{C}}_l\right)\mathbf{x}(k) \tag{4.3.18}$$

where $\hat{\mathbf{x}}(k)$ and $\mathbf{e}(k)$ are the projection of the sample vector onto the principle component and residual space respectively.

To perform sensor fault detection using PCA, the vector's projection on the residual space is monitored. For normal operating conditions, $\mathbf{e}(k)$ will be small due to estimation errors and noise. A statistic, called the squared prediction error (SPE), is a measure that indicates how good the fit of the PCA model is. The SPE is monitored at every time instant k and is defined as

$$\mathrm{SPE}(k)=\left\|\mathbf{e}(k)\right\|^2=\left\|\left(\mathbf{I}_m-\hat{\mathbf{C}}_l\right)\mathbf{x}(k)\right\|^2 \tag{4.3.19}$$

For normal operation, the SPE is lower than a threshold δ^2 [58]

$$\mathrm{SPE}(k)=\delta_{\mathrm{SPE}}^2 \tag{4.3.20}$$

The test suggests an abnormal condition if the SPE surpasses the selected threshold. For the investigation, the SPE is estimated empirically using simulation data.

After a fault condition is detected, the faulty sensor must be isolated. An iterative variable reconstruction method is proposed by [59]. This method is based on the following procedure:

- Suppose the i-th sensor in the measurement vector **x**(k) is faulty.
- For m sensors, assume one is faulty and reconstruct the variable using the PCA model and the remaining m-1 healthy sensors.
- Recalculate the SPE after reconstruction.

Therefore, if the i-th sensor is reconstructed, the SPE will decrease below the threshold since the fault is corrected. However, if a non faulty sensor is reconstructed, the SPE will stay approximately the same.

Next, the variable reconstruction method is presented. The estimation of the i-th variable from the **x**(k) measurement vector is expressed by (4.3.21)

$$x_i(k) = \mathbf{x}(k)\hat{\mathbf{c}}_i = \left[\hat{\mathbf{c}}_{-i}^T \; \mathbf{0} \; \hat{\mathbf{c}}_{+i}^T\right]\mathbf{x}(k) + \hat{\mathbf{c}}_{ii}x_i(k) \tag{4.3.21}$$

with $\left[\hat{\mathbf{c}}_1 \; \hat{\mathbf{c}}_2 \ldots \hat{\mathbf{c}}_m\right] = \hat{\mathbf{P}}_l\hat{\mathbf{P}}_l^T$ and $\hat{\mathbf{c}}_i^T = \left[\hat{\mathbf{c}}_{1i} \; \hat{\mathbf{c}}_{2i} \ldots \hat{\mathbf{c}}_{mi}\right]^T = \left[\hat{\mathbf{c}}_{-i}^T \; \hat{\mathbf{c}}_{ii} \; \hat{\mathbf{c}}_{+i}^T\right]$. The subscripts -i and +i denote a new vector formed by the first (i-1) and last (m-i) elements of the sample vector respectively.

From (4.3.21), it can be seen that the value of the faulty sensor is included in the estimate of the reconstructed sensor. Therefore, the i-th variable $x_i(k)$ is fed back to the input of (4.3.21) and iterated until it converges. The converged value of $x_i(k)$ for $\hat{\mathbf{c}}_{ii} < 1$ is approximately

$$x_i(k) = \frac{\left[\hat{\mathbf{c}}_{-i}^T \; \mathbf{0} \; \hat{\mathbf{c}}_{+i}^T\right]}{\mathbf{1} - \hat{\mathbf{c}}_{ii}}\mathbf{x}(k) \tag{4.3.22}$$

Dunia et al. [59] states that the iteration will always converge.

An important feature that influences the accuracy of reconstruction is the number of principle components. As shown in (4.3.16), the principle components are split into separate matrices to allow projection onto the component space and the residual space. To determine the optimal number of components for the component space, the variance of the reconstruction error is used (VRE) [60]. The proposed index has a minimum corresponding to the best reconstruction. The variance of the reconstruction error, in the direction ξ_i, is

$$\mathrm{VRE}_i \equiv \mathrm{var}\left(\xi_i^T\left(\mathbf{x}(k) - x_i(k)\right)\right) \tag{4.3.23}$$

where $\xi_i = [0 \ldots 1_i \ldots 0]^T$ is the fault direction vector. To determine the optimal number of principle components l, the following objective is minimized

$$\min_l \sum_{i=1}^{m} q_i \mathrm{VRE}_i \tag{4.3.24}$$

where q_i denotes positive weights (can be chosen identical to equalize the reconstruction errors).

To illustrate the application of the PCA method for sensor FDI, an example is presented next. Real noisy sensor data from the prototype PBMM plant (discussed in Chapter 7) is used and include the following process variations: MPS start-up, normal power operation, injection and extraction together with valve operation, and MPS shut down.

In this example, measurements from 16 pressure and temperature sensors are considered. The measurements correspond with the eight inlet monitoring locations identified for the PBMR MPS and are shown in Fig. 4.3.3 (a) and (b). Since the variables are of different units (kPa and °C), the data can be either standardized by dividing each column with its standard deviation or separate models can be constructed for each variable type. The latter is selected and two PCA models are trained for the pressures and temperatures respectively. The data is divided that approximately 90 % is used for training the PCA models and 10 % for testing the various indices. The different data segments are illustrated in Fig. 4.3.4. Figures 4.3.3 and 4.3.4 show that the data segment used for testing (800 samples) includes steady state operation, injection and extraction.

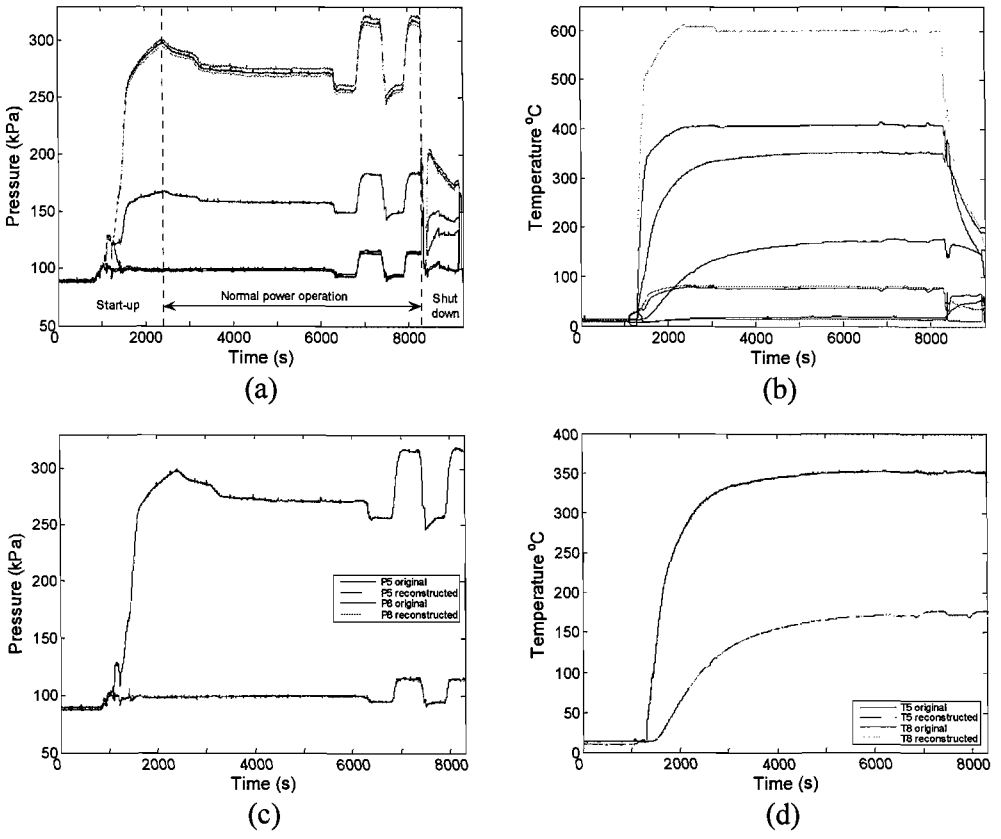

Fig. 4.3.3 Measured and PCA reconstructed values for T and P sensors: (a) measured *P*; (b) measured *T*; (c) reconstructed *P*5 and *P*8; (d) reconstructed *T*5 and *T*8.

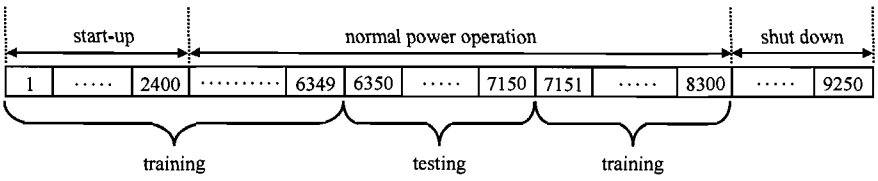

Fig. 4.3.4 The data segments used for training and testing the PCA models.

An initial requirement for the PCA models is the determination of the optimal number of principle components. The first step is to calculate the minimum VRE by reconstructing each sensor from the remaining whilst varying the number of principle components. The optimal number of principle components in the PBMM corresponds to 3 and 4 for the pressure and temperature models respectively. Figure 4.3.3 (c) and (d) illustrate the measurements and reconstruction estimates for the turbine (5) and pre-cooler (8) sensors.

By taking into account the nonlinear nature of the process, the estimations are acceptable. To verify that the proposed PCA models are sufficient for FDI, the four sensor faults depicted in Fig. 4.2.1 (b) - (d) are introduced in the data. Since the pressure data clearly shows when injection and extraction commences, the pressure model is used as an example. Figure 4.3.5 illustrates the calculated SPE index for the fault free measurements. The figure shows that for the fault free case, a threshold of $\delta^2_{SPE} = 0.5$ is selected. In addition, Fig. 4.3.5 (b) shows that the SPE remains below the threshold if a sensor is estimated.

The four sensor faults are introduced in the HPC pressure data P3 at t = 200 seconds (6550 seconds in Fig. 4.3.3 (a)). The fault magnitudes are as follows: bias fault of 1 kPa, drift fault of 0.005 kPa/s, sensor noise with σ = 1 and a complete failure resulting in a reading of 0 kPa. Accordingly, the SPE is used for fault detection and the faulty sensor is reconstructed. The SPE indices and the reconstruction estimates for the four faults are illustrated in Fig. 4.3.6 (a) - (h).

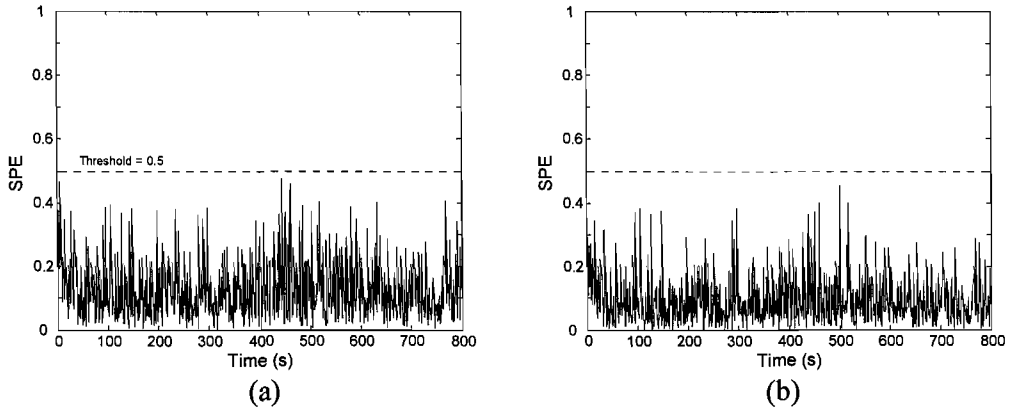

Fig. 4.3.5 The SPE index for the pressure PCA model: (a) without a sensor fault; (b) HPC pressure (P3) estimated.

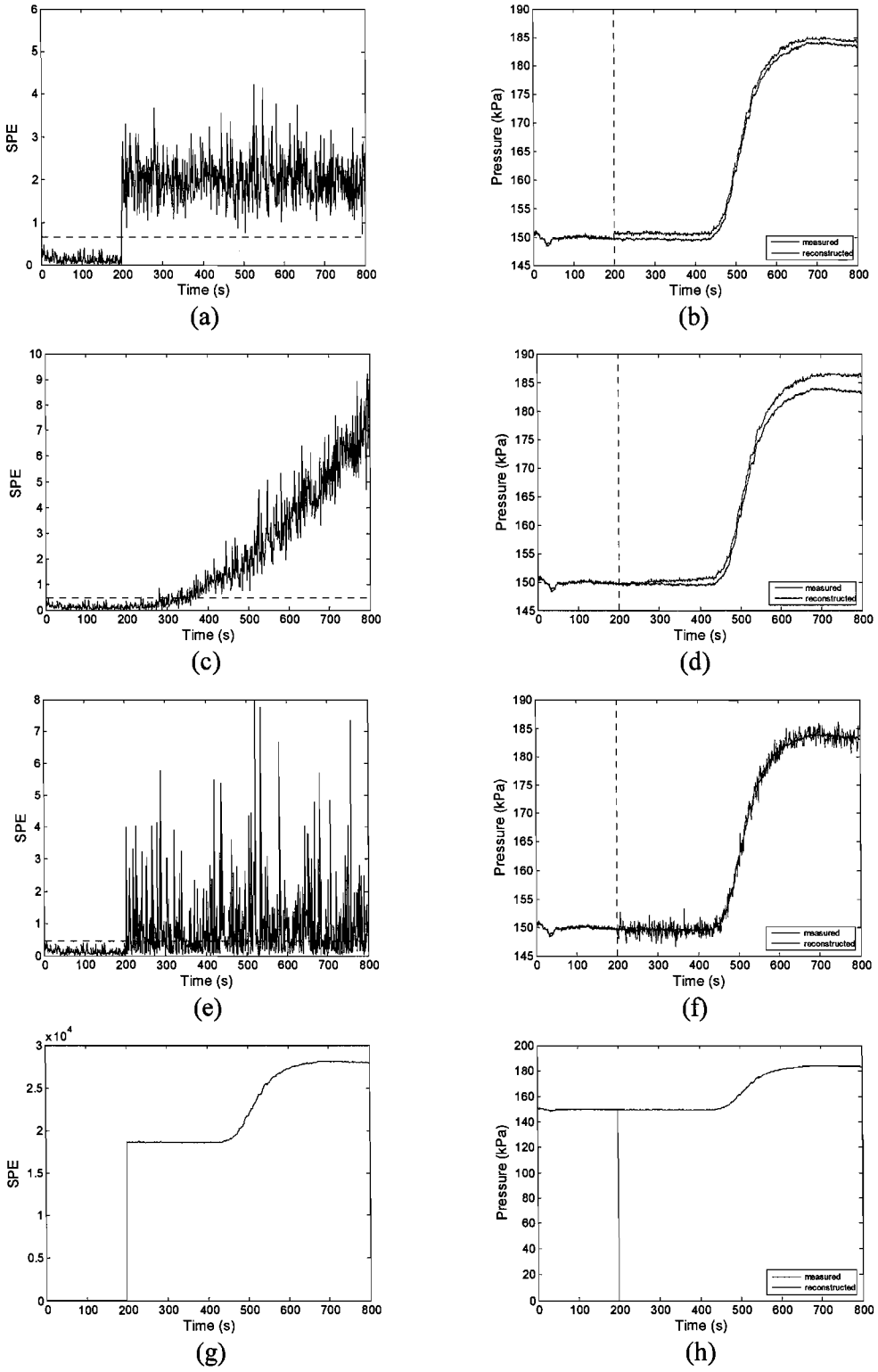

Fig. 4.3.6 The SPE indices for fault detection together with the reconstructed sensors.

The left column in Fig. 4.3.6 illustrates the variation in the SPE index during fault induction, whilst the right column shows the estimation of the faulty sensor. Although reconstruction normally commences after the SPE threshold is exceeded, P3 is estimated for the entire test set in this example.

Fig. 4.3.6 shows that the SPE index is below the selected threshold prior to induction of the different faults. In Fig 4.3.6 (a), the SPE index surpasses the threshold without any time delay after a bias fault is induced. Therefore, by comparing the SPE indices before and after reconstruction, i.e. Fig. 4.3.5 (b) and Fig. 4.3.6 (a), P3 can be isolated.

The figure shows that for the drift fault, the SPE index surpasses the threshold only after some time delay. This is expected since the sensor bias is relatively small for this period. The results therefore indicate that the time delay before fault detection is a function of the magnitude of the drifting sensor and the threshold of the SPE. In Fig. 4.3.6 (d), the SPE index is actually only surpassed at approximately 280 seconds when reconstruction commences.

Fig. 4.3.6 (e) shows that the SPE index fluctuates repeatedly for a noisy or degraded sensor. Therefore, it is concluded that larger values for the SPE index at irregular time intervals can be an indication of a noisy sensor. To identify spikes in the sensed values, the large SPE index will normally appear less frequently. In general, all the reconstructed sensor estimates are in good agreement with the original measured values before fault induction.

In conclusion, the PCA model was able to reduce the high redundancy among the process variables. Although the PBMM plant represents a nonlinear process, most of the variation in the data was captured by forming linear relations between the various sensed values. Also, by using the SPE index for fault detection, the induced faults are detected promptly without uncertainty. The major disadvantage of this method is that multiple sensed variables cannot be corrupted simultaneously, since the reconstruction procedure assumes that (m-1) sensors are healthy. However, for the PBMR MPS, the assumption is made that at any time instant, (m-1) measurement sets will be available with at least one healthy sensor out of three. Therefore, the difficult task is to identify a minimum of 7 healthy pressure and temperature sensors in different measurement sets out of a total of 48.

In the following section, sensor fusion is discussed. In hardware redundant sensor networks, sensor fusion gives a more reliable variable estimate if more than one healthy measurement is available.

4.4 Sensor fusion

In hardware redundant sensor networks, several concurrent values are normally available for each measured variable. Since these values are unavoidably corrupted with random noise, no single sensor can be relied on to give a truthful reading. Also, two sensor readings may be within their operational limits, but lie at different ends of the valid measurement region, resulting in a distribution for each measurement. Consequently, multiple sensor information is combined to provide more reliable and consistent readings for the sensed variables.

In the thesis, the task of sensor data fusion is accomplished by taking the average of the measured quantity weighted by the corresponding confidence values. A fuzzy validation curve is proposed by [61] and is based on fuzzy rules that define the centre of the validation curve. Since the statistical properties of each measurement distribution (residuals) are estimated off-line, these properties are utilized to assign a confidence value for the new measurement. In the investigation, the residual mean (ideally zero) is used to centre the validation gate.

Firstly, the curve is normalized to scale the confidence values between 0 and 1. As discussed in section 4.3.3, the absolute limits of the sensed variable are defined as $\pm 2\sigma$, and accordingly, the borders of the validation gate are set to these values. For the normal probability density function, the confidence values are computed as follows

$$\tau = \begin{cases} 0 & x_i < -2\sigma \\ \dfrac{e^{-\left(\frac{x_i-\mu}{a_{left}}\right)^2} - e^{-\left(\frac{x_i-(-2\sigma)}{a_{left}}\right)^2}}{1-e^{-\left(\frac{x_i-(-2\sigma)}{a_{left}}\right)^2}} & -2\sigma < x_i \le \mu \\ \dfrac{e^{-\left(\frac{x_i-\mu}{a_{right}}\right)^2} - e^{-\left(\frac{x_i-(2\sigma)}{a_{right}}\right)^2}}{1-e^{-\left(\frac{x_i-(2\sigma)}{a_{right}}\right)^2}} & \mu < x_i \le 2\sigma \\ 0 & x_i > 2\sigma \end{cases} \tag{4.4.1}$$

where τ is the confidence value for the sensor, x_i is the sensor value, μ and σ are the mean and standard deviation of the normal distribution (residuals), and a_{left}, a_{right} are modification parameters for the left and right sides of the validation gate. These parameters determine the width of the curve to compensate for external effects such as temperature changes. The fused estimate is calculated by

$$x_f = \frac{\sum_{i=1}^{n} x_i \tau(x_i)}{\sum_{i=1}^{n} \tau(x_i)} \tag{4.4.2}$$

with x_f the fused estimate and x_i the i-th sensor reading. In order to demonstrate the importance of the fusion algorithm, an illustrative example is shown in Fig. 4.4.1. A simple sine wave is measured with three sensors and corrupted with random noise. The original signal is then compared with the fused estimate, and the residuals are calculated for each sensor accordingly. Consequently, μ and σ are approximately 0.0001 and 0.5 for

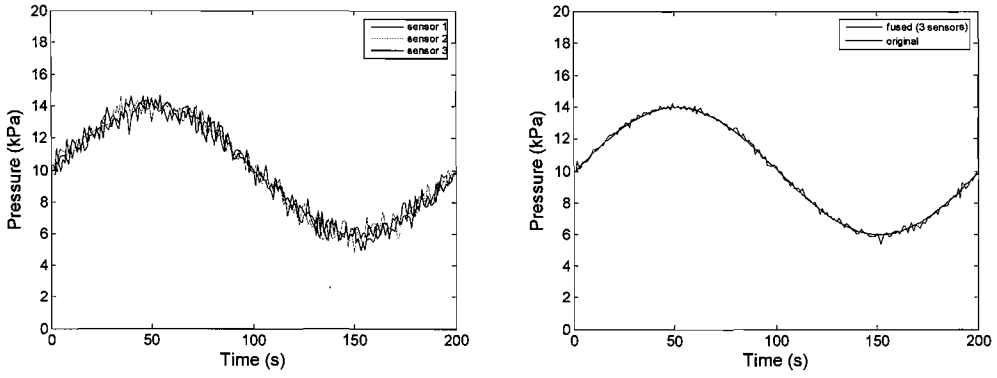

(a) (b)

Fig. 4.4.1 Fusion algorithm applied to random measurements: (a) 3 sensors with noise; (b) fused estimate.

each sensor. The validation gate is therefore centred on zero mean and the limits are set to ± 1 kPa. Fig. 4.4.1 (b) depicts the fused estimate obtained with (4.4.1) and (4.4.2). The figure shows that the fused estimate closely follows the original signal.

To show the improvement in measurement accuracy, the mean squared errors (MSE) of the original and fused measurements are computed and the results are summarized in Table 4.4.1. The table shows that the fused estimate of the sensors produce a better approximation of the original signal than the sensors' mean. Also, it is observed that the MSE decreases with an increase in the amount of sensors utilized for a measured variable.

In conclusion, it is demonstrated that the sensor fusion algorithm produces a better estimate of the measured variable compared to the mean of the sensors. In addition, it is observed that variable estimation is more accurate if measurement redundancy increases.

4.5 Sensor validation and fusion module architecture

This section discusses a comprehensive methodology for intelligent sensor validation and fusion based on the PBMR MPS. By applying an integrated architecture of the methods discussed, the uncertainty inherent in single sensor information is minimized. The Simulink® **SE**nsor validatio**N** and fu**S**ion module, SENSE, intelligently combine information from different sources to increase the accuracy and integrity of the measurements.

SENSE exploits the redundant sensor information by analyzing data from sensors independently, sensors in a measurement group, the immediate history of the previous sample window, and functional redundant sensor estimates. Consequently, the methodology is more robust than any single technique in the sense that different fault sensitivities can be incorporated into each.

Combination	Sensor 1	Sensor 2	Sensor 3	Mean (2)*	Mean (3)*	Fused (2)*	Fused (3)*
MSE	0.11533	0.12131	0.10307	0.06327	0.05304	0.02195	0.01192

Table 4.4.1 MSE results obtained for the sensor fusion algorithm. * ( ) denotes the amount of sensors.

The SENSE methodology comprises the following steps:

- Sensor signal pre-processing.
- Consistency analysis among each redundant measurement set.
- Fusion - 1st layer.
- Sensor configuration selection.
- PCA model analysis, fault isolation and sensor reconstruction.
- Fusion - 2nd layer.
- Residual statistical evaluation, fault detection and isolation.
- Fusion - 3rd layer.

The basic steps of the methodology are depicted in Fig. 4.5.1 and a more detailed reasoning structure of SENSE is illustrated in Fig. 4.5.2.

First, the information from the eight measurement channels/sets comprising 3 sensors per channel is pre-processed by means of the absolute limit and maximum process change indices. The obvious false readings are filtered out based on the absolute limit index. Following this, the maximum process step is checked for the remaining variables and adjusted accordingly. Initially, a large index is chosen to allow the filtered signal to follow the sensed values exactly. Systematically, the index is lowered to filter out the effects of noise and large measurement variations.

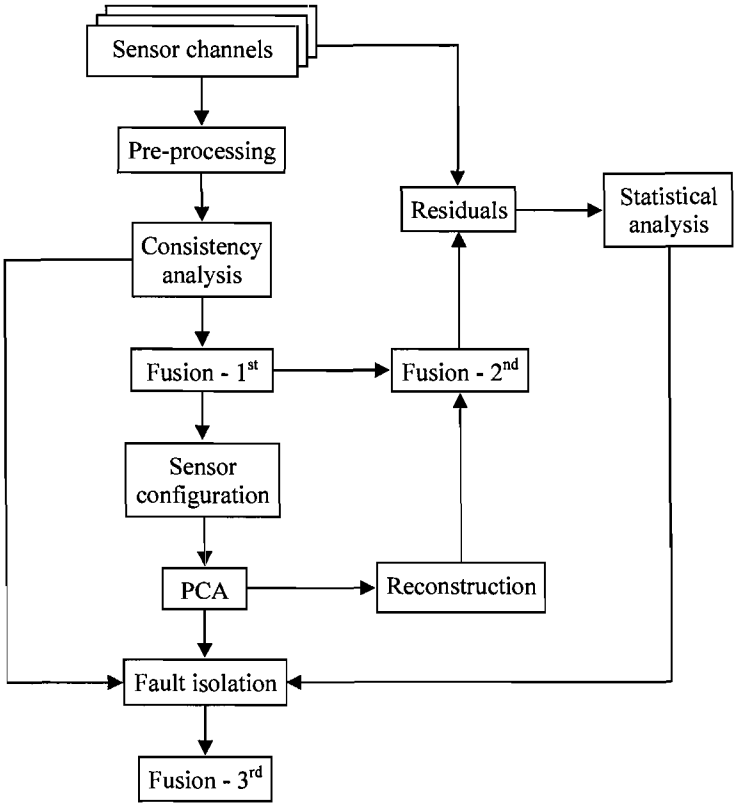

Fig. 4.5.1 A flow chart illustrating the SENSE architecture.

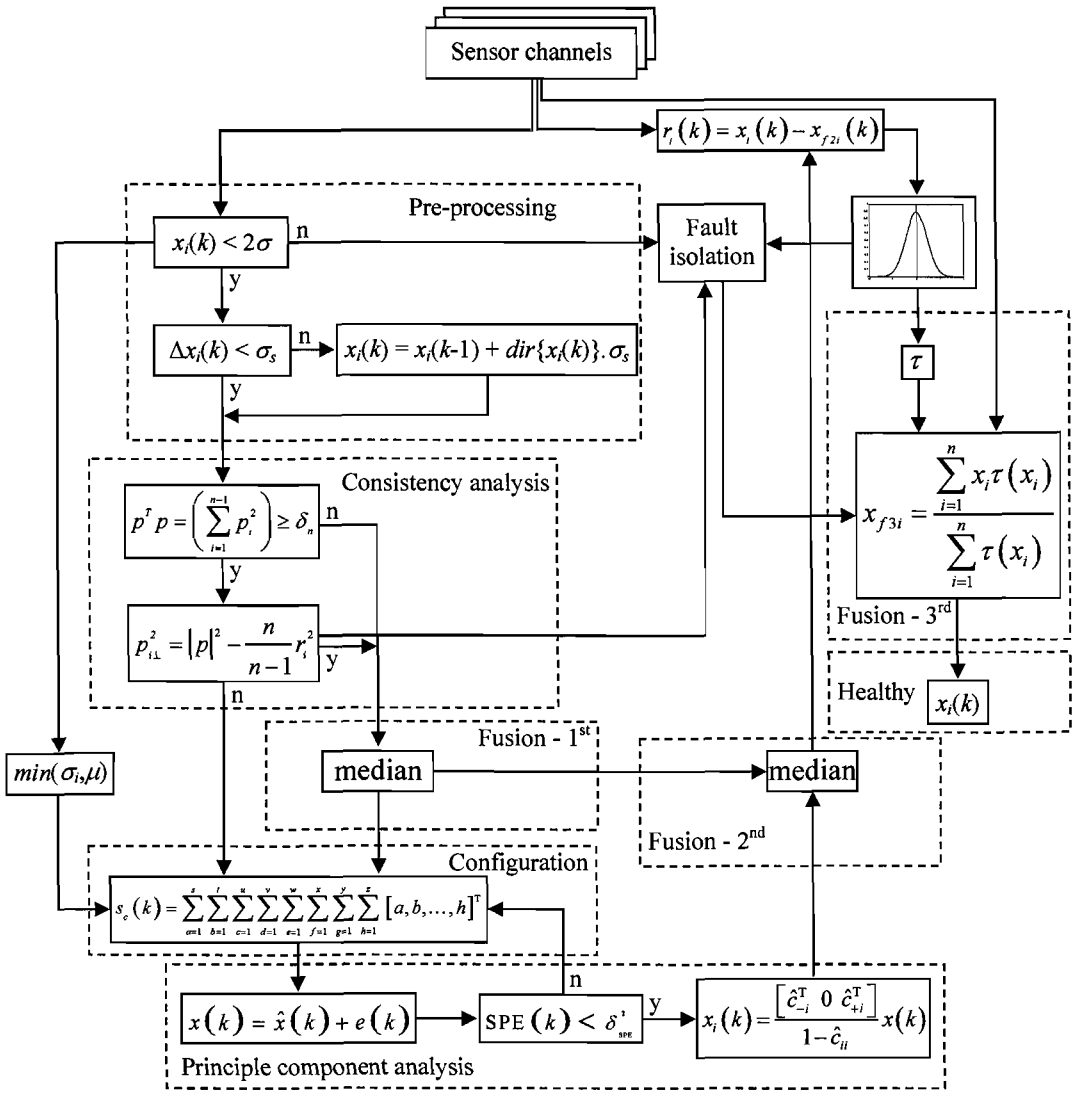

Fig. 4.5.2 A reasoning map illustrating the SENSE architecture.

Next, the filtered signals are validated for consistency using the non-temporal parity space algorithm. As discussed, isolation is not possible during this phase for multiple failures in a measurement channel. Therefore, the inconsistent signals are not combined before PCA analysis. If a single fault occurs, the faulty sensor is isolated and the remaining consistent signals are transferred to the first fusion layer.

Since the residual estimates are not available at this stage, consistent signals are fused based on the median of the readings. Computing the median rather than the mean eliminates any bias induced by outliers within the absolute limits of the sensor. Alternatively, sensor confidence values can be determined based on the previous sample window (residuals). By providing the PCA model with a fused estimate, the uncertainty in each measurement channel (single sensors) is minimized.

Following this, an intelligent search algorithm determines the total number of unique sensor configurations and organizes them with a decrease in the likelihood of failure according to a variance and mean (VM) index. The VM index is determined based on the minimum variance and mean of the (t-1)-th sample. Each configuration includes eight sensor channels with at least one sensor or fused estimate per channel. The total number of unique sensor configurations is given by s_c

$$s_c(k) = \sum_{a=1}^{s}\sum_{b=1}^{t}\sum_{c=1}^{u}\sum_{d=1}^{v}\sum_{e=1}^{w}\sum_{f=1}^{x}\sum_{g=1}^{y}\sum_{h=1}^{z}[a,b,\ldots,h]^T \qquad (4.5.1)$$

with s, t,..., z the number of sensors available in each channel or fused estimate. The impact of the number of faulty sensor configurations on the PCA model is depicted in Fig. 4.5.3. The following constraints are applicable to the figure:

- At any given time, a maximum of 16 sensors may fail. This constraint is based on the assumption that there is always one healthy sensor per measurement channel in the PBMR MPS.

- Sensor configurations must include at least 7 healthy ones to be functional; the eighth can be reconstructed (PCA algorithm requires m-1 healthy sensors).

The figure shows that the number of functional sensor configurations (red) decreases sharply if the number of faulty sensors increases. Therefore, more configurations will be tested by the PCA model before a functional configuration is found. However, this procedure is greatly reduced by means of selecting the most likely functional sensor configurations using the VM index.

Subsequently, each sensor configuration is projected onto the component and residual space by means of the PCA model. The squared prediction error is computed and the process is repeated until a functional sensor configuration is established (SPE < δ^2). To establish functional redundancy, each of the healthy sensors is set to zero and the signal reconstructed utilizing the remaining measurements. By providing functional redundant estimates, the uncertainty in each measurement channel is also decreased.

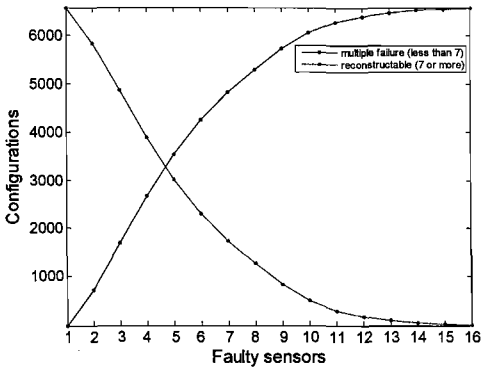

Fig. 4.5.3 Sensor configurations based on the number of faulty sensors.

Next, the PCA model estimates and the first fusion layer are fused (also based on the median) to combine all the redundant sensor information. The fused estimate serves as the expected value for each individual measurement channel.

To compute the sensor residuals, the original sensor values are subtracted from the fused estimate. Since the sensor residuals are assumed to be normally distributed for normal operation, their statistical properties (mean and variance) are monitored for any changes. Any variation in these properties will firstly identify and isolate a faulty sensor and secondly, characterize the type of sensor fault. It must be noted that since the residual distributions are applied, the trade-off is between sample window size and approximation error. A smaller sample size will promote early detection but also increase the approximation error.

To isolate the sensor faults, a simple rule-based expert system is devised and is illustrated in Fig. 4.5.4. The expert system consists of *if-then* statements and the ruling is based on the characteristics of the residuals. The list of rules is given below:

- **If** μ = N **and** σ^2 = S **and** *skew* = S, **then** sensor = normal.
- **If** μ = N **and** σ^2 = L **and** *skew* = S or L, **then** sensor = noise.
- **If** μ = L **and** σ^2 = N **and** *skew* = S, **then** sensor = dead.
- **If** μ = N **and** σ^2 = N **and** *skew* = S, **then** sensor = stuck.
- **If** μ = S **and** σ^2 = S **and** *skew* = S **and** {bias(t) - bias (t-1)} $\approx c$, **then** sensor = bias.
- **If** μ = S **and** σ^2 = S **and** *skew* = S **and** {bias(t) - bias (t-1)} $\neq c$, **then** sensor = drift.

with N, S and L indicating negligible, small and large values. The thresholds for each of these values are selected based on the specific application. Also, it is important to note that the methodology do not only rely on statistical residual evaluation to isolate faulty sensors. During each phase, sensors that do not comply with the given technique's criteria for normal operation are isolated and excluded from the estimates.

The final step is to calculate confidence values for each healthy sensor based on the sensor's residual distribution. To compute the values of the third fusion layer, the healthy sensors are fused together using the proposed method described in section 4.4. This produces the final estimate for each measurement channel.

To evaluate the fault detection and isolation capabilities of SENSE, the methodology is applied to a practical system next.

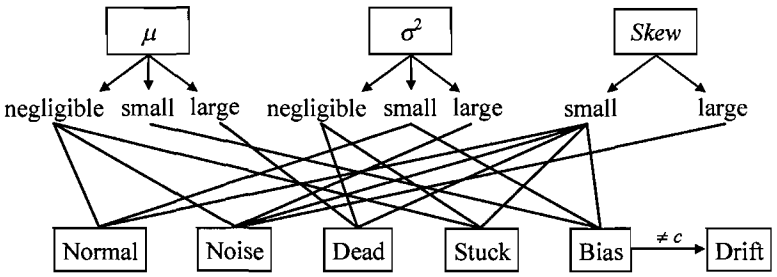

Fig. 4.5.4 Decision-tree illustrating the expert system reasoning.

4.6 Application of sensor FDI in the PBMM and PBMR

This section discusses the implementation of the sensor fault diagnosis methodology in a Brayton cycle-based PCU. Two case studies are presented and comprise applications in the PBMR and PBMM. In both case studies, random noise with different variances is added to the plant data. As a result, three different signals are generated for each measurement channel. The corresponding notation employed to identify the 24 pressure or temperature sensors are illustrated in Fig. 4.6.1. In each of the case studies, eight out of a maximum of 16 sensor malfunctions are introduced and include, noise, spikes, dead sensors, bias and measurement drift.

The *a priori* information of the validation and fusion methodology comprises the following parameters:

- Noise properties of the measured variables/sensors.
- The absolute limits 2σ of the sensor distributions.
- The maximum process change index Δx_i per time step.
- The parity vector threshold δ_n.
- The PCA model together with the number of principle components.
- The SPE threshold δ^2_{SPE}.
- The fusion modification indices a_{left}, a_{right}.
- The thresholds that define the fault range indices N, S and L.

It is important to note that some of the parameters must be defined for different process variations, for example, a valve change or operating point change (injection/extraction) requires a larger maximum process step. As discussed, this step will typically be small during steady state to minimize the effects of random noise.

4.6.1 Case study 1

In the first case study, the PBMM temperature data (normal power operation) depicted in Fig. 4.3.3 (b) is used. A preliminary step is to analyze the noise properties of each sensor distribution during fault free operation. From the data, the absolute limit for each variable is calculated (approximately 1.2) and the maximum process step is selected. Following this, the PCA model is trained with approximately 90 % of the sensor data, i.e. trained with the median of the three noisy sensor values. To determine the optimal number of principle components, the variance of the reconstruction error is used. The minimum VRE is obtained utilizing a PCA model with four principle components. Lastly, the SPE

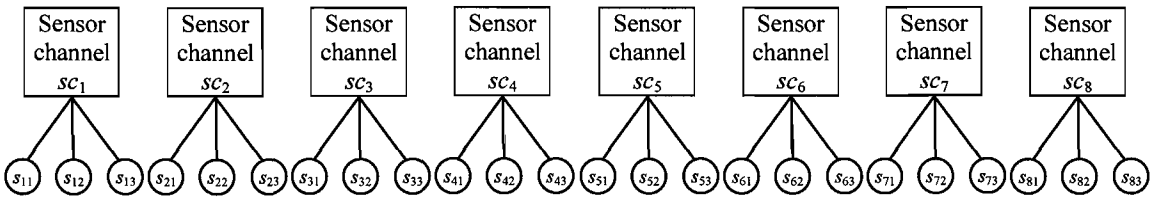

Fig. 4.6.1 Sensor notation utilized in the two case studies.

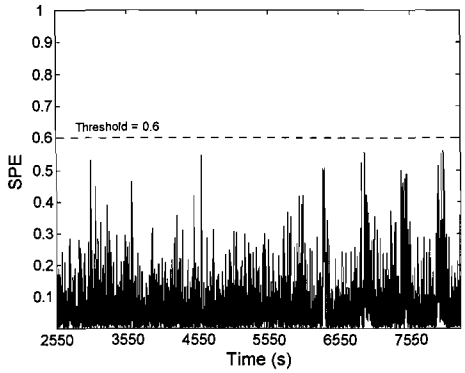

Fig. 4.6.2 The SPE index for the temperature PCA model (normal power operation).

threshold is calculated for the entire dataset (single sensors) during fault free operation and is shown in Fig. 4.6.2. The figure shows that the minimum SPE threshold can be selected as 0.6. For this case study, eight faults are induced in the PBMM sensor data and are listed in Table 4.6.1. The table shows that for two measurement channels, multiple sensor failures occur.

Following the pre-processing algorithm, each of the measurement channels is checked for consistency and the parity space method promptly identifies non-consistent measurements. In the case of faults 3/4, and 6/7, no unique fault isolation is observed after 5500 and 7500 seconds respectively. Therefore, the redundant signals are not fused in the respective measurement channels after these time intervals.

During each sample interval, a healthy sensor configuration is quickly identified by means of the minimum VM index and the PCA model. The SPE index calculated for each of these sensor configurations is shown in Fig. 4.6.3. The figure indicates that the average SPE index is lower than the index observed in Fig. 4.6.2. The reason for this is that the fused estimates for the different measurement channels provide a better approximation of the sensed variable than any single sensor.

Next, the healthy sensor estimates are calculated using the PCA model and fused with the original sensor configurations. These values serve as the expected estimates for each measurement channel. The residuals are determined for all the sensors and are illustrated in Fig. 4.6.4. In the figure, the three redundant measurements are depicted by different colours.

Sensor	Time (s)	Type	Magnitude
1. s_{11}	3000	Noise	$\sigma = 1$
2. s_{23}	Random	Spikes	Random
3. s_{31}	5500	Dead	0
4. s_{33}	4100	Bias	+ 1 °C
5. s_{52}	6200	Drift	+ 0.005 °C/s
6. s_{61}	7500	Bias	+ 1.5 °C
7. s_{62}	4800	Noise	$\sigma = 1$
8. s_{83}	3800	Dead	0

Table 4.6.1 Summary of PBMM temperature sensor faults: Case study 1.

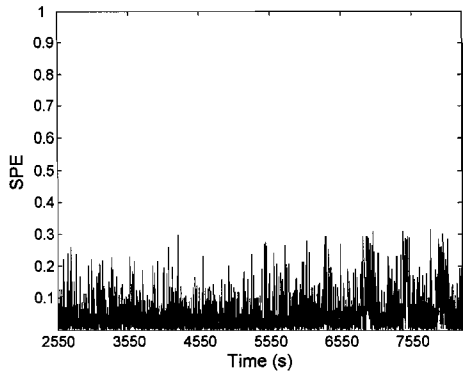

Fig. 4.6.3 The SPE index for the healthy sensor configurations selected for each sample interval.

The figure shows that the different faults can be detected and isolated by means of the sensor residuals. Moreover, since the sensor residuals are computed independently, the isolation of multiple simultaneous sensor failures is possible. By applying the rule based expert system with a sample size of 10, each of the faults is correctly isolated. An important observation is that the residual distributions are centred on zero mean, which indicates that sensor malfunctions can be detected during variations of the normal process. For the healthy sensors, the variations in the residuals are mainly caused by measurement noise.

To emphasize the improvement in measurement accuracy, the MSE of the residuals is computed and the results are summarized in Tables 4.6.2 and 4.6.3 respectively.

Channel	Sensor 1	Sensor 2	Sensor 3	Mean	Fused
1	0.09685	0.09536	0.09610	0.06265	0.02628
2	0.09523	0.09591	0.09860	0.07145	0.02880
3	0.09923	0.09278	0.09517	0.06651	0.02976
4	0.09339	0.09635	0.09847	0.06682	0.02870
5	0.09979	0.09660	0.09747	0.06682	0.02719
6	0.09616	0.09468	0.09666	0.06452	0.02819
7	0.09716	0.09321	0.09641	0.06610	0.02836
8	0.09641	0.09376	0.09797	0.06457	0.02693

Table 4.6.2 MSE results obtained for sensor fusion with no faults present (case study 1).

Channel	Sensor 1	Sensor 2	Sensor 3	Mean	Fused
1	0.27826	0.09678	0.09357	0.07773	0.03211
2	0.09376	0.09747	0.09904	0.07285	0.02976
3	49.8407	0.09376	0.65675	5.16653	0.03553
4	0.09309	0.09511	0.09716	0.06656	0.02897
5	0.09803	4.21563	0.09536	0.61043	0.02989
6	0.21492	0.21632	0.09591	0.09236	0.03460
7	0.09653	0.09666	0.09523	0.06595	0.02853
8	0.09853	0.09691	17309.5	1924.68	0.03276

Table 4.6.3 MSE results obtained for sensor fusion with the eight faults present (case study 1).

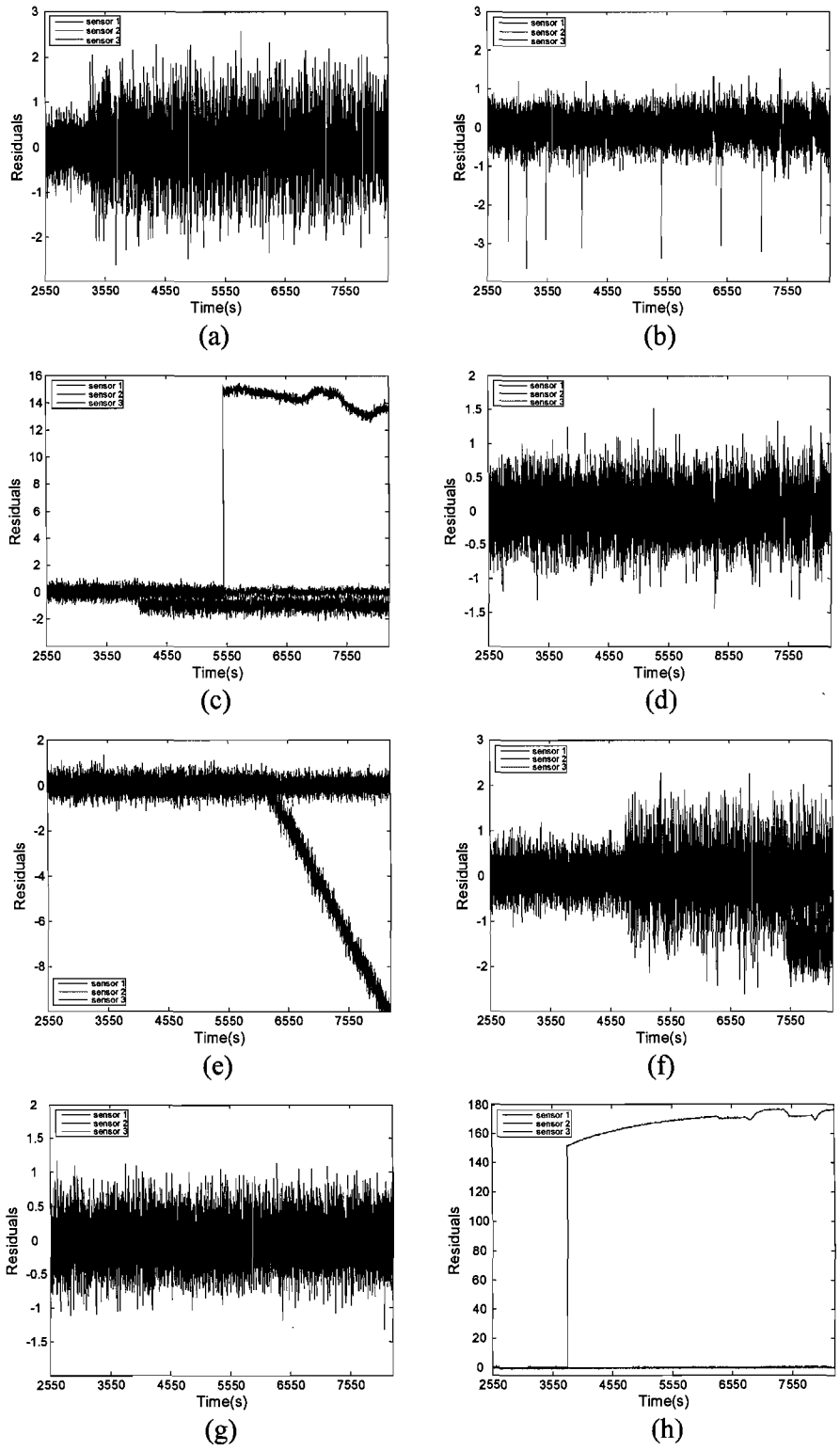

Fig. 4.6.4 The sensor residuals for the eight measurement channels (a-h signifies channel 1-8).

For the eight measurement channels, the MSE is calculated over the entire dataset for: the single redundant sensors, the mean of the redundant sensors, and the fused estimate obtained with the proposed methodology.

Table 4.6.2 lists the results obtained for the fault free measurements. The table shows that even though the mean of the sensors generates a better approximation for each measurement channel, the fused estimate is much lower. Table 4.6.3 shows that if sensors fail in a measurement channel, the mean is not an accurate approximation for the sensed variable. Also, the results show that even though multiple sensor failures occur, the methodology still gives an accurate estimate although slightly poorer than for a single failure. Therefore, the conclusion is drawn that the methodology gives a better estimate if the number of healthy sensors increases.

Figure 4.6.5 illustrates the fused estimates for each of the measurement channels. The figure shows that the fused values produce much 'smoother' signals. As a result, the final estimates correspond to values that are less corrupted with sensor noise.

4.6.2 Case study 2

In the second case study, data is generated by means of the PBMR Flownex model that is discussed in Chapter 3. The simulation starts at steady state 100 % MCR with all the bypass valves fully closed. The following process variations commence after this: valve operation between 100 and 250 seconds, extraction between 500 and 950 seconds, injection between 1300 and 2650 seconds, extraction between 4200 and 6200 seconds and lastly injection between 7500 and 8000 seconds. In order to evaluate sensor FDI during normal variations of the process, the pressure measurements are considered (temperature stays approximately constant). The pressure data for the eight measurement channels are illustrated in Fig. 4.6.6 (a).

In this case study, the same procedure is followed as discussed for case study 1 and is therefore not explained in detail again. The SPE index for the fault free measurements is depicted in Fig. 4.6.6 (b) (single sensors). The figure shows that the minimum threshold can be selected as 0.6.

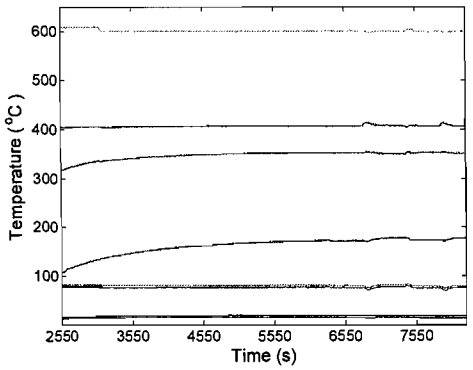

Fig. 4.6.5 Fused estimates for the PBMM temperature measurements after sensor validation.

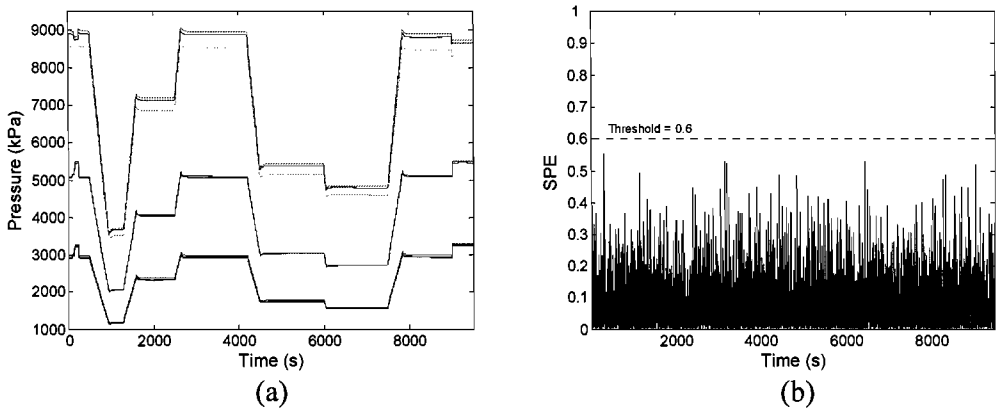

Fig. 4.6.6 The PBMR sensor data: (a) measured P; (b) SPE index for PCA model.

The eight faults considered for the pressure sensors are listed in Table 4.6.4. In this case study, multiple sensor failures occur in measurement channel 2. The parity space algorithm will therefore not be able to isolate the faults after 3600 seconds. The calculated SPE index for each of the selected healthy sensor configurations is illustrated in Fig. 4.6.7. The figure shows that the average SPE index for the fused estimates (first fusion layer) is lower than the index for single sensors.

The sensor residuals for each measurement channel are depicted in Fig. 4.6.8 (a)-(h).

Sensor	Time (s)	Type	Magnitude
1. s_{13}	2500	Dead	0
2. s_{21}	1100	Bias	+ 1.5 kPa
3. s_{22}	3600	Noise	$\sigma = 1$
4. s_{31}	4700	Bias	+ 1 kPa
5. s_{42}	5300	Drift	+ 0.005 kPa
6. s_{51}	Random	Spikes	Random
7. s_{63}	6400	Noise	$\sigma = 1$
8. s_{72}	7800	Dead	0

Table 4.6.4 Summary of PBMR pressure sensor faults: Case study 2.

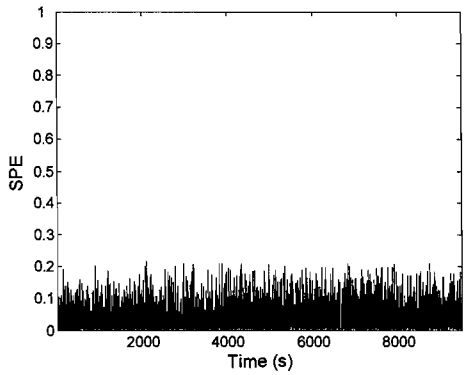

Fig. 4.6.7 The SPE index for the healthy sensor configuration selected for each sample interval.

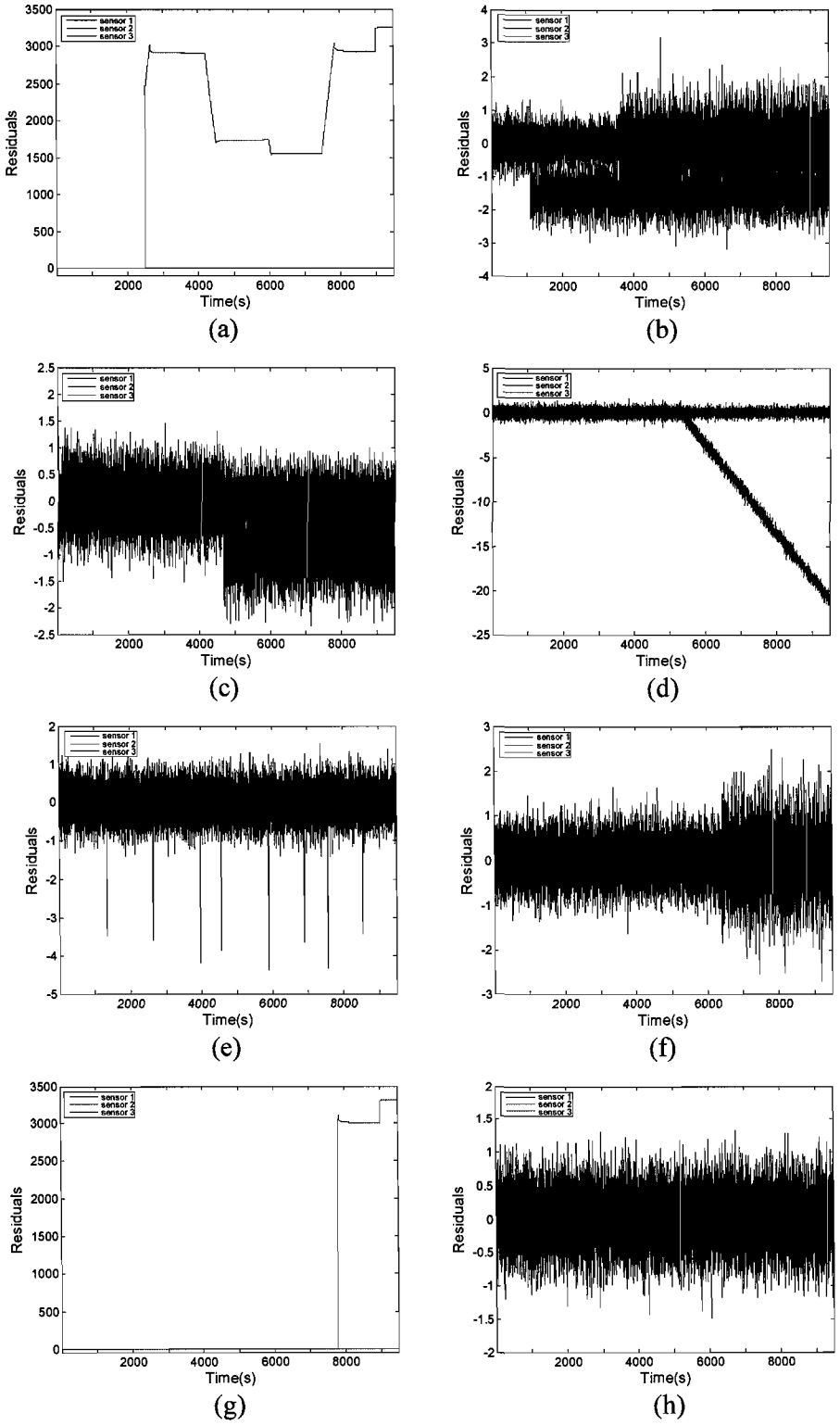

Fig. 4.6.8 The sensor residuals for the eight measurement channels (a-h signifies channel 1-8).

As observed in case study 1, the changes in the residuals are characteristic of the specific types of sensor faults. Also, the figure shows that the proposed methodology can isolate multiple simultaneous sensor failures during different variations of the process.

The results for the MSE of the residuals are summarized in Tables 4.6.5 and 4.6.6 respectively. Similarly, the results are consistent with those observed in case study 1. In Table 4.6.6, the errors in the faulty sensors are large whilst the methodology generates accurate estimates of the sensed variables. Also, similar to case study 1, the fused estimates are slightly less accurate if more than one sensor fails. The final fused values for each measurement channel are illustrated in Fig. 4.6.9.

In conclusion, the two case studies presented are indicative of real processes and demonstrate that the proposed methodology can promptly detect and isolate any of the sensor malfunctions during normal variations of the process. In addition, sensor fault diagnosis is possible for multiple simultaneous sensor failures.

4.7 Summary and conclusions

This chapter discussed an integrated framework for intelligent sensor validation and fusion in the PBMR MPS. The proposed methodology comprises a combination of techniques that exploits their individual strengths.

Channel	Sensor 1	Sensor 2	Sensor 3	Mean	Fused
1	0.07701	0.07563	0.07530	0.04627	0.02051
2	0.07767	0.07728	0.07596	0.04558	0.02286
3	0.07618	0.07574	0.07629	0.04635	0.02155
4	0.07486	0.07701	0.07712	0.04657	0.02059
5	0.07601	0.07486	0.07601	0.04584	0.02238
6	0.07634	0.07612	0.07469	0.04580	0.02135
7	0.07773	0.07629	0.07596	0.04644	0.02193
8	0.07667	0.07773	0.07579	0.04631	0.02226

Table 4.6.5 MSE results obtained for sensor fusion with no faults present (case study 2).

Channel	Sensor 1	Sensor 2	Sensor 3	Mean	Fused
1	0.07601	0.07612	2979538.5	331081.8	0.02512
2	1.83846	0.21400	0.07579	0.22156	0.02859
3	0.41152	0.07728	0.07491	0.07986	0.02515
4	0.07667	23.0236	0.07767	2.68435	0.02509
5	0.08049	0.07607	0.07524	0.04822	0.02187
6	0.07546	0.07431	0.13587	0.05856	0.02292
7	0.07535	306871.6	0.07773	34117.26	0.02347
8	0.07640	0.07790	0.07740	0.04670	0.02235

Table 4.6.6 MSE results obtained for sensor fusion with the eight faults present (case study 2).

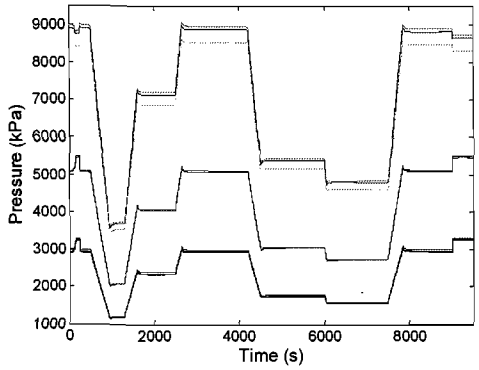

Fig. 4.6.9 Fused estimates for the PBMR pressure measurements after sensor validation.

Section 4.2 listed the most common faults that cause sensors to fail or give erroneous information. The following sensor malfunctions are investigated: sensor bias or offset, dead sensors, excessive noise, sensor drift and random spikes.

The different measurement validation techniques are described in section 4.3. The first technique employed, the non-temporal parity space, checks for consistency among a set of redundant sensors. In the case of the PBMR, three hardware redundant sensors are employed to monitor critical process parameters. The measured signals are pre-processed to exclude or condition any obvious false readings prior to the consistency check.

After the first fusion layer, sensor configurations that comprise inconsistent and fused measurement channels are validated with the PCA model. A healthy sensor configuration is characterized by a minimum of seven healthy or fused sensor estimates in different measurement channels.

Following the second fusion layer, fault isolation is achieved by monitoring the sensor residual distributions with a set of statistical indices. Since each residual distribution is calculated independently, multiple simultaneous sensor faults can be detected and isolated.

Section 4.4 discussed the fusion technique that is used to calculate the final sensor estimates. The technique is based on the average of the measured quantities weighted by corresponding confidence values.

Section 4.5 described the structure of the proposed methodology SENSE, whereafter section 4.6 presented two case studies. The case studies confirmed that the methodology can be successfully applied to a practical Brayton cycle-based PCU.

Some of the important conclusions reached in this chapter are:

- Most of the process variations during normal power operation can be captured with a linear PCA model, and is for the investigation, sufficient for the task of sensor FDI. However, to model all the system characteristics and minimize the estimation error, a nonlinear PCA technique will ideally be employed.

- To ensure that the methodology produces accurate sensor estimates, the different validation techniques must be used in combination. Some of the limitations of the individual methods are:

- No unique fault isolation is possible with the non-temporal parity space algorithm in the case of multiple sensor failures.

- The PCA method requires that m-1 sensors are healthy. This makes the method highly likely to fail in the case of multiple sensor malfunctions.

- Statistical evaluation of the redundant sensor signals alone will not be sufficient for sensor FDI. Since the mean of the sensor distributions constantly change due to process variations, fault isolation will be impossible in the case of multiple sensor failures. This is due to the fact that there will be no mechanism available for cross-reference among redundant measurements, i.e. all sensors will indicate different values.

- To provide the PCA model with a healthy sensor configuration (in the case of multiple failures), an intelligent search algorithm determines the total number of unique sensor configurations and organizes them with a decrease in the likelihood of failure according to a VM index. By applying this algorithm, the PCA model can be used for sensor FDI even though multiple sensors fail. This conclusion is based on the assumption that not all the redundant sensors may fail in (m-1) measurement channels simultaneously.

- An important attribute of the proposed methodology is that incipient faults (drift) can be identified and isolated in multiple sensors by means of evaluating the sensor residuals individually.

In addition to the motivations presented in previous chapters, the sensor fault diagnosis approach is developed since the sensors that measure critical process variables are located within the PPB in the PBMR. This arrangement requires that sensors can only be removed or tested once the PPB is open for maintenance, which will normally only be once every fuel cycle. Therefore, by implementing the proposed approach on-line, sensor readings can be validated in real-time.

Before the *h-s* graph approach for process fault diagnosis is presented in Chapter 6, two traditional methods of process FDI are applied to the PBMR MPS to emphasize their general shortcomings and the difficulties inherent in the implementation of the specific methods.

CHAPTER 5

Application of traditional fault detection techniques

This chapter presents two traditional process FDI techniques that are more readily used for NPP monitoring. The two methods are limit value checking and residual monitoring using a mathematical model of the plant. In order to demonstrate their advantages and limitations, both techniques are applied to the PBMR MPS.

5.1 Introduction

To date, most NPPs use two traditional methods for the task of process supervision. These methods are based on either a model-based or model-free representation of the process. The main objective of this chapter is to show a general implementation of the two methods in the PBMR MPS and investigate the limitations and complexities of these methods.

In section 5.2, the limit value checking approach is applied to the temperature and pressure measurements in the PBMR MPS. The 25 single faults listed in Chapter 3 are induced and the general limitations of this model-free method are illustrated.

Section 5.3 emphasizes the complexities in obtaining an accurate mathematical model that captures all the system dynamics in the PBMR MPS during normal power operation. Although this goal is achievable, the result is a transfer function that is unwieldy and too computational complex for real-time fault diagnosis. In order to simplify the mathematical model structure, only the most dominating system dynamics are included. As a result, the accuracy of the mathematical model is compromised. The development of a linear turbine model for the PBMR MPS is used as an example.

The chapter is summarized and concluded in section 5.4

5.2 Model-free methods - Limit value checking

This approach is widely used in practice because of its simplicity and reliability. Limit value checking performs well if the measurements are wide sense stationary and the system operates close to steady state. Their implementation however becomes more

involved and nontrivial if plant variables vary widely due to transient variations of the process. The method is based on setting limits (thresholds) above and below the normal range of variation, and faults are indicated if the limits are surpassed. Setting the limits is crucial and is usually done by incorporating system operational knowledge or by trail-and-error. Whilst implementation and maintenance are simple, the limit checking approach has several serious limitations:

- The fault detection sensitivity is highly dependent on the threshold width. Ideally, the limits are set around the normal variation of the fault free measurements. If the limits are set too wide apart, the fault detection scheme will be insensitive to incipient fault behaviour (a small deviation in the measurements will not exceed the thresholds). On the other hand, if the limits are too narrow, the number of false alarms will increase due to the normal variation of the process and noise. Also, if the mean of the measurements is not centred between the thresholds, false alarms may be generated due to normal plant variations.

- Single faults may cause several measurements to exceed their limits due to fault propagation through the system. This will trigger numerous alarms which makes isolation of the original fault very difficult.

- In a closed loop system like the PBMR, feedback systems may correct the effect of process faults to some extent, causing the measurements to remain within the normal limits. Detection of these faults will only be possible once the changes in the measurements are large enough (early detection not possible).

- Faults may cause sporadic alarms, i.e. alarms are not generated throughout the duration of the fault condition, but only when the data exceeds the limits. An example is a heat transfer area fault in the heat exchangers. Although debris on the heat transfer area could trigger an alarm, fragmentation break off may cause the data to settle between the thresholds again. An alarm will only be triggered once the fault becomes large enough to surpass the thresholds again. This makes the decision between an ongoing fault condition and a transient effect very difficult.

To demonstrate the performance of the method in a closed system, the 25 single faults are induced in the PBMR MPS. The eight temperature and pressure measurements are captured with the system operating at 100 % MCR. To simulate random noise with $\sigma = 2$ and zero mean, the steady state temperatures and pressures are varied by approximately ± 2 °C and ± 2 kPa. To allow for the variation in magnitude, the thresholds are set to an upper limit of +3 °C or kPa and a lower limit of -3 °C or kPa from the mean. Also, due to normal variations of the process, the thresholds are adaptive (not stationary) and move with the varying signals.

Figure 5.2.1 shows an example of the temperature and pressure measurements for the HPT inlet and the recuperator LP inlet respectively. The graphs illustrate the normal variation of the noisy signals (blue) and the centred fault free limits (red). With the limits set, the fault magnitudes are increased to 1 %. The results are listed in Table 5.2.1 for

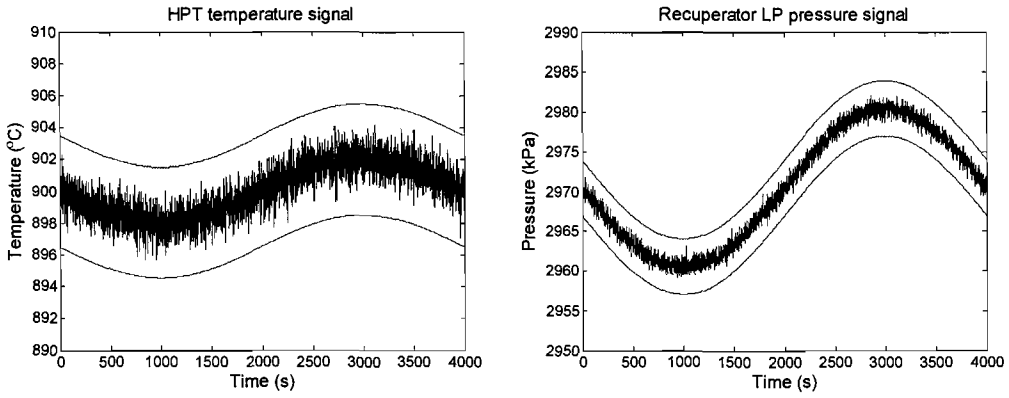

Fig. 5.2.1 Plant measurements at different nodes during normal fault free conditions: (a) HPT inlet temperature; (b) recuperator LP inlet pressure.

each of the 25 fault conditions. An alarm is indicated by '1' if a measurement limit is exceeded.

The following limitations of the method became apparent: by placing empirical thresholds on the measurements, some of the fault conditions can not be detected at an early stage. Faults 3, 7, and 25 did not surpass the thresholds for a small change in fault magnitude. In this case, the trade-off is between the threshold range and the false alarm

Node	Fault number																								
	1	2	3	4	5	6	7	8	9	10	11	12	13	14	15	16	17	18	19	20	21	22	23	24	25
T1	0	0	0	0	**0**	**0**	**0**	0	0	0	0	0	0	0	0	**0**	0	0	0	0	0	0	0	0	0
T2	0	**0**	0	0	1	1	0	0	0	0	0	0	0	0	0	0	**1**	1	0	0	0	0	0	0	0
T3	0	0	0	0	0	0	0	**0**	**0**	**0**	0	0	0	0	0	0	0	**0**	0	0	0	0	0	0	0
T4	0	0	**0**	**0**	0	0	0	1	1	1	0	0	0	0	0	0	0	0	**0**	0	0	0	0	0	0
T5	0	0	0	0	1	1	0	0	0	0	0	0	1	0	0	1	1	1	0	**0**	0	1	1	**0**	**0**
T6	0	0	0	0	0	0	0	0	0	0	**0**	**0**	**1**	**0**	**0**	1	0	0	0	0	**0**	1	1	1	0
T7	0	0	**0**	**0**	1	1	0	0	0	0	0	0	1	1	1	1	1	1	0	0	0	**1**	1	0	0
T8	**0**	0	0	0	0	0	0	1	1	1	0	0	1	1	0	0	0	0	0	0	0	0	**0**	0	0
P1	1	1	0	1	**1**	**1**	**0**	1	1	0	1	1	1	1	1	**1**	1	1	1	1	1	1	1	1	0
P2	0	**1**	0	1	1	1	0	1	1	0	1	1	1	1	1	1	**1**	1	1	1	1	1	1	1	0
P3	0	1	0	1	1	1	0	**1**	**1**	**0**	1	1	1	1	1	1	1	**1**	1	1	1	1	1	1	0
P4	0	0	**0**	**0**	0	0	0	0	0	0	0	0	0	0	0	0	0	0	**1**	0	0	0	0	0	0
P5	0	0	0	0	0	0	0	0	0	0	0	0	0	0	0	0	0	0	1	**1**	1	0	0	**0**	**0**
P6	0	0	0	0	0	0	0	0	0	0	**1**	**1**	**1**	**0**	**1**	1	0	0	1	1	**1**	1	1	1	0
P7	1	1	**0**	**1**	1	1	0	1	1	0	1	1	1	1	1	1	1	1	1	1	1	**1**	1	1	0
P8	**1**	1	0	1	1	1	0	1	1	0	1	1	1	1	1	1	1	1	1	1	1	1	**1**	1	0

Table 5.2.1 Fault alarms for the 25 single faults in the PBMR (alarm = 1, faulty component node = bold).

rate. Reducing the thresholds will improve the missed detection rate of small faults with incipient fault behaviour, but will increase the number of false alarms due to the presence of measurement noise.

The second drawback observed is the effect of fault propagation. Some fault conditions exceeded several thresholds, which will in reality set off a multitude of alarms. Also, it is important to note that the sequence of alarms is not unique, which will make fault isolation impossible. For example, faults 5, 6, 17 and 18 triggered the same set of alarms which makes the decision regarding fault isolation a nontrivial task.

Although the implementation of the method is straightforward, it is evident that the limit value checking method has several shortcomings if applied to the PBMR MPS, and is therefore not recommended as a viable solution to process fault diagnosis in the next generation type nuclear power plants.

5.3 Model-based methods - Mathematical models

In model-based FDI systems, the measured variables are compared to model estimates and various techniques are used to evaluate the residuals. Mathematical models are usually developed to describe the dynamics of the physical system by means of differential or difference equations for a specific operating region [41]. The effectiveness of model-based methods, however, relies on an accurate mathematical model of the process, and building a nonlinear model of a complex plant is very difficult. In addition, priori knowledge about system behaviour is usually exploited in these models, which are limited in the next generation type nuclear power plants.

To date, simulation software like Flownex are used to model thermodynamic processes, but results and system parameter dependencies can be difficult to interpret and identify. In addition, developing an accurate model of the system is the responsibility of the engineer, and it is usually not clear from the simulations what the important parameters are that drive the system dynamics.

This section describes the development of a mathematical model (state equations) of the MPS power turbine, which can be used in model-based FDI techniques like state observers. Although the model gives insight into parameter dependencies and system dynamics, some drawbacks of this type of modelling are emphasized.

5.3.1 Model development and assumptions

In this section, a linear model of the turbine is developed and applied to the PBMR by means of a state observer. A linear model is developed since most model-based methods assume system linearity, and a nonlinear system requires linearization around an operating point or region [40]. The modelling method is discussed next.

A simplified linear modelling method was developed by [62] for the purpose of plant control of a three-shaft Brayton cycle and is adapted for the investigation. This technique is suitable for the purpose of FDI seeing as the model is based on perturbed values that characterize system changes (representative of faults or process variations).

The following assumptions are made regarding the linear model and modelling method:

- The variations in state variables are the result of perturbations in some of the other state variables due to transients (process variations or faults).
- The system operating point is the steady state values of the system prior to the system states being perturbed by a transient.
- The change in system states is small enough for the system to be modelled by a linear approximation during the period of interest (normal power operation).

Assume a system during steady state with no faults present, which is a function of other variables, is described by

$$y = f(x_1, x_2) \tag{5.3.1}$$

If one or all of the variables are perturbed by a small change due to a fault, the result is

$$y_0 + \Delta y = f(x_{01} + \Delta x_1, x_{02} + \Delta x_2) \tag{5.3.2}$$

with: the subscript 0 representing the steady state values;
Δx_1, Δx_2 the changes in variables x_1 and x_2; and
Δy the resulting change in y due to the change in variables.

Applying a first order Taylor expansion (motivated by the third assumption listed above)

$$y_0 + \Delta y \approx f(x_{01}, x_{02}) + \left.\frac{\partial y}{\partial x_1}\right|_{x_{01}, x_{02}} \Delta x_1 + \left.\frac{\partial y}{\partial x_2}\right|_{x_{01}, x_{02}} \Delta x_2 \tag{5.3.3}$$

The steady state term is removed since the partial derivatives are evaluated at the operating point, and as a result, (5.3.3) reduces to

$$\Delta y \approx \frac{\partial y}{\partial x_1}\Delta x_1 + \frac{\partial y}{\partial x_2}\Delta x_2 \tag{5.3.4}$$

5.3.2 The linear turbine model

The following section describes the development of the linear turbine model. The model is based on the following assumptions (assumptions are made to obtain a lower order dynamic model):

- There is no significant volume inside the turbine (infinitely fast pressure transfer).

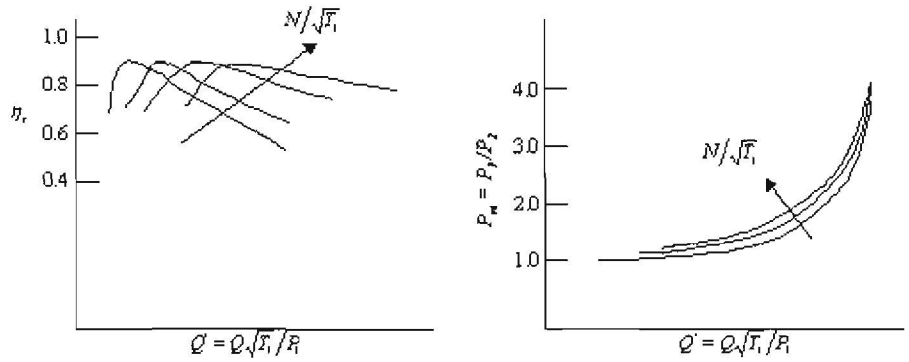

Fig. 5.3.1 Turbine efficiency and pressure ratio to non dimensional mass flow.

- The turbine is described by two maps, i.e. the non dimensional mass flow and non dimensional speed versus pressure ratio and isentropic efficiency (see Fig. 5.3.1).
- Apart from the gas flow and shaft, no energy flows occur across the boundaries of the turbine (e.g. heat losses).
- The inlet and diffuser volumes are modelled by separate models.
- There is no energy storage within the turbine itself and energy storage due to the shaft inertia and volumes (due to the pressure vessel) are modelled by separate models.
- The steady state turbine maps are valid under transient conditions.

Therefore, the turbine model is reduced to a system with four inputs and outputs respectively and is depicted in Fig. 5.3.2. Table 5.3.1 lists the variables and their nonlinear equations that are used in the development of the linear turbine model.

Fig. 5.3.2 The input-output measurements of the turbine model.

Variable	Description	Equation
p_1	Total inlet pressure	
p_2	Total outlet pressure	
t_1	Total inlet temperature	
t_2	Total outlet temperature	
N	Shaft speed	
N'	Non dimensional speed	$N' = N/\sqrt{t_1}$
Q	Mass flow	
Q'	Non dimensional mass flow	$Q' = Q\sqrt{t_1}/p_1$
W	Shaft output power	$W = Qc_p(t_1 - t_2)$
γ	Ratio of specific heats of the gas	$\gamma = c_p/c_v$
p_r	Pressure ratio	$p_r = p_1/p_2$
η	Isentropic efficiency	$\eta = \dfrac{t_2/t_1 - 1}{p_r^{-(\gamma-1/\gamma)} - 1}$

Table 5.3.1 Summary of turbine model variables.

The linear model of the turbine uses the perturbed values as described above with the steady state terms removed. The linear pressure ratio approximation is given by

$$\Delta p_r = \frac{\partial p_r}{\partial p_1} \cdot \Delta p_1 + \frac{\partial p_r}{\partial p_2} \cdot \Delta p_2 \tag{5.3.5}$$

To determine the linear mass flow, it is seen in Fig. 5.3.1 that the pressure ratio is a function of the non dimensional mass flow and non dimensional speed, and hence it follows that

$$\Delta p_r = \frac{\partial p_r}{\partial Q'} \cdot \Delta Q' + \frac{\partial p_r}{\partial N'} \cdot \Delta N' \tag{5.3.6}$$

Since the non dimensional mass flow and the non dimensional speed are calculated by the equations listed in Table 5.3.1, (5.3.6) can be expanded with the chain rule for derivatives and gives

$$\Delta p_r = \frac{\partial p_r}{\partial Q'}\left(\frac{\partial Q'}{\partial Q}\Delta Q + \frac{\partial Q'}{\partial p_1}\Delta p_1 + \frac{\partial Q'}{\partial t_1}\Delta t_1\right) + \frac{\partial p_r}{\partial N'}\left(\frac{\partial N'}{\partial N}\Delta N + \frac{\partial N'}{\partial t_1}\Delta t_1\right) \tag{5.3.7}$$

From (5.3.7), the mass flow rate can be determined as

$$\Delta Q = \frac{\Delta p_r - \frac{\partial p_r}{\partial p_1}.\Delta p_1 - \left(\frac{\partial p_r}{\partial t_1} + \frac{\partial p_r}{\partial t_1}\right)\Delta t_1 - \frac{\partial p_r}{\partial N}.\Delta N}{\frac{\partial p_r}{\partial Q}} \tag{5.3.8}$$

The expansion of change in efficiency follows the same method as for the mass flow expansion. The isentropic efficiency is a function of the non dimensional mass flow and non dimensional speed, and hence it follows that

$$\Delta\eta = \frac{\partial\eta}{\partial Q'}\cdot\Delta Q' + \frac{\partial\eta}{\partial N'}\cdot\Delta N' \tag{5.3.9}$$

Since the non dimensional mass flow and the non dimensional speed are given by the equations listed in Table 5.3.1, (5.3.9) can be expanded with the chain rule for derivatives and gives

$$\Delta\eta = \frac{\partial\eta}{\partial Q'}\left(\frac{\partial Q'}{\partial Q}\Delta Q + \frac{\partial Q'}{\partial p_1}\Delta p_1 + \frac{\partial Q'}{\partial t_1}\Delta t_1\right) + \frac{\partial\eta}{\partial N'}\left(\frac{\partial N'}{\partial N}\Delta N + \frac{\partial N'}{\partial t_1}\Delta t_1\right) \tag{5.3.10}$$

Given the efficiency, the linear change in outlet temperature can be expressed as

$$\Delta t_2 = \frac{\partial t_2}{\partial t_1}\cdot\Delta t_1 + \frac{\partial t_2}{\partial p_r}\cdot\Delta p_r + \frac{\partial t_2}{\partial\eta}\cdot\Delta\eta \tag{5.3.11}$$

Assuming that the specific heat of the gas at constant pressure stays the same, the linear change in shaft power is given by

$$\Delta W = \frac{\partial W}{\partial Q}\cdot\Delta Q + \frac{\partial W}{\partial T}\cdot\Delta T \tag{5.3.12}$$

with the change in temperature given by $\Delta T = (t_1 - t_2)$.

It is important to note that the mechanical efficiency of the turbine must be included in the shaft model and is for this reason not accounted for in the turbine model itself. The turbine equations can now be written in matrix form as

$$\begin{bmatrix} 1 & 0 & 0 & 0 \\ -c_5c_9 & 1 & 0 & 0 \\ 0 & -c_{19} & 1 & 0 \\ -c_{11} & 0 & c_{12} & 1 \end{bmatrix}\begin{bmatrix} \Delta Q \\ \Delta\eta \\ \Delta t_2 \\ \Delta W \end{bmatrix} = \begin{bmatrix} \frac{c_1 - c_{14}}{c_{13}} & \frac{c_2}{c_{13}} & -\frac{c_{15}}{c_{13}} & -\frac{c_{16}}{c_{13}} \\ c_6c_9 & 0 & c_7c_{10} & c_8c_{10} + c_9c_{20} \\ c_1c_{18} & c_2c_{18} & 0 & c_{17} \\ 0 & 0 & 0 & c_{12} \end{bmatrix}\begin{bmatrix} \Delta p_1 \\ \Delta p_2 \\ \Delta N \\ \Delta t_1 \end{bmatrix} \tag{5.3.13}$$

The descriptions and steady state values for the coefficients used in (5.3.13) are given in Table 5.3.2.

Coefficient	Description	Steady state value
c_1	$\frac{\partial p_r}{\partial p_1}$	$\frac{1}{p_{02}}$
c_2	$\frac{\partial p_r}{\partial p_2}$	$-\frac{p_{01}}{p_{02}^2}$
c_3	$\frac{\partial p_r}{\partial Q'}$	Slope of pressure ratio and obtained from pressure ratio map at operating point
c_4	$\frac{\partial p_r}{\partial N'}$	Slope of pressure ratio to non dimensional mass flow and obtained from pressure ratio map at operating point
c_5	$\frac{\partial Q'}{\partial Q}$	$\frac{Q_0'}{Q_0}$
c_6	$\frac{\partial Q'}{\partial p_1}$	$-\frac{Q_0'}{p_{01}}$
c_7	$\frac{\partial N'}{\partial N}$	$\frac{N_0'}{N_0}$
c_8	$\frac{\partial N'}{\partial t_1}$	$-\frac{1}{2}\frac{N_0'}{t_{01}}$
c_9	$\frac{\partial \eta}{\partial Q'}$	Slope of isentropic efficiency and obtained from efficiency map at operating point
c_{10}	$\frac{\partial \eta}{\partial N'}$	Slope of isentropic efficiency to non dimensional mass flow and obtained from efficiency map at operating point
c_{11}	$\frac{\partial W}{\partial Q}$	$\frac{W_0}{Q_0}$
c_{12}	$\frac{\partial W}{\partial T}$	$Q_0 c_p$
c_{13}	$\frac{\partial p_r}{\partial Q}$	$c_3 . \frac{Q_0'}{Q_0}$
c_{14}	$\frac{\partial p_r}{\partial p_1}$	$-c_3 . \frac{Q_0'}{p_{01}}$
c_{15}	$\frac{\partial p_r}{\partial N}$	$c_4 . \frac{N_0'}{N_0}$
c_{16}	$\frac{\partial p_r}{\partial t_1}$	$c_3 . \frac{1}{2}\frac{Q_0'}{t_{01}} - c_4 \frac{1}{2}\frac{N_0'}{t_{01}}$
c_{17}	$\frac{\partial t_2}{\partial t_1}$	$\eta\left(p_r^{-(\gamma-1)/\gamma} - 1\right) + 1$

c_{18}	$\frac{\partial t_2}{\partial p_r}$	$c_{17}.\frac{t_{01}p_{02}}{p_{01}}$
c_{19}	$\frac{\partial t_2}{\partial \eta}$	$c_{17}.\frac{t_{01}}{\eta_0}$
c_{20}	$\frac{\partial Q'}{\partial t_1}$	$\frac{1}{2}\frac{Q'_0}{t_{01}}$

Table 5.3.2 Summary of turbine model coefficients.

It is important to note that the shaft dynamics are not included in the turbine model since the perturbation in torque due to a change in shaft power or speed is given by the net torques acting on the shaft. Owing to the fact that the net torques is a function of the turbine and compressors torques (connected to a single shaft), the shaft model is devised separately.

The turbine state space model equations, derived in explicit form, is given in matrix form by (5.3.14) as

$$\begin{bmatrix}\Delta Q\\ \Delta\eta\\ \Delta t_2\\ \Delta W\end{bmatrix}=\begin{bmatrix}\frac{c_1-c_{14}}{c_{13}} & \frac{c_2}{c_{13}} & \frac{-c_{15}}{c_{13}} & \frac{c_{16}}{c_{13}}\\ c_6c_9+c_5c_9\left(\frac{c_1-c_{14}}{c_{13}}\right) & \frac{c_2c_5c_9}{c_{13}} & c_7c_{10}+c_5c_9\left(\frac{-c_{15}}{c_{13}}\right) & c_8c_{10}+c_9c_{20}+c_5c_9\left(\frac{-c_{16}}{c_{13}}\right)\\ \left\{c_1c_{18}+c_{19}\left(\begin{matrix}c_6c_9+\\ c_5c_9\left(\frac{c_1-c_{14}}{c_{13}}\right)\end{matrix}\right)\right\} & c_2c_{18}+\frac{c_2c_5c_9c_{19}}{c_{13}} & c_{19}\left(c_7c_{10}+c_5c_9\left(\frac{-c_{15}}{c_{13}}\right)\right) & c_{17}+c_{19}\left(c_8c_{10}+c_9c_{20}+c_5c_9\left(\frac{-c_{16}}{c_{13}}\right)\right)\\ \left\{\begin{matrix}c_{11}\left(\frac{c_1-c_{14}}{c_{13}}\right)-\\ c_{12}\left(\begin{matrix}c_1c_{18}+\\ c_{19}\left(\begin{matrix}c_6c_9+\\ c_5c_9\left(\frac{c_1-c_{14}}{c_{13}}\right)\end{matrix}\right)\end{matrix}\right)\end{matrix}\right\} & \left\{\begin{matrix}c_{11}\left(\frac{c_2}{c_{13}}\right)-c_{12}\\ \left(c_2c_{18}+\frac{c_2c_5c_9c_{19}}{c_{13}}\right)\end{matrix}\right\} & \left\{\begin{matrix}c_{11}\left(\frac{-c_{15}}{c_{13}}\right)-\\ c_{12}\left(c_{19}\left(\begin{matrix}c_7c_{10}+\\ c_5c_9\left(\frac{-c_{15}}{c_{13}}\right)\end{matrix}\right)\right)\end{matrix}\right\} & \left\{\begin{matrix}c_{12}+c_{11}\left(\frac{-c_{16}}{c_{13}}\right)-\\ c_{12}\left(\begin{matrix}c_{17}+\\ c_{19}\left(\begin{matrix}c_8c_{10}+c_9c_{20}+\\ c_5c_9\left(\frac{-c_{16}}{c_{13}}\right)\end{matrix}\right)\end{matrix}\right)\end{matrix}\right\}\end{bmatrix}\begin{bmatrix}\Delta p_1\\ \Delta p_2\\ \Delta N\\ \Delta t_1\end{bmatrix} \tag{5.3.14}$$

with Q the mass flow, η the isentropic efficiency, t_1 and t_2 the inlet and outlet temperatures respectively, N and W the shaft speed and output power, p_1 and p_2 the total inlet and outlet pressures respectively.

As discussed, the turbine model uses perturbed values and hence, cannot give a steady state solution, since by definition, all the states are zero for steady state (zero change). A precondition for model development is to obtain a steady state solution to determine the model coefficients listed in Table 5.3.2. This can be done by using simulation software or plant measurements.

In order to validate the linear turbine model, the nonlinear PBMR Flownex model is firstly used to obtain a steady state solution to determine the model coefficients. Following this, the following inputs are varied around their steady state values: the inlet temperature 900 °C, the outlet pressure 2975 kPa and the turbine speed 6000 rpm. The inlet pressure is varied and depicted in Fig. 5.3.3. The perturbed transient values (Flownex minus the steady state solution) is entered into the linear model and the results are shown in Fig. 5.3.4 (a) to (d) for the turbine mass flow, efficiency, outlet temperature and output power.

The results presented in Fig. 5.3.4 (a) to (d) show that the linear turbine model correlates well with Flownex, but showed some deviations for temperature and efficiency. This is an indication that not all the dynamics are included in the model.

Next, the model is validated with a fault condition. A turbine pressure ratio fault, i.e. fault 12 described in Chapter 3, is induced. A scaling factor of 0.001*t is subtracted from the turbine pressure ratio (starting at t = 100 seconds) in the nonlinear model to emulate an internal turbine fault. The outputs of the models are shown in Fig 5.3.4 (e) to (h). To detect the fault condition, a state observer is selected and is discussed next.

Given the linear equations are in state space form and parameters **A**, **B** and **C** are known, a state observer can be designed [4] for fault detection as

$$\begin{aligned} \dot{\hat{x}} &= \mathbf{A}\hat{x}(t) + \mathbf{B}u(t) + \mathbf{H}e(t) \\ e(t) &= y(t) - \mathbf{C}\hat{x}(t) \end{aligned} \tag{5.3.15}$$

with **H** the observer feedback and e(t) the output error. Since the fault acts as an output change Δy, the state estimation error is then given by

$$\begin{aligned} \dot{\tilde{x}} &= [\mathbf{A} - \mathbf{HC}]A\tilde{x}(t) - \mathbf{HM}f_M(t) \\ e(t) &= \mathbf{C}\tilde{x}(t) + \mathbf{H}f_M(t) \end{aligned} \tag{5.3.16}$$

with $\tilde{x}(t) = x(t) - \hat{x}(t)$ and f_M the output fault acting through **M**. The output error e(t) can now be used as residual to detect the fault condition.

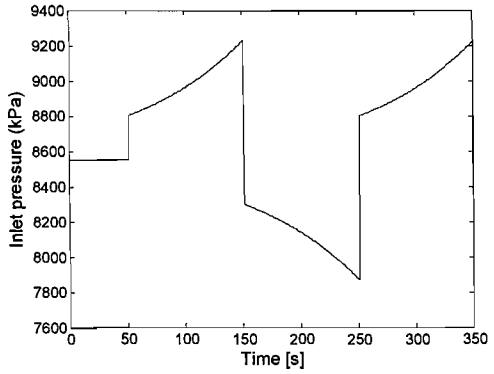

Fig. 5.3.3 Inlet pressure transient for the turbine.

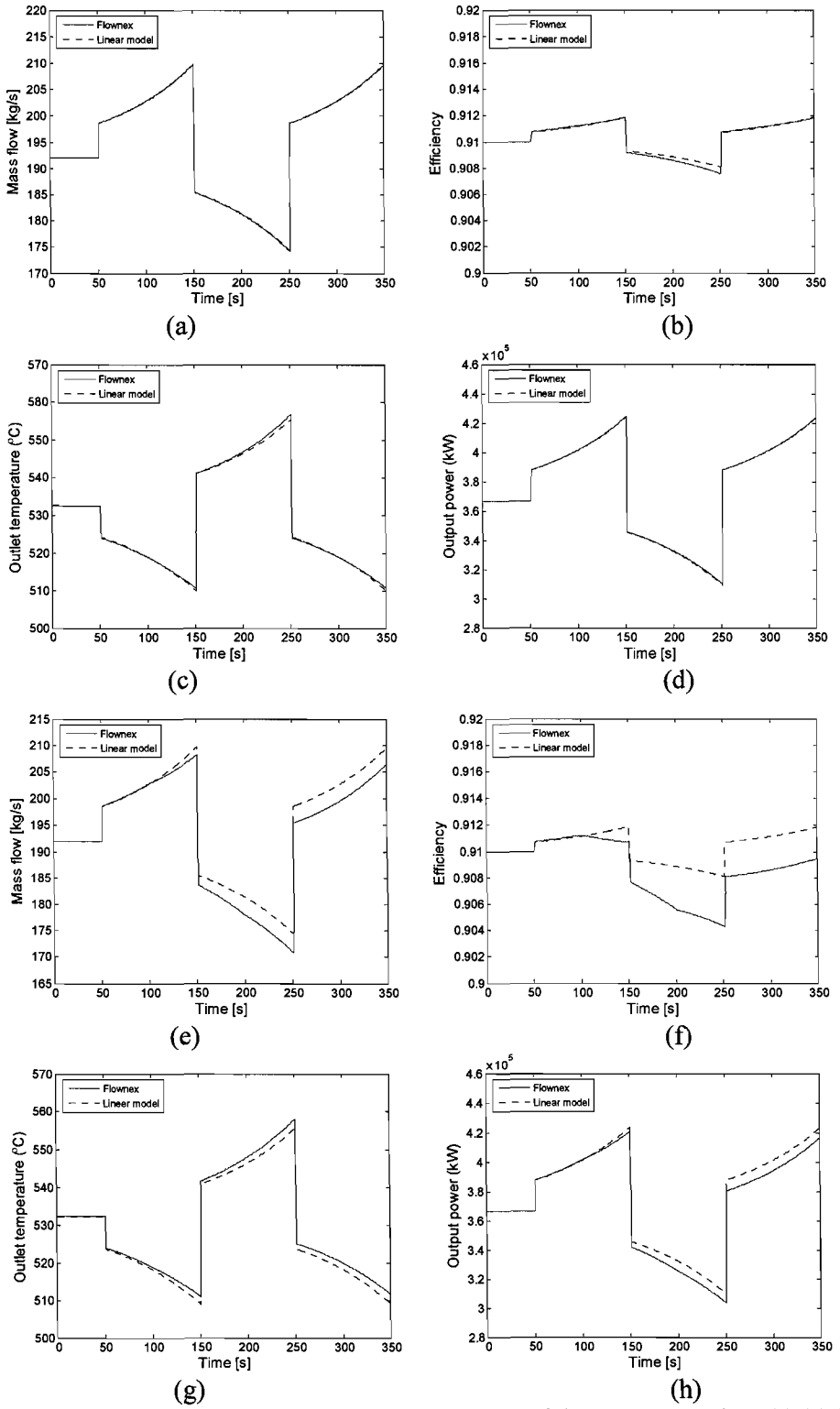

Fig. 5.3.4 Flownex and the linear turbine model response for an inlet pressure transient: (a)-(d) fault free; (e)-(h) pressure ratio fault.

With the linear turbine model developed, the model must be extended to incorporate the dynamics of the system. The system dynamics are illustrated in Fig. 5.3.5 and show the interactions between the individual models that will make up the total turbine model. The dynamics include:

- Leak flows from the HP manifold to the turbine inlet and diffuser respectively.
- The shaft dynamics.
- Energy storage from the shaft inertia and the inlet and diffuser volumes.
- Pressure losses and flow resistances in the turbine inlet and diffuser.
- Gas momentum effects.

The symbols depicted in Fig. 5.3.5 are as follows: V = gas velocity, τ = torque, M = gas momentum, Q = mass flow, N = shaft speed, W = Power, p = pressure, t = temperature.

With all the variables identified, it is now possible to determine the system equations for the total turbine model. Following this approach, the linear equations that describe the complete PBMR MPS can be formulated and must include: heat exchanger models, turbine model, compressor models, valve and pipe models, volume models, leak flow models, energy storage models (e.g. heat storage) and the reactor model.

All these models must be included since [43] states that models of high accuracy are necessary for FDI and some models interact between system components. Looking at (5.3.14) describing a single model and figure 5.3.5 showing the total model, it is evident that combining all these models to obtain a state space model that captures all the nonlinear dynamics in the PBMR MPS, will be a burdensome task. This is not only a very complex process, but will result in symbolic state space equations that may become unwieldy and unmanageable in size. Additionally, several supporting measurements must be taken from the system to calculate the variables defined in these models.

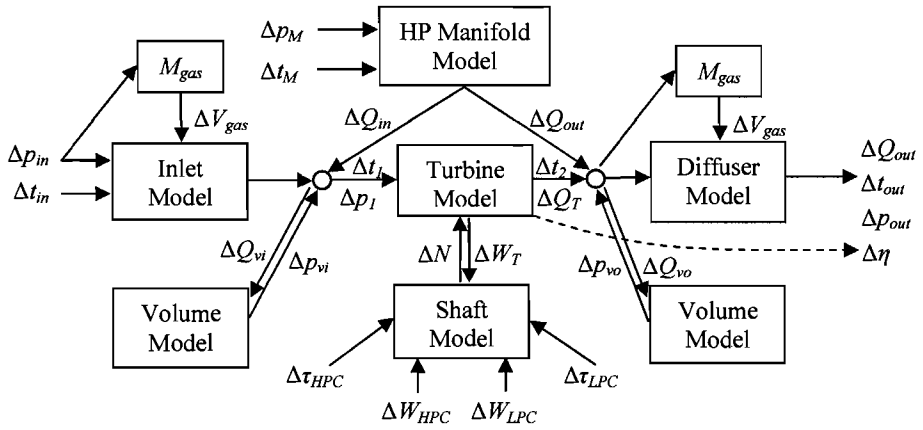

Fig. 5.3.5 Diagram illustrating the interaction between the individual models that make up the total turbine model in the PBMR.

5.4 Summary and conclusions

This chapter discussed the general implementation of two traditional methods for process fault diagnosis in the PBMR MPS.

In section 5.2, the model-free limit value checking technique is examined. To date, a major problem in nuclear power plants is that of alarm flooding during transients due to fault propagation, even though this has been reduced to a certain degree by intelligent alarm handling systems [63]. This difficulty also became apparent during the investigation. Another drawback of the technique is that an in-depth diagnosis of the fault is generally not possible. Therefore, it is concluded that limit value checking is not a suitable solution for process FDI in a complex dynamic system like the PBMR.

Section 5.3 discussed a linear mathematical modelling method for components in a complex dynamic system. Although the development of a linear model gives insight into the dynamic behaviour of the system, some drawbacks are identified if applied to the PBMR. The following can be concluded about mathematical modelling for the purpose of process fault diagnosis in the PBMR MPS:

- The model structure that describes all the dynamics in the system must be known exactly, which is seldom true in practice, especially for a new generation type NPP like the PBMR. The result is modelling uncertainty and modelling errors.

- The level of complexity is much higher due to the complex nonlinear dynamics of the system.

- The amount of monitored system variables increases because of the input dependencies of the models.

- Most model-based FDI techniques assume system linearity, and a linear transformation describing the system around the operating point or region is thus necessary. In addition, most techniques require a state space representation or transfer function of the system to evaluate the monitored residuals.

All these difficulties motivated the development of the *h-s* graph approach for process fault diagnosis in the PBMR MPS.

The following chapter presents the development of the *h-s* graph approach for process FDI in a Brayton cycle-based PCU. In this chapter, the Flownex measurements are corrupted with random measurement noise and **NO** signal conditioning (i.e. SENSE) is applied before process fault diagnosis.

CHAPTER 6

Development of the *h-s* graph approach for process FDI

This chapter discusses the development and implementation of the h-s graph approach for process FDI in a thermodynamic system. The approach is demonstrated by means of an implementation in the PBMR MPS. The single and multiple faults listed in chapter 3 are induced in the system and the approach is applied to detect and isolate the fault conditions.

6.1 Introduction

In Chapter 3, the three main fault classes in the PBMR MPS were identified and discussed. In this chapter, the structure for developing the *h-s* graph approach for process FDI is firstly described. Following this, the method is applied to the PBMR MPS and the 32 single and multiple faults are induced in the system. Lastly, a procedure is derived to detect and isolate the fault conditions.

In section 6.2, the properties h and s are described and their importance in a thermodynamic system is explained, after which the construction of the *h-s* graph is illustrated in section 6.3. Following this, the effects of the different fault conditions are visualized on the *h-s* graph. Although the changes in system states are reflected on the *h-s* graph, the objective is to use the graph to derive uncorrelated static reference fault signatures. Two different methods are derived in section 6.5 and include the error and area error methods.

In section 6.6, the properties of plant noise is firstly described after which the χ^2 hypothesis test is presented for fault detection. Fault isolation is achieved by means of the *h-s* graph and the fault isolation index (*FII*) is defined for fault pattern recognition. To reduce the reference fault database to a minimum, a single fault extraction procedure is devised to isolate single faults from multiple fault conditions. The results show that the extraction procedure together with static reference *h-s* fault signatures reduces the fault database to a minimum.

In order to shift the reference *h-s* graph to different operating points, a shape reconstruction technique is derived in section 6.7. The latter together with the variation surface, allows normal process variations to be characterized with only one reference model.

In section 6.8, the *h-s* graph approach is implemented in the PBMR MPS with added measurement noise. Lastly, section 6.9 summarizes the chapter.

6.2 Enthalpy and entropy - An overview

In a thermodynamic system, the closed cycle comprises several common open systems. For example, in an HTGR, open systems include turbines, compressors, heaters, heat exchangers, valves etc. These systems usually perform or require shaft work instead of boundary work. In order to solve these open systems, the first law of thermodynamics as developed for closed systems is usually applied. This can be a cumbersome task and gave rise to a new property enthalpy h. The property h is a combination of the internal energy (u) and the energy (Pv) necessary to get the working fluid flowing.

For a closed system undergoing a constant pressure process, the heat transfer (Q) is calculated with the first law for steady state, open systems

$$Q = m\left(u_2 - u_1 + P\left(v_2 - v_1\right)\right) \tag{6.2.1}$$

with m the mass flow and v the specific volume. Substituting the $u + Pv$ term, the heat transfer in terms of change in h gives

$$Q = m\left(h_2 - h_1\right) = mc_p\left(T_2 - T_1\right) \tag{6.2.2}$$

The change in enthalpy [64] with constant pressure specific heat (c_p) is thus calculated by means of (6.2.3)

$$\Delta h = h_2 - h_1 = c_p\left(T_2 - T_1\right) \tag{6.2.3}$$

Equation (6.2.3) is valid since the specific heat of the working fluid, helium (He) is assumed to be independent of the temperature. According to (6.2.2), (6.2.3) and assuming the working fluid is heated without a change in pressure, the change in h will equal the heat transfer. Also, the first law states that the energy flowing into the system must equal the energy flowing out of the system (conservation of energy), therefore, consider a turbine losing heat and performing shaft work as an example. The amount of enthalpy converted into shaft work is decreased with heat loss. This concept is illustrated in Fig 6.2.1 and is expressed as

$$mh_{in} = mh_{out} + W + Q \tag{6.2.4}$$

if the first law is applied. From the first law, it is derived that energy cannot be created or destroyed. It follows that energy can only be converted from one form to another, and the second law of thermodynamics and the property entropy s sets limits to this energy conversion. Also, s is a measure of the amount of internal energy not available to perform work. The change in specific entropy [65] in compressible gas flow undergoing a change in temperature is given by

$$\Delta s = s_2 - s_1 = c_p \ln\frac{T_2}{T_1} - R\ln\frac{P_2}{P_1} \tag{6.2.5}$$

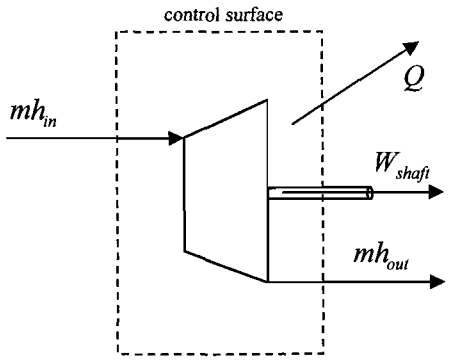

Fig. 6.2.1 Conversion of enthalpy for a steady flow turbine.

where T, R and P are the temperature, gas constant and pressure. Entropy is an abstract property and cannot be measured like T and P. For open systems, the entropy change is always positive except during heat rejection. Also, increasing the heat energy increases the entropy generation

To sum up some common causes of entropy change or generation, the term "irreversibility" is firstly defined. In an irreversible process, everything (system and surroundings) cannot be reversed to the original condition without an input from the environment. Some factors that cause a thermodynamic system to be irreversible [65] include fluid flow with friction, mixing of gases which differ with regard to thermodynamic state, compression, expansion, and heat transfer across a finite temperature difference. The irreversibility of a system is important since entropy is generated in a real irreversible process which can be an indication of component or process faults. Table 6.2.1 summarizes the h and s relationships of the individual open systems in the PBMR MPS. In Table 6.2.1, the relatively small kinetic ($\frac{1}{2}V^2$) and potential (gz) energies are not shown, but are modelled in Flownex [49] (conservation of energy of a control volume).

Component	H	s
Valve	$h_{in} = h_{out}$	
Pipe	$h_{in} = h_{out}$	$S_{gen} = mR\ln\frac{P_{in}}{P_{out}}$ $\quad P_{out} = P_{in} - \Delta P$, $\Delta P < P_{in}$
Turbine (adiabatic)	$m_{in}h_{in} = m_{out}h_{out} + W_{shaft}$	$ms_{in} + S_{gen} = ms_{out}$
Compressor	$m_{in}h_{in} + W_{shaft} = m_{out}h_{out}$	$ms_{in} = ms_{out} + S_{gen}$
Heat exchanger	$(m_{in}h_{in})_{HP} + (m_{in}h_{in})_{LP} = (m_{out}h_{out})_{HP} + (m_{out}h_{out})_{LP}$	$S_{gen} = ms_{HP} + ms_{LP}$
Reactor	$m_{in}h_{in} + Q = m_{out}h_{out}$	

Table 6.2.1 Relationships for h and s in open systems.

In Table 6.2.1, S_{gen} is the entropy generation term and not the entropy change $\Delta s = s_2 - s_1$. This term is dependent not only on the start and end states, but on the path of the process and hence not a thermodynamic property. The entropy generation term is given by [65]

$$S_{gen} = s_2 - s_1 - \int_1^2 \frac{\delta Q}{T} \tag{6.2.6}$$

with $\delta Q/T$ the entropy transfer. From (6.2.6), it is evident that the change Δs can be rearranged to include the S_{gen} and entropy transfer terms. This form is convenient and can easily be calculated with (6.2.5). To summarize, a few properties regarding h and s are emphasized to show why these variables could be used to identify normal irreversibility or changes (fault conditions) in the thermodynamic state of a system [65]:

- Enthalpy increases with fluid friction (more energy required to get the fluid flowing).
- If the working fluid is heated at constant pressure, the change in enthalpy will equal the heat transfer.
- The second law states that the entropy of a closed system can never spontaneously decrease.
- The spontaneous flow of heat between bodies at different temperatures increases the entropy.
- The entropy generated in a system is directly proportional to the decrease in turbine shaft work.
- Entropy transfer accompanies heat transfer.
- There is no entropy transfer associated with the transfer of energy as work or power.
- If the turbine outlet temperature is constant, the decrease in shaft power is proportional to the rate of entropy generation.

These properties are important and make h and s an ideal combination to analyze the thermodynamic state of the process. Since the normal system irreversibility can be calculated or approximated, any changes not associated with these conditions can thus be linked to a contributing fault condition.

6.3 Attributes and construction of the *h-s* graph

To visualize the state of the thermodynamic Brayton cycle, the properties h and s are plotted on an *h-s* graph, also called a Mollier diagram. The theoretical *h-s* graph comprising the eight sub-processes (nodes) is illustrated for a closed Brayton cycle in Fig. 6.3.1 (a). To construct the *h-s* graph, T and P are measured at the inlets of the eight sub-processes in the PBMR MPS. By applying (6.2.3), (6.2.5) and assuming the constant pressure specific heat is not dependent on the temperature, h and s are calculated for the eight nodes respectively. The transformation from *T-P* to *h-s* is important and is motivated in Appendix B.

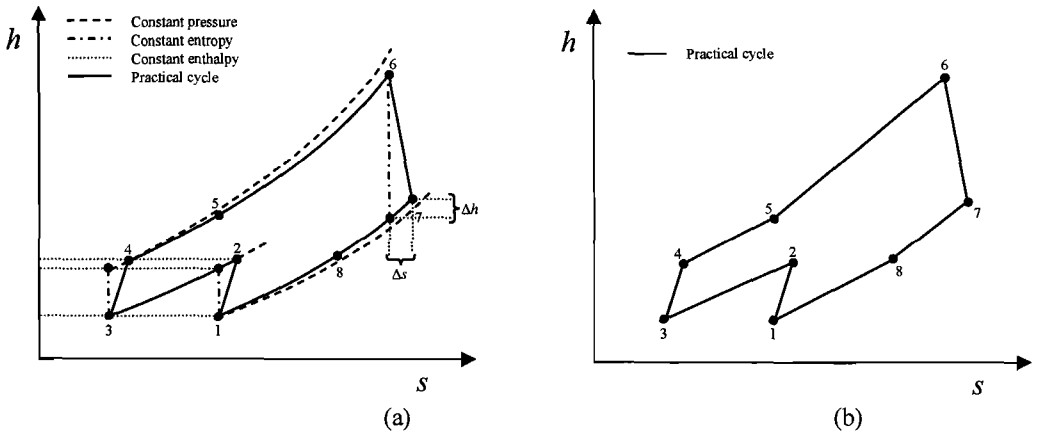

Fig. 6.3.1 The *h-s* graphs of a closed Brayton cycle: (a) theoretical; (b) simplified.

In Fig. 6.3.1 (a), the curvature in the theoretical plot (nodes 2-3, 4-5-6 and 7-8-1) are due to a smaller step size for T and P. Since data for the PBMR MPS is only captured at the eight nodes, the graph reduces to a simplified form (straight lines between nodes) and is shown in Fig. 6.3.1 (b). The simplified *h-s* graph will be used in the calculations throughout the study to minimize computational complexity.

As discussed in Chapter 3, the primary power control of the PBMR is achieved by adding or removing helium inventory from the PPB with the ICS. This type of control allows a constant shape of the *h-s* graph at all power levels above 40 % MCR. For reduced power levels, the graph shifts to a lower absolute pressure, but maintains the shape (proved in Appendix B). Fig. 6.3.2 depicts the shift direction as well as the shape of the *h-s* graph for a decrease in absolute pressure. The figure shows that the graph moves to the right for a decrease in power and to the left for an increase in power. The constant shape of the graph will therefore allow a reference model that remains invariant over the power range (subject to no bypass valve operation). Figure 6.3.3 shows the theoretical *h-s* graph (small step size) for the practical cycle of the PBMR MPS. The specific entropy is referenced to $T_0 = 0$ °C and $P_0 = 10$ MPa.

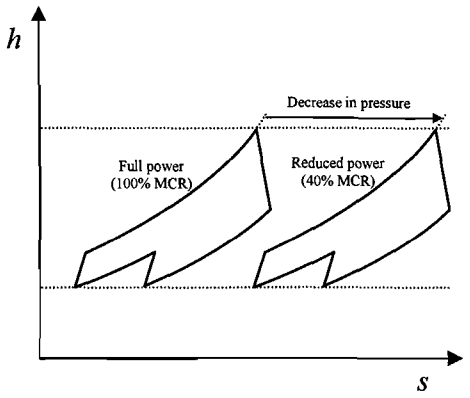

Fig. 6.3.2 Theoretical *h-s* graph of the Brayton cycle for full as well as reduced power (ICS control).

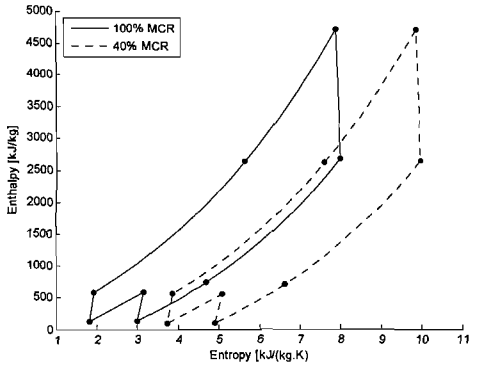

Fig. 6.3.3 The *h-s* graph for the PBMR, shown at full and reduced power (ICS control).

6.4 Effect of faults on the *h-s* graph

This section illustrates the effects of the 32 faults on the *h-s* graph. It is important to note that the main objective of the study is to use the *h-s* graph for fault diagnosis and not to investigate the causes for the changes in *h* and *s* with regard to physics and thermodynamics[3]. To show an example of a typical *h-s* cause-effect scenario, an increase in the pre-cooler inlet resistive losses (fault 23) is discussed for a 5 % change.

The result of fault 23 is an increase in the main flow resistance (class 2) and is modelled in Flownex as a change in the resistive losses of the pre-cooler inlet pipe (nodes 8-1). In order to compare the amount of entropy generated and the available work delivered for an equal amount of heat energy supplied, the reactor power for 100 % MCR is fixed and the recuperator bypass valves (RBP) controlled to ensure an inlet and outlet reactor temperature of 500 °C and 900 °C respectively. Table 6.4.1 lists the Flownex results and the *h-s* calculations for fault 23.

The table shows that the fault condition results in higher cycle temperatures and an increase in pressure loss between the turbine and the LPC. Furthermore, a reduction in mass flow rate is observed throughout the system. The *h-s* calculations show that entropy generation increases, whereas the work delivered by the turbine is considerably less than for the fault free case. According to [65], entropy generation and pressure loss increase with frictional fluid flow whilst available work in the system is lost. In this case, it is evident that useful work must be invested to push the working fluid through the "faulty" pipe section and therefore, the net result is a reduction in available power.

The remaining fault conditions in the PBMR MPS can be described with similar explanations regarding cause and system irreversibility. The main objective now is to investigate the effect of each fault on the shape of the *h-s* graph.

[3]This is a specialized field of study and the reader is referred to [65] for further reading regarding entropy generation and causes of thermodynamic irreversibility in theory and real-world applications.

Node/ component	Normal					Fault 23 (5 % change)				
	P (kPa)	Δ*P* (kPa)	*m* (kg/s)	*h* (kJ/kg)	*s* (kJ/ [kg.K])	*P* (kPa)	Δ*P* (kPa)	*m* (kg/s)	*h* (kJ/kg)	*s* (kJ/ [kg.K])
1-2	2909.80	2179.29	201.34	128.76	2.98	2864.82	2149.18	197.07	134.63	3.04
2-3	5089.09	30.82	202.56	583.04	3.15	5014.00	29.97	198.29	590.91	3.20
3-4	5058.27	3919.76	202.55	130.98	1.82	4984.03	3994.86	198.28	129.78	1.84
4-5	8978.03	81.58	190.21	582.27	1.93	8978.89	72.85	186.00	592.41	1.96
5-6	8896.44	345.13	190.08	2618.80	5.64	8906.04	328.73	185.87	2578.14	5.59
6-7	8551.31	5580.78	190.08	4695.75	7.89	8577.31	5163.69	185.87	4701.04	7.89
7-8	2970.53	41.66	201.19	2660.71	8.00	3413.62	284.97	196.88	2862.63	7.96
8-1	2928.86	19.06	201.33	735.96	4.70	3128.65	263.83	197.06	986.92	5.14

	Heat transfer*/power (kW)	
LPC	91471.30	89907.98
HPC	91405.74	91715.97
Turbine	364027.61	317093.88
Reactor*	395314.30	395200.00
Recuperator*	387164.06	369220.46
Pre-cooler*	122254.54	167957.9
Intercooler*	91568.30	91436.43

Table 6.4.1 Flownex results for fault 23.

In Chapter 3, three fault classes comprising single and multiple fault conditions are identified for the PBMR MPS. To illustrate the effects of the faults on the *h-s* graph, the fault conditions are modelled in Flownex for normal power operation at 100 % MCR. In the simulations, the reactor outlet temperature and manifold pressure are controlled at 900 °C and 9 MPa respectively. Figures 6.4.1 to 6.4.4 illustrate the shift of the *h-s* graph for each fault in addition to the fault-free reference graph. The figures show a 1 %, 5 % and 10 % change in the fault magnitude for single faults (1 to 25) and a 1 % and 5 % change for multiple fault conditions (26 to 32).

The figures show that the fault conditions are reflected as a distinguished shift in the *h-s* graph with regard to direction and magnitude. This feature will be used as basis for the *h-s* graph approach for process fault diagnosis. Although the shift may appear to be similar for some fault conditions, the distinctive properties of the graph will become evident once the fault signatures are derived. In addition, the figures show that the combination of single faults also results in a distinguished shift in the *h-s* graph. Although this feature increases the isolation ability of the approach, the reference fault database will become unmanageable in size if all the fault combinations are modelled. Therefore, it would be favorable to classify any combination of faults with single reference faults only.

To illustrate that the shift in the *h-s* graph itself also reflects the combination of single faults, the graphs of the multiple faults are compared to the graphs of the contributing single faults. The graphs of the multiple faults (Fig. 6.4.4 (b) - (h)) show that the single fault illustrated in Fig. 6.4.1 (g) is clearly one of the contributing faults. This observation is based on the shift direction of the *h-s* graphs between nodes 1 and 2. By repeating this principle and evaluating each section of the *h-s* graph, the second fault can also be identified. To simplify this process, the single fault extraction method is devised and is discussed in section 6.6.4.

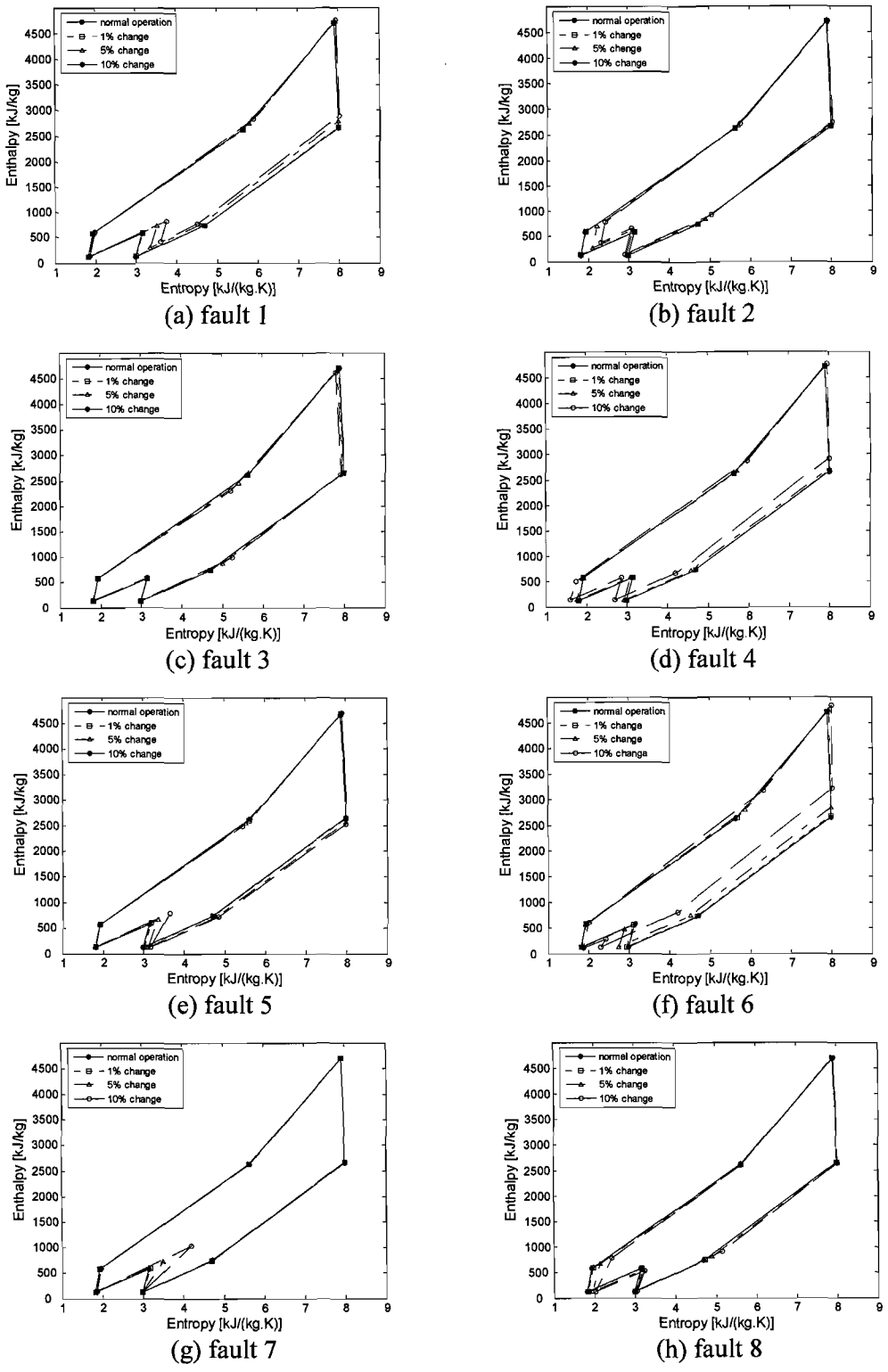

Fig. 6.4.1 The *h-s* graphs for normal power operation: (a) fault 1 to (h) fault 8.

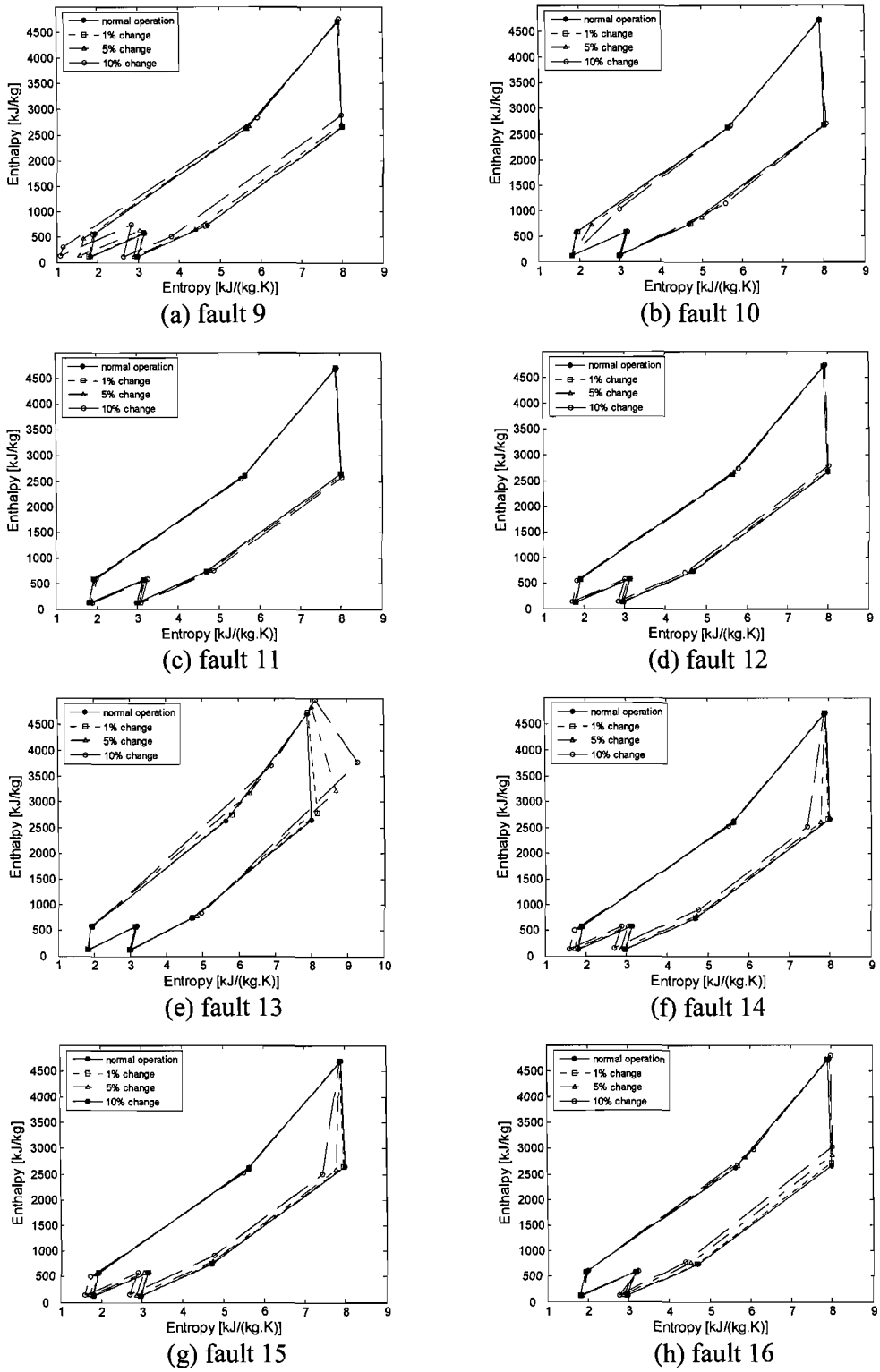

(a) fault 9 (b) fault 10

(c) fault 11 (d) fault 12

(e) fault 13 (f) fault 14

(g) fault 15 (h) fault 16

Fig. 6.4.2 The *h-s* graphs for normal power operation: (a) fault 9 to (h) fault 16.

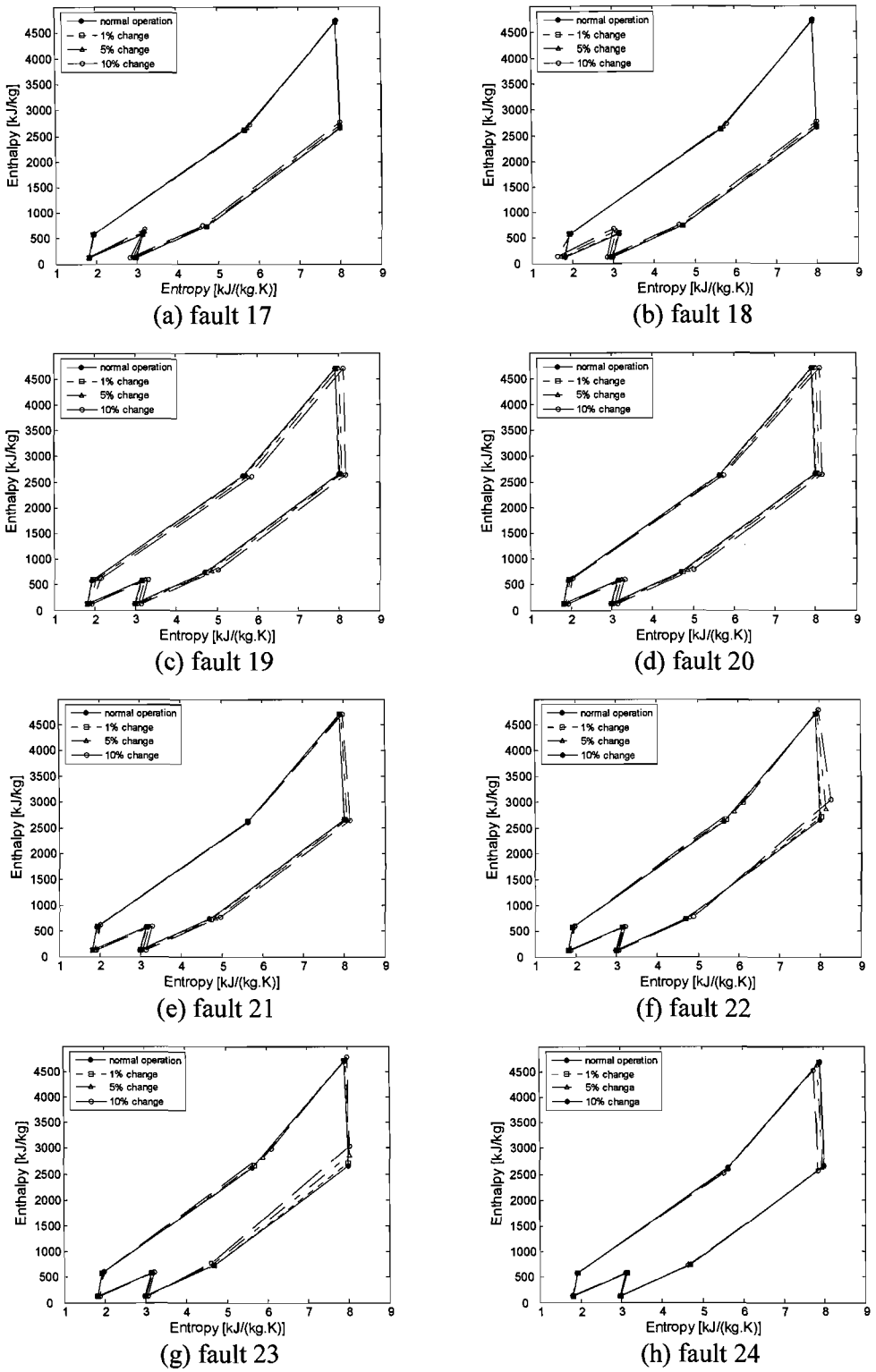

(a) fault 17 (b) fault 18

(c) fault 19 (d) fault 20

(e) fault 21 (f) fault 22

(g) fault 23 (h) fault 24

Fig. 6.4.3 The *h-s* graphs for normal power operation: (a) fault 17 to (h) fault 24.

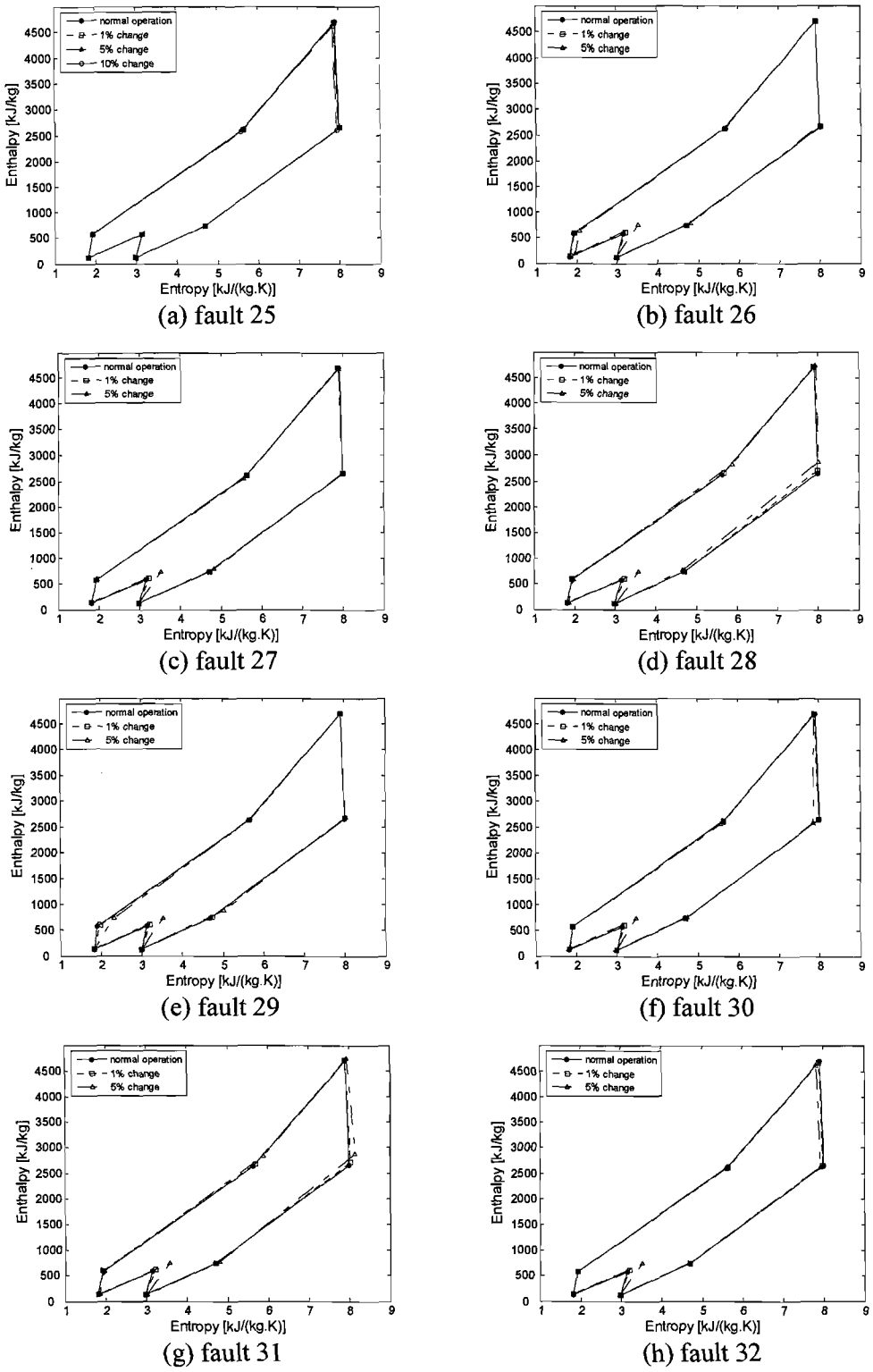

Fig. 6.4.4 The *h-s* graphs for normal power operation: (a) fault 25 to (h) fault 32.

Although the change in system state is reflected on the *h-s* graph, the goal is to utilize the graph to derive uncorrelated reference fault signatures for the faults. To construct the signatures, two different methods are used and are described next.

6.5 Creating reference fault signatures with the *h-s* graph

In order to classify fault conditions in the PBMR MPS, a reference fault signature database must first be established. The first step is to derive reference fault signatures from the *h-s* fault graphs based on some criteria. Two methods are chosen for the *h-s* graph approach and are based on the error between the reference and fault graphs for each node and the area covering the error between consecutive nodes. The latter is termed the 'area error' method.

6.5.1 The error method

The first method is based on the error or shift between the fault and the reference *h-s* graphs and is calculated for each node. By applying this method, the corresponding fault signatures s(i) are determined by

$$s(i) = \frac{p_{ref}(i) - p(i)}{p_{ref}(i)} \quad i = 1, 2, \ldots, n \tag{6.5.1}$$

with $p_{ref}(i)$ the reference parameter value, $p(i)$ the value of the measured parameter (fault) and i the node number. For the PBMR MPS, $s(i)$ corresponds to the *h* and *s* errors.

In (6.5.1), a fault condition with a varying fault magnitude will result in different signatures for the same fault condition. For this reason, it is necessary to normalize the fault signatures in order to obtain a signature independent of the fault magnitude. An important advantage of using the *h-s* graph is the fact that the fault directions stay the same for the different magnitudes of the fault symptoms. Therefore, each signature retains the fault direction for each node and consequently, simplifies fault isolation. An example is illustrated in Fig. 6.5.1 (a) for fault 23. The figure shows that the signatures stay the same for each node with regards to fault direction, but vary in magnitude. To obtain a normalized signature $s_{norm}(i)$ that is independent of the fault magnitude, the following equation is applied

$$s_{norm}(i) = \frac{s(i)}{\max_{i=1}^{n} |s(i)|} \quad i = 1, 2, \ldots, n \tag{6.5.2}$$

The normalized fault signature is shown in Fig. 6.5.1 (b). This figure shows that the signature is highly correlated with regard to fault direction and magnitude if (6.5.2) is applied. Therefore, the conclusion is drawn that the fault conditions can be characterized

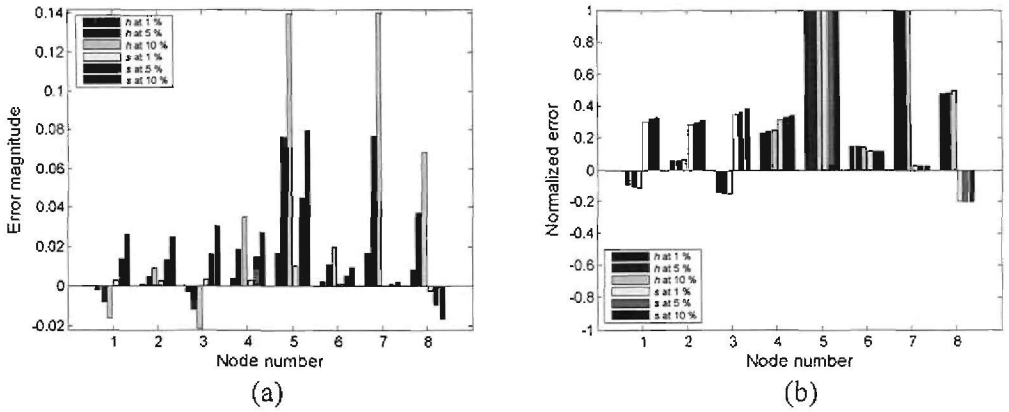

Fig. 6.5.1 Fault signatures for fault 23 for different fault magnitudes: (a) error; (b) normalized error.

with one normalized h and s fault signature for different magnitudes of the fault symptom. This feature will also minimize the number of fault signatures in the reference fault database.

The normalized h and s reference fault signatures are averaged for the different fault magnitudes and are illustrated in Fig. 6.5.2. As discussed, the shift in the h-s graph may appear to be similar for some fault conditions. Fig. 6.5.2 demonstrates that the derived h and s signatures are uncorrelated with regard to fault direction and magnitude.

6.5.2 The area error method

The second method is based on the area defined by the shift between the reference and the fault graphs. Since there is no area between any single reference and fault node (straight line), two consecutive nodes are used. To visualize this concept, Fig. 6.5.3 illustrates the area of the error for different nodes.

The first node is used as an example. The figure shows that area 1 is defined by the first and second nodes of the reference (a) and fault (b) graphs. To define the area, the nodes of the reference and fault graphs are connected with straight lines and are the equivalent of the Euclidean distance given by

$$\mathbf{r}_{area}(i) = \sqrt{\left|\mathbf{h}_a(i) - \mathbf{h}_b(i)\right|^2 + \left|\mathbf{s}_a(i) - \mathbf{s}_b(i)\right|^2} \tag{6.5.3}$$

with $\mathbf{h}_a$, $\mathbf{h}_b$, $\mathbf{s}_a$, $\mathbf{s}_b$ the h and s at the i-th reference and fault nodes respectively. By connecting the reference and fault graphs, each area is therefore defined between four nodes.

However, for some faults the reference and fault graphs cross lines between nodes (area 3). In this case, an intermediate point $i_{i(i+1)}$ is defined between the nodes and the area can be viewed as a summation of two triangular areas.

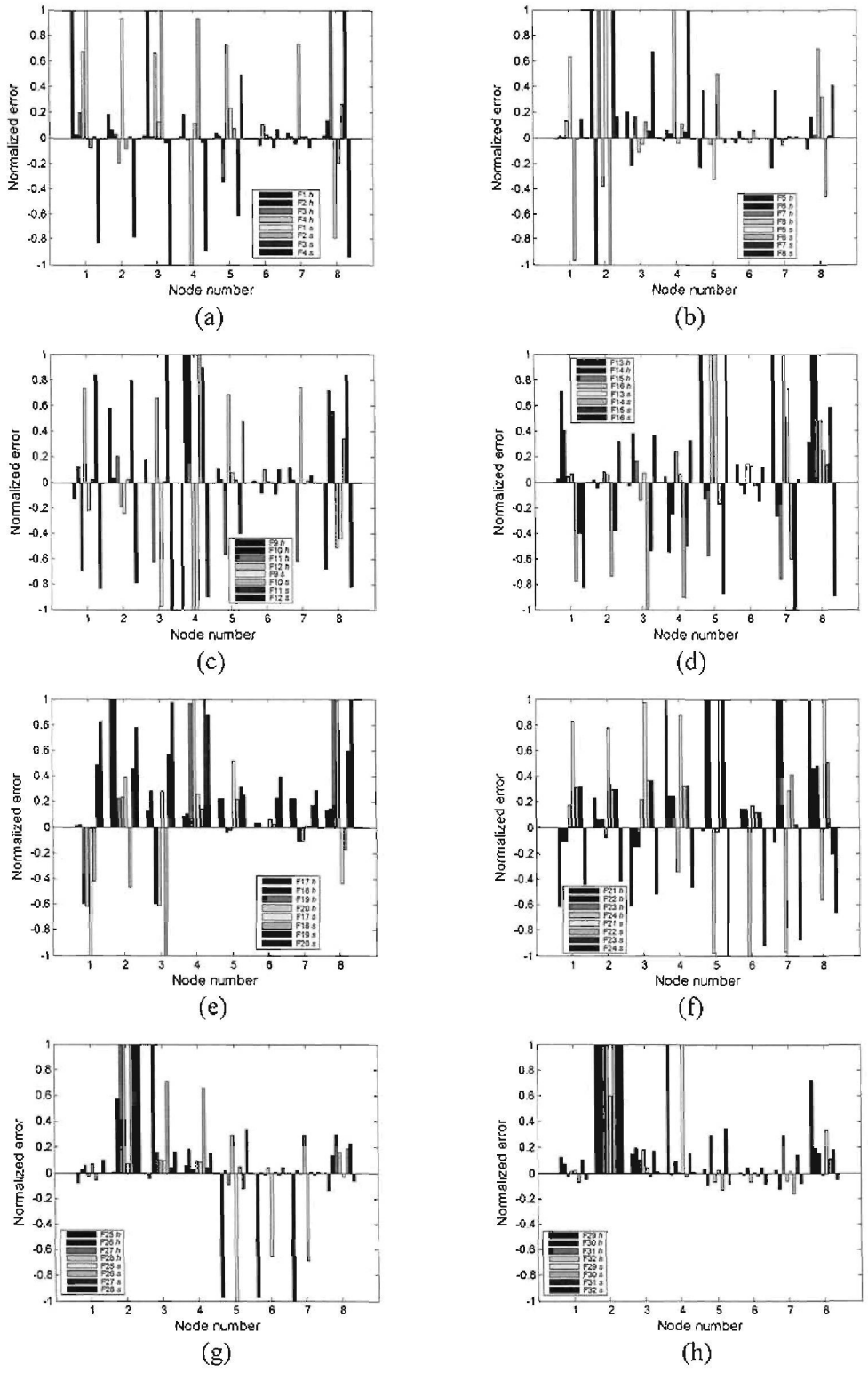

Fig. 6.5.2 The normalized error signatures for the PBMR for normal power operation.

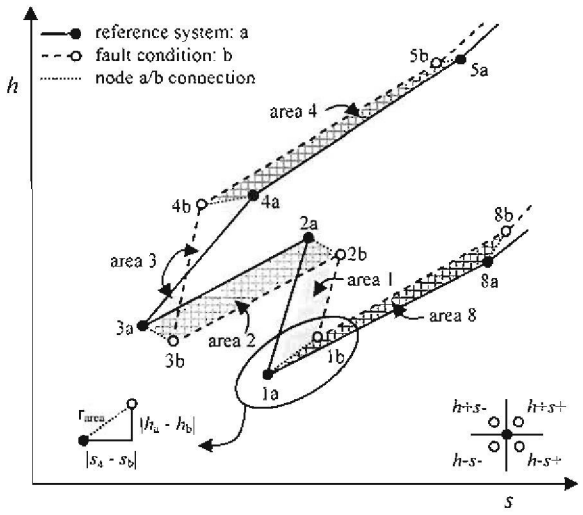

Fig. 6.5.3 Classifying the areas between the reference and fault *h-s* graphs.

In contrast to the error method where *h* and *s* are calculated separately, the area of the error encapsulates the shift in both *h* and *s*. Therefore, it is necessary to define the fault directions independently for *h* and *s* at each node. This concept is visualized in the bottom right corner of Fig. 6.5.3 (solid circle: reference node; unfilled circle: fault node). The figure shows that the sign is different for *h* and *s* in opposite fault directions. Accordingly, the same areas are used for *h* and *s* in combination with the appropriate fault directions. The area error signature $s_{area}(i)$ is calculated for each node with (6.5.4)

$$s_{area}(i) = \begin{cases} \left| \dfrac{\mathbf{r}_{area}(i)\left[\mathbf{r}_{area}(i) \perp (i+1)_b\right] + \mathbf{r}_{area}(i+1)\left[\mathbf{r}_{area}(i+1) \perp (i)_a\right]}{2} \right| . \mathrm{dir}(\mathrm{fault}) & \text{a and b do not cross} \\ \left| \sum_{i}^{i+1} \dfrac{\mathbf{r}_{area}(i)\left[\mathbf{r}_{area}(i) \perp (i_{i|i+1})\right]}{2} \right| . \mathrm{dir}(\mathrm{fault}) & \text{a and b cross} \end{cases} \tag{6.5.4}$$

with $\perp$ the perpendicular distance from $\mathbf{r}_{area}$ to node i and dir(fault) the fault direction. Following (6.5.4), the *h* and *s* signatures are normalized using (6.5.2). To illustrate this notation, fault 11 is used as an example and is shown in Fig. 6.5.4.

In Fig. 6.5.4 (a), the areas are firstly calculated for each node whereafter the fault directions (b) are determined for *h* and *s*. The *h* and *s* signatures are derived in (c) by multiplying (a) and (b) for each node. Lastly, the signatures are normalized in (d) to obtain signatures that are independent of the fault magnitude. The normalized *h* and *s* area error fault signatures are averaged (similar to the first method) for the different fault magnitudes and are illustrated in Fig. 6.5.5. The figure shows that the area error method also produces uncorrelated fault signatures for all the faults.

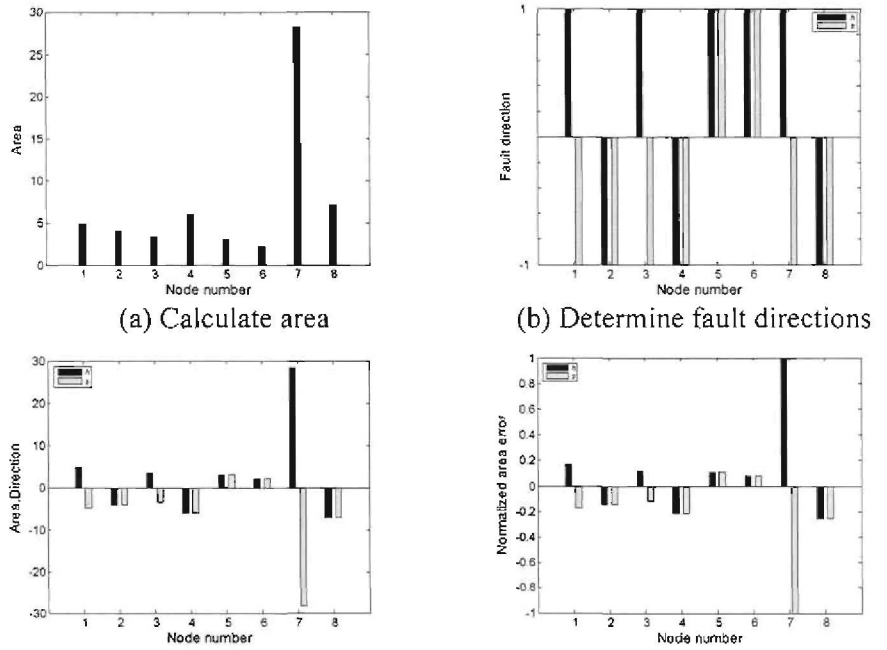

(a) Calculate area (b) Determine fault directions

(c) Derive *h* and *s* by means of (a) and (b) (d) Normalize *h* and *s* signatures

Fig. 6.5.4 Deriving *h* and *s* fault signatures with the area error method for fault 11.

To increase the effectiveness of the proposed method during fault isolation, the derived signatures must be different in the sense that the correlation[4] between any two signatures are low. This characteristic reduces the probability that the correct fault signature is classified as another. Based on this criterion, the 25 single fault signatures are compared and a correlation coefficient (defined by Eq. 6.6.10) is calculated. In total, the correlation coefficients are calculated for 300 cases. The average correlations for the error and area error methods are 24.86 % and 19.95 % respectively. The low correlation averages show that the two methods can be applied to isolate the correct fault signature and reject the remaining signatures.

6.6 Fault detection and isolation with the *h-s* graph approach

In this section, the procedure of fault detection and isolation is discussed based on the *h-s* graph approach. Firstly, some general assumptions are made regarding the properties of measurement and process noise. Also, the single fault extraction procedure is presented together with the construction of the *h-s* graph at different power levels.

[4]The correlation is explained in more detail during the fault isolation phase. In terms of fault signature generation, the term merely describes how similar any two objects are. The mathematical formulation for the correlation coefficient is presented in (6.6.10).

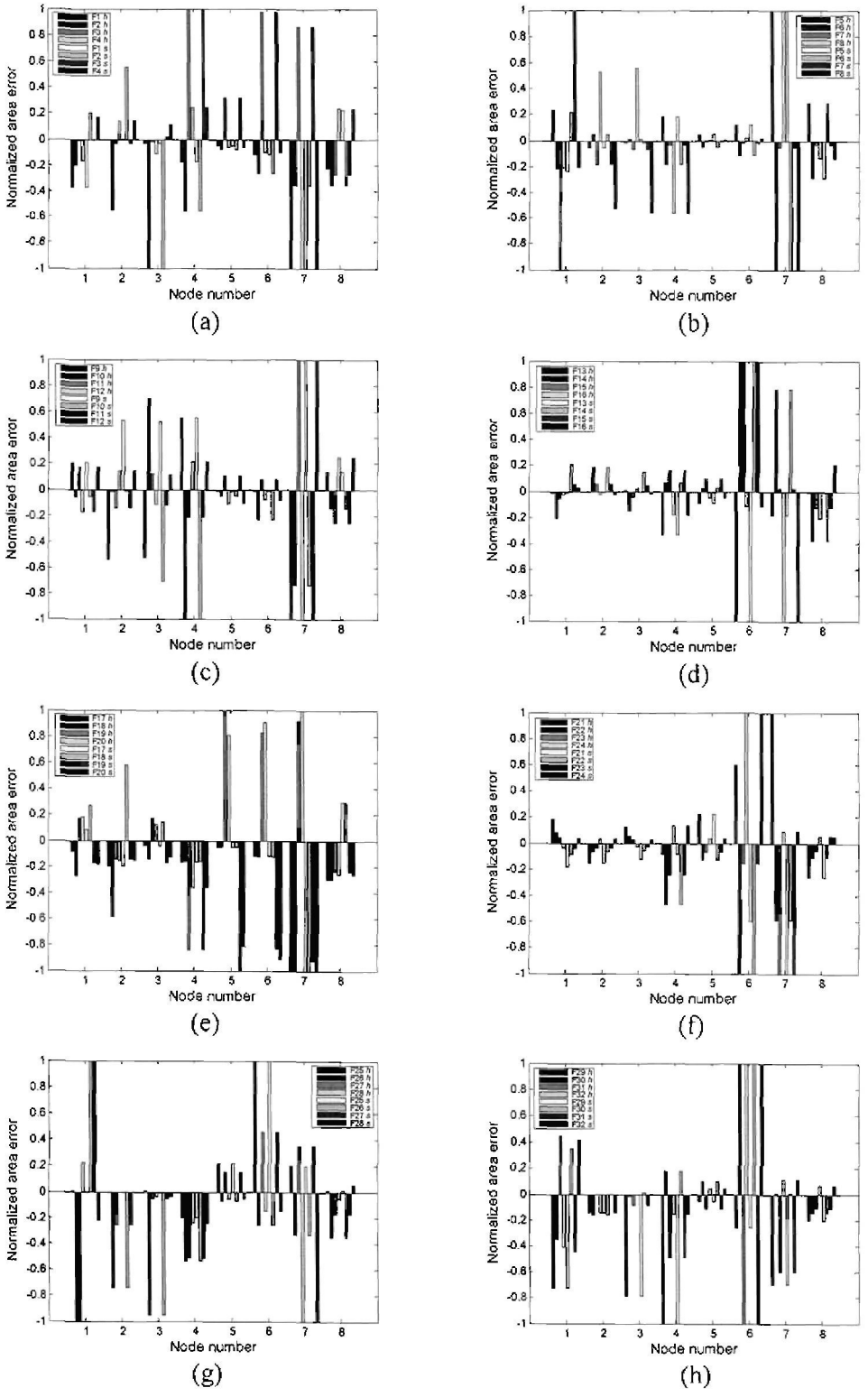

Fig. 6.5.5 The normalized area error signatures for the PBMR for normal power operation.

6.6.1 Noise properties

In real plant conditions, the measurements are normally corrupted with random noise originating from the process, sensors and actuators. If the influence of the noise is known or can be approximated, it follows that the error $\mathbf{r}(t)$ is the sum of the fault condition $\mathbf{r}_f(t)$ and the noise $\mathbf{r}_N(t)$ given by [6]

$$\mathbf{r}(t) = \mathbf{r}_f(t) + \mathbf{r}_N(t) \tag{6.6.1}$$

Firstly, some assumptions are formulated regarding the measurement noise vector $\mathbf{r}_N(t)$:

- The vector is random and normally distributed (central limit theorem).
- The mean of the vector is zero: $E\{\mathbf{r}_N(t)\} = 0$.
- Whiteness of the vector: $\Phi_{vv}(\tau) = E\{\mathbf{r}_N(t)\mathbf{r}_N(t-\tau)^T\} = 0$.
- The vector is uncorrelated: $\Phi_{vv}(0) = E\{\mathbf{r}_N(t)\mathbf{r}_N(t)^T\} = I$.

In the thesis, the noise vector $\mathbf{r}_N(t)$ is modelled with a normally distributed (zero mean) random number generator which is not correlated in time.

6.6.2 Fault detection

In this section, fault detection of the error window average is discussed. To detect a fault condition, the time varying mean of the error is tested for a nonzero value against a given threshold. The reason a threshold value is considered and not zero is because the mean of the errors are generally corrupted with noise and modelling errors, even if no fault is present. The latter is implemented as a statistical hypothesis test and is given by

$$\begin{array}{ll} H_0 : \mu_r < \mu_f & \text{no fault} \\ H_1 : \mu_r \geq \mu_f & \text{fault} \end{array} \tag{6.6.2}$$

with μ_f the threshold value.

To test for a fault condition, the hypothesis test is implemented as a χ^2 test and is mainly based on the central χ^2 distribution [6]. This technique is not computational complex and is employed since the error vector is normally distributed and the test is a choice between only two hypotheses. Consider the error vector in (6.6.1) is given by

$$\mathbf{r}(t) = \left[r_1(t), r_2(t), \ldots, r_n(t)\right]^T \tag{6.6.3}$$

with n the number of measurements. For the PBMR MPS, separate error vectors will consist of *h* and *s* respectively. The window average of the vector series is computed as

$$\tilde{\mathbf{r}}(t,m)=\frac{1}{1+m}\sum_{i=0}^{m}\mathbf{r}(t-i) \tag{6.6.4}$$

with m the time window. Because the error vector is assumed to be normally distributed, the multivariate normal density function for the window average is

$$f(\tilde{\mathbf{r}})=\frac{1}{(2\pi)^{n/2}\left|\psi_{\tilde{r}}\right|^{1/2}}\exp\left[-1/2\,\tilde{\mathbf{r}}^{T}\psi_{\tilde{r}}^{-1}\tilde{\mathbf{r}}\right] \tag{6.6.5}$$

The covariance matrix ψ of the window average is obtained by

$$\psi_{\tilde{r}}=\frac{1}{m+1}\psi_{rr}(0)+\frac{1}{(m+1)^{2}}\sum_{\tau=1}^{m}(m+1-\tau)\left[\psi_{rr}(\tau)+\psi_{rr}^{T}(\tau)\right] \tag{6.6.6}$$

The test for fault detection is performed as

$$\begin{aligned} H_0&: \tilde{\mathbf{r}}^{T}(t)\psi_{\tilde{r}}^{-1}\tilde{\mathbf{r}}(t)<\chi_{\alpha}^{2}\\ H_1&: \tilde{\mathbf{r}}^{T}(t)\psi_{\tilde{r}}^{-1}\tilde{\mathbf{r}}(t)\geq\chi_{\alpha}^{2}\end{aligned} \tag{6.6.7}$$

with $\tilde{\mathbf{r}}^{T}(t)\psi_{\tilde{r}}^{-1}\tilde{\mathbf{r}}(t)$ the test statistic and χ_{α}^{2} the threshold. The thresholds are chosen as

$$\int_{-\chi_{\alpha}^{2}}^{\chi_{\alpha}^{2}} f(\tilde{\mathbf{r}})d\tilde{\mathbf{r}}=1-\alpha \tag{6.6.8}$$

with α the false alarm rate. The false alarm rate, also called the test size, is defined as the probability that H_1 is chosen whilst H_0 occurs. To minimize the number of false alarms, the variable is chosen empirically for the specific application. The hypothesis tests are performed for both *h* and *s* and a fault condition is detected if either of the two tests fire.

6.6.3 Fault isolation

Following the detection of a fault condition, the next important task is fault isolation. To identify the specific location, cause or component responsible for the malfunction, the *h-s* graph procedure is now applied. Firstly, (6.5.1) to (6.5.4) are used to construct the fault signatures describing the actual operating conditions: *h* error, *h* area error, *s* error and *s* area error. With the reference fault database developed in section 6.5, the four signatures are compared to the single faults in the database in order to correctly classify the corresponding fault condition. This task is achieved by applying shape analysis and classification.

To perform the task of fault recognition, a statistical classifier is used to match the fault condition to the corresponding reference fault signature s_{ref} in the database. Three tests are used: (1) the root mean squared error (*RMSE*), (2) the correlation coefficient (*CC*) and (3) the r-square statistic (*RSQ*).

a.) The *RMSE* is also known as the standard error of the regression and is given by

$$RMSE = \sqrt{\frac{1}{n}\sum_{i=1}^{n}\left(s(i) - s_{ref}(i)\right)^2} \tag{6.6.9}$$

A value closer to zero will indicate the best match to a reference fault signature.

b.) The *CC* computes the correlation coefficient between the actual and the reference fault signatures and is calculated by

$$CC = \frac{\left|\sum_{i=1}^{n}\left(s(i) - \bar{s}\right)\left(s_{ref}(i) - \bar{s}_{ref}\right)\right|}{\sqrt{\left(\sum_{i=1}^{n}\left(s(i) - \bar{s}\right)^2\right)\left(\sum_{i=1}^{n}\left(s_{ref}(i) - \bar{s}_{ref}\right)^2\right)}} \tag{6.6.10}$$

An important property of (6.6.10) is that the $CC \leq 1$. A value closer to one indicates the best recognition.

c.) The *RSQ* is the ratio of the sum of squares of the regression and the sum of the squares, given by

$$RSQ = 1 - \frac{\sum_{i=1}^{n} w(i)\left(s(i) - s_{ref}(i)\right)^2}{\sum_{i=1}^{n} w(i)\left(s(i) - \bar{s}\right)^2} \tag{6.6.11}$$

where **w**(i) are the weights. Similar to the *CC*, *RSQ* takes a value between 0 and 1, with a value closer to 1 indicating the best match.

To increase the integrity of the recognition algorithm, all three statistics are combined to match the actual fault signature to the correct reference signature. The fault isolation index, *FII*, is defined and is computed by

$$FII = \sqrt{RMSE^2 + (1 - CC)^2 + (1 - RSQ)^2} \tag{6.6.12}$$

with isolation equal to the reference signature with a minimum *FII*, ideally zero. To correctly identify a fault condition in the PBMR MPS, all four fault signatures must correspond to a minimum *FII* for the same reference fault condition.

It must be noted that the fault signature that corresponds to a minimum *FII*, is the best possible fit to a reference fault, although not necessarily the correct fault condition. To reduce the probability of misclassification, the reference fault database must therefore be designed to include the most probable system faults. As discussed, single faults may

occur simultaneously (multiple faults) and combinations thereof will increase the amount of reference fault signatures significantly. To restrict the fault database to single faults only, a single fault extraction procedure is devised to classify unknown signatures with a high *FII* to possible combinations of single faults. The extraction procedure is discussed next.

6.6.4 Single fault extraction method

During a multiple fault occurrence (unknown signature), the challenge is to identify the single faults comprising the multiple fault condition. A method of single fault extraction is proposed and is based on a systematic subtraction procedure of single reference fault signatures. The procedure is illustrated in Fig. 6.6.1.

Firstly, the multiple fault signature (obtained with 6.5.1) is normalized with the k-th node after which the first reference signature m is subtracted. The remaining single fault signature is normalized and compared to all the signatures in the reference fault database, based on the *FII*. This procedure is repeated until all the reference fault signatures are subtracted. After the multiple fault signature is normalized with all the k-th nodes, the first single fault is classified as the reference fault m corresponding to the minimum *FII*. Lastly, the second single fault is identified as the reference fault signature m used during the subtraction procedure of the first fault.

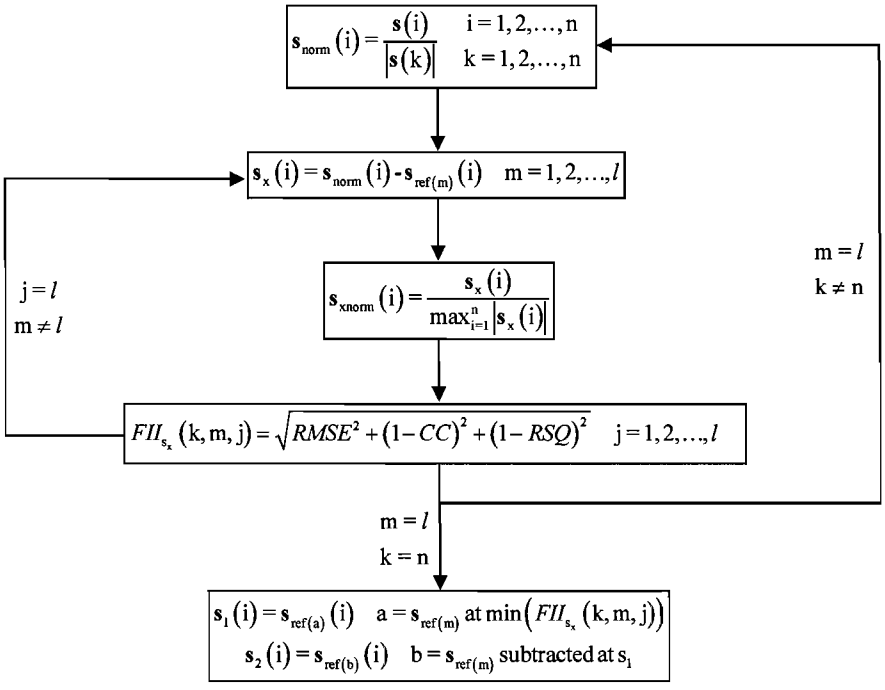

Fig. 6.6.1 Flow diagram of the single fault extraction method.

To demonstrate the implementation of the method, faults 26 to 32 are used to extract the contributing single faults. The fault database is therefore restricted to only single reference faults, i.e. faults 1 to 25. Also, no measurement noise is added in this example. This is done in section 6.7 when the *h-s* graph approach is applied to monitor the PBMR MPS for faults.

Table 6.6.1 summarizes the minimum *FII* values for *h* and *s* together with the average recognition and rejection averages. The *FII* for recognition is calculated as the average of the minimum *h* and *s* values for both faults. Similarly, the *FII* for rejection is computed as the average of the remaining *h* and *s* values. The table shows that both the single faults are correctly identified for all the multiple fault conditions. The minimum *FII* is less than 0.06, which implies that all the single faults were closely matched to their corresponding reference fault signatures. The effectiveness of the method will however be examined when unknown signatures are introduced in the PBMR MPS in noisy conditions.

To illustrate the single fault extraction method, faults 30 and 31 listed in Table 6.6.1 are used as an example. Fig. 6.6.2 illustrates the single extracted *h* and *s* error signatures together with their resultant multiple fault signatures. This figure and figures 6.5.2 (b), (d) and (f) show that the single extracted signatures are highly correlated. Accordingly, low *FII* values are observed. The results indicate that in the PBMR MPS, the single fault signatures superimpose in multiple fault conditions. Note that this observation is only based on the examined fault conditions and the subtraction procedure of the devised method.

6.6.5 The *h-s* graph and reference fault signatures at different power levels

In sections 6.4 to 6.6.4, all the fault simulations corresponded with the system operating at full power, i.e. 100 % MCR and 100 % MCRI. This is usually not the case during real plant conditions seeing that the operating point constantly changes due to varying load demands. To accommodate the varying plant conditions, the *h-s* graph approach must therefore be applicable at different power levels during normal power operation (mode 5b).

Fault number	*FII*					
	Fault 1(*h*)	Fault 1(*s*)	Fault 2(*h*)	Fault 2(*s*)	Ave. recognition	Ave. rejection
26	0.003399	0.067509	0.03341	0.02756	0.03297	2.5991
27	0.008757	0.004962	0.01327	0.00648	0.00836	2.5299
28	0.006173	0.002938	0.03239	0.13774	0.04481	2.6643
29	0.010277	0.018514	0.01199	0.00926	0.01251	2.4993
30	0.012502	0.002728	0.01165	0.16455	0.04786	2.4857
31	0.006268	0.003875	0.03213	0.16967	0.05298	2.8574
32	0.000622	0.003287	0.01923	0.18314	0.05156	2.5419

Table 6.6.1 Classification results with the *FII* for multiple faults 26 to 32 at 100 % MCR.

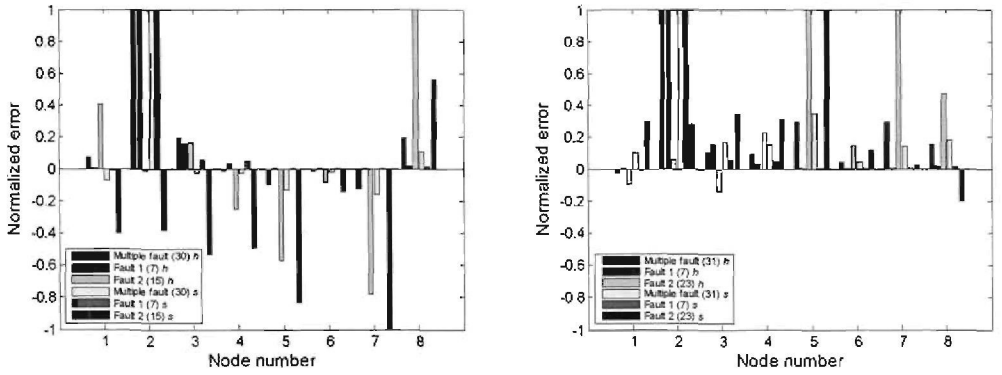

(a) (b)

Fig. 6.6.2 The extracted *h* and *s* error signatures for the two single faults comprising faults: (a) 30; (b) 31.

As discussed in sections 6.3 and 6.5, the most important advantages of using the *h-s* graph for process FDI are:

- The reference plant model remains constant over the operating range.
- Each of the fault conditions is characterized with only one reference fault signature for different fault magnitudes.

To further reduce the fault database, the reference fault signatures must also remain constant, i.e. one signature for different power levels. Based on this assumption, the reference fault signatures are captured whilst the operating point is set to 90 %, 80%,..., 40 % MCR. As an example, the reference fault signatures are computed for faults 11 and 19 and illustrated in Fig. 6.6.3. The fault signatures are presented for the minimum and maximum fault magnitudes and power levels during normal power operation.

The figure indicates that the two fault signatures stay relatively constant over the operating range. Similarly, each of the remaining single fault conditions in the PBMR MPS showed comparable results with little variation. It is therefore concluded that each fault signature is highly correlated during operating point changes and fault magnitude variations, and that the fault signatures are uncorrelated with regard to each other. Accordingly, the fault database is minimized with only one[5] reference fault signature for each single fault condition.

To construct the actual fault signatures during normal power operation of the plant, the reference model must be shifted to different operating points on the *h-s* graph. To achieve this goal, a reference value or point must be known for both *h* and *s*. This value will be used as starting point to reconstruct the reference model at the operating point of interest.

[5]One signature per fault condition comprises one fault signature for *h* and *s*, and is derived with each signature method. This amount to four signatures per fault condition and can for simplicity be stored as a vector (signatures are sequenced) signature.

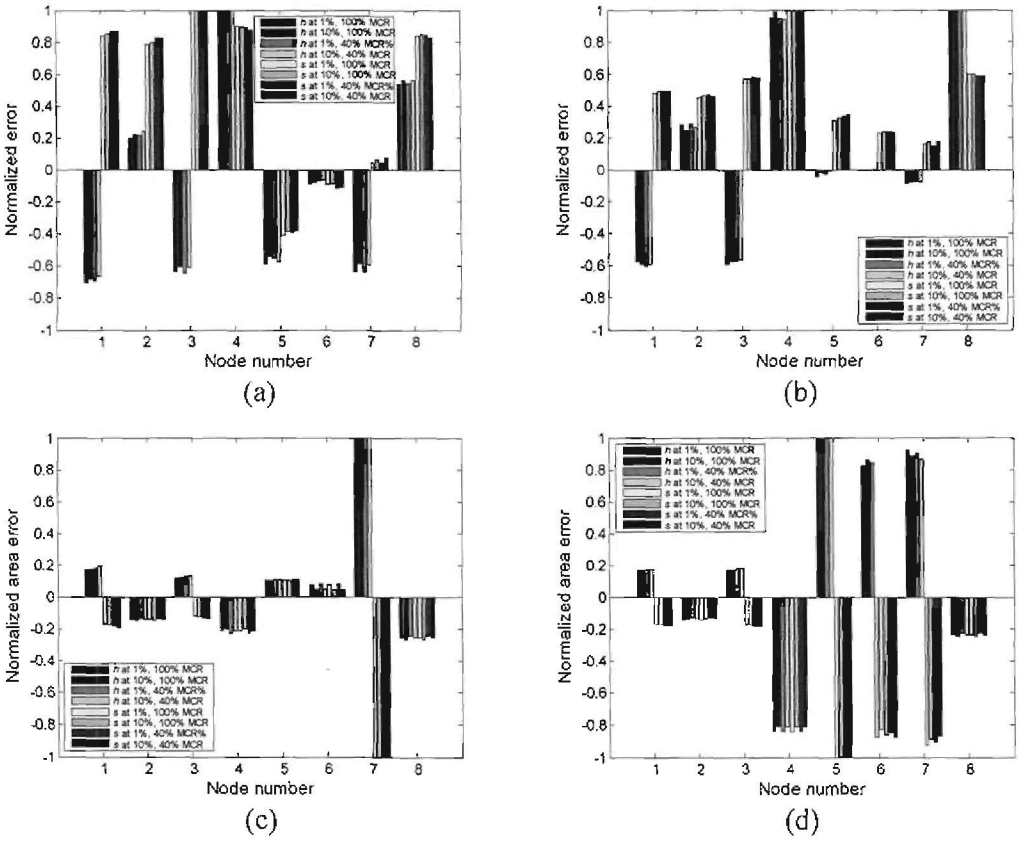

Fig. 6.6.3 The normalized signatures for a 1 % and 10 % change at 40 % and 100 % MCR: (a) fault 11 error; (b) fault 19 error; (c) fault 11 area error; (d) fault 19 area error.

The reference point is selected as the point with the lowest cycle temperature and pressure, the LPC inlet (point 1). Since the *h-s* graph only shifts in the horizontal plane during normal power operation, the reference value for h is chosen as a constant, i.e. zero. The next step is to calculate s at the reference point for different operating points. To obtain the reference values, the plant is ramped from 100 % to 40 % MCR during normal power operation, and back to full power. The reference values are calculated as the average s at each power level.

Following this, shape features are extracted from the reference *h-s* graph to define each of the eight nodes. The two features that are selected are: the length l between the reference point and each node and the angle θ between l and zero h. This parametric representation is illustrated in Fig. 6.6.4 (a) and the reconstruction of the reference *h-s* graph at a different operating point is shown in Fig. 6.6.4 (b). Starting at the reference point (zero h and s at the new operating point), each node is placed at (l_n,θ_n), with n the node number. Based on the proposed reconstruction method, the reference *h-s* graph at 100 % MCR is shifted to the new operating point, and therefore, only one reference model is needed to characterize the system[6].

[6]With regard to one reference model, the improvement in model prediction by means of transformation (*T-P* to *h-s*) is proven for the PBMR MPS and is documented in Appendix B

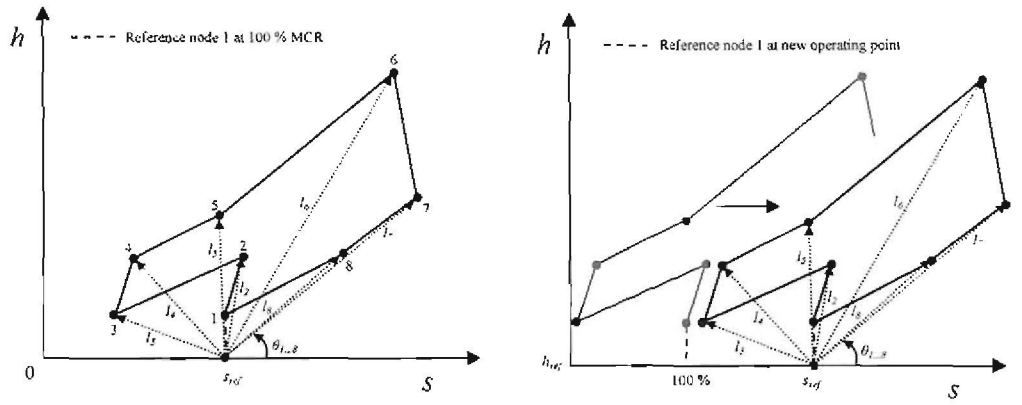

(a) (b)

Fig. 6.6.4 The reference *h-s* graph: (a) shape features; (b) reconstruction.

Although the method is easily applied in theory, real-life application provides more complex challenges. This is due to the fact that some system characteristics change as a result of normal plant variations and alterations of the process. In order to increase the effectiveness of the *h-s* graph approach, the reference model must therefore accommodate these variations and is discussed in the following section.

6.7 Process variations and the reference *h-s* graph

In large scale engineering plants, it is common phenomena that plant characteristics change during the course of operation. This directly affects the performance of the fault diagnosis system and increases the variation (error) between the reference model and the actual system. For this reason, it is important to adjust the reference model (i.e. the shape) to the actual operating conditions to minimize the variation.

Also, faster load changes are achieved in the PBMR by using the GBPC valve in addition to the ICS during normal power operation. Although fast and accurate set point tracking is realized, this method of power control reduces the cycle efficiency and changes the shape of the reference *h-s* graph. The *h-s* graph is illustrated in Fig. 6.7.1 for GBPC valve operation and indicates that the graph shifts simultaneously in the vertical and horizontal directions. Since valve operation is performed during normal power operation of the plant, the additional shift must also be incorporated in the reference model. In the thesis, the following process variations are considered for the PBMR MPS:

(1) Plant efficiencies tend to be slightly lower at reduced power levels.

(2) Performance characteristics of the components change due to normal wear and system maintenance (new or replacement parts).

(3) GBPC valve operation in addition to the ICS.

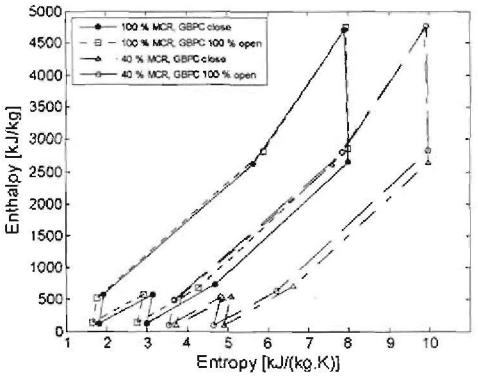

Fig. 6.7.1 The *h-s* graph for GBPC valve operation at different power levels.

Firstly, the reference *h-s* graph is adjusted to include valve operation and reduced plant efficiencies at different operating points. As a proposed solution, an n-dimensional variation surface (*VS*) is defined as the variation between the shape features for the actual operating conditions and the reference model. In this case, the n-dimensional surface encompasses the magnitude of the variation, the normalized percentage of the GBPC valve opening and the power level for each node.

To create the *VS*, the shape features (l_n,θ_n) of the *h-s* graph are extracted during GBPC valve operation. A GBPC valve transient is realized by opening the GBPC valve in 1 % increments whilst ramping the plant from 100 % MCR down to 40 % MCR. This however, amounts to an unmanageable number of operating points. To simplify the problem, the extracted features are reduced to 21 operating points by using an n-dimensional cubic spline interpolation algorithm ('*interpn*' [66]). By applying an n-dimensional factor, additional parameters that can vary the operating point may be defined in the future, e.g. the CWT. The operating points are: 100 %, 90 %,..., 40 % MCR with the GBPC valve closed, 50 % and 100 % open. The variation in each of the shape features is therefore characterized by an enclosed region and is defined by the 21 operating points.

By defining the enclosed surfaces and applying the interpolation algorithm, the variation of the shape features can therefore be estimated at any operating point. To visualize the four-dimensional surface (fourth dimension is the node numbers), three dimensions are varied whilst the fourth is kept constant. The *VS* for each of the shape features is illustrated in Fig. 6.7.2. In Fig. 6.7.2 (a) to (d), the GBPC valve opening is constant for each node whereas the GBPC valve opening is varied in (e) and (f). The figure shows that larger variations occur at reduced power levels and is the result of lower plant efficiencies. Also, the figure illustrates that the magnitude of variation for *l* is very small. This is an indication that the reference model needs minimal adjustment to minimize the variation.

To test the performance of the reference *h-s* graph with the *VS*, three random operating points are selected for the PBMR MPS. The three test cases are (manifold pressure/normalized GBPC valve opening): (1) 6856 kPa (76 %)/0.285; (2) 5569 kPa (62 %) /0.589; and (3) 4641 kPa (51.5 %)/0.862. The normalized *h* and *s* are calculated with both Flownex and the reference *h-s* graph, and are summarized in Table 6.7.1.

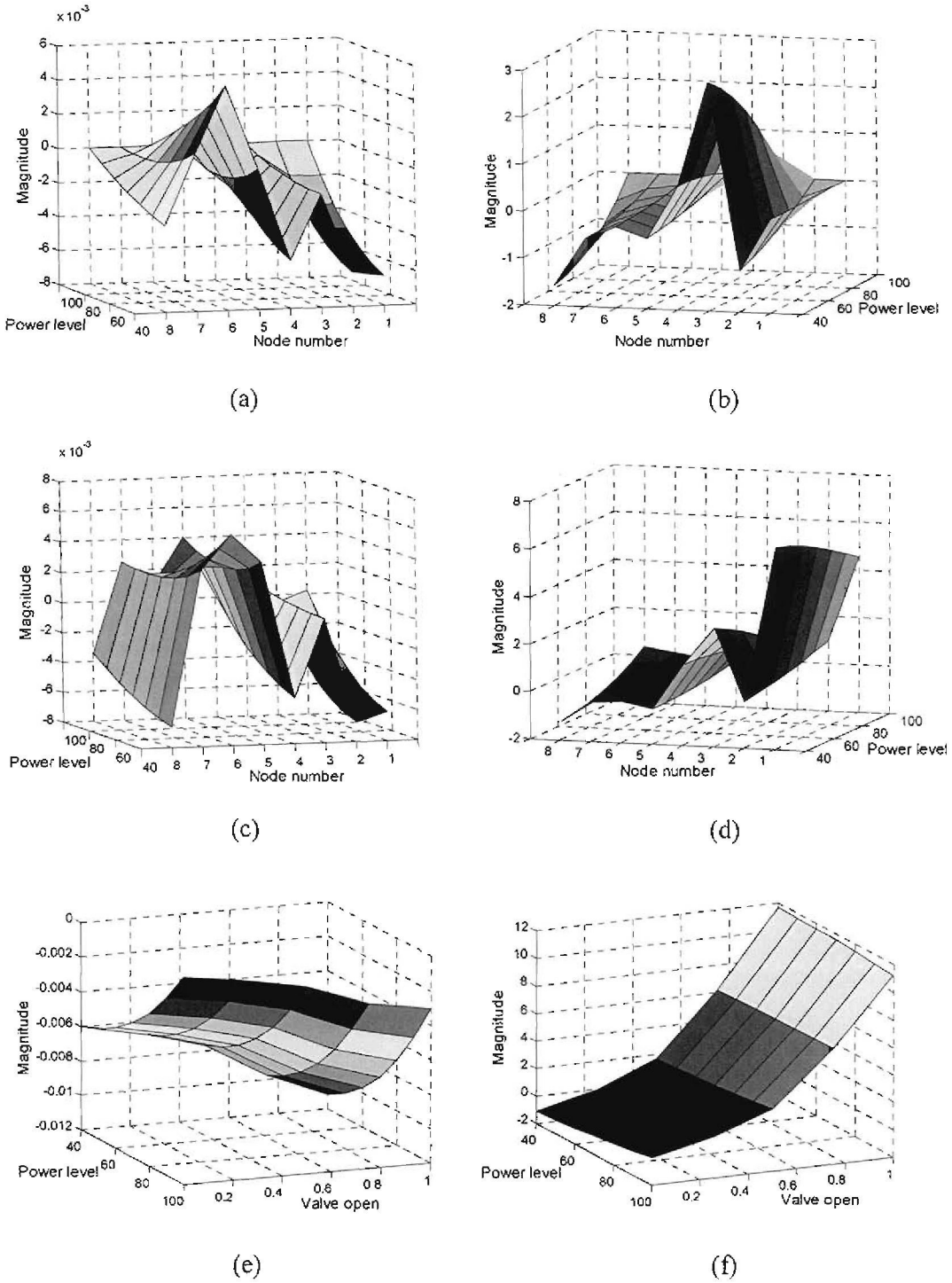

Fig. 6.7.2 Variation surface for valve operation: (all nodes) GBPC 1 % open (a) *l*; (b) θ;
(all nodes) GBPC 25 % open (c) *l*; (d) θ;
(node 2 only) GBPC 0-100 % open (e) *l*; (f) θ.

Node	Test case 1		Test case 2		Test case 3	
	Flownex	*h-s* graph	Flownex	*h-s* graph	Flownex	*h-s* graph
*h*1	0.0224	0.0224	0.0210	0.0214	0.0204	0.0205
*h*2	0.1127	0.1128	0.1104	0.1106	0.1079	0.1083
*h*3	0.0231	0.0232	0.0218	0.0220	0.0211	0.0216
*h*4	0.1124	0.1125	0.1083	0.1084	0.1013	0.1019
*h*5	0.5254	0.5254	0.5333	0.5337	0.5516	0.5505
*h*6	0.9402	0.9402	0.9429	0.9428	0.9482	0.9476
*h*7	0.5329	0.5330	0.5406	0.5410	0.5590	0.5580
*h*8	0.1422	0.1424	0.1377	0.1378	0.1303	0.1311
*s*1	0.3496	0.3472	0.3864	0.3883	0.4121	0.4141
*s*2	0.3667	0.3643	0.4039	0.4057	0.4299	0.4319
*s*3	0.2337	0.2313	0.2719	0.2739	0.3004	0.3023
*s*4	0.2463	0.2438	0.2851	0.2869	0.3143	0.3150
*s*5	0.6226	0.6200	0.6713	0.6734	0.7210	0.7232
*s*6	0.8470	0.8445	0.8917	0.8936	0.9320	0.9317
*s*7	0.8566	0.8540	0.9002	0.9020	0.9385	0.9393
*s*8	0.5207	0.5183	0.5539	0.5557	0.5714	0.5728
% Diff	0.297467		0.247773		0.147321	

Table 6.7.1 Results for the *h* and *s* calculations.

Table 6.7.1 shows that the percentage difference between Flownex and the estimated *h-s* graph values is less than 0.3 %. The high correlation between the values demonstrates that the *h-s* graph is a simple but effective way to estimate the values for the reference model at different operating points. In addition, process variations are characterized by interpolating the *VS* with a reduced number of reference points

To incorporate process variation number (2) in the PBMR MPS, the *VS* is implemented online in real-time during normal power operation of the plant. The two surfaces are adjusted at regular time intervals to minimize the variation between the reference model and the plant, subject to the type of variation (e.g. valve operation) and a healthy system. In addition, the *VS* will also be adjusted after maintenance or repair to describe any altered system characteristics. It is important to note that the time interval of adjustment is dependent on the amount and magnitude of variation, and is only determined after the system is online. In general, the reference model is not altered if the magnitude of variation stays within an acceptable tolerance.

As discussed in section 6.6.5, the reference fault signatures stay constant over the operating range for different magnitudes of the fault. However, to utilize the minimized fault database with only single reference fault signatures, each signature must be highly correlated during process variations (GBPC valve operation). To consider valve operation in the PBMR MPS, the GBPC valve is opened 50 % and 100 % respectively during each of the 25 single fault conditions and the *h-s* graph together with the *VS* is used to estimate the reference model for the specific operating point. Next, the four signatures are calculated for the fault conditions and compared to the reference fault database. As an example, consider the fault signatures of single faults 11 and 23 illustrated in Fig. 6.7.3.

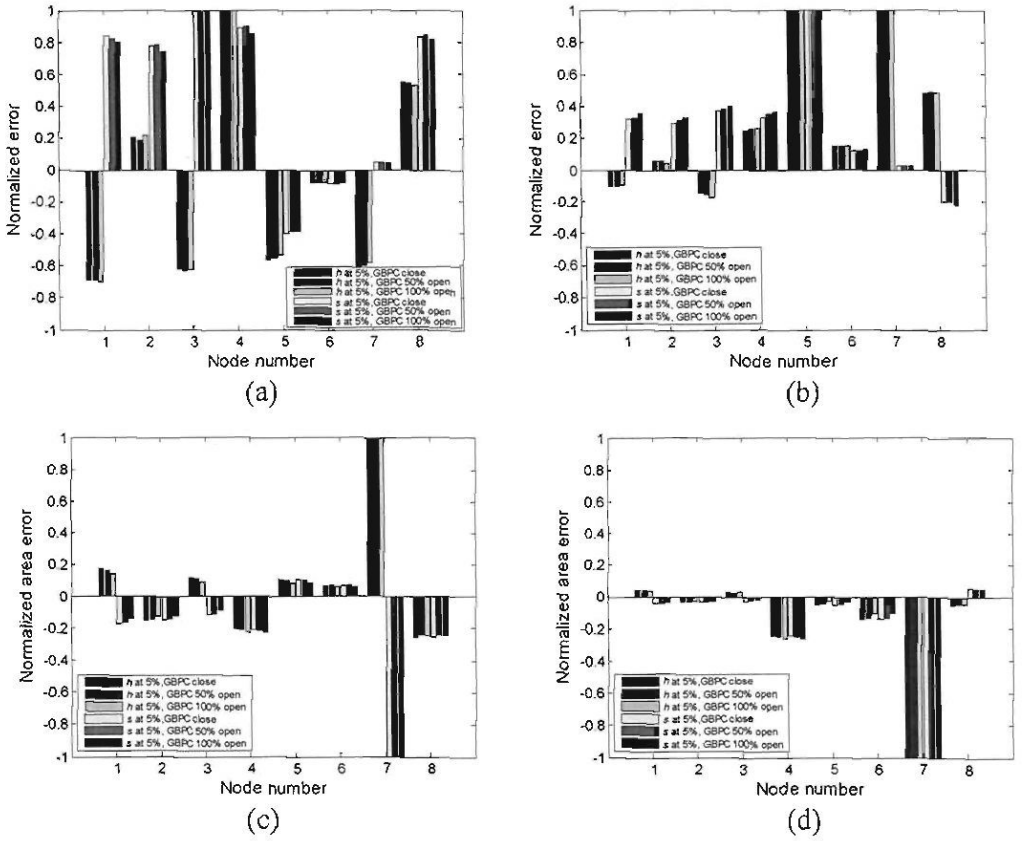

Fig. 6.7.3 The normalized signatures at 100 % MCR for GBPC valve operation: (a) fault 11 error; (b) fault 23 error; (c) fault 11 area error; (d) fault 23 area error.

The figure shows that the correlation between each of the single fault signatures is very high during valve operation. Similarly, each of the remaining single fault signatures in the PBMR MPS showed comparable results if the *VS* corresponds to the minimal variation at the specific operating point. The single reference fault signatures will therefore be sufficient to characterize fault conditions in the PBMR MPS during valve operation.

In conclusion, some important observations regarding the *VS* are summarized as follows:

- By integrating vertical shift into the *h-s* graph by means of the *VS*, various normal process variations can be correctly characterized.

- The single reference fault signatures stay relatively constant for process variations if the reference model incorporates the *VS*.

- The *VS* is implemented in real-time to minimize variation between the actual plant and the reference model, i.e. to minimize modelling errors.

6.8 Application of the *h-s* graph approach in the PBMR MPS

In this section, the proposed process fault diagnosis approach is validated with an application in the PBMR MPS. It is important to note that all the results presented are based on the complex simulation model of the actual plant. Also, to emulate actual plant conditions, random noise is added to all the measurements (discussed in section 6.6.1). The following transient variations are considered:

- Faults are induced during steady state for normal power operation.
- Faults are induced during load following for normal power operation.

To verify that the faults are identified at an early stage, the fault magnitude must be very small at the time of detection. For application in the PBMR MPS, a fault magnitude of 1 % is deemed to be sufficient. The following fault magnitudes are considered:

- Abrupt fault with 1 % bias.
- Drift fault corresponding to a 2 % change in an hour.

One problem that arises during online application is to select the correct fault isolation algorithm, i.e. for a single or multiple fault condition. As discussed in section 6.6, the known single fault reference signatures will show a low *FII*, whereas unknown faults will show high values. To determine the tolerance of the *FII* for known signatures, the faults are randomly induced during steady state operation of the plant.

6.8.1 Fault conditions during steady state operation of the plant

Firstly, the plant is operated at full power in steady state with all the valves fully closed. Since no valve operation is performed, the reference *h-s* graph can be used without the *VS*. Random noise with $\sigma = 1$ is added to the plant measurements and a sampling window of 10 seconds (i.e. 10 samples) is selected.

To simulate the fault conditions during normal power operation, the 32 fault conditions are randomly induced for 10 seconds with a bias value of 1 % (abrupt fault). After each fault condition, the plant is returned to the original steady state conditions before the next fault is induced. The reason the faults are randomly induced in succession is to combine 32 fault simulations into one. To determine the *FII* tolerance for the known signatures in the PBMR MPS, the correct algorithm is selected in this example and depends on the vector fault condition (single or multiple). The vector of randomly induced faults is:

[21,25,9,6,20,5,19,12,7,29,31,10,22,3,14,13,28,1,27,18,15,32,17,23,26,30,4,8,2,16,24,11]

Figure 6.8.1 shows the isolated faults for each of the simulated fault conditions, and Table 6.8.1 summarizes the results of the isolation algorithm and the *FII*.

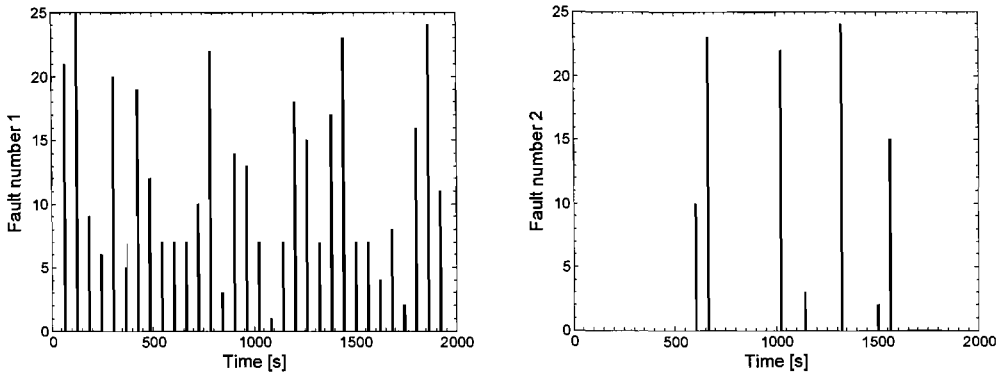

Fig. 6.8.1 The isolated faults during steady state operation of the PBMR at 100 % MCR: (a) single fault 1; (b) single fault 2.

Fault vector	Isolated fault	*FII*				
		Fault 1(error)	Fault 1(area)	Fault 2(error)	Ave. recognition	Ave. rejection
21	21	0.340212	0.061578	0	0.200895	6.134653
25	25	0.330755	0.067270	0	0.199013	5.534043
9	9	0.027219	0.037339	0	0.032279	7.242336
6	6	0.078239	0.011379	0	0.044809	5.485466
20	20	0.044314	0.015763	0	0.030038	8.504902
5	5	0.072332	0.017033	0	0.044683	6.528084
19	19	0.031160	0.020857	0	0.026008	8.171386
12	12	0.162649	0.025451	0	0.094050	6.586299
7	7	0.055919	0.010281	0	0.033110	4.777097
29	29	0.011763	0	0.015805	0.013784	2.502175
31	31	0.111671	0	0.012473	0.062072	2.867006
10	10	0.027143	0.063293	0	0.045218	4.991760
22	22	0.314045	0.046812	0	0.180428	8.798796
3	3	0.102076	0.130887	0	0.116482	4.840005
14	14	0.141838	0.040288	0	0.091063	6.440418
13	13	0.019705	0.005849	0	0.012777	7.218782
28	28	0.087813	0	0.008665	0.048239	2.655320
1	1	0.117890	0.093892	0	0.105891	5.726515
27	27	0.027957	0	0.010244	0.019110	2.532352
18	18	0.045612	0.054659	0	0.050135	6.524358
15	15	0.349312	0.031016	0	0.190164	4.896510
32	32	0.228303	0	0.007329	0.117816	2.537446
17	17	0.045351	0.053808	0	0.049579	5.847439
23	23	0.056249	0.026494	0	0.041371	6.469139
26	26	0.030836	0	0.036241	0.033539	2.596791
30	30	0.101663	0	0.009977	0.055820	2.480615
4	4	0.323812	0.056115	0	0.189963	5.129935
8	8	0.036454	0.035389	0	0.035921	5.903668
2	2	0.107486	0.141373	0	0.124430	6.710999
16	16	0.085756	0.014903	0	0.050329	5.442663
24	24	0.079989	0.045644	0	0.062817	8.584188
11	11	0.061249	0.038322	0	0.049785	5.205250

Table 6.8.1 Summary of isolated faults during steady state by means of a sample window.

The table shows that each of the randomly induced faults is correctly isolated. Also, the results indicate that the *FII* is low for multiple fault conditions if the single fault extraction method is employed. Therefore, by selecting the proper isolation algorithm, each of the faults can be correctly identified.

Table 6.8.1 shows that the average *FII* for all the single signatures is less than 0.45. Accordingly, a *FII* tolerance of 0.5 is chosen for the known single signatures in the PBMR MPS. Once this limit is exceeded, the single fault extraction algorithm determines if the unknown signature is caused by a multiple fault condition.

Next, the isolation ability of the *h-s* graph approach is verified in the presence of process and measurement noise. During each of the single fault conditions, random noise is added to the measurement channels with an increase in variance. For this test case, the sample window average is not computed and approximately 3000 samples are generated for the single fault conditions. Table 6.8.2 summarizes the average (all the samples) and maximum (any single sample) isolation percentages for the 25 single faults consisting of different noise and fault magnitudes. The isolation percentage is determined by

$$isolation\ percentage = \left(\frac{n_{correct}}{n_{total}} \right) \times 100 \qquad (6.8.1)$$

with n the number of total and correct isolations determined by the lowest *FII*.

The table shows that all the single faults are correctly isolated in the noise free measurements. However, the results indicate that the number of correct isolations gradually decreases with an increase in noise magnitude and that the isolation percentage increases if the fault magnitude increases. Therefore, the conclusion drawn from the observations is that random noise affects the isolation ability of the *h-s* graph approach at the beginning of some fault conditions. Nonetheless, the maximum isolation percentages indicate that the method is able to correctly isolate all of the single faults in some cases for larger noise magnitudes.

In addition, Table 6.8.2 indicates that the isolation percentage slightly increases if the error and area error methods are not used in combination for the average calculations. In contrast, the results listed in Table 6.8.1 show that if a sample window is used, the *FII* is lower for the area error method and increases the average isolation percentage. Therefore, the second conclusion drawn is that random noise affects the isolation ability of the signature generation methods if the measurements are not averaged over a sampling window.

	Both methods				Error method			
	1 % change		5 % change		1 % change		5 % change	
Var (σ)	A (%)	M (%)	A (%)	M (%)	A (%)	M (%)	A (%)	M (%)
0	100	100	100	100	100	100	100	100
1	99	100	100	100	100	100	100	100
2	97	100	100	100	99	100	100	100
3	96	100	98	100	98	100	100	100
4	96	100	97	100	97	100	99	100

Table 6.8.2 Average (A) and maximum (M) isolation percentage for 3000 samples (single faults).

The second test validates the ability of the single fault extraction procedure to isolate the contributing single faults in noisy conditions. The previous example is adapted to generate 3000 samples comprising random noise. Table 6.8.3 summarizes the average *FII* of both single faults and the average rejection of the remaining reference fault signatures.

The table shows that the averages of the *FII* are very low, which indicates that the contributing single faults can be correctly isolated. Also, the table shows that an increase in the noise magnitude slightly increases the *FII*. Therefore, it is concluded that the isolation ability of the single fault extraction procedure decreases if the noise magnitude increases.

Next, the *h-s* graph approach is applied during load following in the PBMR MPS.

6.8.2 Fault conditions during load following of the plant

As discussed in Chapter 3, the plant will be mostly operated to accurately follow varying load demands. Since the expected time of normal power operation is more than 325 days per year [47], fault diagnosis is essential to prolong the lifespan of the plant. A typical load following transient of the plant is shown in Fig. 6.8.2 (a). During the transient, the following plant characteristics are relevant:

- Helium is injected and removed from the MPS at a rate of 7.5 kg/s by means of the ICS.
- The outlet temperature of the reactor is controlled at 900 °C with the control rods.
- The bypass valves are 0-100 % open.

Starting at point 1, the plant is operated at full power in steady state with all the bypass valves closed. At point 2, the GBPC valve is opened to 45 % and 100 % respectively. Following this, the GBPC valve is fully closed and helium is extracted and injected from point 4 onwards. At point 12, the GBPC valve is opened to 90 % and then closed for the remaining time of the transient.

Figure 6.8.2 (b) shows the normalized mean error between the Flownex calculations and the *h-s* reference graph with the *VS*. The figure shows that the highest errors occur during valve operation with the valves 90 % to 100 % open. Although the error magnitude is acceptable for the investigation, it can be minimized by incorporating more

	FII (error method)													
	Fault 26		Fault 27		Fault 28		Fault 29		Fault 30		Fault 31		Fault 32	
Var (σ)	I	R	I	R	I	R	I	R	I	R	I	R	I	R
0	0.032	2.599	0.008	2.529	0.044	2.664	0.012	2.499	0.047	2.485	0.052	2.857	0.079	2.541
1	0.033	2.593	0.011	2.531	0.045	2.663	0.013	2.500	0.056	2.476	0.052	2.862	0.117	2.538
2	0.033	2.598	0.019	2.535	0.048	2.657	0.014	2.491	0.056	2.482	0.062	2.831	0.117	2.533
3	0.036	2.599	0.023	2.526	0.051	2.663	0.015	2.492	0.082	2.496	0.063	2.875	0.129	2.545
4	0.036	2.587	0.026	2.528	0.053	2.675	0.015	2.484	0.084	2.487	0.064	2.852	0.136	2.543

Table 6.8.3 The isolation (I) and rejection (R) averages of the *FII* for multiple faults 26 to 32.

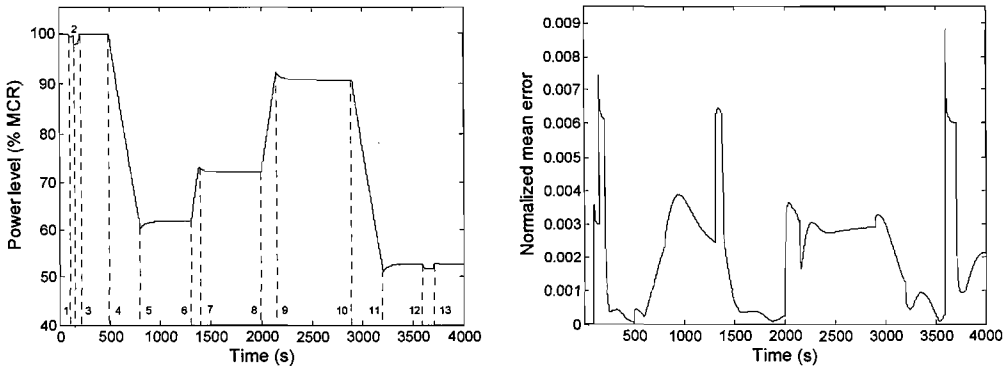

Fig. 6.8.2 Load following transient during normal power operation of the PBMR MPS: (a) power level; (b) normalized error between Flownex and the reference *h-s* graph comprising the *VS*.

reference points in the *VS*. The errors at large valve openings are expected and supported by the larger variations observed in Fig. 6.7.2 (e) and (f).

To emulate fault conditions in the system, each of the single faults are induced at t = 1000 seconds and multiple faults at 1000 and 1700 seconds respectively. In both single and multiple fault simulations, the fault magnitude increases to a maximum of 2 % at 4000 seconds (drift fault). Therefore, regarding multiple faults, the magnitude of each fault is different at the end of the transient. Similar to the steady state simulations, random noise with $\sigma = 1$ is added to the plant measurements and a sampling window of 10 seconds is selected. The missed alarm rate is chosen as $\alpha = 0.01$ and the hypothesis thresholds for fault detection are selected as 2.5 and 0.1 for h and s respectively. The results of the 32 fault simulations are summarized in Table 6.8.4. The notation in the table is as follows: 'Time' denotes the time of fault detection; 'Magnitude' represents the fault magnitude at the time of detection and the 'average *FII*' is calculated for the remaining part of the transient.

An example of fault isolation is illustrated in figures 6.8.3 and 6.8.4 for fault 18. Figure 6.8.3 (a) shows that the single fault is detected after approximately 140 sample windows, i.e. 1400 seconds. Figure 6.8.3 (b) depicts the average *FII* after fault detection which shows that the results correlate well with the values listed in Table 6.8.1.

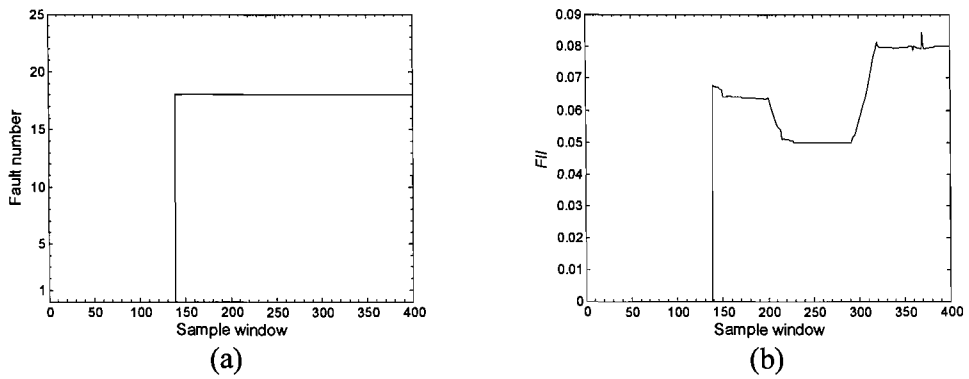

Fig. 6.8.3 Single fault detection during load following: (a) isolated fault; (b) *FII* after detection.

Fault	Sample window	Magnitude (%) change	*FII*		
			Fault 1 (ave.)	Fault 2 (ave.)	Ave. rejection
1	140	0.26	0.12779	0	4.6266
2	160	0.4	0.15017	0	5.4256
3	150	0.33	0.14058	0	5.7899
4	140	0.26	0.22926	0	4.4365
5	140	0.26	0.05392	0	3.4567
6	150	0.33	0.05408	0	4.2355
7	170	0.46	0.03996	0	3.4664
8	150	0.33	0.04335	0	4.6687
9	160	0.4	0.03895	0	4.4777
10	140	0.26	0.05457	0	6.1346
11	150	0.33	0.06008	0	5.5466
12	150	0.33	0.11350	0	4.4566
13	170	0.46	0.01542	0	5.7688
14	160	0.4	0.10990	0	6.3456
15	140	0.26	0.29287	0	5.5467
16	160	0.4	0.06074	0	4.9587
17	160	0.4	0.05983	0	5.4366
18	140	0.26	0.06051	0	3.5393
19	150	0.33	0.03138	0	3.6577
20	150	0.33	0.03625	0	4.6767
21	170	0.46	0.24245	0	5.6626
22	170	0.46	0.21775	0	4.4367
23	160	0.4	0.04993	0	3.4777
24	150	0.33	0.07581	0	5.3425
25	150	0.33	0.30053	0	6.2554
26	150|200	0.33|0.26	0.04047	0.02959	2.4799
27	150|220	0.33|0.43	0.02306	0.01686	2.4628
28	150|210	0.33|0.35	0.05821	0.04256	2.5975
29	150|210	0.33|0.35	0.01663	0.01212	2.3649
30	150|200	0.33|0.26	0.06736	0.04921	2.3587
31	150|210	0.33|0.35	0.07491	0.05476	2.7452
32	150|220	0.33|0.43	0.14219	0.10395	2.4743

Table 6.8.4 Summary of isolated faults (f1|f2) during load following.

The fault signatures are illustrated in Fig. 6.8.4 for normal variations of the process. The variations include: injection at 2100 seconds, steady state operation at 2500 seconds, extraction at 3000 seconds and valve operation at 3650 seconds. The results indicate that the *h* and *s* signatures are highly correlated and stay approximately constant. As a result, one reference signature will be sufficient for isolation during normal variations of the process. Therefore, the conclusion drawn from the observations is that each of the single reference fault signatures is valid during steady state operation and normal transient variations of the process.

As discussed, the classification of unknown signatures (multiple fault conditions) is more complex. To demonstrate the single fault extraction procedure, fault 29 is used as an example and is illustrated in Fig. 6.8.5. Note that the single fault isolation algorithm is used in Fig. 6.8.5 (a). Figure 6.8.5 (a) shows that the first fault is detected after 1500 seconds.

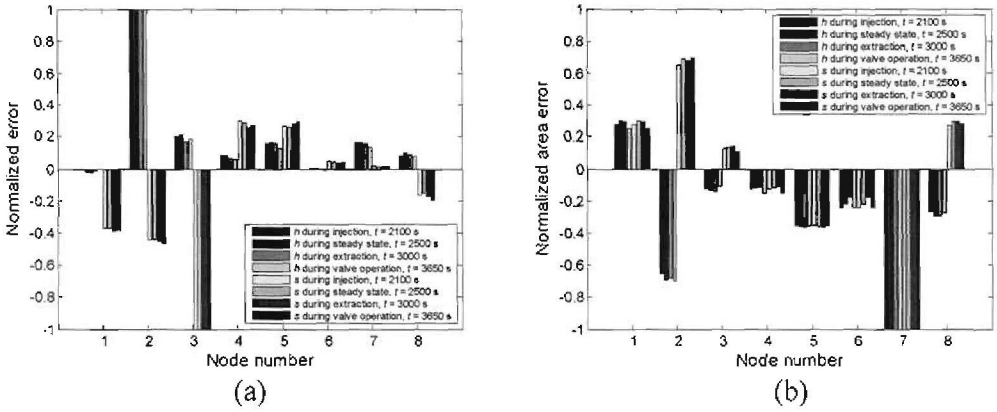

Fig. 6.8.4 The normalized signatures for fault 18 during load following: (a) error; (b) area error.

The figure indicates that the *FII* is steady for the known single fault until the second fault is induced at 1700 seconds. As a result, the *FII* increases owing to the fact that the second fault starts to mask the first (unknown signature). Since the magnitude of the second fault increases faster, it is visible that the second fault becomes more dominating after 2600 seconds. Consequently, the second fault masks the first fault completely (i.e. the *FII* will decrease below 0.5 again) and the multiple fault is classified as the second single fault.

To reduce fault masking, the single fault extraction procedure is used once the *FII* surpasses the single fault limit. Figure 6.8.5 (b) shows that the threshold is exceeded at 2100 seconds, and consequently, the *FII* is calculated for the probable extracted single faults. The figure indicates that the *FII* decreases and stays relatively steady for the known single signatures after isolation, which suggests that the algorithm is less sensitive to the magnitude of the fault. As a result, the probability of fault masking is minimized during multiple fault conditions.

Overall, the results indicate that all the examined faults can be correctly isolated with the *h-s* graph approach during normal power operation of the PBMR MPS.

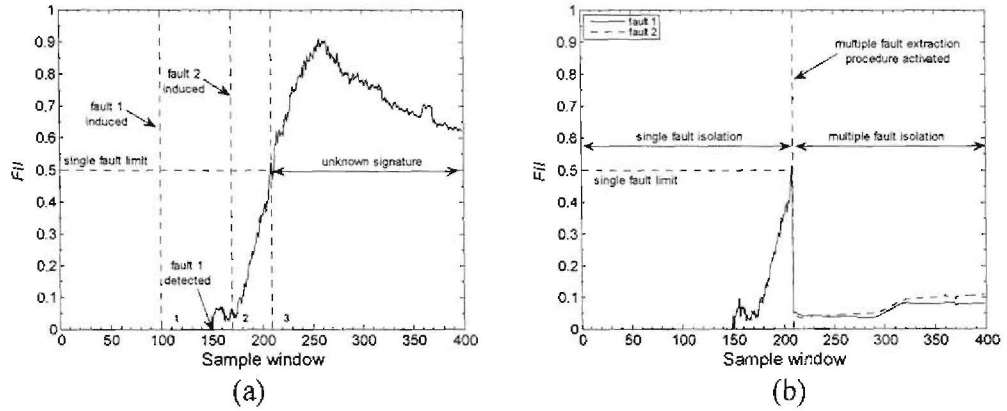

Fig. 6.8.5 Multiple fault detection during load following: (a) *FII* for single fault detection; (b) *FII* for single fault extraction procedure.

6.9 Summary and conclusions

This chapter focussed on the development and implementation of the *h-s* graph approach for process fault diagnosis in the PBMR MPS.

Section 6.2 firstly introduced enthalpy and entropy after which section 6.3 illustrated the general construction of the *h-s* graph. In the thesis, a simplified version of the *h-s* graph is used and comprises eight nodes.

Section 6.4 showed the effects of the reference faults on *h* and *s* and illustrated the shift on the *h-s* graph. Following this, two methods are devised in section 6.5 for generating reference fault signatures.

In section 6.6, the hypothesis for fault detection is discussed and the statistical classifier, the *FII* is devised for recognition. In the final part of this section, the single fault extraction procedure is developed to isolate the contributing single faults in a multiple fault condition.

In section 6.7, an n-dimensional *VS* is defined to incorporate process variations in the reference *h-s* graph. Lastly, the proposed fault diagnosis approach is applied in section 6.8 to the PBMR MPS.

Some of the important conclusions reached in this chapter are:

- The examined faults can be characterized by a distinctive shift in the enthalpy and entropy and are visualized on an *h-s* graph. The Brayton cycle can be described by the *h-s* graph, in which any point on the graph represents the thermodynamic state of the process.

- In the PBMR MPS, primary power control is achieved by using the inventory control system. This type of power control allows the shape of the *h-s* graph to remain constant over the power range during normal operation.

- To isolate a fault condition, the error and area error methods are devised. These methods are applied to create normalized reference fault signatures that stay relatively constant. This statement holds during normal power operation for the following transients:

  - Changes in the fault magnitude.

  - Changes in the operating point.

  - Variations of the normal process, i.e. injection, extraction and valve operation.

  Accordingly, only one reference signature (for each method) is necessary to correctly isolate the fault during normal power operation of the plant.

- Random noise affects the isolation ability of the *h-s* graph approach if the magnitude of the noise increases; however, a larger fault magnitude improves the isolation percentage. As a result, the effects of noise can be averaged by using a sampling window which improves the isolation percentage.

- In order to match the fault signatures to the corresponding reference fault signatures, a statistical classifier is formulated and termed the *FII*.

- To incorporate variations of the normal process into the reference *h-s* graph, n-dimensional interpolation is used together with the *VS*. The n-dimensions can be expanded to include additional variables that alter the shape of the reference model during normal power operation.

- The single fault extraction procedure is devised to isolate the contributing single faults from unknown, multiple fault symptoms.

The following chapter presents the validation of the proposed approach for process fault diagnosis with an application in the PBMM prototype plant.

CHAPTER 7

Validation of the *h-s* graph approach for process FDI

Chapter 6 described the development and implementation of the h-s graph approach for process FDI in a thermodynamic system. This chapter focuses on the validation of the h-s graph approach and demonstrates the feasibility of the method with an application in the prototype PBMM plant.

7.1 Introduction

The main objective of this chapter is to validate the *h-s* graph approach for process fault diagnosis with an application in the Pebble Bed Micro Model (PBMM). The PBMM is a prototype gas turbine power plant and is based on the first configuration of the PBMR. The PBMM, which consists of a closed-loop three-shaft system, was developed to gain understanding into the dynamic behaviour of the PBMR design and to evaluate control methodologies for transition sequences like start up and load rejection. Although the PBMM is not an exact scaled version of the PBMR plant, it has the same topology and main components.

In section 7.2, the differences between the three-shaft and single shaft PBMR models are described and compared with the topology of the PBMM plant. Also, a general layout of the plant is illustrated which emphasizes some of the modelling difficulties discussed in the next section.

Section 7.3 discusses the development of a Flownex simulation model of the PBMM plant. A comparison between the simulation and plant data revealed that unmodelled heat paths from the complex metallic support structure of the turbo machinery caused discrepancies between the Flownex model and the plant measurements. Accordingly, the simulation model was adjusted and the modelling error minimized.

In order to validate the *h-s* graph approach, real plant data (contains process and measurement noise) from two test runs are used. Section 7.4 describes the two sets of data; dataset one encapsulates a turbo failure and the second is logged during a thrust load test. The heater temperature transient is taken as an emulated fault condition in the second dataset.

In section 7.5, the single faults that are considered for the validation process are modelled in Flownex and compared with the PBMM data. Additionally, four extra fault conditions are modelled to extend the reference fault database to six single faults.

Section 7.6 describes the procedure of process FDI with the *h-s* graph approach. Firstly, the distribution of the measured noise is established which is a prerequisite for the hypothesis test used for fault detection. Next, the emulated faults are detected without delay and correctly isolated using the *FII*.

In section 7.7, the improvement in model performance is demonstrated by transforming the measurements. This goal is accomplished by using the *T-P* and *h-s* models derived at full power to predict the reference values at reduced power.

Some concluding remarks are summarized in section 7.8.

7.2 Differences between the PBMR models and the PBMM

The original design of the PBMR is based on a three-shaft, closed-loop intercooled recuperative Brayton cycle. The most noticeable difference between the two models is the number of turbines and shafts. Whilst the three-shaft model has two free running shafts and one shaft running at 50 Hz, the single shaft model has one interconnected shaft running at 50 Hz.

In the MPS, the three shafts are each connected to a separate turbine, the HPT, LPT and the PT. Therefore, to monitor the turbines individually and not as a single unit, two additional nodes are required on the *h-s* graph. Figure 7.2.1 illustrates the layout of the

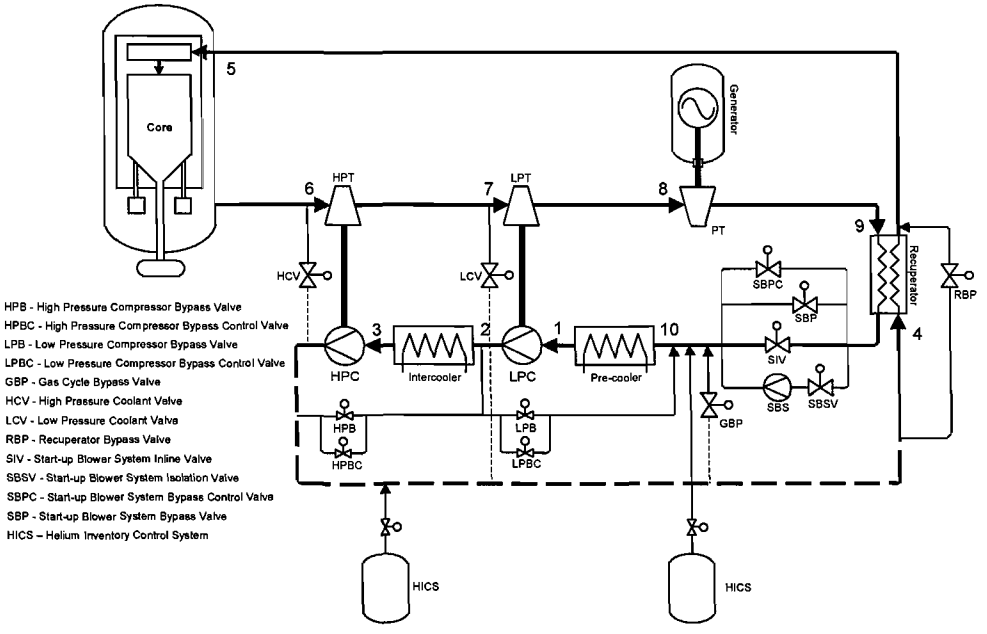

Fig. 7.2.1 Schematic showing the three-shaft MPS of the first PBMR configuration [46].

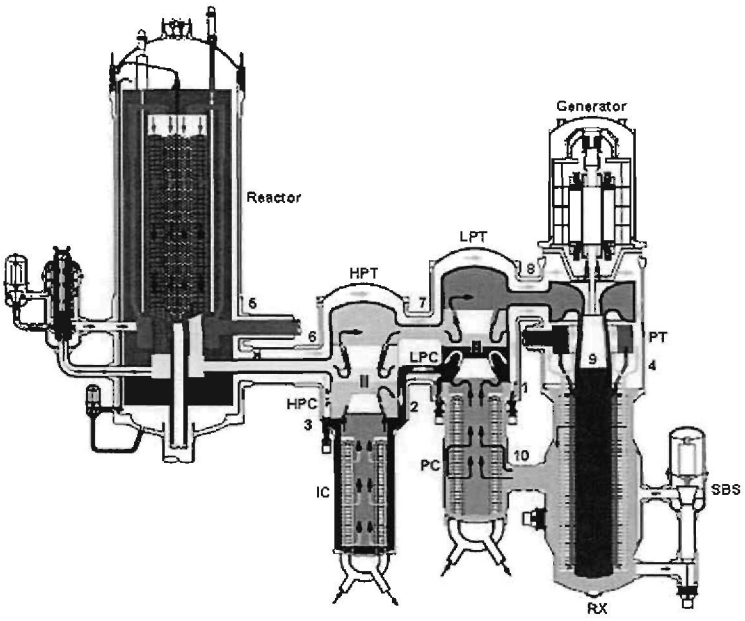

Fig. 7.2.2 Gas flow path through the three-shaft MPS [46].

three-shaft PBMR model and Fig. 7.2.2 depicts the gas flow path through the MPS. The theoretical *h-s* graph with the additional nodes is shown in Fig. 7.2.3.

To verify the operation of the three-shaft configuration, the prototype PBMM plant was constructed at the North-West University. A schematic layout of the PBMM MPS is shown in Fig. 7.2.4. Although the overall performance characteristics of the prototype plant closely resemble that of the PBMR plant, some of the differences are as follows:

- The pebble bed nuclear reactor is emulated by a 420 kW high temperature resistive heater. The heater has like the pebble bed a large thermal capacity and is rated for a maximum outlet temperature of 700 °C.

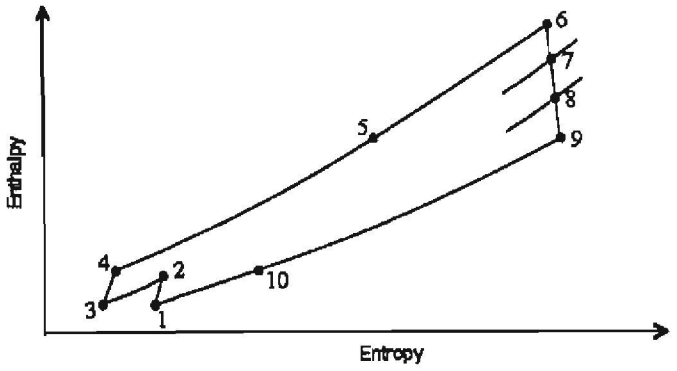

Fig. 7.2.3 The theoretical *h-s* graph for the three-shaft PBMR model.

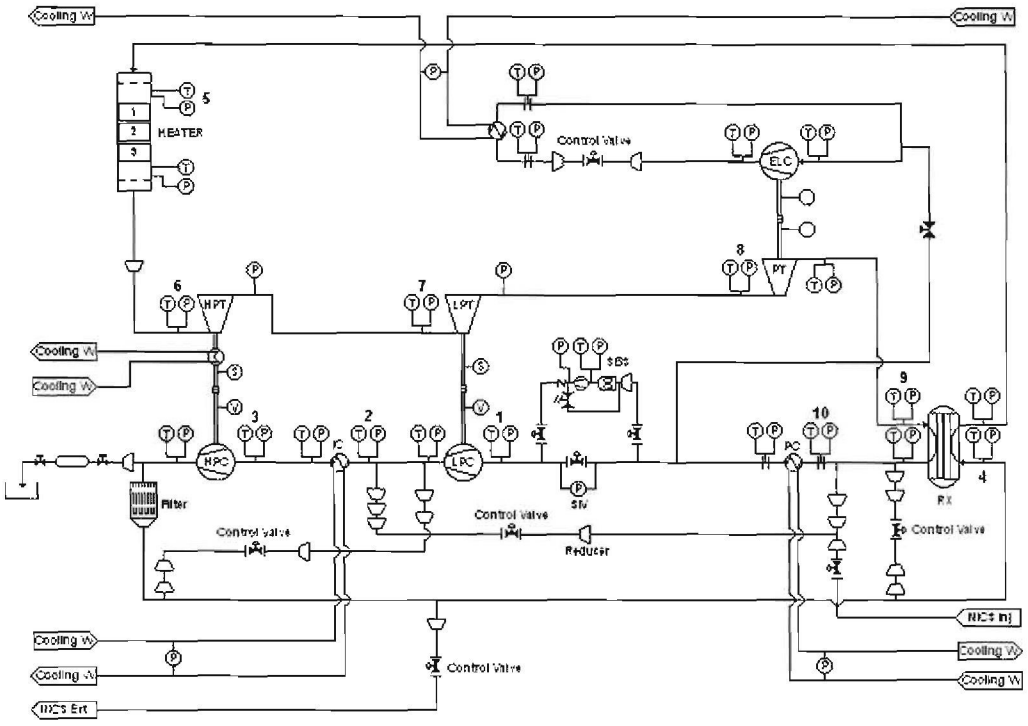

Fig. 7.2.4 Simplified schematic showing the PBMM three-shaft MPS.

- The working fluid of the PBMM is nitrogen instead of helium. The main reason for this is the use of turbochargers that are used in internal combustion engines with air as the working fluid. Nitrogen has basically the same thermo-physical properties as air but contains no oxygen (flammable and corrosive).

- The external load in the PBMM is emulated by a compressor (ELC) and a power dissipation loop which consists of an external load cooler.

- The compressors are single stage centrifugal compressors rather than the multi-stage axial flow turbo machines. The performance characteristics of centrifugal and axial flow machines are essentially the same within the system with reference to pressure ratio and isentropic efficiency versus non-dimensional mass flow.

Similar to the PBMR, the primary method of power control is achieved by injecting or extracting nitrogen inventory from the cycle. This process is slow and faster load changes are accommodated by using the bypass valves. The solid model of the PBMM is shown in figure 7.2.5 which demonstrates the basic layout of the plant.

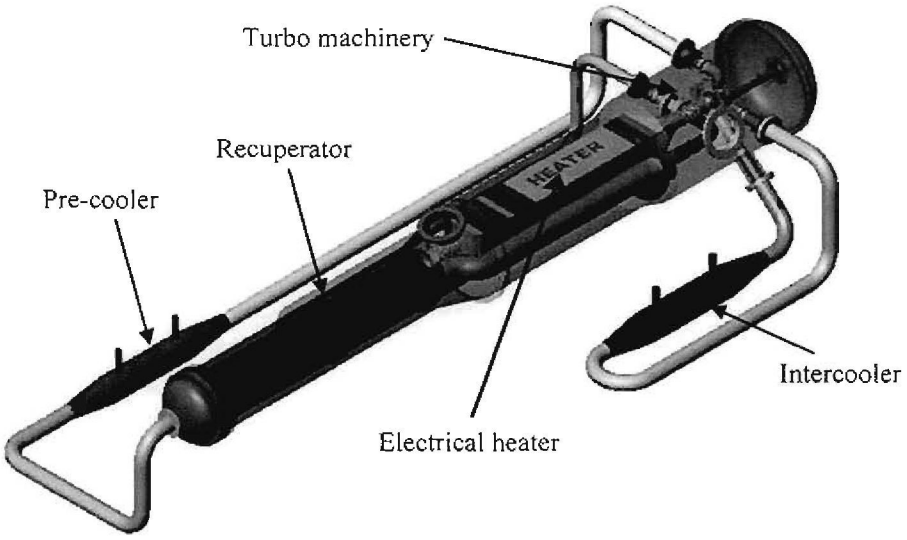

Fig. 7.2.5 Solid model of the PBMM [67].

7.3 Modelling the PBMM plant in Flownex

The steady state operating point of the PBMM plant is dependent on various controlled variables, making each operating point different. The variables are the heater outlet temperature, the suction pressure of the LPC, the valve position in the external power dissipation loop, position of the compressor bypass valves and the cooling water flow rate through each cooler. The cooling water temperature is not a controlled variable as it varies with ambient conditions and has to be measured.

Two steady state conditions were tested against the PBMM data to validate the Flownex model. The schematic diagram of the Flownex model is shown in Fig. 7.3.1 and the plant configuration and equipment details are described in the PBMR micro model data pack [68]. During the two simulations, the LPC suction pressure is changed from 95 kPa to 115 kPa. The heater outlet temperature and other controlled variables are kept constant and are summarized in Table 7.3.1.

Parameter	Value
Heater outlet temperature (°C)	600
Suction pressure of LPC (kPa absolute)	95, 115
Cooling water flow rate through coolers (kg/s)	2.5
Cooling water temperature (°C)	13
Cooling water pressure (kPa)	350
Nitrogen purity (%)	100
ELC valve opening	Open
Compressor bypass valves	Closed

Table 7.3.1 PBMM steady state conditions.

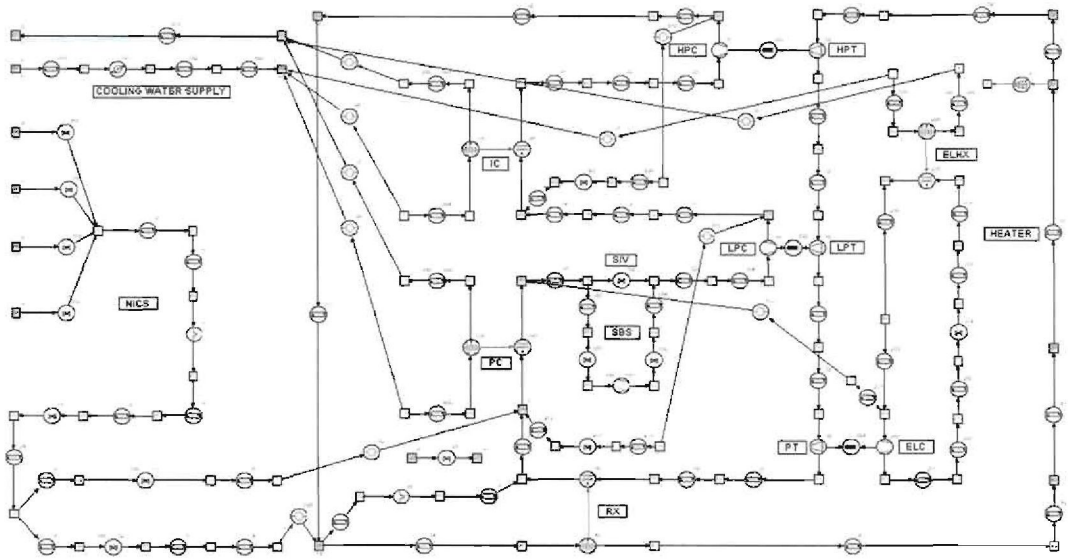

Fig. 7.3.1 Schematic diagram showing the PBMM Flownex model.

Table 7.3.2 lists the results of the measured PBMM data and the Flownex model calculations for the two steady state conditions. The values presented are for the measured nodes depicted in Fig. 7.2.4. The results show that there are considerable differences between the model and the PBMM data [67].

The temperature of the HP gas leaving the HPC is increased by more than 40 °C as a result of gas passing through the pressure vessel which houses the heater and the turbo machinery (Fig. 7.2.5). The increased temperature is believed to come from the heater and the metallic support structure of the turbo machinery.

Component	Temperature (°C)		Pressure (kPa) - 95		Temperature (°C)		Pressure (kPa) – 115	
	PBMM	FLNX	PBMM	FLNX	PBMM	FLNX	PBMM	FLNX
LPC inlet	21.5	15.0	94.1	93.4	24.7	15.2	114.1	113.1
IC inlet	80.7	78.8	147.9	160.7	84.2	79.1	179.2	194.7
HPC inlet	17.4	14.6	148.4	160.2	20.9	14.9	179.4	194.1
RX inlet (HP)	126.7	79.9	255.0	280.1	129.5	80.2	306.6	339.0
Heater inlet	399.2	399.2	254.2	278.5	349.8	394.5	305.8	337.3
HPT inlet	586.0	600.0	252.0	278.1	604.4	600.0	302.7	336.8
LPT inlet	511.8	540.1	171.3	187.5	510.4	540.1	205.9	227.1
PT inlet	433.0	480.5	111.8	123.1	436.9	480.4	132.7	148.9
RX inlet (LP)	400.2	447.7	91.4	95.7	402.0	447.5	112.0	115.8
PC inlet	164.3	130.9	96.6	95.0	172.3	135.9	116.7	115.0
Difference (%)	1.65		8		1.93		8.53	

Table 7.3.2 Steady state values for the two operating points.

Also, the HPC pressure is higher in the simulations than observed in the data. Given that the LPC suction pressure is set, this could be due to either leakage in the cycle or an over-estimation of the compressor performance in the simulations. If the HP manifold pressure is set in the simulations, the effect of the compressor performance would be less noticeable.

The results for the 95 kPa operating point of the PBMM are presented on the *h-s* graph in Fig. 7.3.2 (a). The figure confirms the discrepancies between the Flownex model and the data and shows that the increase in entropy across the turbines is larger than expected. To compensate for the temperature differences, the heat loss from the turbines, heater and the pressure vessel to the ambient are calculated from the PBMM data. Following this, additional heat transfer paths are incorporated in the Flownex simulation model and the heat transfer coefficients adjusted until satisfactory results are achieved.

The heat transfer paths are modelled from measured data seeing as the heat losses occur from undefined, complex geometries [67]. Table 7.3.3 summarizes the results of the Flownex simulation with the additional heat transfer paths. The results indicate that the correlation between the Flownex model and the PBMM data is acceptable with an absolute difference of less than 0.6 %. The results are illustrated on an *h-s* graph and are shown in Fig. 7.3.2 (b). The figure illustrates that the correlation between the improved Flownex model and the PBMM plant data is good. The model is now used to simulate the appropriate operating points in the PBMM data.

7.4 The PBMM data used for fault emulation

This section describes the PBMM plant data used to emulate the fault conditions. Thus far, several successful steady state and transient runs have been completed on the PBMM plant. Due to the high costs of components and the unsafe operating conditions that may occur from directly inducing faults in the system, only experimental data from previous test runs is used for the emulation of faults.

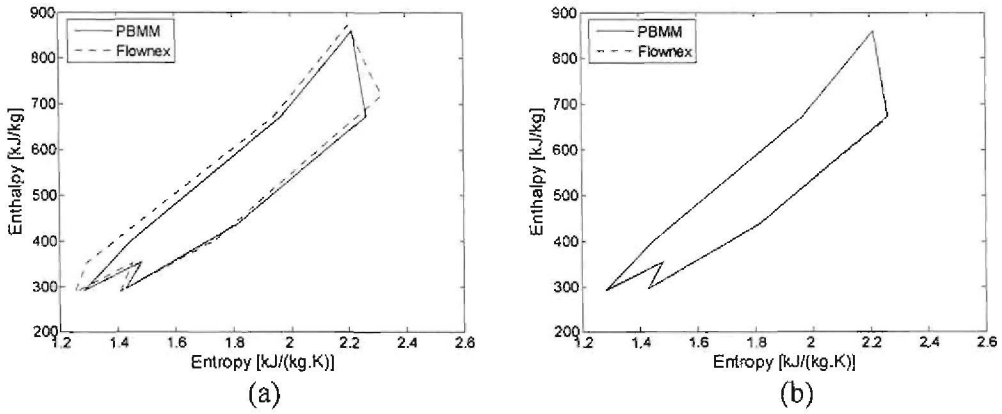

Fig. 7.3.2 The practical *h-s* graphs for the PBMM steady state simulation at 95 kPa: (a) heat losses; (b) additional heat transfer paths modelled.

Component	Temperature (°C)		Pressure (kPa) - 95		Temperature (°C)		Pressure (kPa) - 115	
	PBMM	FLNX	PBMM	FLNX	PBMM	FLNX	PBMM	FLNX
LPC inlet	21.5	21.6	94.1	94.0	24.7	24.6	114.1	114.0
IC inlet	80.7	80.8	147.9	148.1	84.2	83.3	179.2	178.9
HPC inlet	17.4	17.5	148.4	148.0	20.9	21.0	179.4	178.5
RX inlet (HP)	126.7	126.8	255.0	254.8	129.5	129.4	306.6	306.5
Heater inlet	399.2	399.4	254.2	254.0	349.8	349.5	305.8	305.9
HPT inlet	586.0	586.0	252.0	250.3	604.4	604.0	302.7	302.0
LPT inlet	511.8	515.5	171.3	168.2	510.4	514.2	205.9	201.1
PT inlet	433.0	436.4	111.8	109.7	436.9	439.5	132.7	130.5
RX inlet (LP)	400.2	398.8	91.4	90.2	402.0	400.4	112.0	110.9
PC inlet	164.3	164.5	96.6	96.7	172.3	172.9	116.7	116.9
Difference (%)	0.24		0.54		0.12		0.51	

Table 7.3.3 Results for the two operating points (additional heat transfer paths modelled).

Firstly, thrust tests are conducted on the PBMM to determine the thrust load on the turbo units (comprising the turbo/compressor and the turbine). These tests were conducted because of a bearing failure on the HP turbo that resulted in complete failure of the unit after only 60 hours of operation. As discussed, the turbochargers used are 'off-the-shelve' single stage centrifugal machines, generally used in an open cycle configuration on earth moving equipment. In this open cycle configuration, the differential pressure across the turbo unit is almost zero (inlet and outlet to atmospheric pressures), whilst it varies considerably in the closed cycle of the PBMM.

Two sets of data are used to emulate fault conditions in the PBMM. The first is data logged during the failure of the turbo unit and the second is data from a thrust test afterwards. During the thrust test, the heater outlet temperature and LPC suction pressure are increased from bootstrap conditions[7] to 650 °C and 115 kPa respectively which give the variation in thrust. These variations result in changing pressure ratios across the turbo units and are normally not favourable, since the cycle efficiency is a function of the overall pressure ratio of the system. During normal operation of the MPS, these changing pressure ratios can therefore be interpreted as possible component or process anomalies. The differential pressure across the turbo unit is given by (7.4.1)

$$\Delta p = \left(p_{in,turbine} - p_{out,turbine}\right) - \left(p_{out,compressor} - p_{in,compressor}\right) \tag{7.4.1}$$

With the net positive thrust direction from the turbine to the compressor, the thrust force on the turbo unit is calculated as

[7]During bootstrap conditions in the PBMM, the Brayton cycle becomes self-sustainable at approximately T_0 = 580 °C and P_0 = 95 kPa.

$$T_{TU} = -\pi/4 \begin{pmatrix} p_{i,c}\left(d_{1c}{}^2\right) - p_{o,c}\left(d_{2c}{}^2 - d_{3c}{}^2\right) - p_l\left(d_{3c}{}^2 - d_s{}^2\right) \\ +p_l\left(d_{3t}{}^2 - d_s{}^2\right) + p_{i,t}\left(d_{1t}{}^2 - d_{3t}{}^2\right) - p_{o,t}\left(d_{2t}{}^2\right) \end{pmatrix} \tag{7.4.2}$$

with subscripts c and t denoting the compressor and turbine; p_l the lubrication chamber pressure, d_s the shaft diameter, d_3 the shaft diameter at the c or t side, d_2 the c or t outlet diameter and d_1 the c or t inlet diameter. The differential pressures, thrust forces, pressure ratios, pressures, temperatures and vibration levels are illustrated for the turbo units in figures 7.4.1 and 7.4.2 respectively.

In dataset 1, samples 1 to 1510 is used with the failure of the HP turbo unit at approximately sample 1500. In dataset 2, samples 4030 to 5530 are used for the validation. In both datasets, nitrogen is injected or extracted and therefore comprises normal transient variations of the process.

In the first dataset, injection commences from samples 410 to 442, 459 to 499, 524 to 564 and 1131 to 1288, with intervals of approximately 40 samples. In the second dataset, extraction starts from samples 5100 to 5533. Now that the datasets and transient conditions are explained, the emulated fault conditions are described. In dataset 1, the

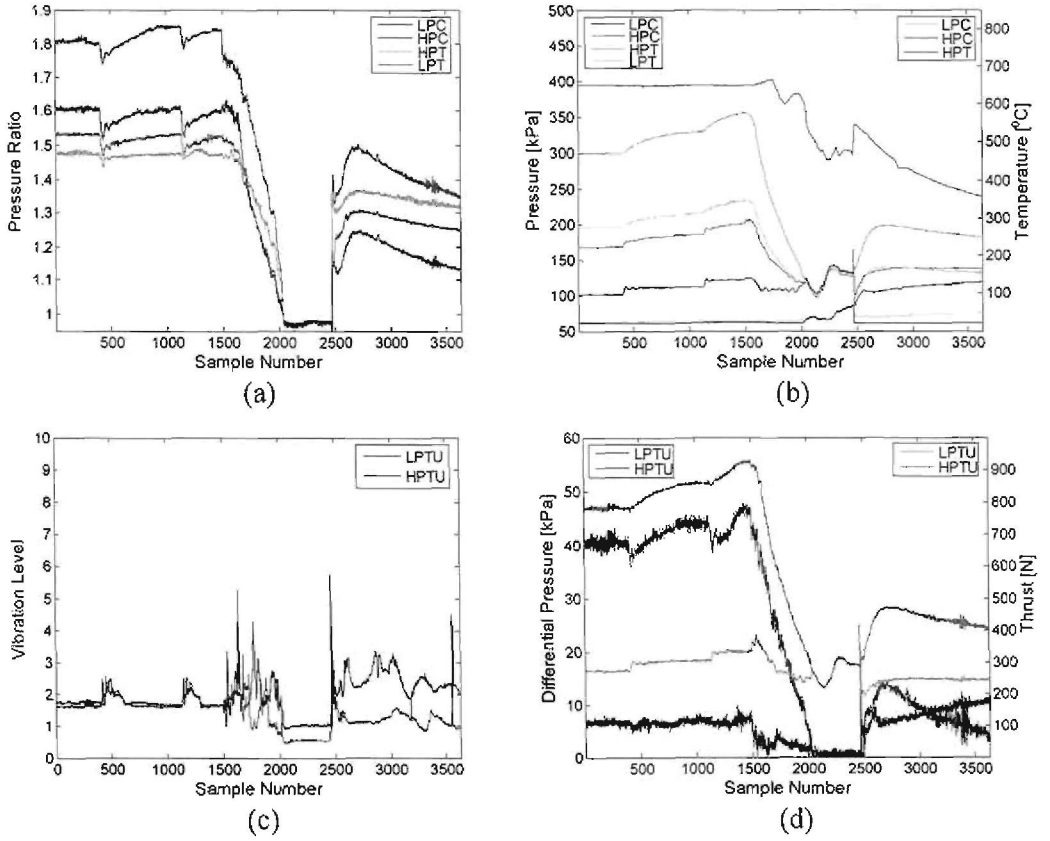

Fig. 7.4.1 Turbo machinery parameters for bearing failure: (a) pressure ratio; (b) pressures/temperatures; (c) vibration level; (d) differential pressure/thrust.

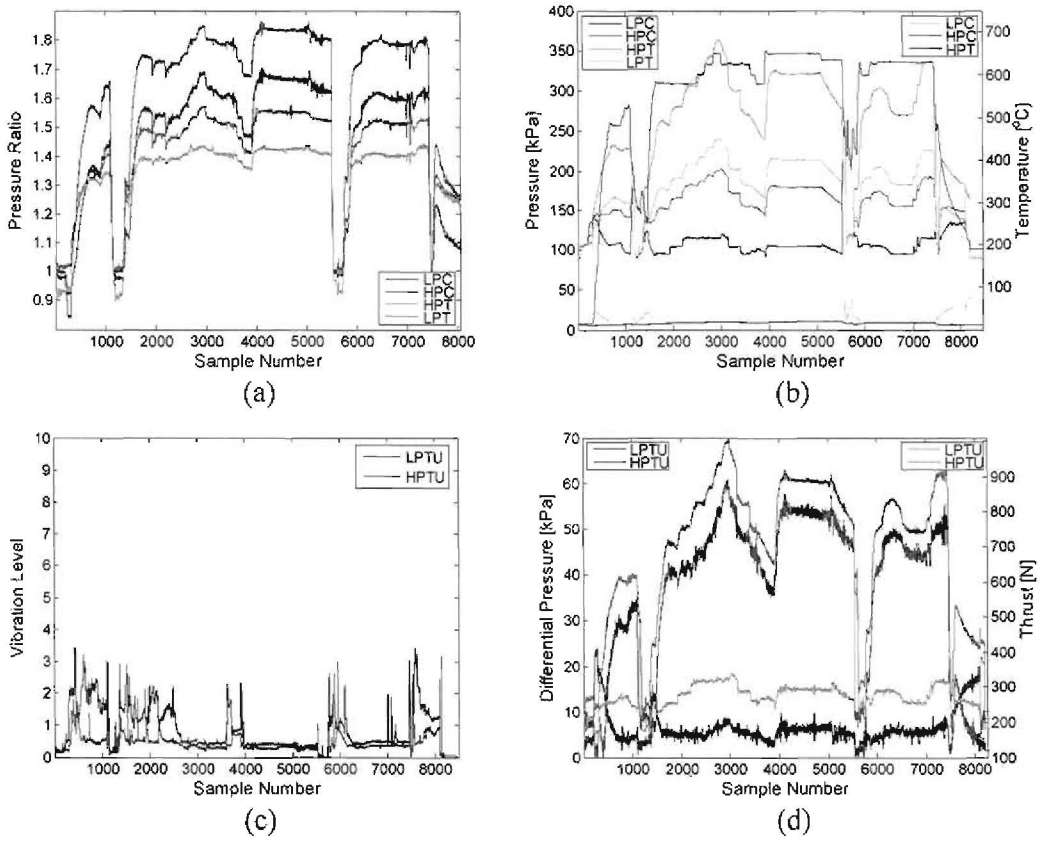

Fig. 7.4.2 Turbo machinery parameters for thrust test: (a) pressure ratio; (b) pressures/temperatures; (c) vibration level; (d) differential pressure/thrust.

pressure ratios of the turbos vary briefly during injection and settles for normal steady state operation. However, the HP compressor pressure ratio shows an increase during injection with a significant increase in thrust force when compared to the LP turbo unit. Also, the differential pressure of the LP turbo unit stays approximately constant, whilst the increase across the HP turbo unit is about 8 kPa. Conversely, Fig. 7.4.1 (c) shows that the vibration levels stay within normal operational limits. This makes analysis of the vibration level (magnitude) less effective to detect the pressure ratio fault in the specific component. A frequency analysis of the vibration level can however be more sensitive to the specific fault condition. The emulated fault condition is modelled as a single fault by means of an increase in the HP turbo pressure ratio starting from 0 % at sample 410 to a maximum of 2 % at sample 1000. The heater outlet temperature is kept constant at 650 °C during the transient.

As discussed, dataset 2 comprises only a section of the total thrust test. The dataset shows a decrease in the pressure ratios of the turbo units whilst the temperatures stay approximately constant. Figure 7.4.2 (b) shows that the HPT inlet temperature decreases following the steady state conditions. Therefore, the second emulated fault is modelled as a decrease in HPT inlet temperature which signifies a probable heater malfunction. It must be noted that during normal operating conditions, the heat source outlet temperature

is controlled and a decrease will be rectified accordingly. For the validation of the *h-s* graph approach, a decrease in temperature is simply used to emulate a change in normal operating conditions.

Similar to the first dataset, Fig. 7.4.2 (c) shows that the vibration levels are within operational limits during the transient. The emulated fault starts at sample 5080 and increases to 2 % at sample 5130. Since the extraction of nitrogen starts at sample 5100, the fault occurs during a transient variation and steady state operation of the process. After a 2 % change in the fault magnitude, the fault stays constant.

7.5 Simulation of the emulated faults in Flownex

The Flownex model described in section 7.3 is now applied to validate the steady state conditions prior to the emulated faults. This is done to validate the integrity of the model to simulate the correct fault signatures. Table 7.5.1 lists the plant parameters for the two steady state conditions during normal power operation of the MPS. The PBMM data are averaged for the periods of interest to minimize the effects of measurement noise. These parameters are used to simulate the corresponding operating points in Flownex. The results of the Flownex simulations are summarized in Table 7.5.2 and are illustrated on the *h-s* graph in Fig. 7.5.1. The table shows a good comparison between the PBMM data and the Flownex results, with a maximum difference of 0.11 %. The model can therefore be used to simulate the emulated fault conditions.

It is important to note that the operating point of the PBMM is dependent on two additional variables. Therefore, the reference model must incorporate the *VS* with n-dimensional interpolation. Since the valve openings and the cooling water flow rate is fixed for the periods of interest, the reference models are simply calculated for the actual operating conditions. To create the reference fault signatures, the model at 100 % MCR (115 kPa) is used.

In order to validate the effectiveness of the *h-s* graph approach, a reference fault database is created with additional fault signatures. The motivation for additional reference signatures is to demonstrate the ability of the method to reject the incorrect signatures. A total of six fault conditions comprising the two emulated and four additional faults are modelled in Flownex. The fault magnitudes are listed in Table 7.5.3 and the results of the Flownex simulations are summarized in Table 7.5.4.

Parameter	Dataset 1	Dataset 2
Heater outlet temperature (°C)	650	650
Suction pressure of LPC (kPa absolute)	101	105
Cooling water flow rate through coolers (kg/s)	PC = 2.5 IC = 2.5	PC = 2.02 IC = 1.68
Cooling water temperature (°C)	~19	~16
Cooling water pressure (kPa)	350	350
Nitrogen purity (%)	100	100
Compressor bypass valves	Closed	Closed

Table 7.5.1 Parameters for the two steady state simulations.

Component	Dataset 1				Dataset 2			
	Temperature (°C)		Pressure (kPa)		Temperature (°C)		Pressure (kPa)	
	PBMM	FLNX	PBMM	FLNX	PBMM	FLNX	PBMM	FLNX
LPC inlet	24.45	24.54	101.02	101.0	22.07	21.98	105.05	105.0
IC inlet	93.07	93.08	167.7	167.93	91.29	92.35	178.94	178.46
HPC inlet	21.20	21.23	167.9	167.4	18.63	18.68	178.37	177.89
RX inlet (HP)	138.48	138.57	303.35	303.19	136.62	136.44	325.5	325.28
Heater inlet	371.3	371.44	302.88	302.07	368.5	368.28	324.05	324.1
HPT inlet	649.97	650.0	301.53	301.78	650.07	650.0	322.92	323.79
LPT inlet	548.97	554.02	196.8	197.5	550.6	550.48	213.01	212.99
PT inlet	462.14	458.13	130.09	131.24	472.8	473.21	137.95	138.76
RX inlet (LP)	428.75	428.15	101.88	102.94	427.06	427.23	106.73	107.78
PC inlet	185.14	185.18	102.13	102.14	187.4	187.79	107.01	107.04
Difference (%)	0.03		0.11		0.05		0.08	

Table 7.5.2 Steady state results for the two PBMM datasets.

In order to create reference fault signatures, the error and area error methods are used. The normalized signatures of the six faults are shown in Fig. 7.5.2. The figure shows that the correlation between the different signatures is low, which indicates that the reference fault database of the PBMM is unique.

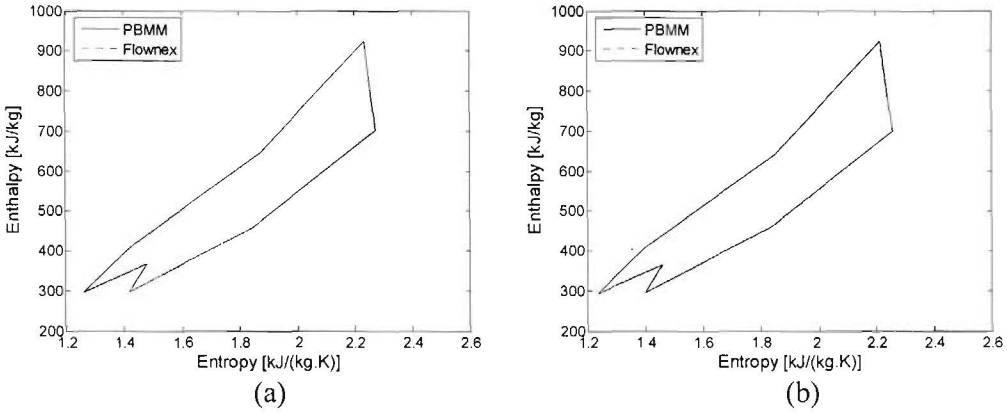

Fig. 7.5.1 The *h-s* graphs for the steady state PBMM datasets: (a) dataset 1; (b) dataset 2.

Fault	Direction	Normal	Limit (2 %)
1. HPC pressure ratio	Increase	1.0	1.1 (scaling factor)
2. Heater outlet temperature	Decrease	650 °C	635 °C
3. LPC pressure ratio	Decrease	1.0	0.9 (scaling factor)
4. HPT pressure ratio	Increase	1.0	1.1 (scaling factor)
5. Intercooler heat transfer area	Decrease	36.5 m^2	30 m^2
6. Recuperator heat transfer area	Decrease	257.3 m^2	250 m^2

Table 7.5.3 PBMM emulated fault conditions modelled in Flownex.

Node	Fault 1		Fault 2		Fault 3		Fault 4		Fault 5		Fault 6	
	T (°C)	P (kPa)	T (°C)	P (kPa)	T (°C)	P (kPa)	T (°C)	P (kPa)	T (°C)	P (kPa)	T (°C)	P (kPa)
1.	24.6	101.0	21.8	105.0	24.5	101.0	24.5	101.0	24.6	101.0	24.6	101.0
2.	92.9	167.7	88.0	172.5	94.5	171.3	92.2	166.7	92.8	167.5	93.1	167.9
3.	21.2	167.2	18.4	171.9	21.3	170.8	21.2	166.2	22.5	167.0	21.2	167.4
4.	138.6	302.3	135.5	308.9	138.3	310.6	140.5	312.7	139.1	301.4	138.6	303.2
5.	371.7	301.2	364.1	307.7	369.1	309.4	369.3	311.7	372.1	300.3	370.0	302.1
6.	650.0	300.9	635.0	307.4	650.0	309.1	650.0	311.4	650.0	300.0	650.0	301.8
7.	548.9	198.7	536.7	203.6	549.3	203.5	544.4	197.8	549.0	198.2	549.0	199.2
8.	472.9	131.2	463.0	135.4	472.1	133.0	469.2	130.9	473.1	131.1	472.8	131.4
9.	428.4	103.5	420.2	107.5	426.3	103.7	425.4	103.5	428.7	103.5	428.2	103.5
10.	185.1	102.8	184.8	106.9	185.8	102.9	184.5	102.8	185.0	102.8	186.7	102.8

Table 7.5.4 Flownex results for the six emulated fault conditions.

For each of the six faults, four reference fault signatures are created. As a result, the reference fault database comprises 24 single fault signatures. The database is now used together with the single fault FDI algorithm to classify any of the modelled fault conditions in the PBMM data.

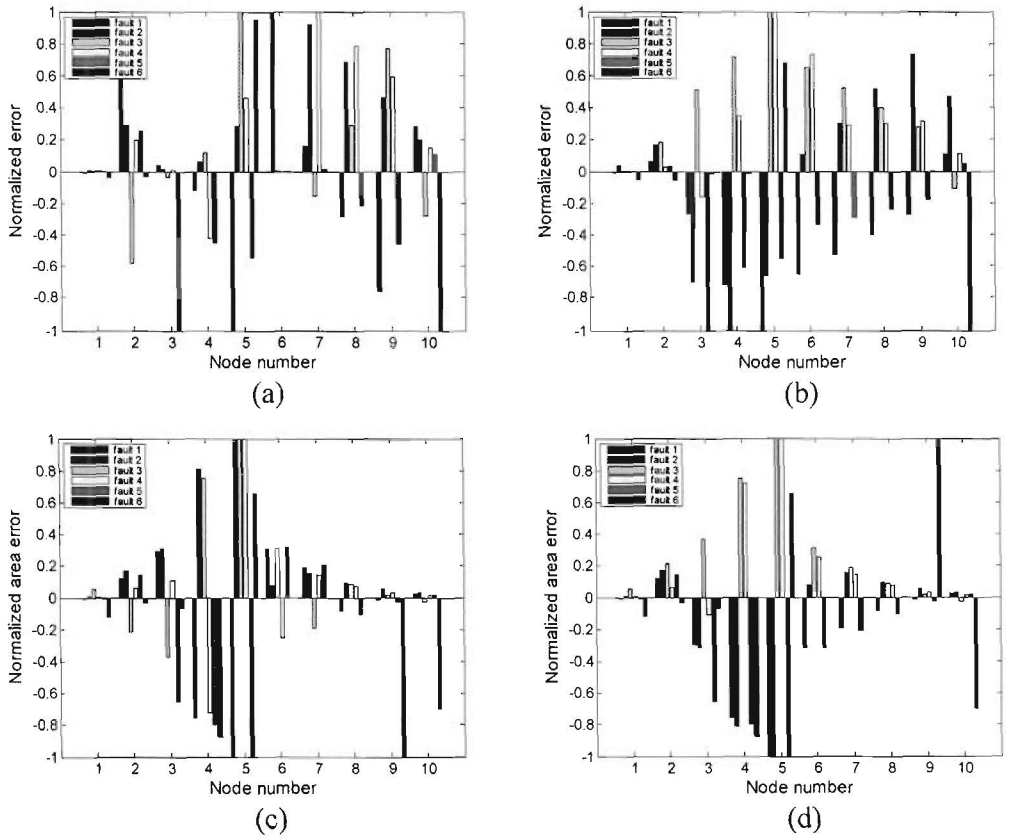

Fig. 7.5.2 Normalized fault signatures for the 6 PBMM faults: (a) *h* error; (b) *s* error; (c) *h* area error; (d) *s* area error.

7.6 Fault detection in the PBMM

The PBMM plant is similar to the PBMR subjected to random process and measurement noise as seen in figures 7.4.1 and 7.4.2. One of the reasons the measurement data is corrupted with noise is because no signal conditioning (sensor FDI) is implemented in the PBMM due to time and budget constraints. In the previous chapter, random noise with a normal distribution and zero mean is added to the Flownex data to emulate a normally distributed error vector for the fault detection algorithm. In a real application like the PBMM, these properties cannot be assumed and must be determined. Firstly, an analysis of the temperature and pressure measurements is done to determine the magnitude and the statistical properties of the noise, i.e. the distribution, μ and σ^2. The noise component of the PBMM measurements is determined by taking the residuals (average of the data minus the data) of the variables during the fault free steady state simulations.

To determine the distribution of the random noise component, a normal probability plot is used with a linear line joining the first and third quartiles of the data. This is done to evaluate the linearity of the data. The normal probability plots are shown in Fig. 7.6.1 for a temperature and pressure measurement of the PBMM. Both plots are linear, which means that the data can be approximated by a normal distribution (other distributions will introduce curvature in the plot). Table 7.6.1 lists the estimated statistical properties of the measurement noise for the PBMM data. The results show that the mean of the residuals are zero and the variance in temperature and pressure are very small.

The single fault FDI algorithm is now applied to classify the emulated faults in the data. The enthalpy and entropy residual vectors for the PBMM are given by

$$\mathbf{r}_h(t) = \left[r_h^1(t), r_h^2(t), ..., r_h^{10}(t) \right]^T \text{ and } \mathbf{r}_s(t) = \left[r_s^1(t), r_s^2(t), ..., r_s^{10}(t) \right]^T \qquad (7.6.1)$$

The missed alarm rate is selected as $\alpha = 0.01$, the *FII* limit for known reference signatures is chosen as 0.5, the sample time window comprises 10 samples, and the hypothesis thresholds for h and s are selected as 2.5 and 0.1 respectively.

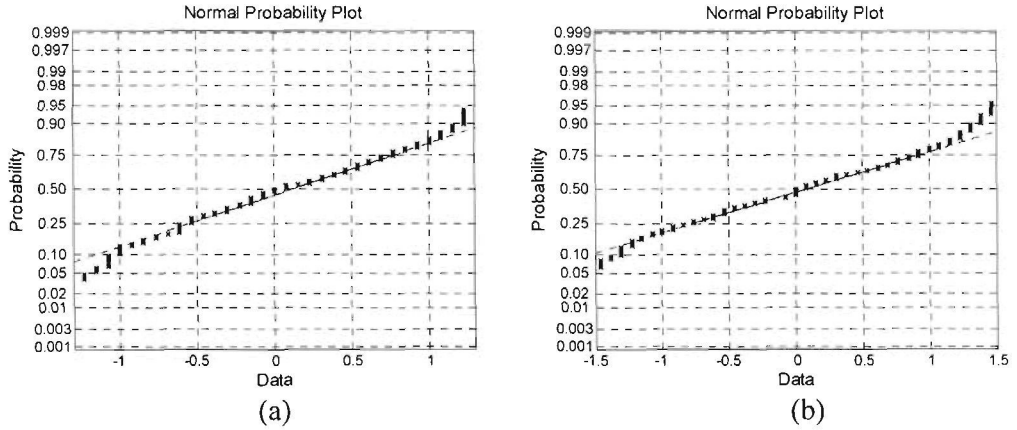

Fig. 7.6.1 Normal probability plots for measurements in the PBMM: (a) temperature; (b) pressure.

Statistic	Temperature (°C)	Pressure (kPa)
Mean (μ)	0	0
Variance (σ^2)	0.1988	0.1445
Max. deviation	2.9423	2.5729
Distribution	Normal	Normal

Table 7.6.1 Statistical properties of the PBMM measurement noise.

As discussed, the emulated faults start at approximately sample 410 in dataset 1 and at sample 1080 in dataset 2. In dataset 1, the H_{1h} and H_{1s} fault detection tests fired at the next sampling interval (sample 420). In dataset 2, H_{1h} fired at the next sampling interval (sample 1090) and H_{1s} fired at sample 1270. Table 7.6.2 summarizes the results of the fault detection in the two datasets. The table shows that during the steady state runs prior to the fault conditions, no false alarms are triggered. Also, after the introduction of the faults, no missed alarms are observed. The thresholds selected for the hypothesis tests are therefore sufficient to the limit the false alarm rate during normal noisy conditions and trigger the *h-s* graph method for fault isolation after fault detection. The fault isolation procedure is summarized as follows: firstly, the four fault signatures are created for each sample window and compared to the six reference fault signatures by calculating the *FII*. The *FII* is calculated for the error and area error methods and is determined for *h* and *s*. The results of the *FII* for the error and area error methods are shown in Fig. 7.6.2 and the average *FII* for each method is summarized in Table 7.6.3. In dataset 1 and 2, 109 and 41 sample windows are calculated respectively after fault detection.

Figure 7.6.2 (a) shows that the fault in dataset 1 is correctly isolated (*FII* decreases below unknown reference signature limit) after approximately 15 sample windows (570 samples). This is expected since the pressure ratio first showed a decrease (unknown signature) before increasing after 600 samples. Following sample window 72 (1140 samples), the pressure ratio decreases again before increasing to a maximum. The *FII* responded correctly by increasing beyond the unknown reference signature limit. In Fig. 7.6.2 (b), the fault in dataset 1 is correctly isolated with the area error method after only a few sample windows. Although the average *FII* is lower, the area error method responded slowly to the unknown signature at sample window 72 for the decrease in pressure ratio. The slow response of the *FII* can be attributed to the fact that the fault magnitude of the unknown signature is smaller than 1%.

Figure 7.6.2 (c) and (d) indicate that the fault in dataset 2 is correctly isolated with the error and area error methods. The figures show that the *FII* is below the known reference signature limit commencing at the first sample window after detection.

Action	Dataset 1		Dataset 2	
	Steady state (samples)	Fault (samples)	Steady state (samples)	Fault (samples)
False alarms	0	–	0	–
Fault detection	0	420	0	1090
Missed alarms	–	0	–	0

Table 7.6.2 Alarms during fault detection for the PBMM datasets.

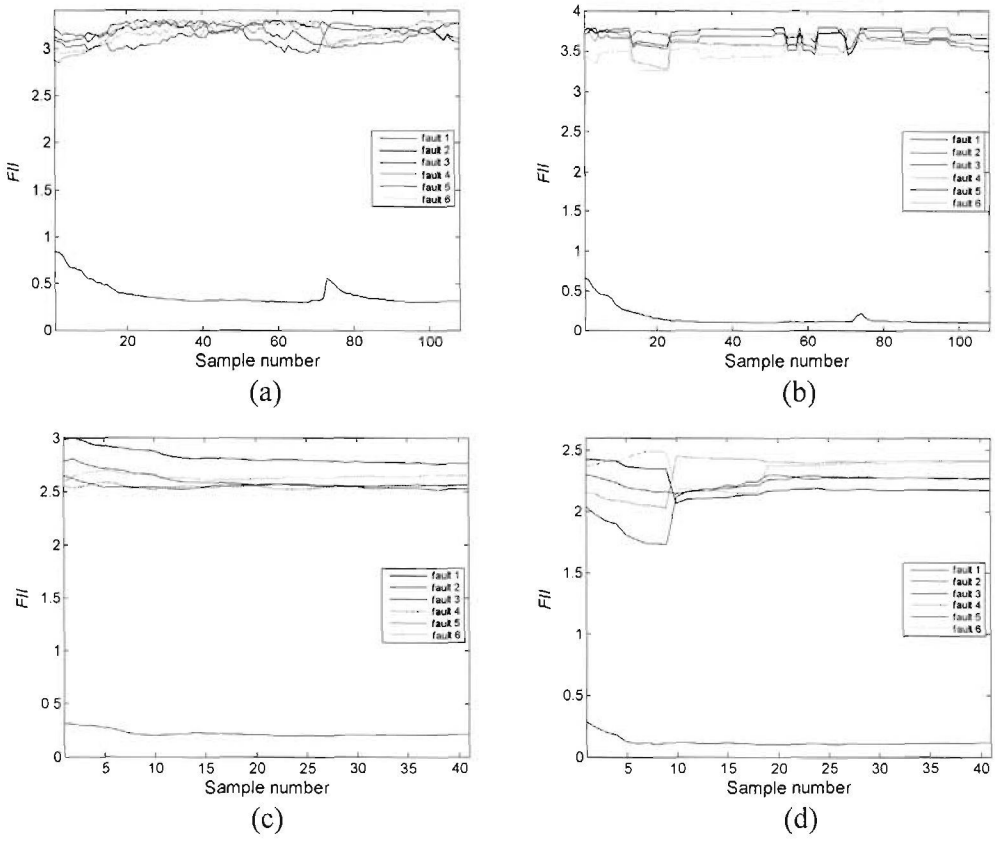

Fig. 7.6.2 *FII* for the emulated faults in the PBMM after fault detection: (a) dataset 1, error; (b) dataset 1, area error; (c) dataset 2, error; (d) dataset 2, area error.

Table 7.6.3 shows that on average, the *FII* is 0.218 for the isolated fault signatures and 2.925 for the rejection of the incorrect signatures. The results presented therefore indicate that the proposed *h-s* graph approach can be successfully applied to isolate known faults during normal plant operation. Similarly, as demonstrated for the PBMR, the reference fault database can be expanded to include all the probable system faults. This will minimize the probability of incorrect isolation.

7.7 The *T-P* and *h-s* models applied to the PBMM

In this section, data from the PBMM is used to show that the transformation of measurements can improve model performance in a practical application. Firstly, the

Average *FII*	Dataset 1		Dataset 2	
	Error	Area	Error	Area
Recognition	0.3791	0.1536	0.2201	0.1211
Rejection	3.1625	3.6434	2.6291	2.2635

Table 7.6.3 Average *FII* for the PBMM fault conditions after fault detection.

reference *T-P* and *h-s* graphs (without *VS*) are derived for the 100 % MCR (115 kPa) steady state data. Following this, the models are used to reconstruct the reference graphs for 40 % MCR (95 kPa). The plant data from the PBMM operating at 40 % MCR is used as reference instead of Flownex. The *T-P* and *h-s* graphs are illustrated in Fig. 7.7.1 for the two operating points and Table 7.7.1 summarizes the calculated values for 40 % MCR (turbines are monitored as one unit, i.e. only 8 nodes).

The table shows that the percentage difference for *P* is not as large as observed in the PBMR at reduced power (Appendix B). This is due to the fact that the pressure difference between full and reduced power is in the order of several MPa for the PBMR, whilst only a few kPa in the PBMM. The results listed indicate that the transformation of the measurements improves the error between the actual data and the model estimates by 0.25 % and 8.45 %. The modelling error of the reference *h-s* model is therefore sufficient to correctly estimate the values at different operating points (provided the temperatures and pressure ratios stay constant).

7.8 Summary and conclusions

This chapter focussed on the validation of the *h-s* graph approach by applying the method to real plant data from the prototype PBMM plant.

Firstly, section 7.2 describes the differences between the PBMR and the PBMM topologies. The PBMM, which is a scaled version of the three-shaft PBMR configuration, requires ten monitoring nodes to supervise all the main components in the MPS.

Section 7.3 discussed the development of a PBMM simulation model in Flownex. The results of the first Flownex model revealed a number of differences between the plant measurements and the model and it was concluded that the extra heat was gained from the heater and the metallic support structures in the pressure vessel. Additional constraints were imposed on the Flownex model and the final model showed satisfactory results.

In section 7.4, the noisy plant data is used to emulate two fault conditions. The main

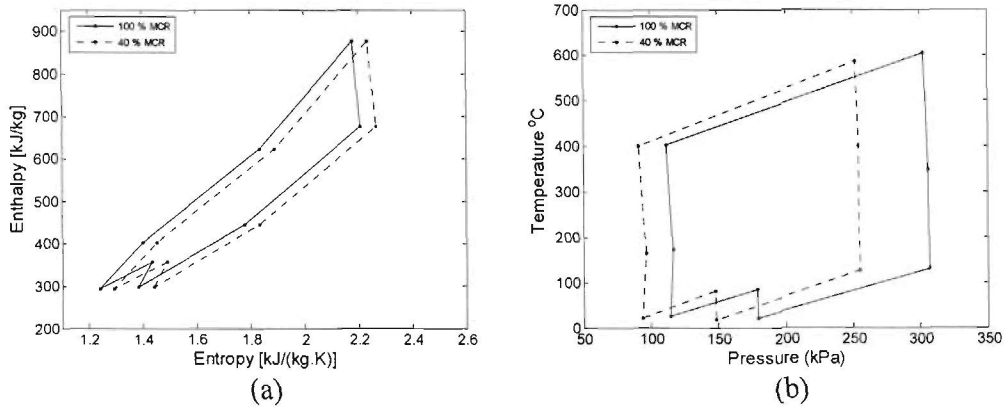

Fig. 7.7.1 Practical graphs of the Brayton cycle for full and reduced power (measured): (a) *h-s*; (b) *T-P*.

Node	*T*		*P*		*h*		*S*	
	Data	M	Data	M	Data	M	Data	M
1.	21.5	24.7	94.1	94.1	294.66	297.86	1.439	1.439
2.	80.7	84.2	147.9	158.9	353.86	357.36	1.489	1.491
3.	17.4	20.9	148.4	159.1	290.56	294.06	1.293	1.296
4.	126.7	129.5	255	286.3	399.86	402.66	1.452	1.455
5.	399.2	349.8	254.2	285.5	672.36	622.96	1.888	1.892
6.	586	604.4	252	282.4	859.16	877.56	2.234	2.237
7.	400.2	402	91.4	91.7	673.36	675.16	2.267	2.264
8.	164.3	172.3	96.6	96.4	437.46	445.46	1.834	1.836
Diff	0.45		8.56		0.20		0.09	

Table 7.7.1 Results for the reference models (PBMM operating at 40 % MCR).

reason faults are not directly induced in the system is because of possible system damage and unsafe operating conditions.

To validate the selected fault conditions, the faults are simulated in Flownex and compared with the emulated data in section 7.5. The results confirmed that Flownex can accurately model the thermodynamic system.

Section 7.6 described the fault detection and isolation procedure with the *h-s* graph approach. By applying the proposed method, the emulated fault conditions are quickly detected and correctly isolated.

Lastly, section 7.7 presented a comparison between the *T-P* and *h-s* reference models at reduced power levels. The results indicated that even though the operating range of the PBMM plant is much smaller compared to the PBMR, the transformation of measurements improves model performance considerably.

The following are some of the important conclusions reached in this chapter:

- The *h-s* graph approach is only dependent on the thermodynamic cycle being represented on an *h-s* graph. The type of and number of components do not affect the effectiveness of the method (PBMM comprises ten nodes with an electrical heater as heat source).

- The *h-s* graph approach can be implemented in a real nonlinear dynamic system comprising noisy measurements.

- The implementation of the *h-s* graph approach is not dependent on a linear transformation, state space representation or transfer function describing the complex nonlinear system. Furthermore, given the many unknown factors in the PBMM, this will undoubtedly be a complex task.

- Since the *h-s* graph comprises a closed cycle, the effects of fault propagation are incorporated in the reference fault signatures.

CHAPTER 8

Conclusions and recommendations

This chapter summarizes the conclusions drawn in the thesis and documents the original contributions of the study. Recommendations and suggestions for future research are also presented.

8.1 Introduction

As discussed in Chapter 1, the main concern of the thesis is to develop a novel approach to fault diagnosis in a nonlinear dynamic HTGR NPP.

Chapter 2 surveyed advanced techniques for sensor and process fault diagnosis. Redundant and non-redundant techniques for sensor fault diagnosis were evaluated together with process history-and model-based methods for process fault diagnosis.

Chapter 3 discussed the general topology of the PBMR MPS. From this chapter onwards, the PBMR was used as the reference HTGR NPP. In the second part of Chapter 3, the probable fault symptoms of the PBMR MPS were derived.

The sensor fault diagnosis methodology was developed in Chapter 4. The integrated reasoning architecture was presented and the sensor validation and fusion module, SENSE was proposed.

Application of traditional process FDI techniques was the topic of Chapter 5. Process supervision with limit value checking was presented and linear mathematical modelling of a power turbine was demonstrated. Based on the criterion for an advanced fault diagnosis technique, their limitations did not favour them for implementation in the PBMR.

The *h-s* graph approach for process fault diagnosis was derived in Chapter 6. The method uses the *h-s* graph as a reference model to describe the health of the system. Based on residuals between the graph and plant observations, fault signatures are generated for fault pattern recognition. For the case of multiple fault symptoms, a single signature subtraction procedure was proposed.

The validation of the *h-s* graph approach for process fault diagnosis was presented in Chapter 7 by means of an application to real plant data from the prototype PBMM.

The following sections summarize the conclusions drawn from this study.

8.2 Conclusions

The conclusions presented are grouped according to the following thesis objectives:

1. *Determine the most relevant mechanisms for component degradation in an HTGR MPS and formulate suitable fault classes.*

2. *Develop* a novel integrated architecture for sensor fault diagnosis in *an HTGR MPS.*

3. Develop a novel approach for process fault diagnosis *in an HTGR MPS.*

4. *Validate the proposed process fault diagnosis approach through an application in the PBMM.*

8.2.1 Component degradation and suitable fault classes

During the lifespan of any engineering system, faults are unavoidable factors that degrade system performance. Firstly, a sensitivity analysis was conducted to determine the parameters that influence the performance of the MPS. Direct relations between these parameters and known fault symptoms (caused by the degradation mechanisms) were then derived.

Concerning the parameters that result in degraded component behaviour, it is concluded that three universal types of parameter changes result in MPS underperformance. The parameters are grouped into three fault classes and comprise the resistance in fluid flow, leakages between components and efficiency changes in components.

In addition, it was observed from the sensitivity analyses that for some faults, a small parameter change reflected only as a marginal change in system performance. Therefore, the conclusion was drawn that incipient behaviour of these faults would be very difficult to detect and supported the motivation for the development of an advanced process fault diagnosis approach.

8.2.2 Sensor fault diagnosis

One of the main concerns is the detection of common mode failure (drift in the same direction at the same rate) among a set of redundant measurements. Although this phenomenon is extremely uncommon with only a few occurrences over several decades [16], the sensor fault diagnosis system must provide for these situations. Techniques based on consistency checks will surely fail in this case. To provide for common mode failure of one group of redundant measurements, the PCA technique is adopted into the sensor fault diagnosis methodology. The challenge however is to determine which sensor configuration will deliver a valid estimate for the faulty variables. The following are concluded about the proposed integrated architecture:

- The intelligent search algorithm provides the PCA model with the most likely healthy (m-1 sensors) sensor configurations. However, if more than one input is corrupted in a configuration, it cannot produce a valid estimate.

- The PCA technique can model most of the nonlinear process behaviour if the process dynamics are relatively slow, as for an HTGR NPP. This was verified experimentally on PBMR and PBMM data. The obvious question now is, "Why don't we use the same PCA model for process fault diagnosis?" The reason is: PCA fault isolation is based on one faulty variable in a group of correlated signals (faults occur independently in each sensor), whilst in the process, faults are reflected in many variables simultaneously, therefore, isolation would be impossible.

- Since the sensor residuals are calculated for each sensor independently, multiple simultaneous failures can be detected. Therefore, this integrated architecture will be capable of detecting common mode failure among a group of redundant sensors.

- The proposed approach produces a better fused estimate for the sensed variable than any single sensor.

- One of the motivations for the proposed integrated architecture is that it can be implemented independent of the mathematical structure of the process.

- The results obtained and documented in the thesis show that the objective regarding detection of instrument drift was realized. The data utilized in the first case study was representative of a real process, which served as validation for the proposed approach.

8.2.3 Process fault diagnosis

In Chapter 1, the desirable qualities for an advanced process fault diagnosis approach are listed. With these objectives in mind, this thesis demonstrated the *h-s* graph approach for process fault detection and isolation in an HTGR NPP. The following conclusions were drawn regarding this graphical model-based approach (based on normal power operation):

- The overall health of the system can be quantified with a minimal amount of measured variables.

- The mathematical structure of the process is not a requirement for the development of the reference plant model.

- Faults in the system can be characterized by distinctive deviations in the shape of the *h-s* graph.

- Since the temperature and pressure ratios remain relatively constant over the operating region, the process can be described with only one reference *h-s* graph (no GBPC operation). This, however, is not the case for the temperature and pressure graph.

- Normalized static fault signatures can be extracted from the *h-s* graph with the error and area error methods that are representative of a dynamic fault condition.

- The normalized *h-s* fault signatures stay relatively constant with negligible variation for: changes in the fault magnitude, changes in the operating point and transient variations (injection, extraction and valve operation) of the normal process. Therefore, a fault condition can be characterized at any operating point with only one reference fault signature.

- The results obtained showed that the proposed single fault extraction method can successfully isolate the contributing single faults by sequentially subtracting reference fault signatures.

- During multiple fault symptoms, the contributing single faults appear to superimpose on each other.

- Normal plant ageing is incorporated into the graph with an n-dimensional variation surface. It is concluded from the obtained results that the error surface needs minimal training data to make a meaningful interpolation. The variation surface is trained for new conditions (typically after plant inspection or maintenance) when the conditions are deemed normal.

- If an accurate simulation model of the process is not available, the reference *h-s* graph can be developed with real data from the process. This will inherently reduce the modelling error between the model and the process.

The desirable qualities listed in objective 2 of this thesis are realized to a certain degree with the *h-s* graph approach for process fault diagnosis. The following are concluded about the qualities listed:

- Fault propagation is inherently accommodated in the reference fault signatures since the cycle is closed. Faults take approximately 5 seconds to propagate throughout the system.

- Noise magnitude influences the isolation ability of the approach. However, the approach performed well on the PBMM data which comprised process and measurement noise.

- Modelling errors between the simulation model and the plant influence the isolation ability of the approach to some extent. This conclusion is based on the results

obtained from the verification procedure in Chapter 7 (modelling uncertainties between the plant data and the Flownex model were discussed).

- Model development and re-training are rather simplistic. Model development requires only steady state data for one operating point subject to no valve operation. Furthermore, the model is re-trained by adding the new operating point to the variation surface.

- The simulations showed that a small change in the fault magnitude (i.e. 1 %) produced signatures that are highly correlated. Therefore, the fault symptoms can be characterized by single reference signatures.

- This thesis demonstrated that the *h-s* graph approach can be applied during transient variations of the normal process.

- Isolation of multiple fault symptoms was achieved by devising a single fault extraction procedure. It is demonstrated in this study that the contributing single faults can be isolated.

8.2.4 Validation of the process fault diagnosis approach

This objective was achieved by application of the proposed *h-s* graph approach to real noisy plant data from the PBMM. The validation was realized experimentally by emulated fault symptoms in two datasets. The following conclusions were drawn regarding the validation process in the PBMM:

- The approach is not dependent on the number of nodes (components) represented on the *h-s* graph. It was demonstrated that a reference model and fault signatures could be developed for a thermodynamic system with additional components (PBMM plant comprises three turbines).

- The tasks of process fault detection and isolation were achieved without deriving a mathematical model of the plant.

8.3 Original contributions

The original scientific contributions of the thesis in order of significance are as follows:

- The application of the *h-s* graph to visualize heat and work transfer in a closed-or open cycle thermodynamic system is not new. However, applying the *h-s* graph in a new way for the tasks of fault detection and isolation in an HTGR NPP is an original idea. Power control by means of an inventory control system facilitates a graphical *h-s* reference model that remains invariant over the power range (proved). Consequently, the devised error and area error methods provide static reference *h-s* fault signatures that remain invariant to operating point changes, transient variations of the normal process and changes in the fault magnitude.

- Techniques like the non-temporal parity space algorithm, principle component analysis, data fusion with confidence estimation and statistical analyses are not new. The contribution of the thesis lies in the integration of these ideas to form a new comprehensive methodology to sensor fault diagnosis. Individually, these techniques were proven to be unsuccessful for fault diagnosis in some situations. By combining their strengths in an integrated architecture, an advanced sensor fault diagnosis approach is realized that enables reliable and accurate estimates of the sensed variables.

8.4 Recommendations for future research

Although there are still many factors to consider before real life implementation, the study forms a basis for a new approach to process fault diagnosis in an HTGR NPP. The following areas warrant further research:

- The *h-s* graph approach needs to undergo a full Monte Carlo analysis to fully comprehend the influence of noise and modelling uncertainty on the detection and isolation abilities of the graph. Both these factors were investigated to some extent, but not simulated for every possible operating point change or fault magnitude variation.

- In the thesis, the constant reference fault signatures for different variations of the normal process were experimentally verified. A formal analytical prove for the universal applicability of the method over the entire operating range needs to be done. This will prove that the reference fault signatures are static provided that the correct reference model is utilized at the operating point.

- The devised error and area error fault signature generation methods need to be compared. Although both methods provided uncorrelated fault signatures for the given fault conditions, the possibility of combining these signatures to improve fault isolation needs to be investigated.

- The investigated fault symptoms need to be extended to cover a wider range of system malfunctions. The critical faults discussed in Chapter 3 could be accommodated into the reference fault database.

- Given the previous recommendation, the method needs to be extended for supervision during mode and state transitions of the plant. In addition, the fault diagnosis system would be a valuable asset during plant start-up.

- In the thesis, the *h-s* graph approach uses reference plant data to determine the correct position of the reference model. A more intelligent method must be devised to position the reference graph in the *h-s* plane for different operating point variations.

- The applicability of the proposed approach needs to be investigated for other thermodynamic systems comprising open-or closed cycles.

Bibliography

[1] J. Reifman, "Survey of artificial intelligence methods for detection and identification of component fault in nuclear power plants", Nuclear Technology, vol. 119, 1997, pp. 76-97.

[2] J. R. Patton, P. M. Frank, R. N. Clark, "Issues of fault diagnosis for dynamic systems: Introduction", New York: Springer-Verlag, 2000, pp. 1-13.

[3] K. Wang, "Intelligent condition monitoring and diagnosis systems: A computational intelligence approach", Frontiers in artificial intelligence and applications, vol. 93, IOS Press, Amsterdam, 2003.

[4] J. Prock, "On-line detection and diagnosis of sensor and process faults in nuclear power plants", in: J. R. Patton, P. M. Frank, R. N. Clark, Issues of fault diagnosis for dynamic systems, New York: Springer-Verlag, 2000, pp. 339-377.

[5] B. W. Johnson, "Design and analysis of fault tolerant digital systems", Addison-Wesley publishing co., 1989.

[6] J. J. Gertler, "Fault detection and diagnosis in engineering systems", New York: Marcel Dekker, 1998.

[7] R. Isermann, "Integration of fault detection and diagnosis methods", in J. R. Patton, P. M. Frank, R. N. Clark, Issues of fault diagnosis for dynamic systems, New York: Springer-Verlag, 2000, pp. 15-41.

[8] N. Kaistha, B. R. Upadhyaya, "Incipient fault detection and isolation of field devices in nuclear power plant systems using principal component analysis", Nuclear Technology, vol. 136 no. 2, 2001, pp. 221-230.

[9] B.R. Upadhyaya, K. Zhao, B. Lu, "Fault monitoring of nuclear power plant sensors and field devices", Progress in nuclear energy, vol. 43 no. 1-4, 2003, pp. 337-342.

[10] R. Dunia, J. Qin, T. F. Edgar, T. J. McAvoy, "Sensor fault identification and reconstruction using principal component analysis," Proceedings of the 13th IFAC world congress, vol. N, 1996, pp. 259.

[11] X. Xu, J. W. Hines, "Sensor validation and fault detection using neural networks", Proc. MARCON 99, vol. 2, May 1999.

[12] S. J. Qin, W. Li, "Detection, identification and reconstruction of faulty sensors with maximized sensitivity", AIChE Journal, vol 45 (9), 1999.

[13] B. R. Upadhyaya, E. Eryurek, "Application of neural networks for sensor validation and plant monitoring", Nuclear Technology, vol. 97, 1992, pp. 170-176.

[14] S. Simani, C. Fantuzzi, S. Beghelli, "Improved observer for sensor fault diagnosis of a power plant", Proceedings of the 7th Mediterranean conference on control and automation (MED99), Haifa, Israel, June 1999.

[15] J. W. Hines, D. J. Wrest, "Signal validation using an adaptive neural fuzzy inference system", Nuclear Technology, 1997, pp. 181-193.

[16] J. W. Hines, R. Seibert, "Technical review of on-line monitoring techniques for performance assessment", NUREG/CR-6895 vol. 1, U.S. Nuclear Regulatory Commission, Washington D.C., January 2006.

[17] Hyvarinen, J. Karhunen, E. Oja, "Independent component analysis", New York: John Wiley and Sons, 2001.

[18] Rasmussen, J. W. Hines, R. E. Uhrig, "A novel approach to process modeling for instrument surveillance and calibration verification", Proc Third American nuclear society international topical meeting on nuclear plant instrumentation, control and human-machine interface technologies, Washington, D.C., November 2000.

[19] Rasmussen, J. W. Hines, R. E. Uhrig, "Nonlinear partial least squares modeling for instrument surveillance and calibration verification", Proc. Maintenance and reliability conference (MARCON 2000), Knoxville, TN, May 2000.

[20] P. Geldi, B. Kowalski, "Partial least squares regression: A tutorial", Analytica Chemica Acta, vol. 185, 1986, pp. 1-17.

[21] C. L. Black, R. E. Uhrig, J. W. Hines, "System modeling and instrument calibration verification with a non-linear state estimation technique", Proc. Maintenance and reliability conference (MARCON 98), Knoxville, TN, May 1998.

[22] J. W. Hines, A. Usynin, "MSET performance optimization through regularization", Nuclear engineering and technology, vol. 3 no. 2, April 2005.

[23] J. W. Hines, R. E. Uhrig, "Use of auto associative neural networks for signal validation", Journal of intelligent and robotic systems, Kluwer Academic Press, 1998, pp.143-154.

[24] D. L. Mattern, L. C. Jaw, T. Guo, R. Graham, W. McCoy, "Using neural networks for sensor validation", 34th Joint propulsion conference, AIAA, Cleveland, Ohio, July,1998.

[25] NRC Project No. 669, "Safety evaluation by the office of nuclear reactor regulation: Application of on-line performance monitoring to extend calibration intervals of instrument channel calibrations required by the technical specifications - EPRI Topical Report (TR) 104965 On-Line Monitoring of Instrument Channel Performance", U.S. Nuclear Regulatory Commission: Washington, D.C., July, 2000.

[26] J. W. Hines, E. Davis, "Lessons learned from the U.S. nuclear power plant on-line monitoring programs", Progress in Nuclear Energy for a special issue on Lessons Learned from Computational Intelligence in Nuclear Applications, Elsevier, 2005.

[27] R. H. Dieck, "Measurement Uncertainty: Methods and Applications", 3rd ed., The instrumentation, systems and automation society, 2002.

[28] J. W. Hines, D. Garvey, R. Seibert, "On-line sensor calibration monitoring challenges and effective Monte Carlo based uncertainty estimation", Topical meeting on nuclear plant instrumentation, controls and human-machine interface technologies, Columbus, OH, September, 2004.

[29] J. Ding, A. V. Gribok, J. W. Hines, B. Rasmussen, "Redundant sensor calibration monitoring using independent component analysis and principal component analysis", Real-time systems, vol. 27 no.1, May 2004.

[30] J. E. Potter, M. C. Suman, "Thresholdless redundancy management with arrays of skewed instruments", Integrity in electronic flight control systems, AGARDOGRAPH, vol. 224, 1977, pp. 15-1 to 15-25.

[31] J. M. Renders, A. Goosens, F. de Viron, M. De Vlaminck, "A prototype neural network to perform early warning in nuclear power plant", Fuzzy sets and systems, vol. 74, 1995, pp. 139-151.

[32] K. Mo, S. J. Lee, P. H. Seong, "A dynamic neural network aggregation model for transient diagnosis in nuclear power plants", Progress in nuclear energy, vol. 49, 2007, pp. 262-272.

[33] K. Nabeshima, T. Suzudo, S. Seker, E. Ayaz, B. Barutcu, E. Torkcan, T. Ohno, K. Kudo, "On-line neuro-expert monitoring system for Borssele nuclear power plant", Progress in nuclear energy, vol. 43 no. 1-4, 2003, pp. 397-404.

[34] Shahla Keyvan, "Traditional signal pattern recognition versus artificial neural networks for nuclear plant diagnostics", Progress in nuclear energy, vol. 39 no. I, 2001, pp. l-29.

[35] E. Zio, G. Gola, "Neuro-fuzzy pattern classification for fault diagnosis in nuclear components", Annals of nuclear energy, Article in press, 2006.

[36] K. Zhao, B. R. Upadhyaya, "Adaptive fuzzy inference causal graph approach to fault detection and isolation of field devices in nuclear power plants", Progress in nuclear energy, vol. 46 no. 3-4, 2005, pp. 226-240.

[37] B. Lu, B. R. Upadhyaya, "Monitoring and fault diagnosis of the steam generator system of a nuclear power plant using data-driven modeling and residual space analysis", Annals of nuclear energy, vol. 32, March 2005, pp. 897-912.

[38] M. Claudio, S. Rocco, E. Zio, "A support vector machine integrated system for the classification of operation anomalies in nuclear components and systems", Reliability engineering and system safety, vol. 92, 2007, pp. 593-600.

[39] C. Guimarães, D. C. Cabral, C. M. Lapa, "Adaptive fuzzy system for degradation study in nuclear power plants' passive components", Progress in nuclear energy, vol. 48, 2006, pp.655-663.

[40] V. Venkatasubramanian, R. Rengaswamy, K. Yin, S. N. Kavuri, "A review of process fault detection and diagnosis Part I: Quantitative model-based methods", Computers and chemical engineering, vol. 27, 2003, pp. 293-311.

[41] R. Isermann, "Model-based fault detection and diagnosis - Status and applications", Annual reviews in control, vol. 29, 2005, pp. 71-85.

[42] R. Isermann, P. Ballé, "Trends in the application of mode-based fault detection and diagnosis of technical processes", Control engineering practice, vol. 5 no. 5, 1997, pp. 709-719.

[43] P. M. Frank, E. A. Garcia, B. Köppen-Seliger, "Modelling for fault detection versus modelling for control", Mathematical and computer modelling of dynamic systems, vol. 7 no.1, 2001, pp.1-46.

[44] C. Angeli, A. Chatzinikolaou, "On-line fault detection techniques for technical systems: A survey", International journal of computer science and applications, vol. I no. 1, 2004, pp.12-30.

[45] K. Natesan, A. Purohit, S. W. Tam, "Material behavior in HTGR environments", NUREG/CR-6824, U.S. Nuclear Regulatory Commission, Washington D.C., February 2003.

[46] A. P. George, "Introduction to the Pebble Bed Modular Reactor (PBMR)", Doc. 009949-185, PBMR (Pty.) Ltd., South Africa, 2001.

[47] C. Nieuwoudt, "Demonstration plants operations summary", Doc. MS000- 000574-4005 rev. 4, PBMR (Pty.) Ltd., South Africa, 2002.

[48] P. G. Rousseau, G. P. Greyvenstein, B. W. Botha and C. G. du Toit, "Sensitivity analysis of the PBMR gas cooled reactor with the aid of a simplified simulation model", IFAC, 2000.

[49] "Flownex user manual", Version 6.9, M-Tech Industrial (Pty.) Ltd., Potchefstroom, South Africa, 2006.

[50] J. P. Holman, "Heat transfer", New York: McGraw Hill, 1989.

[51] H. Cohen, G. F. C. Rogers, H. I. H. Saravanamuttoo, "Gas turbine theory", Fourth edition, Longman group Ltd, England, 1996.

[52] S. Yung, "Signal processing in local sensor validation", PhD Dissertation, University of Oxford, England, 1992.

[53] S. K. Young, D. W. Clarke, "Local sensor validation", Measurement and control, vol. 22, 1989, pp.132.

[54] J. W. Hines, A. V. Gribok, B. Rasmussen, S. Wagerich, "On-line sensor monitoring techniques: How accurate are they?", IFPAC 2003: Seventeenth international forum process analytical chemistry, Scottsdale, Arizona, 2003.

[55] T. N. Pranatyasto, S. Qin, "Sensor validation and process fault diagnosis for FCC units under MPC feedback", Control engineering practice, vol. 9, 2001, pp. 877-888.

[56] J. T. Yang, "Principle component analysis and factor analysis", in: Multivariate statistical methods in quality management, Digital engineering library, McGraw-Hill, 2004.

[57] J. E. Jackson, "A user's guide to principal components", Wiley-Interscience, New York, 1991.

[58] B. M. Wise, N. L. Ricker, "Recent advances in multivariate statistical process control: improving robustness and sensitivity", Proceedings of the IFAC, 1991.

[59] R. Dunia, S. J. Qin, T. F. Edgar, "Identification of faulty sensors using principal component analysis", AIChE Journal, vol. 42 no. 10, 1996, pp. 2797-2812.

[60] S. J. Qin, R. Dunia, "Determining the number of principal components for best reconstruction", Journal of process control, vol. 10, 2000, pp. 245-250.

[61] K. Goebel, A. M. Agogino, "Fuzzy sensor fusion for gas turbine power plants", Proc. SPIE Conference on sensor fusion: architectures, algorithms, and applications III, Orlando, FL, vol. 3719, 1999, pp. 52-61.

[62] J. F. Pritchard, "Development of a linear model of the Brayton cycle", Plant control, Doc. 013202-318, PBMR (Pty.) Ltd., South Africa, 2002.

[63] International Atomic Energy Agency, "Modern instrumentation and control for nuclear power plants: A guidebook", Technical reports series no. 387, IAEA, Vienna, 1999.

[64] A. Bejan, "Heat transfer". John Wiley & Sons, Inc., New York, 1993.

[65] A. Bejan, "Entropy generation minimization". CRC Press, Florida, 1996.

[66] Matlab, "User guide", R14 version 7, 2004.

[67] O. Widlund, G. Geffraye, J. Van Ravenswaay, N. Tauveron, W. Van Niekerk, "Comparison of the thermal-fluid analysis codes Cathare and Flownex with experimental data from the Pebble Bed Micro Model", 4th International conference on heat transfer, Fluid mechanics and thermodynamics, Cairo, Egypt, 2005.

[68] J. T. Labuschagne, "PBMR micro model data pack", North-West University, no. PBMM-0066 rev. 2, Potchefstroom, South Africa, 2003.

[69] E. Kreysig, "Advanced engineering mathematics", 7th edition, John Wiley & Sons, Canada, 1993.

Appendices

A. Normal distribution and the central limit theorem

Consider a set of independent random variables that have the same distribution function x_1, x_2,..., x_n. Since their distributions are identical, they have the same mean μ and variance σ^2. Let $y_n = x_1 + x_2 + \ldots + x_n$. The central limit theorem states that the variable

$$z_n = \frac{y_n - n\mu}{\sigma\sqrt{n}} \tag{A.1.1}$$

is asymptotically normal with mean 0 and variance 1. This is the distribution function $F_n(x)$ of z_n that satisfies [69]

$$\lim_{n\to\infty} F_n(z_n) = \frac{1}{\sqrt{2\pi}} \int_{\xi=-\infty}^{x} e^{-\xi^2/2} d\xi \tag{A.1.2}$$

It is important to note that the distribution type of the x variables is not important. Although the theorem states the equality only for n in the limit, the standard normal distribution is a good approximation even if the observations are limited in size [6].

Therefore, if the distribution of the x variables is known, the approximation error can be computed for any number of observations.

B. The temperature-pressure versus enthalpy-entropy graphs

As discussed in Chapter 6, the shape of the *h-s* graph remains approximately constant over the operating range for power control with the ICS. For control options comprising the control valves, the reference model needs minimal adjustment by means of the *VS*. This is one of the primary motivations for the transformation from temperature-pressure (*T-P*) to *h-s*. For different power levels, the *h-s* graph shifts to the correct absolute pressure, but maintains the constant shape. In contrast, the shape of the *T-P* graph changes in the *P*-plane due to constant pressure ratios at different power levels.

Figure B.1.1 (a) and (b) shows the shift direction and shape of the theoretical *h-s* and *T-P* graphs for full and reduced power levels. Figure B.1.1 (c) and (d) shows the graphs for the practical cycle of the PBMR (specific entropy is referenced to T_0 = 0 °C and P_0 = 10 MPa). The graphs show that the transformation to *h-s* results in a constant graph over the power range. For this reason, one graph can be used as reference model.

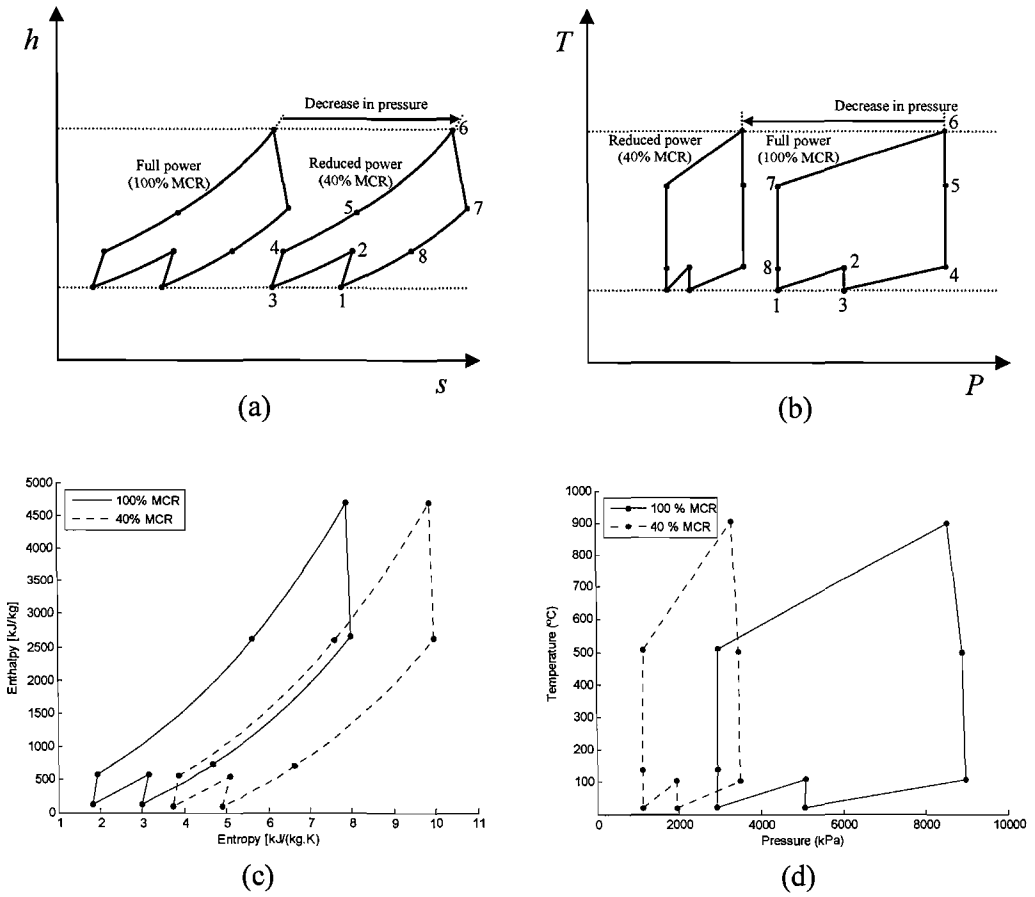

Fig. B.1.1 Theoretical and practical graphs of the Brayton cycle for full and reduced power: (a) *h-s*; (b) *T-P*; (c) PBMR *h-s*; (d) PBMR *T-P*

B.1 The *h-s* graph shape at different power levels

To show that the transformation from *T-P* to *h-s* improves model performance[1], an analytical prove for the constant shape of the *h-s* graph at different power levels is provided subject to power control with the ICS and no valve operation.

Let x and y be different operating points with $[s^1,h^1]$ and $[s^2,h^2]$ any two successive points on the *h-s* graph. Let $[P^1,T^1]$ and $[P^2,T^2]$ be the corresponding temperatures and pressures at these points on the graph. Since the mapping from T to h is calculated by (6.2.3) and given that the temperatures stay constant over the operating range, it follows that the enthalpy is also constant.

Given that the pressure ratios stay constant at different operating points, the pressure ratios for any two successive points are given by (B.1.1)

$$P_x^2 / P_x^1 = c_x^P, \quad P_y^2 / P_y^1 = c_y^P \tag{B.1.1}$$

with $c_x^P = c_y^P$ the pressure ratios. From (6.2.5) it follows that

$$\text{At operating point } x\text{: } \Delta s_x = c_p \ln\left(\frac{T_x^2}{T_x^1}\right) - R\ln\left(\frac{P_x^2}{P_x^1}\right) \tag{B.1.2}$$

$$\text{At operating point } y\text{: } \Delta s_y = c_p \ln\left(\frac{T_y^2}{T_y^1}\right) - R\ln\left(\frac{P_y^2}{P_y^1}\right) \tag{B.1.3}$$

Under normal operating conditions, the shape will be a constant only if $\Delta s_x = \Delta s_y$ and $\Delta h_x = \Delta h_y$. Therefore (B.1.2) and (B.1.3) must be equal and can be written as

$$c_p \ln\left(\frac{T_x^2}{T_x^1}\right) - R\ln\left(\frac{P_x^2}{P_x^1}\right) = c_p \ln\left(\frac{T_y^2}{T_y^1}\right) - R\ln\left(\frac{P_y^2}{P_y^1}\right)$$

$$\therefore c_p\left(\ln\left(\frac{T_x^2}{T_x^1}\right) - \ln\left(\frac{T_y^2}{T_y^1}\right)\right) + R\left(\ln\left(c_y^P\right) - \ln\left(c_x^P\right)\right) = 0$$

$$\therefore c_p \ln\left(\frac{T_x^2 T_y^1}{T_x^1 T_y^2}\right) + R\left(\ln\left(c_y^P\right) - \ln\left(c_x^P\right)\right) = 0$$

$$\therefore c_p \ln(1) + R(0) = 0 \tag{B.1.4}$$

Equation (B.1.4) shows that $\Delta s_x = \Delta s_y$. Since the enthalpy is constant over the operating range, it follows that $\Delta h_x = \Delta h_y$. This proves that the transformation from *T-P* to *h-s* results in a constant shape between successive points for different operating points.

[1]Model performance in this context signifies the error between the calculated Flownex and predicted (derived by the reference model) values. The minimal error corresponds to the better performance.

B.2 The *T-P* and *h-s* models applied to the PBMR

Following the validation of the constant shape of the *h-s* graph at different power levels, the 100 % MCR operating point is used to compare model performance. As described in section 6.6.5, the first node (LPC inlet) is used as reference for each operating point. To evaluate model performance, the same set of features is extracted from the PBMR *T-P* graph at 100 % MCR. By using the extracted features and the reconstruction procedure discussed in section 6.6.5, the reference graphs are reconstructed at different operating points.

To demonstrate the improvement in model performance between the two devised reference models, six operating points are chosen. At each of the operating points, the Flownex model is used to calculate the values for *T*, *P*, *h* and *s*. By reconstructing the reference models at the different operating points, the values for *T*, *P*, *h* and *s* are derived analytically. Tables B.2.1 and B.2.2 summarize the results for *T-P* and *h-s* at the six operating points. The *T*, *P*, *h* and *s* are normalized with the following reference values: 900 °C, 9000 kPa, 5000 kJ/kg and 10 kJ/(kg.K) respectively. The notation in the tables is as follows: FL is the value calculated with Flownex, RM is the value derived by the reference model (*T-P* or *h-s*) and *Diff* is the absolute difference between the Flownex and reference models in percentage (%).

Since node one is used as reference point for the reconstruction of the graphs, it can be seen from Tables B.2.1 and B.2.2 that the errors between Flownex and the reference models are very small for this node. Conversely, Table B.2.1 shows that the percentage error between Flownex and the reference *T-P* model is large over the entire power range. This is expected as Fig. B.1.1 (d) showed a large difference between the 100 % MCR and 40 % MCR graphs in the *p*-plane. The transformation to *h-s* improves model performance by more than 32 % for reduced power and Table B.2.2 shows that the error between the models is less than 0.25 % for all power levels.

Node	90 % MCR		80 % MCR		70 % MCR		60 % MCR		50 % MCR		40 % MCR	
	FL	RM	FL	RM	FL	RM	FL	RM	FL	RM	FL	RM
T1	0.0255	0.0254	0.0252	0.0254	0.0250	0.0254	0.0252	0.0254	0.0253	0.0254	0.0253	0.0254
T2	0.1214	0.1211	0.1212	0.1211	0.1211	0.1211	0.1214	0.1211	0.1216	0.1211	0.1219	0.1211
T3	0.0244	0.0243	0.0241	0.0243	0.0239	0.0243	0.0236	0.0243	0.0234	0.0243	0.0240	0.0243
T4	0.1185	0.1181	0.1186	0.1181	0.1188	0.1181	0.1189	0.1181	0.1189	0.1181	0.1189	0.1181
T5	0.5554	0.5545	0.5548	0.5545	0.5551	0.5545	0.5551	0.5545	0.5555	0.5545	0.5555	0.5545
T6	0.9996	0.9995	0.9994	0.9995	0.9994	0.9995	0.9995	0.9995	0.9997	0.9995	0.9998	0.9995
T7	0.5672	0.5672	0.5665	0.5672	0.5661	0.5672	0.5661	0.5672	0.5661	0.5672	0.5662	0.5672
T8	0.1549	0.1554	0.1548	0.1554	0.1542	0.1554	0.1542	0.1554	0.1542	0.1554	0.1544	0.1554
P1	0.2892	0.2892	0.2547	0.2547	0.2222	0.2222	0.1899	0.1899	0.1576	0.1576	0.1253	0.1253
P2	0.5058	0.5313	0.4457	0.4969	0.3890	0.4643	0.3321	0.4321	0.2754	0.3997	0.2193	0.3675
P3	0.5027	0.5279	0.4430	0.4934	0.3866	0.4609	0.3301	0.4286	0.2737	0.3963	0.2179	0.3640
P4	0.8923	0.9634	0.7870	0.9290	0.6872	0.8964	0.5875	0.8642	0.4877	0.8318	0.3880	0.7996
P5	0.8841	0.9544	0.7798	0.9199	0.6809	0.8874	0.5821	0.8551	0.4833	0.8228	0.3844	0.7905
P6	0.8496	0.9160	0.7491	0.8816	0.6539	0.8490	0.5587	0.8168	0.4636	0.7844	0.3685	0.7521
P7	0.2953	0.2959	0.2602	0.2615	0.2271	0.2289	0.1942	0.1967	0.1612	0.1643	0.1282	0.1321
P8	0.2911	0.2913	0.2564	0.2568	0.2237	0.2243	0.1912	0.1920	0.1586	0.1597	0.1262	0.1274
Diff	3.64		7.93		12.67		18.28		25.00		33.16	

Table B.2.1 Temperature and pressure results for the Flownex and reference models.

Node	90 % MCR		80 % MCR		70 % MCR		60 % MCR		50 % MCR		40 % MCR	
	FL	RM	FL	RM	FL	RM	FL	RM	FL	RM	FL	RM
*h*1	0.0256	0.0258	0.0251	0.0258	0.0247	0.0258	0.0247	0.0258	0.0246	0.0258	0.0244	0.0258
*h*2	0.1165	0.1166	0.1160	0.1166	0.1155	0.1166	0.1154	0.1166	0.1153	0.1166	0.1153	0.1166
*h*3	0.0259	0.0262	0.0253	0.0262	0.0248	0.0262	0.0241	0.0262	0.0235	0.0262	0.0238	0.0262
*h*4	0.1162	0.1165	0.1156	0.1165	0.1152	0.1165	0.1147	0.1165	0.1142	0.1165	0.1144	0.1165
*h*5	0.5240	0.5238	0.5229	0.5238	0.5227	0.5238	0.5222	0.5238	0.5221	0.5238	0.5218	0.5238
*h*6	0.9388	0.9391	0.9381	0.9391	0.9377	0.9391	0.9372	0.9391	0.9370	0.9391	0.9366	0.9391
*h*7	0.5319	0.5321	0.5311	0.5321	0.5306	0.5321	0.5304	0.5321	0.5303	0.5321	0.5302	0.5321
*h*8	0.1465	0.1472	0.1462	0.1472	0.1455	0.1472	0.1452	0.1472	0.1447	0.1472	0.1451	0.1472
*s*1	0.3216	0.3216	0.3474	0.3474	0.3754	0.3754	0.4084	0.4084	0.4474	0.4474	0.4950	0.4950
*s*2	0.3383	0.3381	0.3643	0.3639	0.3925	0.3919	0.4257	0.4249	0.4648	0.4639	0.5126	0.5115
*s*3	0.2049	0.2049	0.2307	0.2307	0.2587	0.2587	0.2911	0.2917	0.3296	0.3307	0.3779	0.3783
*s*4	0.2169	0.2165	0.2430	0.2423	0.2714	0.2704	0.3041	0.3033	0.3427	0.3423	0.3903	0.3899
*s*5	0.5879	0.5875	0.6136	0.6133	0.6420	0.6414	0.6745	0.6744	0.7134	0.7133	0.7610	0.7609
*s*6	0.8127	0.8128	0.8388	0.8386	0.8670	0.8666	0.8997	0.8996	0.9386	0.9386	0.9863	0.9862
*s*7	0.8227	0.8230	0.8486	0.8488	0.8767	0.8768	0.9092	0.9098	0.9479	0.9488	0.9955	0.9964
*s*8	0.4925	0.4932	0.5187	0.5190	0.5464	0.5471	0.5789	0.5800	0.6177	0.6190	0.6656	0.6666
Diff	0.03		0.09		0.13		0.20		0.24		0.21	

Table B.2.2 Enthalpy and entropy results for the Flownex and reference models.

The errors observed in h and s are due to a small change in cycle efficiency at reduced power levels. For the purpose of fault detection and fault signature generation, the errors are acceptable. To demonstrate the improvement in model performance, the manifold leakage to turbine inlet fault is used as an example and illustrated in Fig B.2.1. The normalized error fault signatures are created for T, P, h and s at 40 % and 100 % MCR respectively. Although the statement regarding constant signatures for h and s is discussed in section 6.6.5, this figure illustrates the signatures for T and P.

The T and h signatures showed similar results as calculated in Tables B.2.1 and B.2.2. As expected, the P signatures did not show any similarities for the different power levels (large P errors observed in Table B.2.1). The figure shows that the transformed s signatures are highly correlated at different power levels and can therefore be characterized with one fault signature. The transformation to h-s is thus important since the faults will be characterized with different T-P signatures at different operating points.

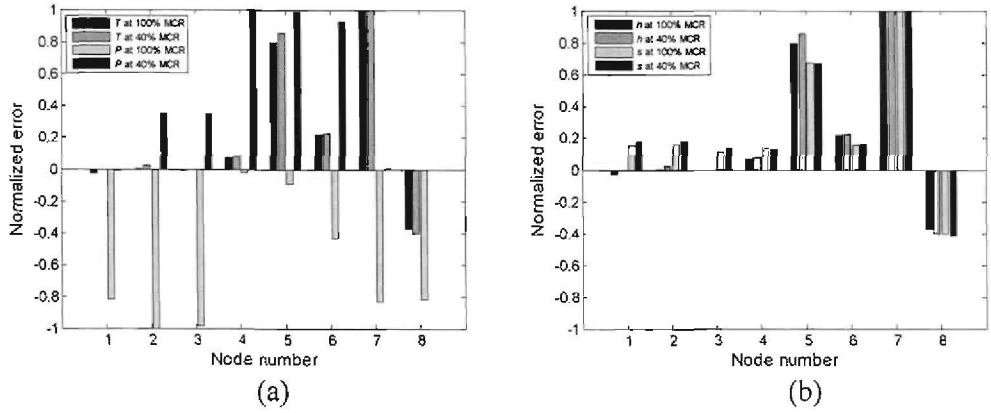

Fig. B.2.1 Normalized error signatures for fault 15: (a) T-P; (b) h-s.